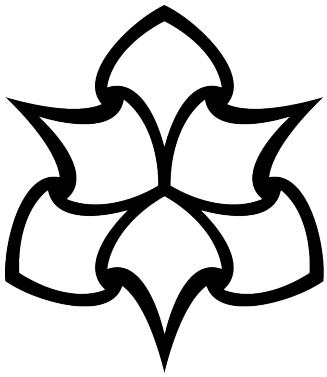

NEXT GENERATION SCREEN-PRINTED ENERGY-STORAGE DEVICES BASED ON CARBON NANOMATERIALS

P M HALLAM

PhD 2013

NEXT GENERATION SCREEN-PRINTED ENERGY-STORAGE DEVICES BASED ON CARBON NANOMATERIALS

Philip Mark Hallam

Submitted in partial fulfilment of the requirements of Manchester Metropolitan University for the degree of Doctor of Philosophy

2013

School of Science and the Environment
Division of Chemistry and Environmental Science
Manchester Metropolitan University

This thesis reports on the development of novel screen-printed electrodes for use as energy-storage (supercapacitor) devices. The thesis covers four primary topics; the first considers the basic fundamentals of electrochemistry, which are essential for understanding and furthering the development of energy-storage devices.

Section two reports on the electrode materials, highlighting the important contribution of each material towards the electrochemical mechanisms involved at their surfaces. Furthermore, a novel, yet simplistic methodology for characterising various carbon nanomaterials (in terms of their edge and basal content) without recourse to expensive laboratory equipment is presented. Section three describes the processes involved in screen printing but moreover, illustrates how the modification of the electrode with nanomaterials can transform a seemingly redundant electrode into a highly desirable and sometimes ideal option targeted towards the application of energy-storage. The development of true screen-printed supercapacitors utilising transition metal nanomaterials, shows proof of concept for the future advancement of screen-printed electrodes as thin, highly flexible energy-storage devices.

The final section highlights some of the limitations found in electrical impedance spectroscopy that are often overlooked. Lastly, a simple methodology is described that has been found to offer improved accuracy in the galvanostatic (charge/discharge) measurement of capacitance.

The primary focus of this thesis is to investigate and evaluate carbon-based, screen-printed electrochemical platforms as a foundation for next-generation energy-storage devices through the development and integration of novel nanomaterials. The objectives of this study are described in greater detail below:

Objectives

1) To establish the impact of carbon nanomaterials designed for the enhancement of energy-storage devices such as supercapacitors. Quantification of edge-plane sites (reactivity sites) of carbon nano-materials and determination of the relationship between electron transfer and material composition.

2) Explore methodologies for producing carbon/nanomaterial composites. A fundamental approach exploring mass transport, electron transfer and related principal parameters.

3) To design, assess and develop new supercapacitors based upon novel nanomaterials and identify/understand their physical interactions, in particular, the synthesis of micro- and nano-particle loaded screen-printed electrodes to be used as the primary working electrodes in next generation supercapacitors.

4) Construction of optimal working prototype. Performance and electrochemical characteristics to be compared with current literature and state-of-the-art, commercially available supercapacitors.

I would like to offer my thanks to Dr Craig Banks, firstly for gifting me this opportunity but furthermore for the unprecedented knowledge and continued support he has afforded me throughout the past few years. I would like to give a special mention and thanks to Dimitrios Kampouris in addition to all members of the Banks research group, who have helped me stay the course throughout my studies.

Finally, I would not have been able to complete my studies without the selfless sacrifices made by my grandmother Vera Goodwin, father Mark Brian and mother Karen Anne Hallam, for which I am forever grateful. It is unto them, as only proper, I dedicate this thesis.

“A science is any discipline in which the fool of this generation can go beyond the point reached by the genius of the last.”

Max Gluckman, Politics, Law and Ritual, 1965

TABLE OF CONTENTS

LIST OF TABLES

LIST OF SCHEMES

LIST OF FIGURES

AC	Alternating current
BDDE	Boron-doped diamond
BPPG	Basal-plane pyrolytic graphite
CE	Counter electrode
CNT	Carbon nanotube
CPE	Constant phase element
CTCC	Carbo-thermal carbide conversion
CV	Cyclic voltammetry
CVD	Chemical vapour deposition
DC	Direct current
EC	Electrochemical capacitor
EDAX	Energy-dispersive X-ray spectroscopy
EDL	Electric double layer
EDLC	Electric double layer capacitor
EIS	Electrochemical impedance spectroscopy
EMF	Electromotive force
EPPG	Edge-plane pyrolytic graphite
ESR	Equivalent series resistance
GCE	Glassy carbon electrode
HOPG	Highly ordered pyrolytic graphite
HRTEM	High resolution transmission electron microscope

IHP	Inner Helmholtz plane
IR	Infra-red
MWNT	Multi-walled nanotube
OHP	Outer Helmholtz plane
RBM	Radial breathing mode
RE	Reference electrode
RGO	Reduced graphene oxide
RSD	Relative standard deviation
SCE	Saturated calomel electrode
SCNR	Solid carbon nanorod
SEM	Scanning electron microscope
SPE	Screen-printed electrode
SWNT	Single walled nanotube
TEM	Transmission electron microscope
TGA	Thermogravimetric analysis
WE	Working electrode
WHO	World health organisation
XRD	X-ray diffraction

1.1 FUNDAMENTAL CONCEPTS

1.1.1 ELECTROANALYSIS

Electro-analytical techniques are concerned with the interaction between electricity and chemistry, specifically the measurements of electrical quantities, such as current, potential, or charge, and their relationship to chemical parameters. In contrast to many chemical measurements that involve bulk solutions, electrochemical processes take place at the electrode-solution interface. These electrochemical techniques can be characterised into two principle types; potentiometric and potentiostatic measurements, differentiated via the electrical signal used for quantification. Equally both techniques require at least two electrodes (conductors) and a contacting sample (electrolyte) solution, this constitutes the electrochemical cell. The surface of the electrode represents the junction between an ionic conductor and an electronic conductor. The electrode that responds to the target analyte(s) is termed the working electrode, the second, termed the reference electrode, is of constant potential (that is, independent of the properties of the solution). Electrochemical cells can be classified as electrolytic (consuming energy from an external source) or galvanic (producing electrical energy). Controlled-potential (potentiometric) techniques deal with the study of charge-transfer processes at the electrode-solution interface based on dynamic (non-zero current) situations. In this situation, the electrode potential is used to drive an electron-transfer reaction, where the resulting current is measured. This is effectively "electron pressure", forcing a chemical species to either gain or lose an electron (reduction and oxidation respectively). The advantages of using controlled-potential techniques include high sensitivity and selectivity towards electroactive species where extremely low limits of detection (nanomolar) can be achieved with very small sample volumes (5-20μL). In addition

to the extensive array of electrode materials now available, permitting the assay of unusual environments.

1.1.2 FARADAIC PROCESSES

The intention of controlled-potential electro-analytical experiments is to obtain a current response that is interrelated to the concentration of the target analyte. This is achieved by recording the transfer of electron(s) during the redox process of the analyte:

$$O + ne^- \rightleftharpoons R \tag{1.1}$$

where O and R are the oxidised and reduced forms, respectively, of the redox couple. This reaction will occur in a potential region that makes the electron transfer thermodynamically or kinetically favourable. Within systems that are controlled by the law of thermodynamics, the potential of the electrode can be used to establish the concentration of the electroactive species [$c_o(0, t)$ and $c_R(0, t)$ where c_o and c_R simply represent the concentration of the oxidised and reduced forms, respectively] at the surface (distance from surface (x) = 0) at time (t) according to the *Nernst equation*:

$$E = E^o + \frac{2.3\,RT}{nF} \log \frac{C_O\,(0,t)}{C_R(0,t)} \tag{1.2}$$

At standard conditions (298 K):

$$E = E^o + \frac{0.059}{n} \log \frac{C_O\,(0,t)}{C_R(0,t)} \tag{1.3}$$

where E is the potential at which the peak is truly measured, E^o is the standard potential for the redox reaction (see Table 1.1), R is the universal gas constant (8.314 J K^{-1} mol^{-1}), T is the temperature (in Kelvin), n is the number of electrons transferred in the reaction, and F is the Faraday constant (96,485.33 C mol^{-1}).

Alternatively the *Nernst equation* can be expressed as:

$$E = E^{o} + (RT/nF)\, ln(a_{P}/a_{R}) \quad (1.4)$$

where a_{P} and a_{R} are the standard activities of the products and reactants respectively.

For systems with negative E^{o} values, the oxidised reactants tend to be reduced thus the forward reaction (*i.e.* reduction) becomes more favourable. The current produced, resulting from the change in oxidation state of the electroactive species is termed the Faradaic current because it obeys Faraday's law (that is the reaction of 1 mole involves a change of n x 96,485.33 C). The Faradaic current is a direct measure of the rate of redox reaction. The resulting current-potential plot, known as a *voltammogram*, is a display of current signal (vertical axis) versus the excitation potential (horizontal axis). The exact shape and magnitude of the voltammetric response is governed by the processes involved in the electrode reaction. The total current is the summation of the Faradaic currents for the sample and blank solution, as well as the non-Faradaic charging background current.

The reaction route undertaken at the electrode can be quite complicated, sometimes involving a sequence of different phases. The rate of such a reaction is determined by the slowest step in the sequence. Simple reactions involve only the mass transport of the electroactive species to the electrode's surface, the electron transfer across the interface, and the transport of the product back to the bulk solution. More complex reactions involve additional chemical and surface reactions that precede or follow the actual electron transfer. The overall rate of the reaction, and thus the measured current, may be limited by the mass transport of the reactant or the rate of electron transfer. The slowest process will be the rate-determining step. Determining whether a given reaction is controlled by the mass transport or electron transfer depends on the type of compound being measured and the experimental conditions (electrode material, media, operating potential, mode of mass transport, time scale,

etc.). Therefore the rate determining step of a given system may thus depend on the potential range under investigation. If the overall reaction is governed solely by the rate at which the electroactive species reaches the electrode's surface (*i*.e. a facile electron transfer), the current is said to be mass-transport limited. Such reactions are called Nernstian or reversible, because they obey thermodynamic relationships.

Table 1.1 Standard electrode potentials for aqueous solutions (298 K). [3]

Half Reaction	E / V	Half Reaction	E / V
$Li^{+} + e^{-} \rightarrow Li$	–3.04	$H^{+} + e^{-} \rightarrow \frac{1}{2} H_2$	0.00
$K^{+} + e^{-} \rightarrow K$	–2.92	$\frac{1}{2} Sn^{4+} + e^{-} \rightarrow \frac{1}{2} Sn^{2+}$	+0.15
$\frac{1}{2} Ca^{2+} + e^{-} \rightarrow \frac{1}{2} Ca$	–2.76	$Cu^{2+} + e^{-} \rightarrow Cu^{+}$	+0.16
$Na^{+} + e^{-} \rightarrow Na$	–2.71	$\frac{1}{2} Cu^{2+} + e^{-} \rightarrow \frac{1}{2} Cu$	+0.34
$\frac{1}{2} Mg^{2+} + e^{-} \rightarrow \frac{1}{2} Mg$	–2.37	$2\ H_2O + O_2 + 4\ e^{-} \rightarrow 4\ OH^{-}$	+0.40
$\frac{1}{3} Al^{3+} + e^{-} \rightarrow \frac{1}{3} Al$ (0.1M NaOH)	–1.71	$Cu^{+} + e^{-} \rightarrow Cu$	+0.52
$\frac{1}{2} Mn^{2+} + e^{-} \rightarrow \frac{1}{2} Mn$	–1.18	$\frac{1}{2} I_2 + e^{-} \rightarrow I^{-}$	+0.54
$H_2O + e^{-} \rightarrow \frac{1}{2} H_2 + OH^{-}$	–0.83	$\frac{1}{2} O_2 + H^{+} + e^{-} \rightarrow \frac{1}{2} H_2O_2$	+0.68
$\frac{1}{2} Zn^{2+} + e^{-} \rightarrow \frac{1}{2} Zn$	–0.76	$Fe^{3+} + e^{-} \rightarrow Fe^{2+}$	+0.77
$\frac{1}{2} Fe^{2+} + e^{-} \rightarrow \frac{1}{2} Fe$	–0.44	$\frac{1}{2} Hg^{2+} + e^{-} \rightarrow \frac{1}{2} Hg$	+0.79
$\frac{1}{2} Cr^{3+} + e^{-} \rightarrow \frac{1}{2} Cr$	–0.41	$Ag^{+} + e^{-} \rightarrow Ag$	+0.80
$\frac{1}{2} Cd^{2+} + e^{-} \rightarrow \frac{1}{2} Cd$	–0.40	$\frac{1}{3} NO_3^{-} + \frac{4}{3} H^{+} + e^{-} \rightarrow \frac{1}{3} NO + \frac{2}{3} H_2O$	+0.96
$\frac{1}{2} Co^{2+} + e^{-} \rightarrow \frac{1}{2} Co$	–0.28	$\frac{1}{2} Br_2\ (l) + e^{-} \rightarrow Br^{-}$	+1.06
$\frac{1}{2} Ni^{2+} + e^{-} \rightarrow \frac{1}{2} Ni$	–0.23	$\frac{1}{4} O_2 + H^{+} + e^{-} \rightarrow \frac{1}{2} H_2O$	+1.23
$\frac{1}{2} Sn^{2+} + e^{-} \rightarrow \frac{1}{2} Sn$	–0.14	$\frac{1}{2} MnO_2 + 2H^{+} + e^{-} \rightarrow \frac{1}{2} Mn^{2+} + H_2O$	+1.21
$\frac{1}{2} Pb^{2+} + e^{-} \rightarrow \frac{1}{2} Pb$	–0.13	$\frac{1}{2} Cl_2 + e^{-} \rightarrow Cl^{-}$	+1.36
$\frac{1}{3} Fe^{3+} + e^{-} \rightarrow \frac{1}{3} Fe$	–0.04	$\frac{1}{3} Au^{3+} + e^{-} \rightarrow \frac{1}{3} Au$	+1.52

1.1.3 MASS TRANSPORT-CONTROLLED REACTIONS

Mass transport arises from three different modes:

- *Diffusion* – the spontaneous movement of particles under the influence of concentration gradient (i.e. from regions of high concentration to regions of lower concentrations), aimed at minimizing concentration differences.

- *Migration* – movement of charged particles along an electric field (i.e. the charge is carried through the solution by ions according to their transference number).

- *Convection* – transport to the electrode by a gross physical movement, such as stirring or flow of the solution with rotation or vibration of the electrode (i.e. forced convection) or attributed to density gradients (i.e. natural convection).

These modes of mass transport are illustrated in Figure (1.1).

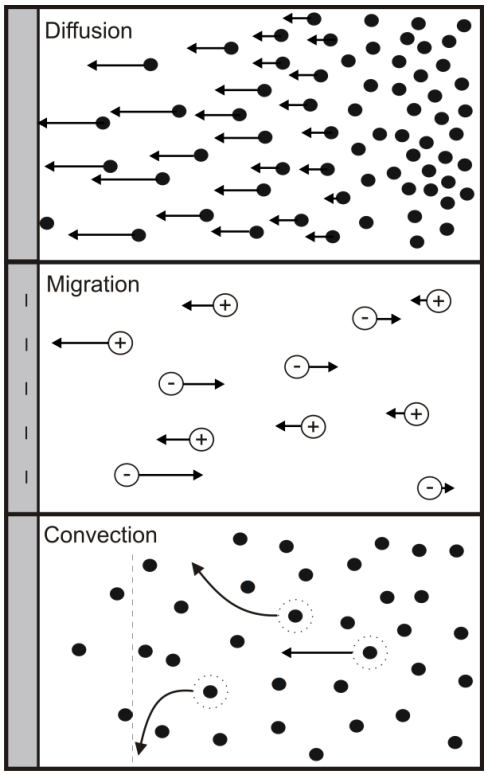

Figure 1.1 Three modes of mass transport towards an electrode surface.

The flux (J) is the measure of the rate of mass transport at a fixed point. It is defined as the number of molecules penetrating a unit area of an imaginary plane in a unit of time, and has the units of mol cm^{-2} s^{-1}. The flux to the electrode surface is described mathematically by a differential equation, known as the *Nernst-Planck equation* given here for one dimension:

$$J(x,t) = -D\frac{\partial c(x,t)}{\partial x} - \frac{zFDc(x,t)}{RT}\frac{\partial \phi(x,t)}{\partial x} + c(x,t)\,V(x,t) \qquad (1.5)$$

where D is the diffusion coefficient (cm^{-2} s^{-1}, D typically ranges between 10^{-5} and 10^{-6} cm^{-2} s^{-1}), $\partial c(x,t)/\partial x$ is the concentration gradient (at distance x and time t), $\partial \phi(x,t)/\partial x$ is the potential gradient, z and $c(x,t)$ are the charge and concentration respectively of the electroactive species, and $V(x,t)$ is the hydrodynamic velocity (in the x direction) in aqueous media.. The current (i) is directly proportional to the flux:

$$i = -nFAJ \qquad (1.6)$$

where n is the number of electrons transferred per molecule and A is the area of the electrode.

As shown by equation (1.5), the situation is relatively complex when the three modes of mass transport take place simultaneously. This impediment makes it particularly difficult to relate the current to the analyte concentration. The situation can be simplified significantly by suppressing the electromigration or convection, through the addition of surplus salt or the use of a quiescent solution respectively. Under these conditions, the movement of the electroactive species is limited by diffusion. The reactions that transpire at the surface of the electrode produce a concentration gradient adjacent to the surface, thus resulting in a diffusional flux. Consequently, equations prevailing over diffusion processes are applicable to many electro-analytical procedures.

Fick's first law illustrates how the rate of diffusion adjacent to the surface (*i.e.* the flux) is directly proportional to the slope of the concentration gradient:

$$J(x,\ t) = -D\frac{\partial C(x,t)}{\partial x} \tag{1.7}$$

Combining equations (1.6) and (1.7) yields a general expression for the current response:

$$i = -nFA\ D\frac{\partial C(x,t)}{\partial x} \tag{1.8}$$

Therefore, the current (at any time) is proportional to the concentration gradient of the electroactive species. As shown by the above equation, the diffusional flux is time dependant. Such dependence is described by Fick's second law (for linear diffusion):

$$\frac{\partial C(x,t)}{\partial t} = D\frac{\partial^2 C(x,t)}{\partial x^2} \tag{1.9}$$

This equation mirrors the rate of change with time to the concentration between parallel planes at points x and $(x + dx)$ (which is equal to the difference in flux at the two planes). Fick's second law is valid when assuming the condition that the parallel planes are perpendicular to the direction of diffusion. In contrast, for the case of diffusion towards a spherical electrode (where the lines are not quite parallel but are perpendicular to segments of the sphere), Fick's law has the form:

$$\frac{\partial C}{\partial t} = D\left(\frac{\partial^2 C}{\partial r^2} + \frac{2}{r}\frac{\partial C}{\partial r}\right) \tag{1.10}$$

where r is the distance from the electrode. Overall, Fick's 2nd law describes the flux and the concentration of the electroactive species as a function of position and time.

1.1.4 POTENTIAL STEP/SWEEP BASED EXPERIMENTS

The current-time relationship of such experiments can be explained through the resulting concentration-time profiles. The region within which the solution is depleted of reactants (O is this case) is known as the *diffusion layer*, its thickness is given by δ. The concentration gradient is sharp at first, with a thin diffusion layer. As the time period increases, the

diffusion layer expands, resulting in a decrease in the concentration gradient (see Figure 1.2). The slope of the concentration gradient is given by $(c_o(b,t) - c_o(0,t))/\delta$ where $c_o(b,t)$ and $c_o(0,t)$ are the bulk and surface concentrations of O respectively. The change in the slope, and hence the resulting current, is due to changes of both $c_o(0, t)$ and δ.

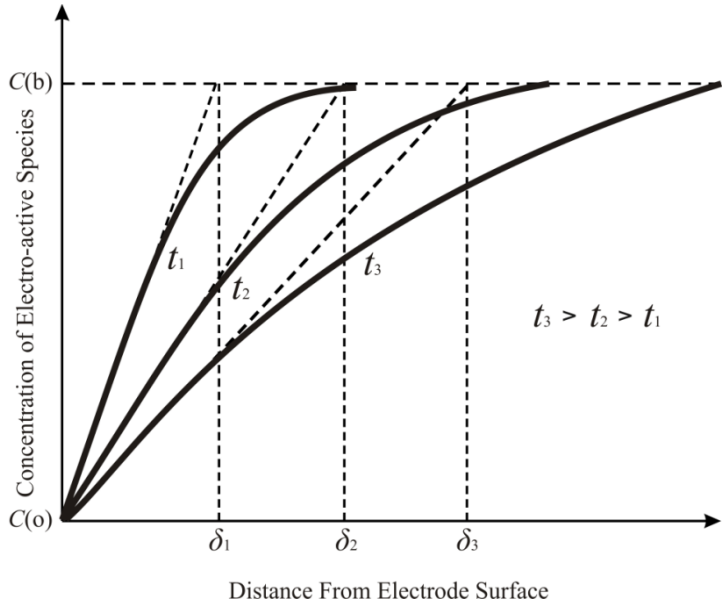

Figure 1.2 Concentration profiles for potential step based experiments over various times (t).

As the scanned potential approaches the standard potential (E^o) of the redox couple, the surface concentration rapidly changes in accordance with the Nernst equation (equation 1.2). At a potential (E) equal to E^o the concentration ratio is balanced ($c_o(0,t)/c_R(0,t) = 1$). At further negative potentials (>59 mV) than E^o, $c_R(0,t)$ is present at 10 fold excess ($c_o(0,t)/c_R(0,t) = 1/10$, n =1). The decrease in $c_o(0,t)$ is allied with an increase in the diffusion layer thickness, dominating the change in the slope after $c_o(0,t)$ approaches zero, resulting in a peak-shaped voltammogram. The current decrease (within a time-dependent concentration profile) is proportional to the square root of time, described by the *Cottrell equation*:

$$i(t) = \frac{nFAD_o C_o(b)}{(\pi D_o t)^{1/2}} + \frac{nFAD_o C_o(0)}{r} \qquad (1.11)$$

with $(\pi D_o t)^{1/2}$ corresponding to the diffusion layer thickness. Under constant stirring, the bulk concentration can be maintained at distance δ, hence, the concentration-distance profile become solely dependent on the change in surface concentration ($c_o(0, t)$) and no longer influenced by the surface electron transfer reaction.

1.1.5 REACTIONS CONTROLLED BY THE RATE OF ELECTRON TRANSFER

Reactions with sufficiently fast mass transport, [those controlled by the rate of electron transfer ($O + ne^- \underset{k_f}{\overset{k_b}{\rightleftharpoons}} R$)] display a different current-potential relationship to those discussed previously for mass transport-controlled reactions. The actual electron transfer step involves transfer of the electron between the conduction band of the electrode and a molecular orbital of O or R. The rate of the forward (oxidation) reaction, V_f, is given by:

$$V_f = k_f C_R(0, t) \tag{1.12}$$

while the reversed (reduction) reaction, V_b is given by:

$$V_b = k_b C_O(0, t) \tag{1.13}$$

where k_f and k_b are the forward and backward electrochemical rate constants respectively. These constants are dependent on the operating potential according to the following expressions:

$$k_f = k^o \exp[-\alpha n F(E - E^o)/RT] \tag{1.14}$$

$$k_b = k^o \exp[(1 - \alpha) n F(E - E^o)/RT] \tag{1.15}$$

where k^o is the electrochemical rate constant and α is the transfer coefficient. The value of k^o (in cm s^{-1}) reflects the reaction between the chosen electrode material and the particular reactant. The value of α (typically between 0.5 and 1) reflects the symmetry of the free energy curve with respect to the reactants and products. Thus, for symmetric curves, the

resulting α value will be close to 0.5. Overall, equations (1.14) and (1.15) indicate that changing the applied potential influences k_f and k_b exponentially. Thus positive and negative potentials speed up the formation of oxidation and reduction products, respectively. For oxidation, the energy of the electrons found in the donor orbital in R must be equal to or higher than the energy of the electrons in the electrode. Conversely, for reduction, the energy of the electrons found in the electrode must be higher than the electrons in the receptor orbital of R.

1.1.6 ACTIVATED COMPLEX THEORY

The effect of the operating potential upon the rate constant is best understood in terms of the free energy barrier. Figure (1.3) show a typical Morse potential energy curve for the reaction: O + ne$^-$ $\rightleftharpoons$ R at an inert metallic electrode (with O and R being soluble). The slender variance in the structure of O and R results in a barrier, associated with changes in bond lengths and bond angles, towards electron transfer. Hence, in order for the transition from one arrangement to its counterpart to occur, it is required to overcome the *free energy activation*, $\Delta G^{\dagger}$. The frequency at which the electron passes the energy barrier as it moves from the electrode to the electroactive complex (or rate constant) is given by:

$$k = A\mathrm{e}^{-\Delta G^{\dagger}/RT} \tag{1.16}$$

Thus, any change in $\Delta G^{\dagger}$ will have an influence on the rate of the reaction. If ΔG is increased, the rate of reaction will decrease. At equilibrium, the cathodic and anodic activation energies are equal ($\Delta G^{\dagger}_{c,0} = \Delta G^{\dagger}_{\alpha,0}$) and as such, the chance of electron transfer is the same in both directions. A, known as the *frequency factor,* is given as a function of the Boltzman constant k' and the Planck constant, h:

$$A = \frac{k'T}{h} \tag{1.17}$$

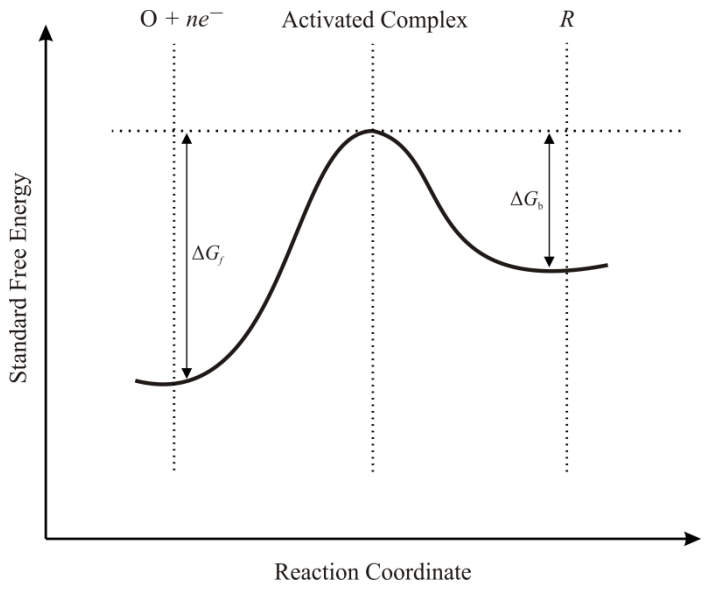

Figure 1.3 A typical Morse plot 'energy curve' of a redox process.

Varying the potential of the working electrode stimulates the free energy of its resident electrons, producing a 'more favourable' reaction pathway. Varying the potential (E) from equilibrium shifts the O + ne⁻ curve up or down by $\phi = -nFE$. Such a change, for the case of a positive E, is displayed (dotted line) in Figure (1.4).

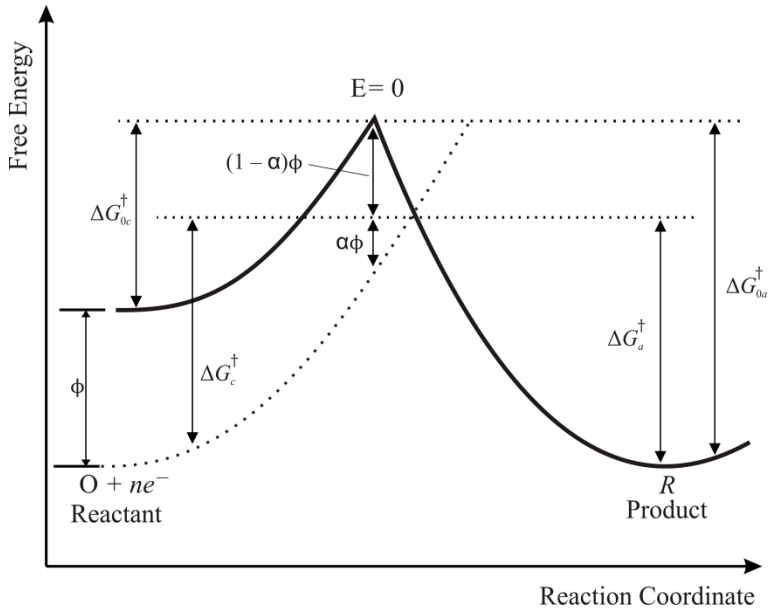

Figure 1.4 Effect of changes on the applied potential towards the free energies of oxidation and reduction.

Under these conditions the barrier for reduction, $\Delta G_c^{\dagger}$, is larger than $\Delta G_{0c}^{\dagger}$. Inspection of the curve reveals that only a fraction (α) of the energy shift ϕ is actually used to increase the activation barrier, thus accelerating the rate of reaction. Established on the symmetry of the two potential curves, the fraction (or transfer coefficient) of the reactant and products, ranges between the values of 0 and 1. In aqueous solutions, this value is typical found to lie amid 0.2 and 0.8. Consequently, α can be perceived as the degree of symmetry for the activation barrier. If α = 0.5 then the activated complex is exactly half way between the reagents and the products on the reaction coordinate, this is common for metallic electrodes with a simple electron transfer process.

1.1.7 REFERENCES

1. J. Wang, "*Analytical Electrochemistry*", 2nd ed.; Wiley-VCH; New York, **2001**.
2. A. J. Bard, L. R. Faulkner, "*Electrochemical Methods"*, 2nd ed.; Wiley: New York, **2001**.
3. R. G. Compton, C. E. Banks, *Understanding Voltammetry*, World Scientific Ltd., 1st edn. **2007**.

2.1 STUDY OF ELECTRODE REACTIONS

2.1.1 CYCLIC VOLTAMMETRY

Cyclic voltammetry is the most extensively used technique for acquiring qualitative information about electrochemical reactions. It tenders the rapid identification of *redox* potentials distinctive to the electroactive species, providing considerable information about the thermodynamics of a redox process, kinetics of heterogeneous electron-transfer reactions, coupled electrochemical reactions or adsorption processes. Cyclic voltammetry consists of scanning (linearly) the potential of the working electrode using a triangular potential wave form (Figure 2.1).

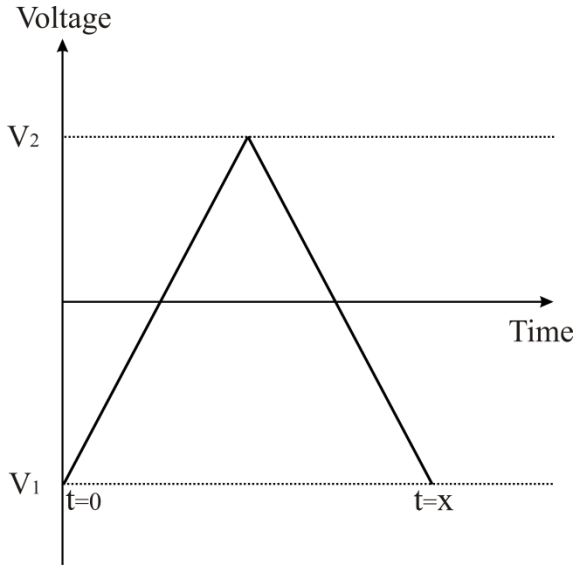

Figure 2.1 Voltage (potential) – time excitation signal utilised in cyclic voltammetric experiments.

Depending on the information sought, either single or multiple cycles can be performed. For the duration of the potential sweep, the potentiostat measures the resulting current that arises via the applied voltage (potential). The plot of current versus potential (voltage) is termed a 'cyclic voltammogram'. A Cyclic voltammogram is complex and

dependent on time along with many other physical and chemical properties. An illustration of a typical (reversible) redox couple is shown in Figure 2.2. Assuming only O is present initially, a negative potential scan is selected for the first half-cycle, originating from a potential where no reduction transpires. As the applied potential advances towards the characteristic E^{o} for the redox process (unique to each process), the cathodic current increases until a peak is reached. Once the potential region (or window) in which the reduction process arises is traversed, the direction of the sweep potential is reversed. In this stage of the scan, R molecules (generated in the first phase of the sweep) that accumulate near the surface of the electrode are re-oxidised back to O, resulting in an anodic (current) peak.

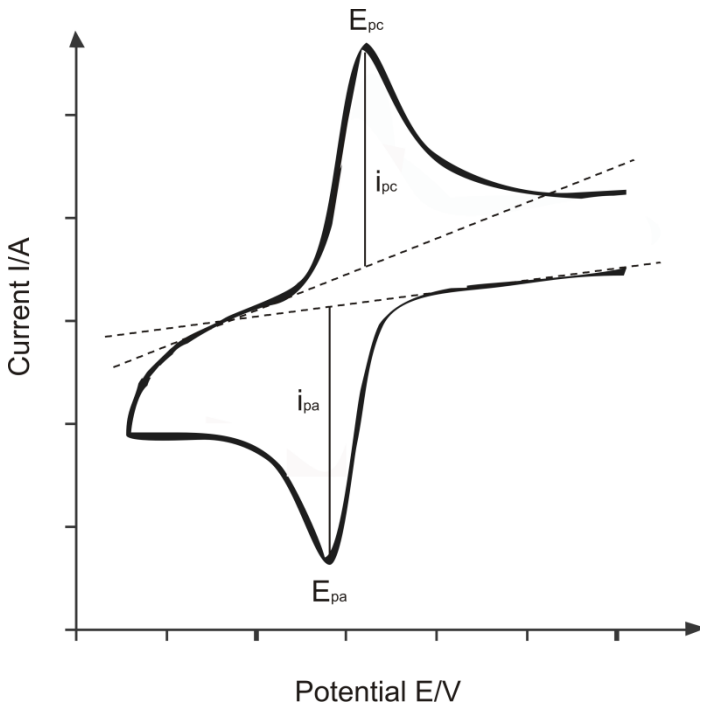

Figure 2.2 Typical cyclic voltammogram for a reversible redox process, where E_{pa} and E_{pc} correspond to the potential values at which the maximum anodic and cathodic peak currents (i_{pa} and i_{pc}, respectively) are recorded.

The characteristics of the peaks distinguished in a cyclic voltammetry are attributed to diffusion layers that occur near the electrode's surface (see chapter 1). The resulting current peaks are thus reflections of the continuous change in the concentration gradient with time. Therefore, increased peak current can be attributed to the achievement of diffusion control, while the current drop (beyond the peak) exhibits a $t^{-1/2}$ dependence (independent of the applied voltage/potential). Thus the reversal current displays a similar shape to the forward reaction.

2.2 INTERPRETATION OF DATA

The cyclic voltammogram is characterised by several key parameters. The two peak currents and peak potentials (observed visually), provide the basis for the diagnostic analysis of the voltammetric response.

2.2.1 NERNSTIAN (REVERSIBLE) SYSTEMS

The peak current tendered via a reversible redox couple is given by the *Randles–Ševćik equation*:

$$I_p = 0.4463 \left(\frac{F^3}{RT}\right)^{1/2} n^{3/2} A D^{1/2} C v^{1/2} \tag{2.1}$$

where I_p is the voltammetric peak current, F is the Faraday constant, A is the electrode area (in cm^2), D is the diffusion coefficient of the analyte (in $cm^2\ s^{-1}$), v is the applied scan rate (in $V\ s^{-1}$), C is the concentration of the electro-active species (in $mol\ cm^{-3}$) and n is the number of electrons transferred in the electrochemical process. Accordingly, the current is directly proportional to the concentration and increases with the square root of the scan rate. The ratio of forward-to-reverse peak currents should be equivalent for a simple reversible couple. However, the peak ratios can be strongly affected by chemical reactions coupled with the

redox system. Peak currents (or heights), are normally measured by extrapolating the preceding baseline current.

The position (or potential) of the peaks (E_p) is related to the standard potential of the redox process. The formal potential for a reversible system is centred between $E_{p,a}$ and $E_{p,c}$:

$$E^{o} = \frac{E_{p,a} + E_{p,c}}{2} \tag{2.2}$$

The peak separation (at 298 K) is given by:

$$\Delta E_p = E_{p,a} - E_{p,c} = \frac{0.059}{n} \text{ V} \tag{2.3}$$

Hence, the peak separation can be used to determine the number of electrons transferred. Accordingly, a fast one-electron process should exhibit a ΔE_p of 59 mV (where $\Delta E_p = 2.3 \frac{RT}{F}$ = 59, see equation 1.2). Note both peak potentials are independent of scan rate.

For multiple electron transfer (reversible processes) the voltammogram will contain of several discrete peaks if the E^{o} values of the individual processes are consecutively higher and distinctly separated.

When a redox reaction is slow, or coupled with a chemical reaction, the situation changes significantly. It is these 'non-ideal' processes that are frequently of greatest chemical interest, for which the diagnostic power of cyclic voltammetry is most useful.

2.2.2 IRREVERSIBLE AND QUASI-REVERSIBLE SYSTEMS

For an irreversible system (those with slow electron exchange), the individual peaks are reduced in magnitude and widely separated. Totally irreversible systems are characterised by a shift in the peak potential (see Figure 2.3): [1]

$$E_{\mathrm{P}} = E^{\mathrm{o}} - \frac{RT}{\alpha n_a F}\left[0.78 - \ln\frac{k^o}{D^{1/2}} + \ln\left(\frac{\alpha n_a F v}{RT}\right)^{1/2}\right] \quad (2.4)$$

where α is the transfer coefficient, v is the scan rate and n_a is the number of electrons involved in the charge-transfer step. Hence, E_{P} occurs at potentials higher than E^{o}, with the over potential related to k^{o} (the electrochemical rate constant) and α (the voltammogram becomes increasingly 'drawn out' as αn decreases). The shift of the peaks potential can be compensated by applying an appropriate change in the scan rate.

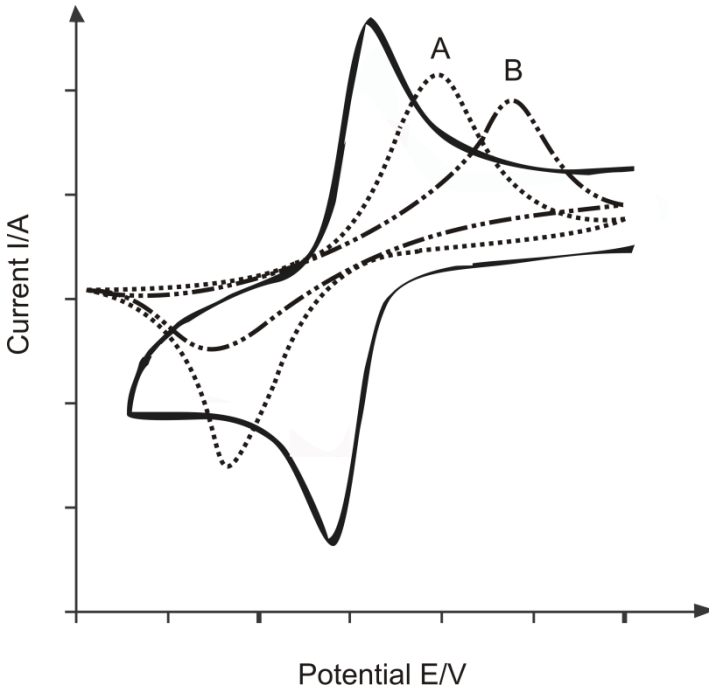

Figure 2.3 Examples of cyclic voltammograms for a quasi-reversible (curve A, dotted) and irreversible (curve B, dash-dot) redox processes. The solid line represents a typical cyclic voltammogram for a reversible redox process.

The peak current in this case (at standard conditions), given by:

$$i_{\mathrm{p}} = (2.99 \times 10^5) n(\alpha n_a)^{1/2} \mathrm{ACD}^{1/2} v^{1/2} \quad (2.5)$$

where n is the total number of electrons transferred and n_a is the number of electrons involved in the charge-transfer step, as mentioned above, is still proportional to the bulk concentration,

but decreased in height (dependent on the value of α). Assuming a value of 0.5 for α, the reversible-to-irreversible current peak ratio is 1.27:1; thus the resulting peak current for the irreversible process is approximately 80% of that attained for the reversible system.

Quasi-reversible processes are controlled via both charge transfer and mass transport. The rate of the electron kinetics is measured via the electron chemical rate constant (k^o), whilst the rate of mass transport is measured by the mass transport coefficient:

$$m_T = \frac{D}{\delta} \tag{2.6}$$

Where δ is the diffusion layer thickness, and as discussed earlier, is dependent on time (t) according to:

$$\delta \sim \sqrt{\pi D t}$$

$$t \sim \frac{RT}{Fv}$$

The distinction between fast and slow electrode kinetics relates to the dominant rate of mass transport given by:

$$k^o >> m_T \text{ (reversible)}$$

$$k^o << m_T \text{ (irreversible)}$$

The transition limits between a system that is reversible and irreversible can be defined through the parameter Λ, first introduced by Matsuda and Ayabe: [4]

$$\Lambda = \frac{k^o}{\left(\frac{FDv}{RT}\right)^{1/2}} \tag{2.7}$$

They proposed the subsequent ranges for the three classifications of systems at stationary macroelectrodes (at 298 K, assuming α ~ 0.5):

Reversible	$\Lambda \geq 15$	$k^{o} \geq 0.3v^{1/2}$ cm s^{-1}
Quasi-reversible	$15 > \Lambda > 10^{-3}$	$0.3v^{1/2} > k^{o} > 2 \times 10^{-5}\, v^{1/2}$ cm s^{-1}
Irreversible	$\Lambda \leq 10^{-3}$	$k^{o} \leq 2 \times 10^{-5}\, v^{1/2}$

These conditions show that reversible and irreversible behaviour observed for a given electrochemical rate constant is dependent on the applied scan rate. At sufficiently fast scan rates, at least in principle, all processes can appear electrochemically irreversible (Figure 2.4).

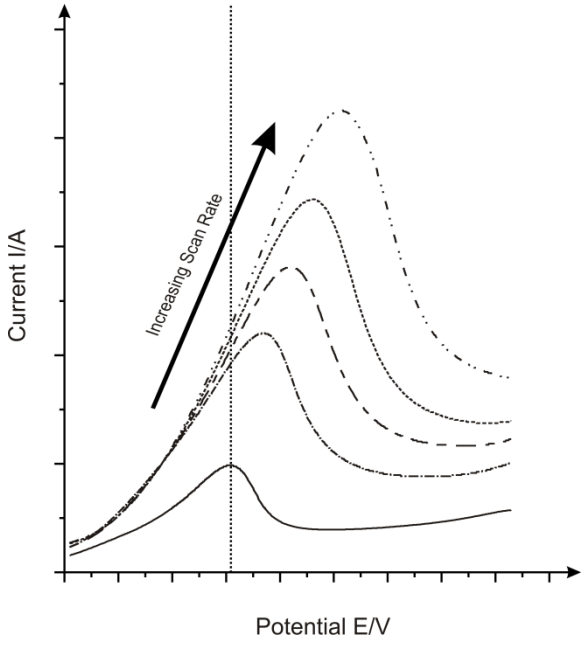

Figure 2.4 Example of shifting peak potentials with increased scan rates.

Cyclic voltammetry offers an indispensable tool for the determination of the experimental electrochemical rate constant. Numerical calculations developed by Nicholson [5] provide a basis for calculating the electrochemical rate constant (k^{o}) via the peak separation potential ($\Delta E_p = E_{p,a} - E_{p,c}$) observed during cyclic voltammetric analysis. This

method relates k^o to the peak separation (ΔE_p) through the dimensional parameter ψ as described in the following equation:

$$\psi = \frac{\gamma k^o}{(\pi a D_o)^{1/2}} \tag{2.8}$$

where $a = nF\nu/RT$, ν is the scan rate and $\gamma = \frac{D_o}{D_R}$, this represents the ratio of diffusion constants for the oxidized and reduced forms. Thus if $\gamma = 1$, the equation becomes;

$$\psi = \frac{k^o}{\left[\pi D_o \frac{nF\nu}{RT}\right]^{1/2}} \tag{2.9}$$

Or

$$k^o = \psi \left[\pi D_o \frac{nF\nu}{RT}\right]^{1/2} \tag{2.10}$$

The equations above are applicable to peak separations between 61 and 212 mV, outside of these values the limits of the simulation software used to calculate these values are reached. ΔE_p values as a function of ψ are presented in Table (2.1). Note these values may alter; subject to temperature.

Table 2.1 Peak separation potentials (ΔE_p) in milli-volts as a function of the kinetic parameter ψ.

ψ	ΔE_p	ψ	ΔE_p	ψ	ΔE_p
20	61	0.91	86	0.26	140
7	63	0.80	89	0.25	141
6	64	0.75	92	0.20	160
5	65	0.61	96	0.16	176
4	66	0.54	104	0.14	188
3	68	0.50	105	0.12	200
2	72	0.38	117	0.11	204
1	84	0.35	121	0.10	212

The shape of the voltammogram is a function of $k^o/\sqrt{\pi a D}$ (where $a = nF\nu/RT$). Small values of $k^o/\sqrt{\pi a D}$ (i.e. at rapid scan rates, ν) the system displays irreversible behaviour. (As $k^o/$

$\sqrt{\pi aD}$ increases, the system approaches the reversible case.) To summarise, the voltammograms of the quasi-reversible system are increasingly drawn out, displaying larger peak separations compared to those found for a reversible system (see Figure 2.3).

2.3 REACTION MECHANISMS

Qualitative diagnosis of chemical reactions that precede or succeed the redox process is one of the most important applications of cyclic voltammetry. Such reaction mechanisms are frequently characterised by the letters E and C (electrochemical/redox and chemical steps, respectively) in the order of the mechanisms or steps that occur in the reaction scheme. Such chemical reactions directly affect the available surface concentration of the electroactive species, common to redox processes of various key organic and inorganic compounds. Alterations in the cyclic profile of the system, resulting from the chemical competition for the electrochemical reactant or product, are enormously useful for determining the reaction pathways of the system, tendering reliable information about the reactive intermediates.

If we consider the following redox system, perturbed by a subsequent chemical reaction (an EC mechanism):

$$O + ne^- \rightleftharpoons R \rightarrow Z \qquad (2.11)$$

The cyclic voltammogram will display a smaller reverse peak because the product R is chemically removed from the surface (Figure 2.5).

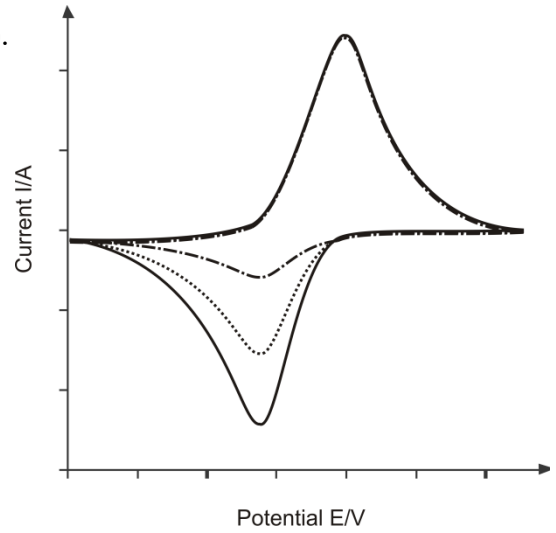

Figure 2.5 A cyclic voltammogram of a redox couple with subsequent chemical reaction (EC mechanism) causing a reduction in the reverse wave peak height.

The peak ratios of the forward and reverse peaks will thus be less than 1 (not equal); the exact value can be used to estimate the rate constant of the chemical step. In some (extreme) cases, the chemical reaction may process so rapidly that all of R is converted to Z, resulting in no reverse wave being observed. By varying the scan rate, further information on the rates of these coupled reactions can be obtained, however background subtraction is required for the large charging currents produced under ultra-fast scan rates. Frequently encountered electrochemical mechanisms involving coupled chemical reactions are displayed in Table (2.2). Some $\boldsymbol{E_rC_r}$ mechanisms (in special cases) result in the catalytic regeneration of the starting material (O) via the chemical step:

$$\mathrm{O} + n\mathrm{e}^- \rightleftharpoons \mathrm{R} \tag{2.12}$$

$$\mathrm{R} + \mathrm{A} \rightleftharpoons \mathrm{O} \tag{2.13}$$

Note, the production of highly reactive species via electron transfer may tender rapid chemical reactions (in comparison to the electron-transfer process), thus the system displays EE mechanistic behaviour (two successive charge transfer steps). If, for the case of a CE reaction mechanism, the chemical step preceding the electron transfer is slow, the current ratio for the reverse and forward peaks ($i_{P,r}$ /$i_{P,f}$) is typically greater than 1 (although this value is approached at slower scan rates). This is associated with the subsequent forward reaction no longer being directly related to the square root of the scan rate, while the reverse peak is mostly un-affected by the coupled reaction.

ECE processes contain a chemical step interposed between the electron transfer steps;

$$\mathrm{O}_1 + n\mathrm{e}^- \overset{\mathrm{E}}{\rightleftharpoons} \mathrm{R}_1 \overset{\mathrm{C}}{\rightarrow} \mathrm{O}_2 + n\mathrm{e}^- \overset{\mathrm{E}}{\rightarrow} \mathrm{R}_2 \tag{2.14}$$

This system can be easily explored via cyclic voltammetry as the two redox couples are observed separately. The rate constant of the chemical step is subsequently estimated via the relative magnitudes of the two voltammetric peaks.

*Table 2.2 Electrochemical mechanisms involving coupled chemical reactions.**

1. Reversible electron transfer, no chemical complications:

$$O + ne^- \rightleftharpoons R$$

2. Reversible electron transfer followed by a reversible chemical reaction, $\boldsymbol{E_rC_r}$ mechanism:

$$O + ne^- \rightleftharpoons R \rightleftharpoons Z$$

3. Reversible electron transfer followed by an irreversible chemical reaction, $\boldsymbol{E_rC_i}$ mechanism:

$$O + ne^- \rightleftharpoons R \rightarrow Z$$

4. Reversible chemical reaction preceding a reversible electron transfer, $\boldsymbol{C_rE_r}$ mechanism:

$$Z \rightleftharpoons O + ne^- \rightleftharpoons R$$

5. Reversible chemical reaction preceding an irreversible electron transfer, $\boldsymbol{C_rE_i}$ mechanism:

$$Z \rightleftharpoons O + ne^- \rightarrow R$$

6. Reversible electron transfer followed by an irreversible regeneration of starting materials, catalytic $\boldsymbol{E_rC_i}$ mechanism:

$$O + ne^- \rightleftharpoons R + Z \rightarrow O$$

7. Irreversible electron transfer followed by an irreversible regeneration of starting materials, catalytic $\boldsymbol{E_i}$ mechanism:

$$O + ne^- \rightarrow R + Z \rightarrow O$$

8. Multiple electron transfer with intervening chemical reactions – **ECE** mechanism:

$$O + \boldsymbol{n_1}e^- \rightleftharpoons R \qquad R \rightleftharpoons Y \qquad Y + \boldsymbol{n_2}e^- \rightleftharpoons Z$$

**Adapted from reference 1.*

Both reactants and products can be involved in adsorption-desorption processes. Cyclic voltammetry can be used to evaluate the interfacial behaviour of the electroactive compounds. Such behaviour occurs in studies of many organic compounds along with metal complexes (through specific adsorption of the ligand). A gradual increase in the cathodic and anodic peak current is typically observed, indicating progressive adsorption accumulating at the electrode's surface. Ideal Nernstian behaviour of non-reacting species (in a reversible system only) results in symmetrical cyclic voltammetric peaks ($\Delta E_p = 0$). The peak current can be related directly to the surface coverage (Γ, in moles of adsorbed molecules per surface area) and the potential scan rate:

$$i_p = \frac{n^2 F^2 \Gamma A v}{4RT} \tag{2.15}$$

As mentioned previously, Nernstian behaviour of diffusing species yields a $v^{1/2}$ (scan rate) dependence. However in practice, this 'ideal' behaviour is only approached at relatively slow scan rates; with an adsorption layer that displays no intermolecular interactions and fast electron transfer.

The peak area at saturation, indicated by a static peak current following consecutive scans, can be used to calculate the area (or surface coverage) occupied by the adsorbed molecule:

$$Q = nFA\Gamma \tag{2.16}$$

where Q is the electric charge obtained via integration of the peak (Figure 2.5).

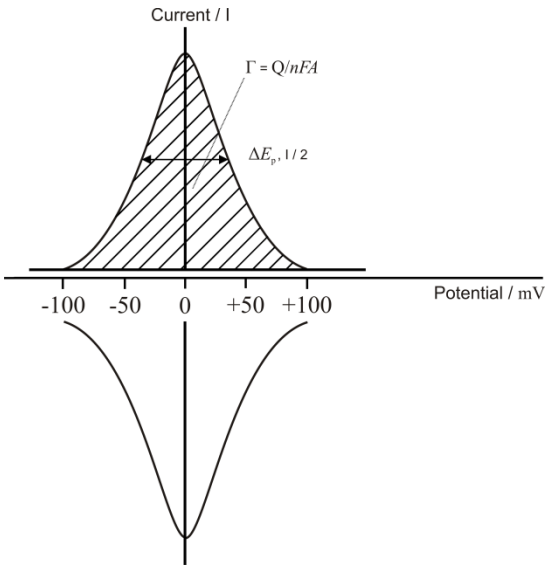

Figure 2.6 Ideal cyclic voltammetric behaviour for a surface layer at an electrode surface. The surface coverage, Γ, can be obtained from the area under the peak.

The surface coverage is commonly related to the bulk concentration via the adsorption isotherm, frequently used is the *Langmuir isotherm*:

$$\Gamma = \Gamma_m \left(\frac{Bc}{1+Bc}\right) \tag{2.17}$$

where Γ_m is the surface concentration (monolayer coverage) in mol cm^{-2}, B is the adsorption coefficient and c is the bulk concentration. This isotherm assumes no interaction between adsorbed species. Closely related to the *Langmuir isotherm* is the BET theory ("BET" represents the first initials of the publishers family names). BET analysis is an important base for the measurement of the specific surface area of a material. An extension of the previous isotherm, BET theory allows for multilayer adsorption, where gas molecules adsorb onto a solid in layers infinitely, however this concept assumes that there is no interaction between layers and that the *Langmuir* theory can be applied to each layer. The resulting equation is expressed below:

$$\frac{1}{V[(P_o/P)-1]} = \frac{c-1}{V_m c}\left(\frac{p}{p_o}\right) + \frac{1}{V_m c} \tag{2.18}$$

where p and p_o are the equilibrium and saturation pressures of adsorbates respectively (at the temperature of adsorption), V is the volume of adsorbed gas and V_m is the monolayer adsorbed gas volume. In this case c is the BET constant, which can be expressed as:

$$c = \exp\left(\frac{E_1 - E_L}{RT}\right) \tag{2.19}$$

where E_1 is the heat of adsorption for the first layer and E_L represents the heat of adsorption for the second and higher layers.

2.5 THIN-LAYER EFFECT

It is important that care is taken when interpreting the cyclic voltammetry of redox couples at electrode surfaces modified with dispersed carbon nanotube meshes. Streeter *et al.* have reflected on the cyclic voltammetry of such systems, proposing that the apparent current response should be understood in terms of a semi-infinite (planar) diffusion towards the macroelectrode surface and a finite diffusion model describing the redox reaction of the electroactive species confined to solvent pockets trapped between the immobilised layers.[2] This condition can be described via a diffusion model developed to define voltammetry within a thin-layer cell of a specific diffusion layer thickness, l. In a thin-layer cell, the working electrode and an adjacent insulating surface are separated by a small distance l. Trapped between these surfaces is a thin-layer of solution.

In a potential sweep experiment, current is drawn as the electron transfer becomes thermodynamically and kinetically favourable. If the layer of solution becomes significantly depleted of the electroactive species then the current will be diminished. This can result in a peak-to-peak separation considerably less than anticipated when applying the simple semi-infinite planar diffusion model. Consequently, the perceived voltammetric behaviour of redox couples at electrode surfaces modified with single walled nanotubes (SWNTs) may reflect a combination of both semi-infinite and thin-layer finite diffusion effects; with the pockets of

solution trapped in between layers of nanotubes being equivalent to the small volume of solution found in a thin-layer cell.

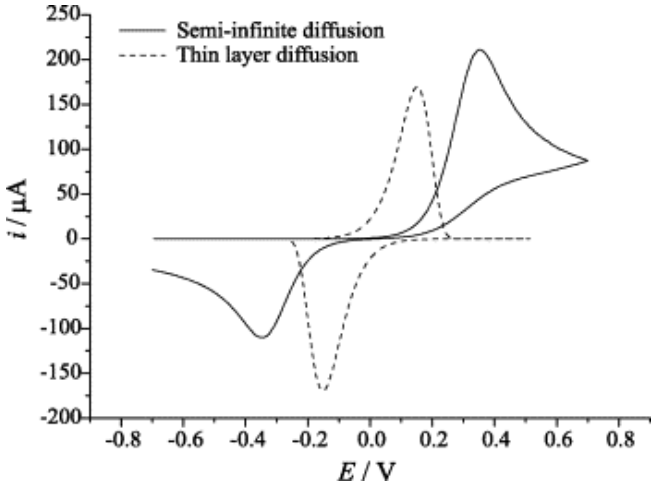

Figure 2.7 Comparison of linear sweep voltammetry using semi-infinite and thin layer planar diffusion models. For both models $k^o = 10^{-4}$ *cm* s^{-1}*;* $D = 10^{-3}$ cm^2 s^{-1}*;* $v = 0.1$ V s^{-1}*;* $C = 10^{-6}$ *mol* cm^{-3}*. Semi-infinite diffusion electrode area,* $A = 1$ cm^2*, thin layer area,* $A = 30$ cm^2*: thickness* $l = 1\mu m$*. Figure reproduced from reference 2.*

For a fast reversible electron transfer system, the peak potential arises at the formal electrode potential, conversely in the case of a fully irreversible electron transfer process, the peak potential (E_p) can be described by the following equation: [2]

$$E_P = E_f + \frac{RT}{\alpha F} ln\left(\frac{\alpha F v}{RT l k_o}\right) \tag{2.17}$$

where E_f is the formal electrode potential. As the layer thickness (l) decreases, the peak shifts to less oxidative potentials; this is attributed to the reduced time period required to deplete the layer of electroactive species. Figures (2.8) and (2.9) illustrate the effect of increasing layer thickness on voltammetric analysis.

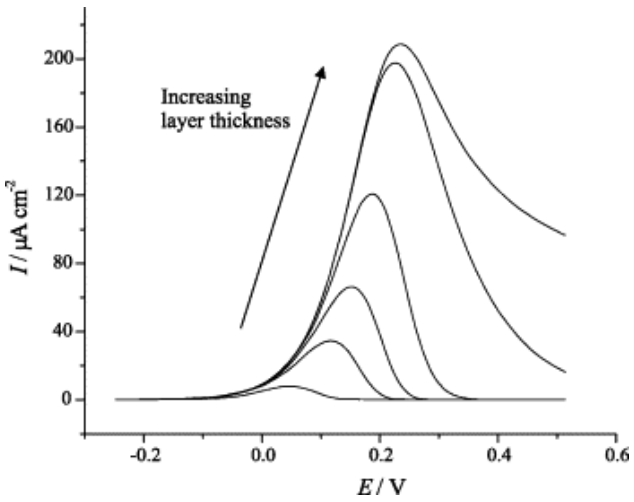

Figure 2.8 Linear sweep voltammetry simulated at thin layer cells with the following layer thicknesses: $l = 1\times10^{-4}$, 5×10^{-4}, 10^{-3}, 2×10^{-3}, 5×10^{-3} and 1 cm. other parameters: $k^o = 10^{-4}$cm s^{-1}; $D = 10^{-3}$ cm^2 s^{-1}; $v = 0.1$ V s^{-1}; $C = 10^{-6}$ mol cm^{-3}. Figure reproduced from reference 2.

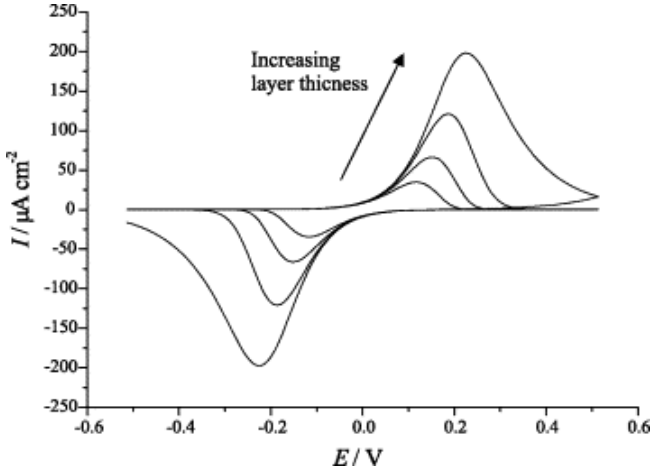

Figure 2.9 Cyclic voltammetry simulated at thin layer cells with the following layer thicknesses: $l = 5\times10^{-4}$, 10^{-3}, $2\times10^{-3}$and 5×10^{-3}cm. other parameters: $k^o = 10^{-4}$cm s^{-1}; $D = 10^{-3}$ cm^2 s^{-1}; $v = 0.1$ V s^{-1}; $C = 10^{-6}$ mol cm^{-3}. Figure reproduced from reference 2.

2.6 OTHER EXPERIMENTAL TECHNIQUES

2.6.1 CHRONOAMPEROMETRY

The electrochemical technique of chronoamperometry involves stepping the potential applied to the working electrodes initially held at a value at which no Faradaic reaction occurs before jumping to a potential at which the surface concentration of the electroactive species is zero (Figure 2.10A) where the resulting current time dependence is recorded (Figure 2.10C).

The mass transport process throughout this process is solely governed by diffusion, and as such the current-time curve reflects the change in concentration at the electrode's surface. This involves the continuing growth of the diffusion layer associated with the depletion of reactant, thus a decrease in the concentration gradient is observed as time progresses (Figure 2.10B). The current decay with time is given by the *Cottrell equation* mentioned previously (equation 1.11).

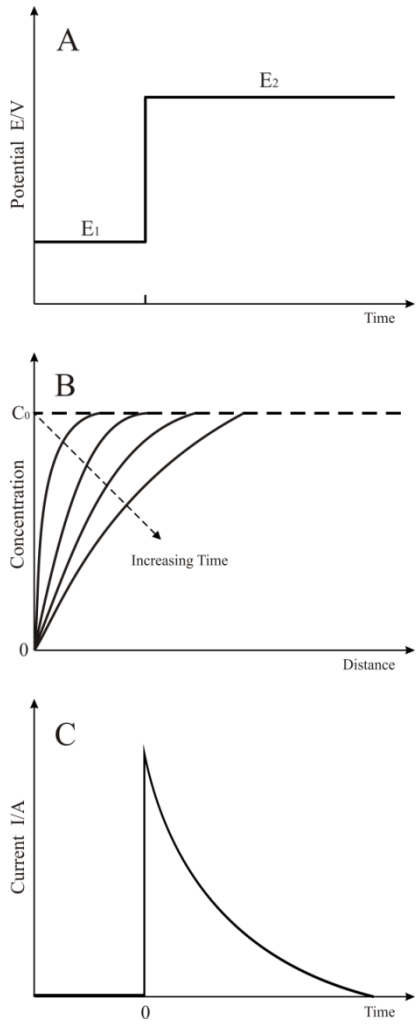

Figure 2.10
Chronoamperometric experiment: A) potential-time waveform; B) change of concentration gradient; C) resulting current-time response.

2.6.2 SQUARE-WAVE VOLTAMMETRY

Square-wave voltammetry is a large-amplitude differential technique in which a symmetrical waveform is superimposed onto a base staircase potential (Figure 2.11). The current is sampled twice during each square-wave sample, the first at the end of the forward

pulse (t_1) and the other at the end of the reverse scan (t_2). The large amplitude grants the reverse pulse the capacity to sources the inverse reaction of the product formed during the forward pulse.

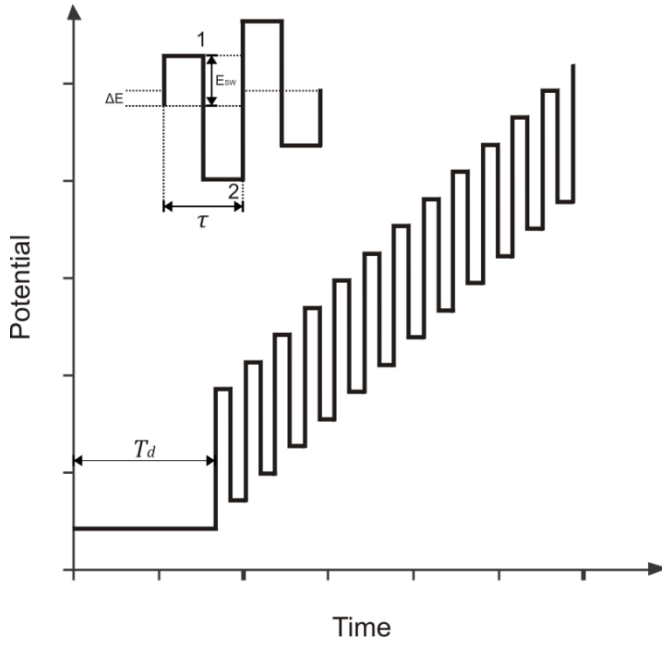

Figure 2.11 Square-wave waveform showing the amplitude (E_{SW}); step height (ΔE); square-wave period (τ); time delay (T_d) and current measurement positions (1 and 2).

The difference between the forward and reverse measurements is plotted versus the base staircase potential. The resulting peak shaped voltammetry is symmetrical about the half-wave potential, with the peak current directly proportional to the concentration. The outstanding sensitivity offered via this technique arises from the fact that the net current is a measurement of the difference between the forward and reverse currents and thus larger than its discrete components. Coupled with the diminished influence of the charging background current, extremely low limits of detection (approaching 1×10^{-8} mol L^{-1}) can be attained. In addition, the current produced from dissolved O_2 is subtracted, thus there is no need to degas prior to experimental measurement.

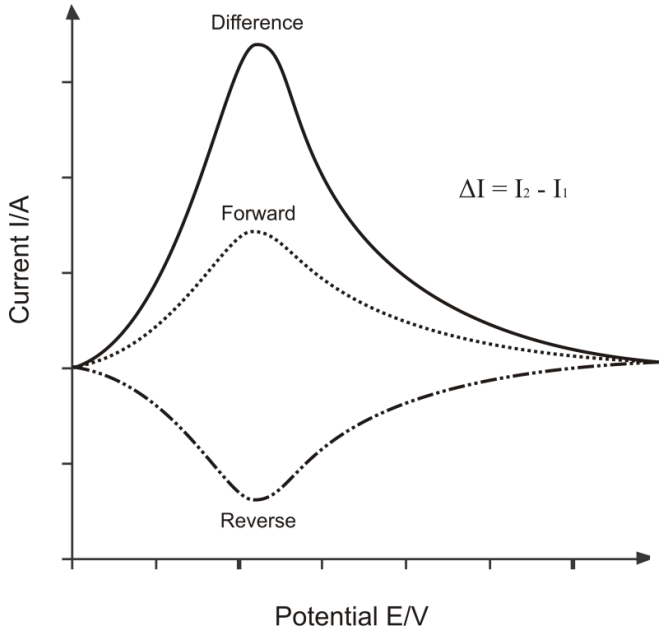

Figure 2.12 Square-wave voltammograms for reversible electron transfer. The dotted line represents the forward current; the double dot-dash line represents the reverse current, finally the solid line represents the net current.

Differential pulse techniques only consider the forward pulse and as such tenders inferior sensitivities. Evaluating the case of reversible and irreversible systems, the currents offered via square-wave voltammetry are 4 and 3.3 times higher, respectively, however its key advantage is it speed, with complete voltammetric analysis taking only a few seconds in contrast to the several minutes offered via differential-pulse.

2.7 REFERENCES

1. J. Wang, "*Analytical Electrochemistry*", 2nd ed.; Wiley-VCH. **2001**.
2. I. Streeter, G. G. Wildgoose, L. Shao, R. G. Compton, *Sensors and Actuators B*, **2008**, 133, 462.
3. A. J. Bard, L. R. Faulkner, "*Electrochemical Methods"*, 2nd ed.; Wiley: New York, **2001**, Chapter 6, pp.226-260.Chapter 11, pp.452-458.
4. H. Matsuda, Y. Aybe, *Z. Electrochem.*, **1955**, 59, 494.
5. R. S. Nicholson, I. Shain, *Anal. Chem*., **1965**, 37, 179.

3.1 INTRODUCTION TO ELECTROCHEMICAL ENERGY PRODUCTION AND STORAGE

The quickly evolving commercial industries, focused towards developing portable electronic devices and other related electronics such as electric vehicles (EV) necessitate the need for high-performance energy-storage systems. Recent global issues have resulted in academics exploring clean alternative energies. Electrochemical capacitors (ECs), also called supercapacitors or ultracapacitors, are electronic components that can be rapidly charged and discharged, yet relied upon to store energy reliably for long periods. Note, the specific energy of a supercapacitor is several orders of magnitude higher than those displayed by a traditional electrostatic capacitor (hence the 'super' or 'ultra' prefix), see Figure 3.1. Emergent as an archetypal model, they have been pushed as an answer to the disparity between the rapid surge in the power requisite of new devices and the inability of batteries to suffice the needs of applications which require transient but high/peak power pulses. ECs were first reported in 1957 (Becker's patent),[1] appearing commercially in 1978 (gold capacitors from Panasonic/Matsushita).[2] Often used as uninterruptible power supplies, such as backup sources for memories and microcomputers, ECs also have potential use in hybrid and electric vehicles. It has been reported [3] that the Airbus A380 has applied electrochemical double-layer capacitors (EDLCs) within its emergency doors. When matched alongside batteries, ECs provide higher power densities, rapid power delivery/uptake and outstanding reversibility with low equivalent series resistance (ESR) and a long cycle life. As found in the Ragone plot [(specific power density vs. specific energy density) Figure 3.2], ECs bridge the gap between conventional capacitors and batteries; their high specific area allowing for significantly higher specific capacitances than conventional capacitors. With regards to the

electrode-active material, it has been discovered that specific surface area and pore size are two fundamental aspects that strongly influence the specific capacitance of the capacitor. Initially, it was believed that enlargement of the pores would offer beneficial characteristic; allowing for greater ion adsorption, resulting in higher capacitances values. Intriguingly, Gogotsi *et al*. [4] established that capacitance can be significantly improved with pores equivalent in size to that of a solvated ion. Interpretation of the charge storage mechanism permits the classification of ECs into two discrete groups: electrochemical double-layer (EDLCs) and pseudo capacitors. Since the 1990s, advances amid the materials investigated for use in electrochemical supercapacitor has been strongly based on carbonaceous materials such as activated carbon, carbide-derived carbon, graphene and carbon nanotubes, all tendering high surface areas essential for the residing charge. Pseudo-capacitors combine electrosorption with rapid surface redox reactions to store energy, where the total charge held is relative to the applied voltage. Typically transition metal oxides are used, though electronically conductive polymers are considered a viable alternative electrode material. Impressively, the specific capacitance of this type of systems can be anything between 10 and a 100 times larger than those displayed at EDLCs.

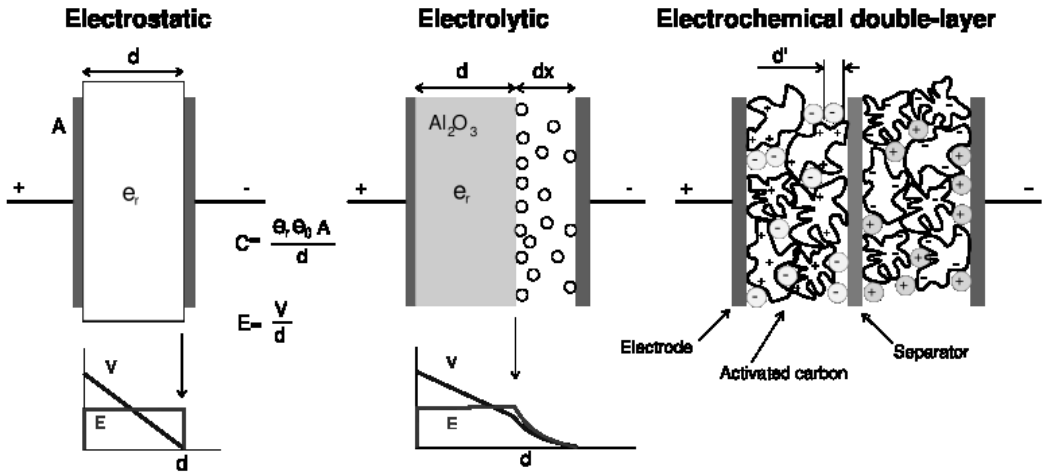

Figure 3.1 Schematic representations of electrostatic, electrolytic and electrical double layer capacitors.

Explanation of Figure 3.1:

In a conventional capacitor, energy is stored through the migration of charge carriers, typically electrons, from one metal plate to another. This separation of charge creates a potential between the two plates, which can be harnessed in an external circuit. The total energy stored in this approach rises with both the volume of charge stored and the potential between the plates. The amount of charge stored per unit voltage is fundamentally a function of the plate dimensions, separation distance, and the physical characteristics of the plate material/dielectric (the material in between the plates), while the potential between the plates is limited by the field strength of the dielectric. The capacitor's voltage is controlled by the dielectric controls. An electrolytic capacitor uses an electrolyte (an ionic conducting liquid) as one of its plates to achieve a larger capacitance per unit volume.

EDLCs do not have a conventional dielectric, instead of having an insulator amid the two separate plates; these capacitors use virtual plates that consist of two layers about the surface of the substrate. The electrochemical properties of this "electrical double layer", results from the effective separation of charge despite the ultra-thin (in the order of nanometers) physical separation of the layers. Without the need for a large layer of dielectric, the porosity of various carbon materials, allows the packing of plates with much larger surface areas, resulting in increased/high capacitances in much smaller packages.

In an electrical double layer, each layer by itself is quite conductive, but the physics at the interface where the layers are effectively in contact means that no significant current can flow between the layers. Importantly, the double layer can withstand only a low voltage, as such; electric double-layer capacitors rated for higher voltages must be made of matched, series-connected individual EDLCs.

While supercapacitors profit from the highest known power capability (10 kW kg^{-1}), a high current capability, simplistic maintenance and long-term cyclic stability (>10^6 cycles), their widespread deployment in routine technology is hindered by their limited energy density hinders. Clean and renewable energy media are still inadequate in satisfying performance and cost requirements, in particular, providing insufficient power boosts to start the engine or to assist acceleration.

In order to make capacitors a viable alternative, their energy-storage capabilities need to increase significantly, with adequate energy to quench the elevated requirements of advanced, cutting-edge devices; this challenge is more ominous than first thought and still the focus for many academics. There has been a widespread effort, committed to improving the specific capacitance of supercapacitors via introduction of pseudo-capacitive metal oxides. Compared with EDLC-based capacitors, pseudo-capacitors, focused around transition metal oxide electrodes, have enticed a substantial volume of attention as they yield improved capacitances over that of a double-layer carbonaceous material. Despite their prominence, efforts are still required to further enhance the applied use of metal oxide supercapacitors. The use of transition metals as the active material within electrochemical electrodes has increased significantly over the past 10 years and may be classed as either noble or based metal oxides. Noble metal oxides (RuO_2, IrO_2, etc.) have impressive conductivities and excellent power densities, yet their comparatively high cost and potentially (reported) harmful nature to the environment has limited their widespread application in supercapacitors. Base metal oxides (MnO_2, NiO, Fe_3O_4, etc.) display exceptional pseudo-capacitive behaviour, environmental compatibility, practical availability and reduced cost when compared to the state-of-the-art supercapacitor material RuO_2. The maximum specific capacitance of these materials and energy density in aqueous solution is detailed in Table (3.1).

Table 3.1 Maximum specific capacitance and energy density of metal oxide.

Material	Specific Capacitance ($F\ g^{-1}$)	Theoretical Energy Density ($Wh\ kg^{-1}$)
RuO_2	1580	342
NiO	1329	46
Ni(OH)	3152	109
MnO_2	698	78
$Co(OH)_2$	3108	276

**Adapted from reference 1.*

3.2 FUNDAMENTALS

Energy consumption/production that is dependent on combustion of fossil fuels is forecast to have a pronounced impact on world economics and ecology. Electrochemical energy production is under serious consideration as an alternative energy/power source; this is, as long as this energy consumption is considered to be more sustainable and environmentally friendly. Systems for electrochemical energy-storage include batteries, fuel cells and electrochemical capacitors (ECs). Although the energy-storage and conversion mechanisms may be different, there are 'electrochemical similarities' between all the systems, that is, the energy providing process takes place at the phase boundary or interface between the electrode and the electrolyte, plus electron and mass transport are separated. Batteries, fuel cells and supercapacitors all comprise of two electrodes in contact with an electrolyte solution. In batteries and fuel cells, electrical energy is produced through conversion of chemical energy via redox reactions at the anode and cathode. Reactions at the anode usually take place at lower electrode potentials that at the cathode, thus the terms negative and positive (indicated by minus and plus poles respectively) are used. In electrochemical capacitors (or supercapacitors) energy is not necessarily delivered via redox reactions but by the orientation of electrolyte ions at the electrode/electrolyte interface, these

electric double layers (discussed later in section 3.2.4) are fashioned and released, resulting in a parallel drive of electrons in the external wire (in the energy delivering process).

'Specific energy' [expressed in watt-hours per kilogram (Wh kg^{-1})] and 'energy density' [in watt-hours per litre (Wh L^{-1})] are used to compare the energy content of a system, whereas the rate capability is expressed as 'specific power' (in W kg^{-1}) and 'power density' (W L^{-1}). To compare the different power and energy capabilities of various systems, a representation known as the Ragone plot or diagram had been developed. A simplified version is shown below (Figure 3.2).

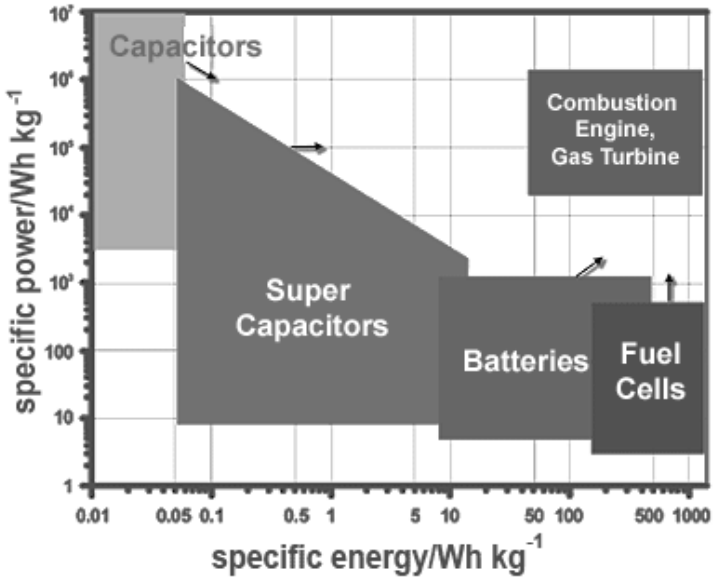

Figure 3.2 Simplified Ragone plot of energy-storage domains for various electrochemical energy conversion systems. Figure reproduced from reference 6.

This plot shows that fuel cells can be considered to be high energy systems, whereas supercapacitors are considered high power systems.

3.2.1 THERMODYNAMICS

The energy-storage and power characteristics of electrochemical energy conversion systems follow directly from the thermodynamic and kinetic formulations for chemical reactions as adapted to electrochemical reactions. The basic thermodynamic equations for a reversible electrochemical transformation are given by:

$$\Delta G = \Delta H - T\Delta S \tag{3.1}$$

and

$$\Delta G^\circ = \Delta H^\circ - T\Delta S^\circ \tag{3.2}$$

where ΔG is the Gibbs free energy (free energy of available reaction for useful work), Δ*H* is the enthalpy (energy released via the reaction), Δ*S* is the entropy and *T* is the absolute temperature, with *T*Δ*S* being the heat associated with the organisation/disorganisation of materials. The terms ΔG, Δ*H,* and Δ*S* are state functions and depend solely on the identity of the materials as well as the initial and final states of reactions. The degree symbol indicates that the value of the function is for the material in its standard state (25 $^\circ$C and 1 atmospheres pressure) and unit activity.

Since ΔG represents the net useful energy of a system available via a given reaction, in electrical terms, the net available electrical energy given by the cell is given by:

$$\Delta G = -nFE \tag{3.3}$$

and

$$\Delta G^\circ = -nFE^\circ \tag{3.4}$$

where *n* is the number of electrons transferred per mole of reactant, *F* is the Faraday constant and *E* is the voltage of the cell (or emf of the cell reaction). The voltage of the cell is unique for each reaction couple. The amount of electricity produced, *nF*, is determined by the total amount of material available for reaction and can be thought of as a capacity factor, while the

cell voltage can be considered as an intensity factor. Spontaneous processes have a negative free energy and a positive emf with the reaction written in a reversible fashion, which goes in the forward direction.

The van't Hoff isotherm identifies the free energy relationship for bulk chemical reactions as:

$$\Delta G = \Delta G^{\circ} + RT \ln(A_P/A_R) \tag{3.5}$$

where R is the gas constant, T is the absolute temperature, A_P and A_R are the standard activities of the products and reactants respectively. Combining equations (3.4) and (3.5) provides us with the Nernst equation for electrochemical reactions described in chapter 1:

$$E = E^{o} + (RT/nF) \ln(a_P/a_R)$$

3.2.2 KINETICS

Thermodynamics describe reactions at equilibrium and the maximum energy release for a given reaction. Compared to the equilibrium voltage (or open circuit voltage, E_{OCV}), the voltage drops when current is drawn from the cell. This is due to the kinetic limitations of reactions and other processes that must occur in order to sustain a flow of current during operation. Electrochemical reaction kinetics differ from chemical reaction kinetics in two important aspects: 1) the effect of the potential drop in the electric double layer at the electrode interface (see section 3.2.4) directly influences the activated forces; 2) reactions at the electrode interface proceed in two-dimensions, not three. The actual mechanics of electrode reaction used for energy-storage and generation typically involve a series of physical, chemical and electrochemical steps, including charge-transfer and charge transport reactions. The rate of these processes defines the kinetics of the electrode, and thus the cell. In a simplified electrochemical cell, three primary types of polarization exists, all of which participate in the observed rate kinetics; 1) *activation* polarization relates to the kinetics of the

electrochemical redox (charge transfer) reactions that occur at the electrode/electrolyte interface; 2) *ohmic* polarization is associated with the resistance of individual cell components and the resistance generated by contact problems between them; 3) *concentration* polarization is connected to the limitations of mass transport during cell operations. Polarization, η, is given by:

$$\eta = E_{OCV} - E_T \tag{3.6}$$

where E_{OCV} is the voltage of the cell at open circuit and E_T is the terminal cell voltage with current, I, flowing.

Activation polarization arises from the kinetic hindrance associated with charge-discharge reaction occurring at the electrode/electrolyte interface. This type of kinetics is best understood using the absolute reaction rate theory. The reaction route involves an activated complex, where the rate limiting step is the dissociation of the activated complex. The rate, current flow, i ($I = I/A$ and $I_0 = I_0/A$, where A is the electrode surface area) of a charge transfer controlled battery reaction is given by the Butler-Volmer equation:

$$i = i_0 \exp(\alpha F\eta/RT) - \exp((1-\alpha)F\eta)/RT \tag{3.7}$$

where i_0 is the exchange current density, ($i_0 = k^o FA$, k^o is the reaction rate constant for the electrode reaction and α is the activity product of the reactants), η is the polarization (departure or overpotential) from equilibrium ($\eta = E_{OCV} - E_T$) and α is the transfer coefficient. The exchange current density (i_0) is directly correlated to the reaction rate constant (k^o), the activity of reactants/products (α) and the potential drop across the double layer. Reactions that result in a large i_0 have a greater reversibility and lower polarization for a given current flow. Electrodes that produce high exchange currents (i_0 in the range of 10^{-2} A cm^{-2}) are preferential in energy-storage (battery) applications. The build-up and decay of the activation

polarization is rapid (between 10^{-2} and 10^{-4} s) and can be identified through the voltage change upon current interruption.

Ohmic polarization transpires due to the resistance tendered by the electrolyte, conductive diluent, electrode material, current collectors, terminals and contacts between particles of the active mass or resistive film present at the surface of the electrode. Ohmic polarization ensues (appears and dissipates) almost instantaneously ($\leq 10^{-6}$ s) when current flow ceases. Under the effect of ohmic resistance, R, there is a linear relationship between I and η.

$$\eta = IR \tag{3.8}$$

As the redox reactions proceed, the availability of electro active species at the electrode/electrolyte interface alters. Restrictions in the diffusion (limited mass transport capabilities) of active species towards and away from the electrode to replace the reacted material (sustaining the reaction) gives rise to a concentration polarization. Diffusion limitations are relatively slow, build-up and decay taking $\geq 10^{-2}$ s to appear. For limited diffusion, the concentration polarization can be expressed as:

$$\eta = (RT/n) \ln(C/C_o) \tag{3.9}$$

where C is the concentration at the electrode's surface and C_o is the concentration of the bulk solution. The movement or transport of reactants from the bulk solution to the reaction sites at the electrode interface and back is a typical characteristic of all electrode reactions. Most battery electrodes are porous structures in which an interconnected matrix of small solid particles, containing both nonconductive and electronically conductive material, filled with electrolyte. Porous structures increase the availability of active surface area and lower current density for greater efficiency.

3.2.3 CURRENT DISTRIBUTION AND POROUS ELECTRODES

The majority of practical electrodes are a complex composite of powders which consist of particles of active material, a conductive diluent (typically carbon or a metal powder) and a polymer binder (to hold the mixture together, plus bind it to a conductive current collector). A typical electrode utilised within a battery system has ~30% porosity with a complex surface extending throughout the volume of the porous electrode. This offers a much larger surface area for reaction than the actual geometric area, lowering polarization. The pores situated within the electrodes structure are occupied by the electrolyte. Even though the matrix may be a well-defined surface, there is an intricate reaction surface throughout the volume of the porous electrode, thus the effective (active) surface area may be many times the geometric area. Ideally when an electrode produces current, the reaction sites at which this occurs would be uniform throughout the electrodes structure. Non-uniform current distribution introduces inefficiencies, lowering the expected performance of the system.

Current distribution can be distinguished into two types; primary and secondary. Primary distribution is governed by the cell geometry. The placement of the current collectors has a strong influence on the current distribution on the electrodes geometric surface area. The monopolar construct is the most commonly applied. The difference in current distribution between top and opposite connection positions is shown in Figure 3.3. A more uniform current distribution is provided with an opposite connection arrangement, resulting in a more efficient use of the active material. A bipolar structure (Figure 3.3) gives uniform current distribution (and resistance) by using the anode terminal of one cell as a current collector and cathode terminal of the next cell in the construct.

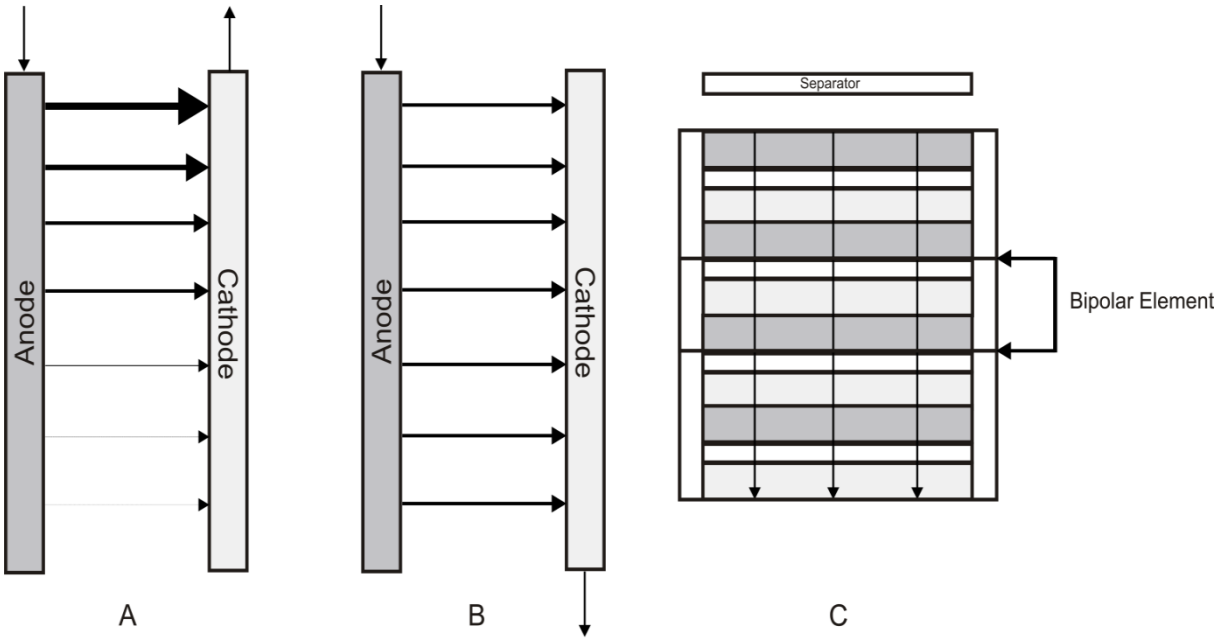

Figure 3.3 Primary current distribution on the front surface of the electrode based on Kirkhof's law calculation for three different cell configurations; A) top connections only, producing high resistance pathways at the bottom of the electrode, reducing current flow, resulting in non-uniform current distribution. B) opposite connection points, all pathways have equal resistance (uniform current distribution).C) depiction of a bipolar structure (equal resistance throughout).

Secondary current distribution relates to the current production sites located within the porous electrode itself. The incorporation of a porous (electrode) structure increases the active surface area and shortens diffusion lengths to the reaction sites. Current-producing reactions can penetrate into the porous electrode structure to substantial depths beneath the surface of the electrode. A simple graphical representation is given in Figure 3.4.

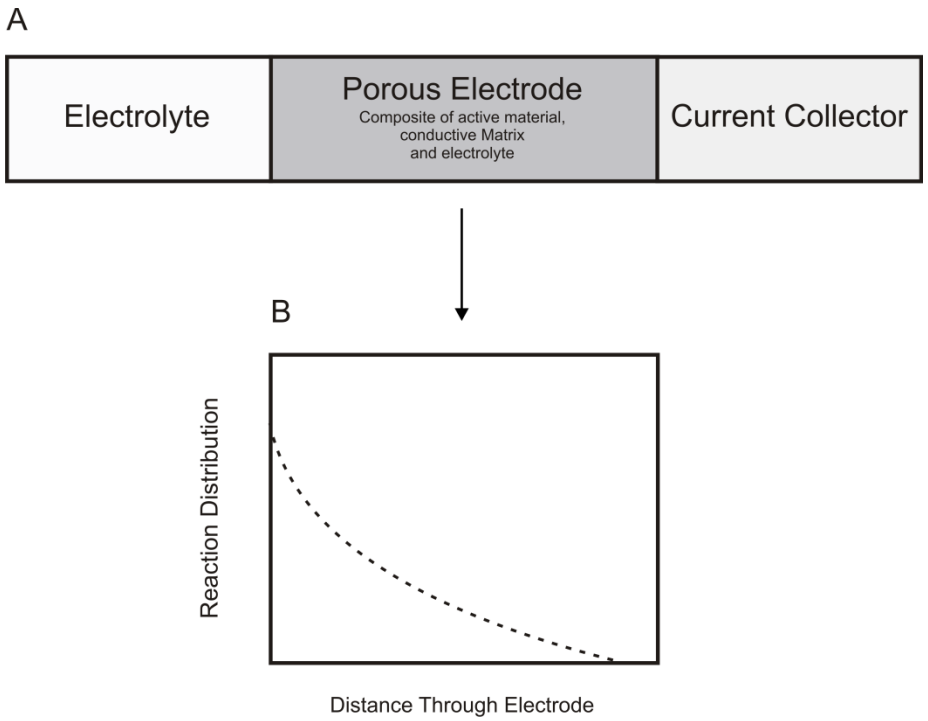

Figure 3.4 Schematic of porous electrode structure: A) Electrons from the external circuit flow in the current collector that is in contact with the conductive matrix amid the electrodes structure. The redox reaction at the electrode's surface produces electrons that enter the external circuit and flow through the load to the cathode, where the reduction reaction at the cathode accepts the electrons from the eternal circuit. The ions in the electrolyte transport the current through the device. B) Reaction distribution in the porous electrode is depicted (where the conductivity of the electrode matrix is higher than the conductivity of the electrolyte).

The positioning of the reaction sites inside the porous electrode is highly dependent on the characteristic of the active material and the reaction itself. Parameters that must to be considered include; conductivity of the electrode matrix, electrolyte conductivity, the exchange current, total current flow and the diffusion characteristics of the reactants and products in addition to porosity, pore size, tortuosity of the electrode and the thickness of the porous layer. The effectiveness of a porous electrode can be estimated through reflection of

its active (or specific) surface area, along with the penetration depth (L_P) of the reaction into the porous electrode.

3.2.4 CHARACTERISTICS OF THE ELECTRICAL DOUBLE LAYER

When an electrode (electronic conductor) is immersed into an electrolyte solution (ionic conductor) a spontaneous organization of charge takes place at its surface, forming an electric double layer (EDL) at the interface, with one layer situated inside the conductor, the other in the electrolyte as shown in Figure 3.5. These two charged layers behave similarly to physical capacitors with the charge separated by a distance in the order of molecular dimensions. The physical characteristics of any EDL system are contingent to the structure of the electrode's surface, the composition of the electrolyte and the potential field amid the charges found at the interface. Subject to the surface charge of the electrode material (positive or negative); counter ions from the electrolyte produce the solution EDL at the interface. A simplified example is shown in Figure 3.5.

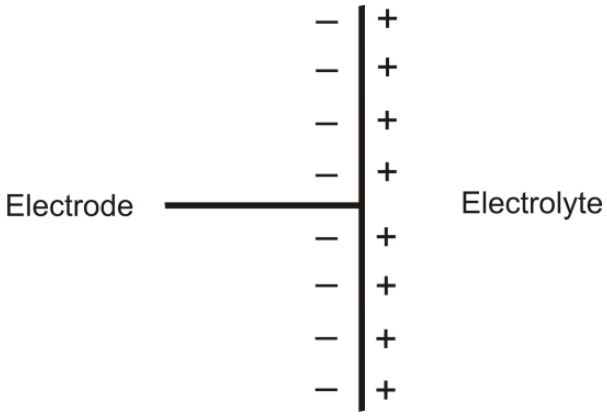

Figure 3.5 Simple Helmholtz model of the electric double layer (essentially a picture of a conventional capacitor).

Rendering from this simplified Helmholtz model, the charges are concentrated on each side of the electrode's surface. In reality, the EDL model is much more complex and should reflect the difference in ion dimensions and their reactivity with the surface (Figure 3.6).

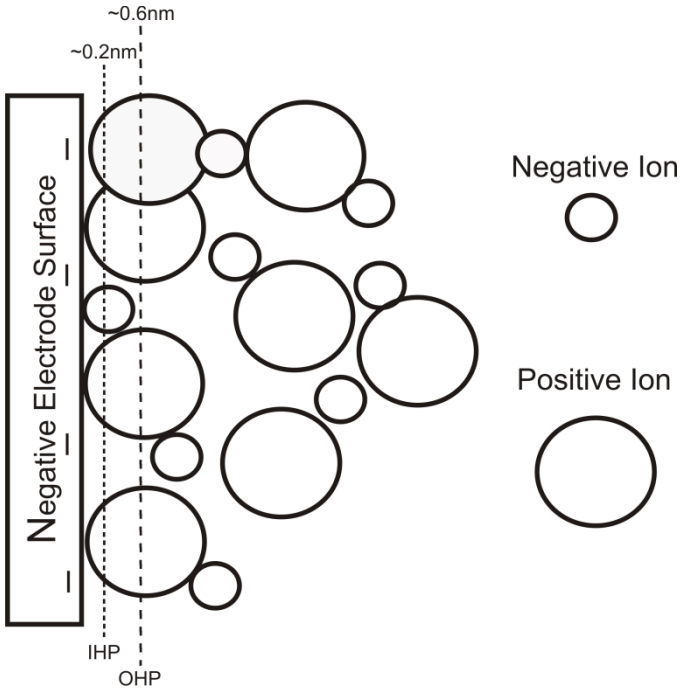

Figure 3.6 Depiction of the electric double layer at the surface of the negative electrode, displaying the outer Helmholtz plane (OHP) and the inner Helmholtz plane (IHP), referring to the distance of ions, orientated at the interface by Coulomb forces and distance of closest approach of specifically adsorbed ions and solvent molecules to the electrode surface, respectively.

The outer Helmholtz plane (OHP) refers to the distance of closest approach of non-specifically adsorbed ions (cations generally) in solution. The cations that populate the OHP are typically solvated and thus generally larger than the less solvated anions.

The ion interactions of the OHP with the surface charge have similar characteristics to coulombic interactions. The inner Helmholtz plane (IHP) refers to the distance of closest approach for specifically adsorbed ions (generally anions) and/or adsorbed solvent molecules

to the electrode's surface. Chemical affinity of the ions determines the adsorption processes that take place at the electrode's surface and the field strength of the EDL.

The double layer found at the electrode's surface occurs and dissipates almost instantaneously, with a time constant (time of formation) of ~10^{-8} s. This allows the structure of the double layer to rapidly respond to potential changes within the same time frame, this process involves a simple charge rearrangement, not a chemical reaction. This rapid change is in contrast to the conditions situated at redox electrode reaction typical to batteries and fuel cells. The time constant in these systems is much slower (in the range of 10^{-2} – 10^{-4} s, depending on the impedance of the reaction). Redox reactions contribute to the 'polarization capacitance' associated with electrode reactions. The reversibility (short time constant) tendered from the EDL allows for increased cycle life compared to batteries and fuel cells; hindered by stress caused via detrimental side reactions at redox electrodes.

When carbon electrodes are placed in an electrolyte, they typically assume a voltage near the zero charge point of the EDL. In aqueous media, this is near 0 V versus hydrogen. Applying an external voltage permits vast movement of ions and electrons towards the double layer, increasing the capacitance C (charge per applied voltage, $C = Q/U$). Normally, carbon and metals produce a double layer capacitance in the range of 10 – 40 μF cm^{-3}, although the exact values depend primarily on the voltage and the extent of participation of the IHP in the electric double layer. High surface-area carbon electrodes can yield capacitance near 4 F g^{-1}.

3.2.5 ELECTROCHEMICAL CAPACITOR OPERATION

As noted previously, electrochemical capacitors are close cousins of the battery. Figure 3.7 illustrates their basic (circuit) operations.

Figure 3.7 Basic circuit operations of a double layer capacitor.

were C_a and C_c are the double layer capacitance of the anode and cathode respectively. R_i is the internal resistance of the cell. For capacitors in series the following equations are given:

$$1/C = 1/C_a + 1/C_c \tag{3.10}$$

If $C_a = C_c$, as would be expected for a supercapacitor then;

$$C = \frac{Ca}{2} \tag{3.11}$$

High surface-area carbon is highly sought after, combining a large surface area (wetted via electrolyte), high electronic conductivity, chemical and electrochemical stability with low costs. Capacitance values of these devices can be several orders of magnitude larger than that of conventional dry electrolyte capacitors. The voltage for aqueous-based electrochemical capacitors is around 1 V, limited by the voltage stability of the electrolyte. Switching to an organic-based electrolyte, it is possible (in practice) to push the voltage up to 2.7 V. However, the organic electrolyte produces a lower double layer capacitance and reduced conductivity.

Since energy-storage is given by:

$$\frac{1}{2}CV^2 \tag{3.12}$$

(where *C* is the Capacity in Farads) the higher voltage permitted by the organic electrolyte significantly increases the capability of the EC to store charge. The resistivity of the organic electrolyte is ~100 times greater than that of an aqueous electrolyte and thus the time constant for the response to a large pulse is slower.

The charge-discharge process for a symmetric EC (composed of two carbon electrodes with similar mass present in an aqueous solution) is depicted in Figure 3.8. With zero applied charge (*Q*), both electrodes retain the same voltage. The potential of the electrodes increase in opposing directions during the charging process (as each electrode has the same capacitance). The maximum cell voltage is attained when one of the electrodes reaches the stability limit of the electrolyte.

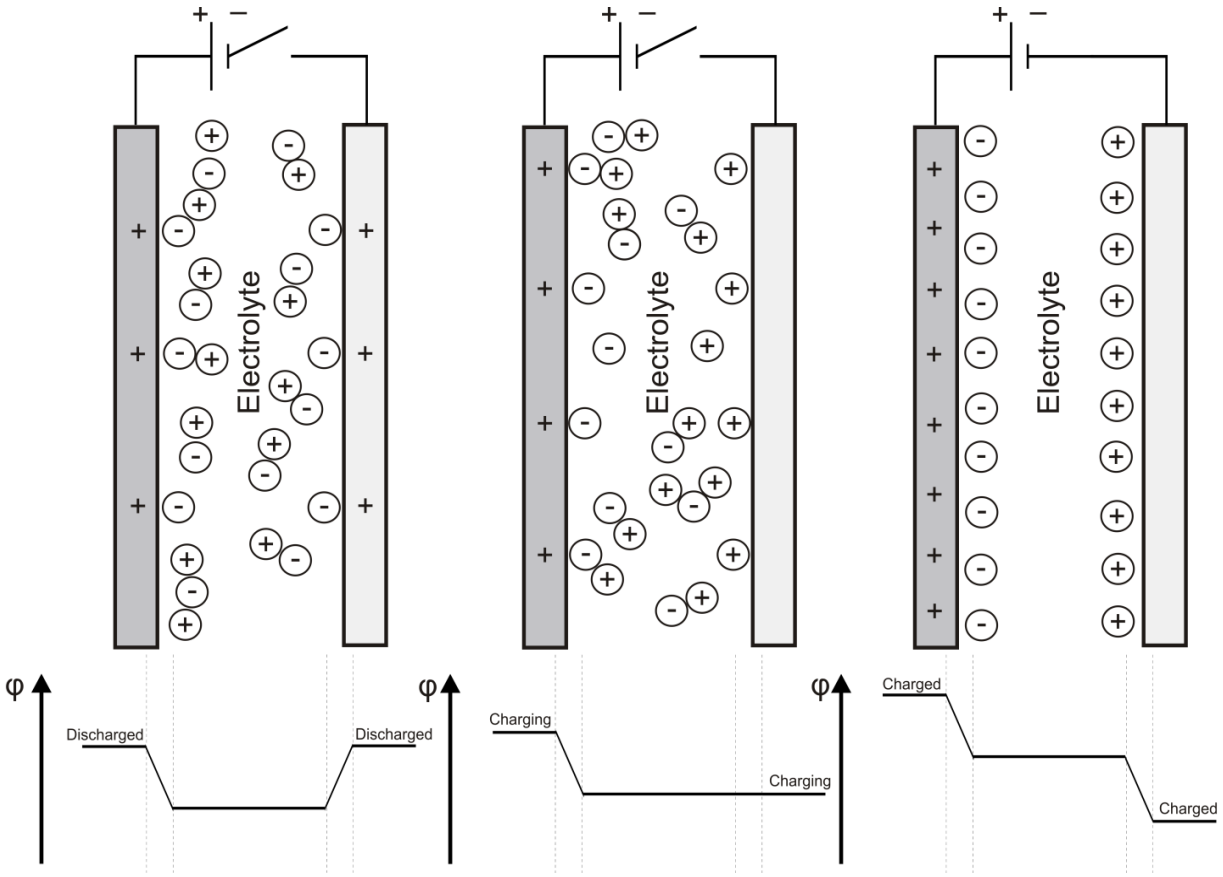

Figure 3.8 Operation principle of an EC in a discharged, charging and charged state, where φ represents the phase shift.

The asymmetric EC incorporates a battery-like electrode, that is, a redox-based (typically a metal) electrode. The redox reaction produces ~10 times the capacitance values offered by the electric double layer. If a nickel (NiOOH) cathode electrode is substituted into the asymmetric capacitor, substituting $C_c = 10\ C_a$ into equation (3.10), the capacitance value of the EC is essentially doubled.

$$1/C = 1/\ C_a + 1/10\ C_a \tag{3.13}$$

$$C \approx C_a \tag{3.14}$$

This type of asymmetric EC is often termed a 'hybrid capacitor'. Because the redox electrode displays capacitance many times greater than that of the double layer electrode, its remains at an invariant voltage during charge-discharge, resulting in a reduced fall rate in the discharge voltage of the hybrid capacitor to that of the carbon-carbon EDL capacitor. A graphical representation is shown below (Figure 3.9).

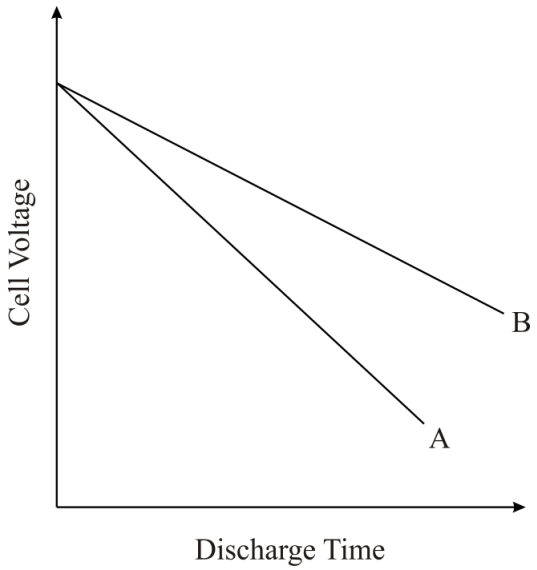

Figure 3.9 Voltage discharge graph of A) EDL and B) hybrid capacitors.

In certain cases, the redox charge-discharge proceeds almost as quickly and reversibly as the EDL charging. Thin-film redox electrodes based on lithium ($Li_4Ti_5O_{12}$) and RuO_2 intercalation/insertion principle exhibit high reversibility, fast rate kinetics and long cycle lifes, yielding capacitance values in the hundreds of μF. Moreover, they are easily fabricated as thin films.

3.3 OVERVIEW OF RECENT DEVELOPMENTS

Significant efforts have been focused towards transition metal oxides, not solely because they offer favourable structural, mechanical or electronic characteristics, but their capacitive properties, ascribed to their multiple oxide states, sanctions the exhibition of pseudo capacitances to which their carbon counterparts typically cannot. In general, assignment of transition metal oxides fall into two classifications, the first being noble transition metal oxides, displaying impressive capacitive properties but have the flaw of being relatively expensive. Alternatively, base metal oxides, which are considerably cheaper, while not on an equivalent level, still exhibit good capacitive properties. More importantly however, with the environmental concerns that have arisen recently, they are environmentally friendly in contrast to the noble transition metals. Careful understanding and manipulation of the nanostructural composition that acts as a framework for the material can result in its electrochemical performances being ameliorated. The aim of this short review is to detail the recent studies applying metal oxides as electrode materials for deployment in electrochemical capacitors, highlighting the fundamental advances in understanding the observed electrochemical reactivity at metal oxides, resulting in improved a capacitive characteristic which is essential for their continual use in energy-storage systems.

3.3.1 NOBLE METAL OXIDES

Noble metal oxides such as RuO_2 and IrO_2 were amid the first transition metals found to exhibit strong capacitive properties with rich electrochemical performances. Iridium dioxide is just one of several transition metal oxides that demonstrate a rutile structure. [9] It has applications in optical switching layers found inside electrochromic displays, plus ferroelectric capacitors for non-volatile memories and supercapacitors.[9- 13] The reason for the lack of interest in IrO_2 compared to RuO_2 (for use in supercapacitors) can primarily be attributed to its relatively small value of mass-specific capacitance which is hindered by its heavy relative atomic mass. Chen *et al.* constructed an IrO_2/multi-walled carbon nanotube composite. This cell assembly produced a low specific capacitance of only 69 F g^{-1}.[14] Later, the authors fabricated IrO_x nanofoils with high surface areas. Sputtered on multi-wall carbon nanotubes, the active materials showed improved energy-storage characteristics, displaying a specific capacitance of 370 F g^{-1}, still poor compared with RuO_2.[9] Consequently, the focus of this section is turned towards the electrochemical characteristics of ruthenium oxide (RuO_2).

3.3.1.1ENERGY-STORAGE MECHANISM OF RUO_2

As a typical pseudo-capacitor electrode material, ruthenium oxide has a vastly different mechanism to that of an electrochemical double-layer material, exhibiting multiple redox states alongside good electrical conductivity. It is important that RuO_2 has three discrete oxidation states accessible within 1.2 V. In acidic solution, its pseudo-capacitive behaviour can be described by the equations (3.15) and (3.16): [3, 15]

$$RuO_2 + xH^+ + xe^+ \rightleftharpoons RuO_{2-x}(OH)_x \; 0 \leq x \leq 2 \qquad (3.15)$$

or

$$RuO_x(OH)_y + \delta H^+ + \delta e^- \rightleftharpoons RuO_{x-\delta}(OH)_{y+\delta} \qquad (3.16)$$

As defined above, protons participate in the electrochemically reversible redox reaction, with RuO_2 acting as a proton condenser. The amorphous structure of RuO_2 is the crucial parameter in defining the observed specific capacitances, as the proton can be easily intercalated into the bulk $RuO_2 \cdot xH_2O$ but not into the crystalline phase.[15,16] Studies suggest that hydrated ruthenium dioxide has enhanced capacitive properties over those observed for the anhydrous structure. The hydrous regions have increased permeability towards the protons. Proton conduction inside ruthenium dioxide is dominant over electron conduction. [17]

3.3.2 BASE TRANSITION METAL OXIDES

While RuO_2, IrO_2 and correlating structures display outstanding capacitive affinities, they are not devoid of drawbacks. Their relative high cost has resulted in scientists exploring low cost substitutes which retain good capacitive characteristics. As such, attention has been focused on base transition metal oxides (MnO_2, NiO and Fe_3O_4) for electrode active materials of ECs in recent years.

3.3.2.1 ENERGY-STORAGE MECHANISM OF NICKEL-OXIDE/HYDROXIDE

Compared to RuO_2, $Ni(OH)_2$ and NiO are environmentally benign in nature, relatively cheap and available in abundant yields. Furthermore, impressive chemical/thermal stability and high theoretical specific capacitance (NiO - 2573 F g^{-1}) [18, 19] has drawn a significant volume of interest. The redox reaction at the nickel electrode is widely considered to be a solid-to-solid transformation.[20] In a basic solution, NiO displays similar electrochemical behaviours to that of $Ni(OH)_2$. The mechanisms have been defined in the following equations:

$$Ni(OH)_2 + OH^- \rightleftharpoons NiOOH + H_2O + e^- \quad (3.17)$$

$$NiO + OH^- \rightleftharpoons NiOOH + e^- \quad (3.18)$$

3.3.2.2 ENERGY-STORAGE MECHANISM OF MANGANESE OXIDE

The advantages of using Manganese oxide (MnO_2) are copious: low cost, no toxicity, easily obtained and high specific capacitances, consequently considered as a highly auspicious material towards development in EC technologies. The reported, theoretical, specific capacitance of MnO_2 is 1370 F g^{-1}; [21] its perceived high specific capacitance endorsed by the redox oxidation of superficial oxy-cation species at various oxidation states. [22] Figure 3.10 illustrates a typical cyclic voltammogram of a MnO_2 electrode in a mild aqueous electrolyte, displaying a near rectangular mirror image characteristic of double-layer capacitive behaviour. The ellipses aid in highlighting the reversibility of the system.

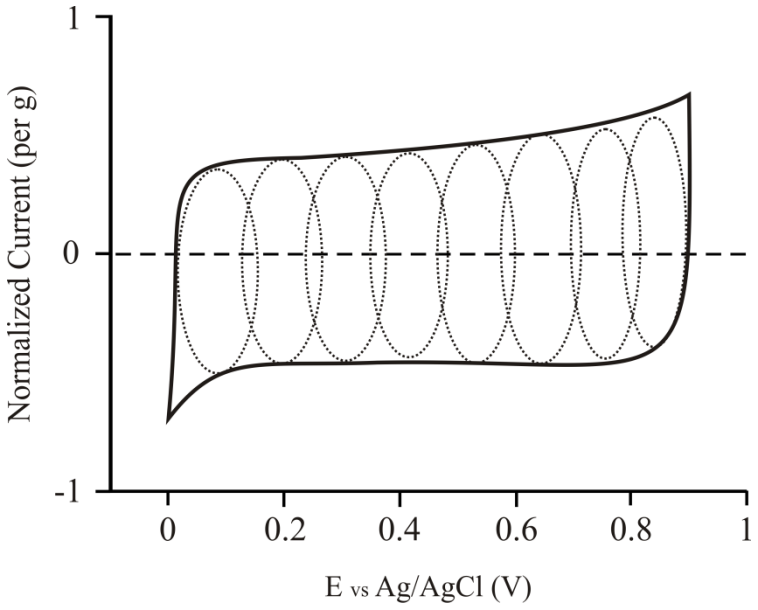

Figure 3.10 Typical cyclic voltammogram of a MnO_2 electrode. [5]

There are two diverse interpretations regarding the mechanistic behaviour of MnO_2 charge storage characteristics. One opinion is that protons and/or alkali metal cations intercalate with the bulk material upon reduction and de-intercalate upon the electrochemical oxidation processes, shown in the following equation: [23,24]

$$MnO_2 + C^+ + e^- \rightleftharpoons MnOOC \qquad (3.19)$$

where C+ represents protons or alkali metal cations. This behaviour is similar to that observed at RuO_2. Note, only a limited section of MnO_2 [25] electrode material is electrochemically active. The other viewpoint is that the redox process occurs solely at the surface of MnO_2 electrode, as described below:

$$(MnO_2)_{surface} + C^+ + e^- \rightleftharpoons (MnO_2 - C^+)_{surface} \quad (3.20)$$

Though the two perspectives have subtle differences, they both indicate a redox reaction between the III and IV oxidation states of manganese.

3.3.3 FURTHER BASE METAL OXIDES AND COMPOSITE MATERIALS

Other base metal oxides, such as iron oxide, indium oxide, tin oxide, and vanadium oxide also have their applications in ECs. Typically in the form of a powder, transition metal oxides can be used to construct composite electrodes or be directly placed onto a conducting substrate to overcome their poor conductive performance. Du *et al*. developed a Fe_3O_4 nanoparticle modified active carbon supercapacitor via a microwave fabrication methodology, producing a resultant nano structure Fe_3O_4 with an average particle sizes of 35 nm. This AC– Fe_3O_4 hybrid supercapacitor delivered a specific capacitance of 37.9 F g^{-1} while retaining 82% of its initial capacitance over 500 cycles. [25]

3.3.4 COMPOSITE METAL OXIDES

Composite metal oxides used as the active materials in supercapacitor exploit the characteristics of multiple metals, manipulating its structural attributes, improving the overall electrochemical properties of the composites. [27,28] Some research, pursuing improved blends of composite metal oxides (such as Ni–Co, V–Sn, Ru–Ti and Ru–Co), has described how the inclusion of cobalt oxide (within the composite) results in enhanced electronic and redox properties.[27-31] The insertion of Co into the lattice of nickel hydroxide, not only greatly

increases its conductivity but additionally, shift the redox peaks of $Ni(OH)_2$ to less positive potentials.[32, 33] Kim *et al*. prepared a Ru–Co mixed oxide. The Ru–Co composite was co-deposited onto single-walled carbon nanotubes (SWNTs), offering a specific capacitance of 570 F g^{-1}, considerably improved over the equivalent RuO_2 electrode (475 F g^{-1}), owed to the enhanced electronic conduction; attributed to the structural support offered by Co throughout the active Ru species.[28]

3.3.5 ASYMMETRICAL SUPERCAPACITORS

It is widely accepted that the effective energy density of a supercapacitor is related to the operational potential window. [34,35] Asymmetrical supercapacitors (ASC) commonly exploit ionic liquids (salt containing liquids, typically displaying poor electrical conductivity and high viscosity with non-ionizing (e.g. non-polar) properties) or organic reagents as electrolytes to improve cell voltage. [36,37] Often, the working electrode materials will be tailored to provide a wide potential window, resulting in a substantially broadening of the cells voltage in order to attain high energy densities. [34, 38-44] In an ASC, the active material in the working electrode is dissimilar to that used in the counter electrode amid a cell system. One example, reported by Qu *et al.* displayed an ASC, fabricated using an active carbon (AC) based anode, while the cathode was constructed from MnO_2. [41] The supercapacitor demonstrated an energy density of 17 Wh kg^{-1} at 2 kW kg^{-1} with a voltage of 1.8 V in a 0.5 mol L^{-1} K_2SO_4 aqueous solution, significantly greater than its symmetrical counterpart ($AC/K_2SO_4/AC$). Ganesh *et al.* found similar conclusions, also suggesting that ASCs provide higher capacitance value than their symmetrical equivalents, (NiO/KOH/AC) and (NiO/KOH/NiO) respectively. [40] Bearing in mind the pacification of power density, caused by the poor conductivity found with metal oxides, scientists have amalgamated metal oxides with materials that display enhanced electrical conductivity such as active carbon, graphene and carbon nanotubes to fabricate electrodes which offer improved electrochemical

properties. As such, reduced graphene oxide sheets (RGO) and their ruthenium oxide modified equivalent (RGO–RuO_2) has given rise to the assembly of a cell displaying energy densities in the region of 26.3 Wh kg^{-1}. [44]

3.4 REFERENCES

1. H. E.Becker, *U.S. Patent,* 2800616, **1957**.
2. R. Kotz, M. Carlen*, Electrochim. Acta*, **2000**, 45, 2483.
3. P. Simon, Y. Gogotsi, *Nat. Mater*., **2008**, 7, 845.
4. C. Largeot, C. Portet, J. Chmiola, P.-L. Taberna, Y. Gogotsi, P. Simon, *J. Am. Chem. Soc*., **2008**, 130, 2730.
5. W. Deng, X. Ji, Q. Chena, C. E. Banks, *RSC Adv*., **2011**, 1, 1171.
6. M. Winter, J. B. Brodd, *Chem. Rev*. **2004**, 104, 4245.
7. J. Wang, "*Analytical Electrochemistry*", 2nd ed.; Wiley-VCH. **2001**.
8. A. J. Bard, L. R. Faulkner, "*Electrochemical Methods"*, 2nd ed.; Wiley: New York, **2001**.
9. Y.-M. Chen, *Nanotechnology*, 2011, 22, 355708.
10. Y. Chen, Y. Huang, K. Lee, D. Tsai, K. Tiong, *J. Mater. Sci.: Mater. Electron.*, **2011**, 22, 890.
11. D.-Q. Liu, S.-H. Yu, S.-W. Son, S.-K. Joo, *ECS Trans*., **2008**, 16, 103.
12. T. Sakoda, T. S. Moise, Scott R. Summerfelt, L. Colombo, G. Xing, S. R. Gilbert, A. L. S. Loke, S. Ma, R. Kavari, L. A. Wills, J. Amano, *Jpn. J. Appl. Phys*., **2001**, 40, 2911.
13. K. Nishio, Y. Watanabe, T. Tsuchiya, *Thin Solid Films*, **1999**, 350, 96.
14. Y. M. Chen, *Nanotechnology*, **2011**, 22, 115706.
15. J. Zheng, P. Cygan, T. Jow, *J. Electrochem. Soc*., **1995**, 142, 2699.
16. J. P. Zheng, T. R. Jow, *J. Electrochem. Soc*., **1995**, 142, L6.
17. W. Sugimoto, H. Iwata, K. Yokoshima, Y. Murakami, Y. Takasu, *J. Phys. Chem. B*, **2005**, 109, 7330.
18. K.-C. Liu, M. A. Anderson, *J. Electrochem. Soc*., **1996**, 143, 124.
19. K. W. Nam, K. B. Kim, *J. Electrochem. Soc*., **2002**, 149, A346.
20. W. G. Pell, B. E. Conway, *J. Power Sources*, **2001**, 96, 57.
21. F. Ataherian, K.-T. Lee, N.-L. Wu, *Electrochim. Acta*, **2010**, 55, 7429.

22. M. Toupin, T. Brousse, D. Be´langer, *Chem. Mater*., **2004**, 16, 3184.
23. M. Toupin, T. Brousse, D. Be´langer, *Chem. Mater*., **2002**, 14, 3946.
24. M. Ghaemi, F. Ataherian, A. Zolfaghari, S. Jafari, *Electrochim.Acta*, **2008**, 53, 4607.
25. X. Du, C. Wang, M. Chen, Y. Jiao, J. Wang, *J. Phys. Chem. C*, **2009**, 113, 2643.
26. N.-L. Wu, *Mater. Chem. Phys*., **2002**, 75, 6.
27. C.-C. Hu, H.-Y. Guo, K.-H. Chang and C.-C. Huang, *Electrochem. Commun.,* **2009**, 11, 1631.
28. B. C. Kim, G. G. Wallace, Y. I. Yoon, J. M. Ko, C. O. Too, *Synth. Met*., **2009**, 159, 1389.
29. S. I. C. d. Torresi, K. Provazi, M. Malta, R. M. Torresi, *J. Electrochem. Soc*., **2001**, 148, A1179.
30. M. Vidotti, M. R. Silva, R. P. Salvador, S. I. C. d. Torresi, L. H. Dall'Antonia, *Electrochim. Acta*, **2008**, 53, 4030.
31. M. Jayalakshmi, M. M. Rao, N. Venugopal, K.-B. Kim, *J. Power Sources*, **2007**, 166, 578.
32. A. K. Sood, *J. Appl. Electrochem*., **1986**, 16, 274.
33. K. Provazi, M. J. Giz, L. H. Dall'Antonia, S. I. Co´rdoba de Torresi, *J. Power Sources*, **2001**, 102, 224.
34. C. Peng, S. Zhang, X. Zhou, G. Z. Chen, *Energy Environ. Sci*., **2010**, 3, 1499.
35. M. D. Stoller, R. S. Ruoff, *Energy Environ. Sci*., **2010**, 3, 1294.
36. P. C. Chen, G. Shen, Y. Shi, H. Chen, C. Zhou, *ACS Nano*, **2010**, 4, 4403.
37. L. L. Zhang, X. Zhao, *Chem. Soc. Rev*., **2009**, 38, 2520.
38. C. Peng, S. Zhang, X. Zhou, G. Z. Chen, *Energy Environ. Sci*., **2010**, 3, 1499.
39. N. W. Duffy, W. Baldsing, A. G. Pandolfo, *Electrochim. Acta*, **2008**, 54, 535.
40. V. Ganesh, S. Pitchumani, V. Lakshminarayanan, *J. Power Sources*, **2006**, 158, 1523.
41. Q. Qu, P. Zhang, B. Wang, Y. Chen, S. Tian, Y. Wu, R. Holze, *J. Phys. Chem. C*, **2009**, 113, 14020.
42. H. Wang, Y. Liang, T. Mirfakhrai, Z. Chen, H. S. Casalongue, H. Dai, *Nano Research*, 1.
43. C. Xu, H. Du, B. Li, F. Kang, Y. Zeng, *J. Electrochem. Soc*., **2009**, 156, A435.
44. J. Zhang, J. Jiang, H. Li and X. S. Zhao, *Energy & Environmental Science*, **2011**.

4.1 INTRODUCTION TO ELECTRODE MATERIALS

Development of an electrochemical cells intended for energy-storage rely heavily on the working electrode. The material selected can enhance or hinder the desirable characteristics sought by researchers since all electrochemical processes take place at the working electrode surface.

Carbon is a highly utilised electrode material. Carbon is readily available, cheap (depending on its form), easily modified and chemically inert. Carbon gives rise to diamond, graphite, carbon fibres and activated carbon, tendering the hardest, highest strength and highest surface area respectively of any materials commonly found. It presents varying properties depending on its allotropic form, many of which are under intense research, such as carbon nanotubes or graphene.

The choice of material used for the working electrode also depends on the system being electrochemically investigated. Elemental metals can be highly reactive, undergoing electrochemical processes, forming oxides which limit their electrical conductivity. Typically gold or platinum are exploited but their high cost makes them unfavourable (especially for disposable electrodes).

The types of carbon exploited in this thesis include BDDE (boron-doped diamond electrode), GCE (glassy-carbon electrode), carbon nanotubes and graphene. The rapid progress and constant expansion of applications applying carbon allotropes is undeniable.

4.2 CARBON-BASED MATERIALS

Solid electrodes based on carbon are now widely used in electroanalysis because they offer a wide potential window, low background current; rich surface chemistry, low cost and chemical inertness. Unfortunately, the electron transfer rate observed at carbon surfaces are often slow (compare to traditional metal electrodes). The electron transfer rate is strongly affected by the orientation of the carbon surface. Although all (frequently encountered) carbon electrode materials share the same rudimentary six-membered aromatic ring and sp^2 bonding, every one holds relatively different densities of edge and basal-plane amid their surface. The edge orientation is more reactive towards electron transfer and adsorption processes than the graphite basal-plane. [1,2] Thus, materials with different edge-to-basal ratios can exhibit significantly different electron transfer kinetics for a given redox analyte. The most commonly exploited carbon materials are described below. [1,2]

4.2.1 CARBON NANOMATERIALS

The structural conformation and thus, the degree of hybridisation, strongly influences the physical, chemical, and electronic characteristics of carbon based nanomaterials. The orbital configuration of carbon's six electrons (in its ground-state) is $1s^2$, $2s^2$, $2p^2$. The small energy gap between the 2s and 2p electron shells aids in the promotion of one s orbital electron to the higher energy p orbital that is unoccupied in this ground state. Conditional to the bonding interactions with adjacent atoms, the promotion credits carbon with the ability to hybridize its electron orbitals into a sp, sp^2, or sp^3 configuration. Covalent bonding with adjacent atoms tenders increased stability, compensating for the higher energy state of this electronic configuration. This return is approximately equal for the sp^2 and sp^3 hybridization states after the out-of-plane π bonding among un-hybridised p orbitals is considered.

The variability of these hybridization states account for the diversity and considerable differences observed amongst the structures of carbon's bulk organic compounds. At elevated

temperatures or pressures, carbon adopts the thermodynamically favourable tetrahedral sp^3 'diamond' configuration. At lesser temperatures however, carbon adopts the planar sp^2 arrangement and formulates monolayer sheets, bound by three covalent sigma bonds and a single π bond. Van der Waals forces and the interaction between overlapping π orbitals of parallel sheets constitute the entirety of the weak out-of-plane interactions observed at carbon nanomaterials. Mild shear forces, physical separation, and chemical modification disturb these weak interplanar forces, causing graphite planes to slip past each other.

On the nano-scale, graphite sheets are more thermodynamically stable when arranged into a three-dimensional configuration. Reduction in the unfavourable 'dangling' bonds compensates for the strain energy created via the curvature of the planar graphite sheet. This results in the formulation of fullerenes and nanotubes; both share many of graphite's fundamental attributes, but additionally display a discrete and tuneable set of characteristics, owed to quantum effects at the nano-scale, quantum confinement (see carbon nanotube section) of wave functions in one or more dimensions, enhanced sp^3 character of the bonds, and closed topology. Thus, carbonaceous nanomaterials adhere to parallel bonding configurations to those establish at macroscopic carbon structures; however their characteristics and morphology are subject to the stability of select resonance structures rather than the bulk medians of their crystalline forms.

4.2.1.1 GRAPHITE

Graphites' low cost and ease of manipulation has established its use as an electrode material in electrochemistry. Hybridisation of the carbon atom changes the crystal structure of the material. In the case of sp^2 hybridisation, the carbon atom remains with one free electron in the 2p orbital. Each of the sp^2 hybridised orbitals then combines with other hybridised atoms/orbitals to form a series of planar hexagonal structures (Figure 4.1). The free delocalised orbital is orientated perpendicular to this plane. Thus the electron can move

easily from one side of the carbon atom layer to the other but cannot easily move from one layer to the other. This phenomenon makes the material anisotropic.

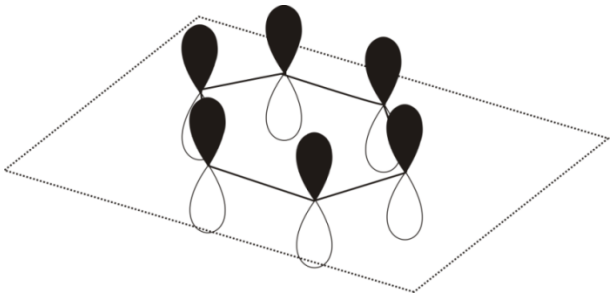

Figure 4.1 Schematic of sp^2 hybridised structure of graphite (free 2p orbitals shown).

Graphite is comprised of a series of parallel planar layers, termed basal-planes. Graphite has a perfect (defect free) hexagonal, crystallographic structure (shown below) and should not be confused with other graphitic materials. The stacking of the basal-plane occurs in two ordered structures, hexagonal or rhombohedral. The most commonly found stacking order is hexagonal (or alpha) with a –ABABAB– sequence, superimposing the carbon atoms of alternating basal-planes as shown in Figure (4.2).

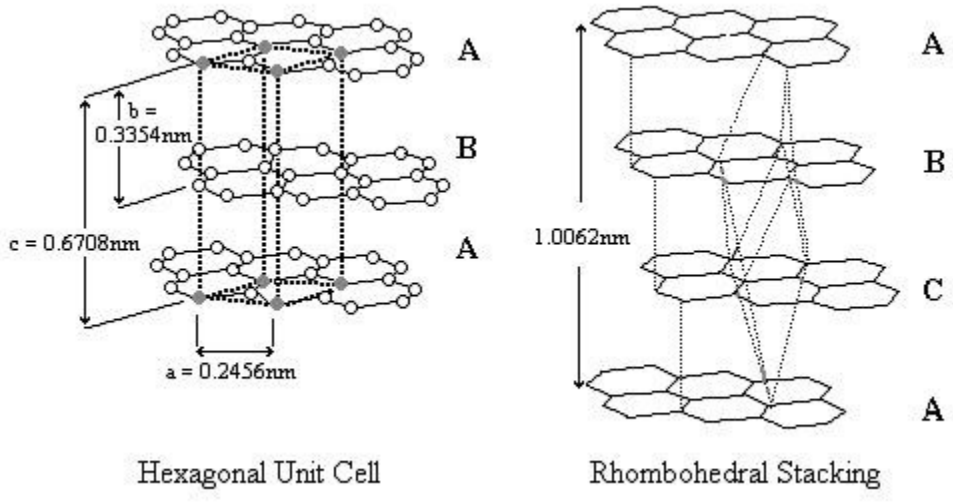

Figure 4.2 Schematics of hexagonal and rhombohedral graphite stacking arrangements, adapted from reference 1.

A rhombohedral structure (Figure 4.2) displays a –ABCABC– stacking order, thus the carbon atoms of every third basal layer are superimposed. This type of structure is not found in a pure form but in a blend with the hexagonal arrangement. The rhombohedral configuration converts to the hexagonal form, which is thermodynamically more stable, after heat treatment (over 1300 °C). [1]

The significant difference between the two structures is found in the distance between the basal layers (C_o), 0.6708 nm and 1.0062 nm for hexagonal and rhombohedral systems respectively. No direct overlap of carbon atoms between adjacent layers is found in either structure.

The graphitic crystal (basal) layer has two faces (zig-zag or arm-chair), depending on the orientation of the basal layer (Figure 4.3); these two configuration display different electron conductivities (important for carbon nanotubes (described later)).

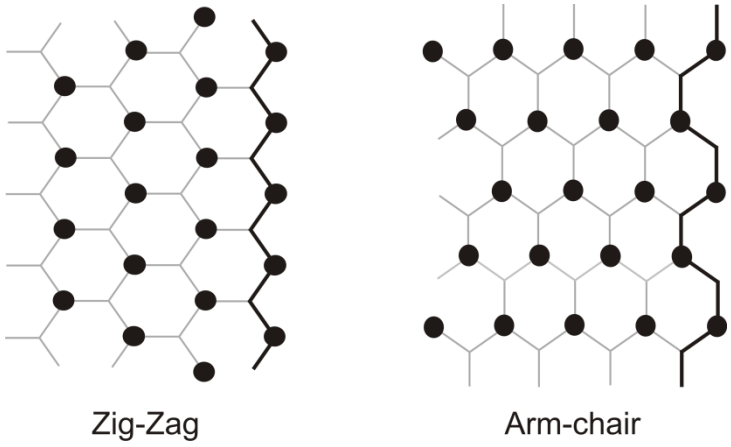

Figure 4.3 Schematic of a zig-zag (left) and arm-chair (right) graphitic crystal formations.

In line with the basal-plane is what researchers have termed the 'edge-plane'. The edge-plane is formed via the termination sites found around the perimeter of the basal-plane layers. Basal and edge-plane sites exhibit significantly different surface energies (0.11 J/m^2

and 5 J/m^2 respectively). Thus, the reaction rate at the edge-plane sites is considerably faster than that found at the basal-plane. This parameter is important when constructing or tailoring a graphite electrode for a specific system. Evidently, for processes that require fast electro-catalytic reactions, the working surface area should contain an elevated percentage of edge-plane-like sites/defects. Concurrently, the reverse is true for systems favourable to slow electro-catalytic processes. Edge-plane and basal-plane pyrolytic-graphite electrodes (EPPG and BPPG respectively) are fashioned from highly-ordered pyrolytic-graphite (HOPG). The HOPG surface consists of islands of basal-plane graphite, surrounded by nano bands of edge-plane sites, which lie parallel to the surface. Defects along the surface occur in the form of steps exposing the edges of the graphite layers. Graphites' layered structure tenders low resistivity along the plane (~ 2.5 to 5 × 10^{-6} Ω·m), conversely through (perpendicular to) the plane, resistivity values approach close to 3000 × 10^{-6} Ω·m. This consequently results in electrodes, consisting entirely of edge-plane *viz*. an edge-plane pyrolytic-graphite electrode, displaying a near reversible voltammogram, while an electrode consisting mostly of basal-planes will show irreversible behaviour; it should be noted that this is highly dependent on the percentage of edge-plane exposed.

Graphene (or graphene plane) has received extensive interest recently, becoming one of the hottest topics in the fields of materials science, physics, chemistry and nanotechnology. Comprised of a single graphitic, one-atom-thick planar sheet of sp^2 bonded (basal-like) carbon, graphene displays some special properties when paralleled alongside other carbon structures, such as unusual structural characteristics and electronic flexibility. Characteristics like high planar surface area (~2630 m^2/g), exceptional electrical (~2000 S cm^{-1}) and thermal (5300 W mK^{-1}) conductivity, outstanding mechanical strength (Young's modulus, ~1100 GPa) and transparency to visible light, are all highly anticipated to benefit many technologies. Graphene along with its closely related cousin, carbon nanotubes, are two

allotropes which possess identical composition, thus, one would believe that the properties of both materials would also be similar; this is not always the case. The structural characteristics found at graphitic materials are conditional to the intraplanar microcrystallic sizeL_a, and interplanar size L_c, shown schematically in Figure (4.4) for the case of HOPG and graphene. The intra-/inter-planar characteristics (L_a and L_c) refer to the atomically ordered hexagonal plane, known as the basal-plane, and its corresponding the edge-plane sites-defects (discussed earlier). Shown in Figure (4.4) is a range of L_a and L_c values for a variety of graphitic forms; HOPG displays L_a and L_c values exceeding 1 μm whereas carbon black and polycrystalline graphite exhibit values ranging between 1-10 nm and 10-100 nm respectively. L_a values for graphene range from < 50 to over 3000 nm, while true (monolayer) graphene possess an L_c value of only 0.35 nm. The smallest L_a values (as low as 10 Å (1 nm)) are found in amorphous carbon, glassy carbon and carbon black. Carbon fibres and pyrolytic graphite are considered intermediary, with L_a values of approximately 100 Å (10 nm) and 1000 Å (100 nm) respectively.

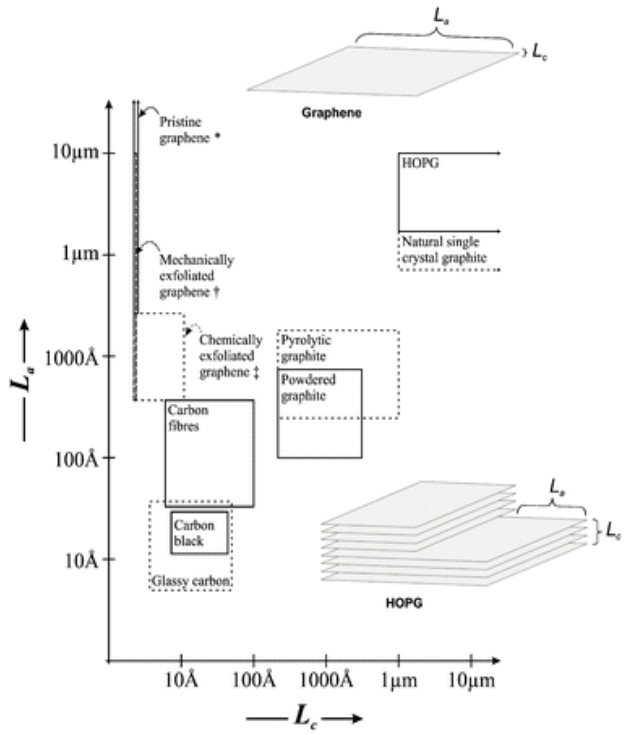

Figure 4.4 The approximate ranges of L_a and L_c values for various sp^2 carbon materials: Note, there is large variation of L_a and L_c with sample history and thus the values shown should be considered representative, yet approximate. A schematic representation of the L_a and L_c microcrystalline characteristics of graphene and HOPG is also shown. Figure reproduced from reference 6.

4.2.1.2 PYROLYTIC GRAPHITE

Pyrolytic graphite is a unique form of graphite produced via chemical vapour deposition (CVD). An organic precursor, such as methane, typically contained within hydrogen (or a similar mixture), flows through a gas chamber. Inside is a preheated substrate where the methane is deposited on its surface and slowly decomposed into continuously growing layers of carbon via the following reaction scheme: methane → benzene → poly-aromatic hydrocarbons → carbon. This material is consequently heat treated at 2500 °C, reordering the crystal structure into its final form. Depending on the temperature and pressure applied, pyrolytic graphite can take three different forms: columnar, laminar and isotropic. Isotropic pyrolytic graphite displays a reduced size in the basal-plane's surface area, with greater interlayer spacing when compared to the other forms. The layered pyrolytic graphite is then cut. The orientation of the material determines the electro-catalytic properties, fashioning an electrode surface consisting of either basal (basal-plane pyrolytic graphite, or BPPG) or edge (edge-plane pyrolytic graphite, or EPPG) like sites. EPPG electrodes display enhanced electro-catalytic properties (fast electron transfer reactions, lower overpotentials etc) compared to the same electrode material with a basal-plane orientation (BPPG). Typically in electrochemical measurements, a body allegedly capable of increasing the electro-catalytic response of the working electrode's surface is initially tested on a BPPG orientated electrode. The analyte is deposited on the basal-plane-like surface of the BPPG electrode prior to electrochemical analysis. When the current response from the modified BPPG is augmented in comparison to its typically electrochemical spectra (approaching or even surpassing that of an EPPG electrode), the newly incorporated material is deemed to have enhanced the electro-catalytic behaviour of the working electrode's surface (since BPPG itself exhibits slow electro-catalytic behaviour). An example of a HOPG electrode is shown in Figure 4.5.

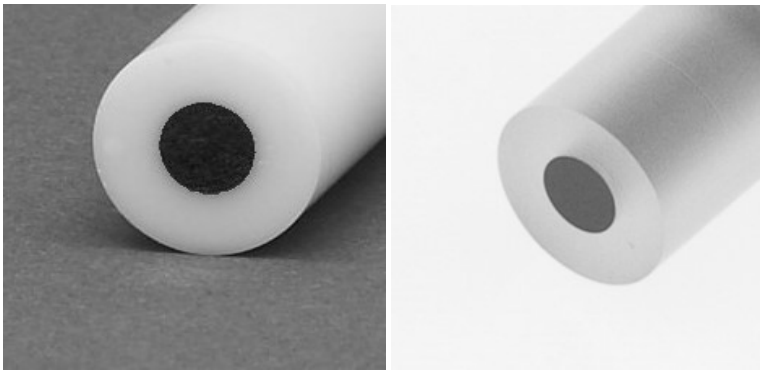

Figure 4.5 Image of a HOPG (left) and glassy carbon (right) electrode.

4.2.1.3 CARBON NANOTUBES

A Carbon Nanotube (CNT) is conceptually a single dimensional, micrometer scale graphene sheet, rolled into a cylinder of nano-scale diameter, crowned with a spherical fullerene (fullerenes are zero dimensional enclosed cage-like carbon structures). Pairing a nano-scale diameter with a micro- to centimeter length yields CNT structures with remarkable aspect ratios. Extensive published literature is available on the synthesis and structural conformations of CNTs. [3] The sidewalls of CNTs, like graphene, have a hexagonal sp^2 conformation; however, the degree of curvature witnessed at carbon nanotubes is not limited to a single dimension. The stronger sp^3 bonding characteristics found at the nanotube reduce the strain energy at the walls and render the carbons less susceptible to chemical modification and rearrangement than spherical fullerene structures.

Nanotubes are distinct from graphene planes in two ways; firstly the geometric single dimensionality of the nanotube induces quantum confinement in the radial and circumferential directions. Quantum confinement describes how the electronic properties (the organization of energy levels into which electrons can climb or fall) change when the material sampled is sufficiently small in size - typically 10 nanometers or less. Specifically, the phenomenon results from electrons and holes (holes are the positively-charge species left

when an electron vacates its position in a crystal) being squeezed into a dimension that approaches a critical quantum measurement, called the exciton Bohr radius. Secondly, the potential for structural indeterminacy is acquainted with the confinement of graphene's two-dimensional hexagonal structure is into a single dimension. As mentioned previously, the orientation of the rolled graphene sheet has an important influence over the electronic characteristics of the CNT. Despite the fact that bulk graphite is a semiconductor, isolated single-walled nanotubes (SWNTs), typically of small diameters, can display metallic, semi-metallic or semiconducting characteristics subject to the orientation of the hexagonal carbon lattice. Typically, in high yield synthesis techniques, the nanotube adopts the metallic arm-chair structural conformation.

Double-walled and multi-walled nanotubes (MWNTs) share many of the properties of bulk SWNTs as the coupling across the 0.34 nm interlayer is weak (Figure 4.6). Unlike SWNT, MWNTs display semiconducting characteristic akin to bulk graphite.

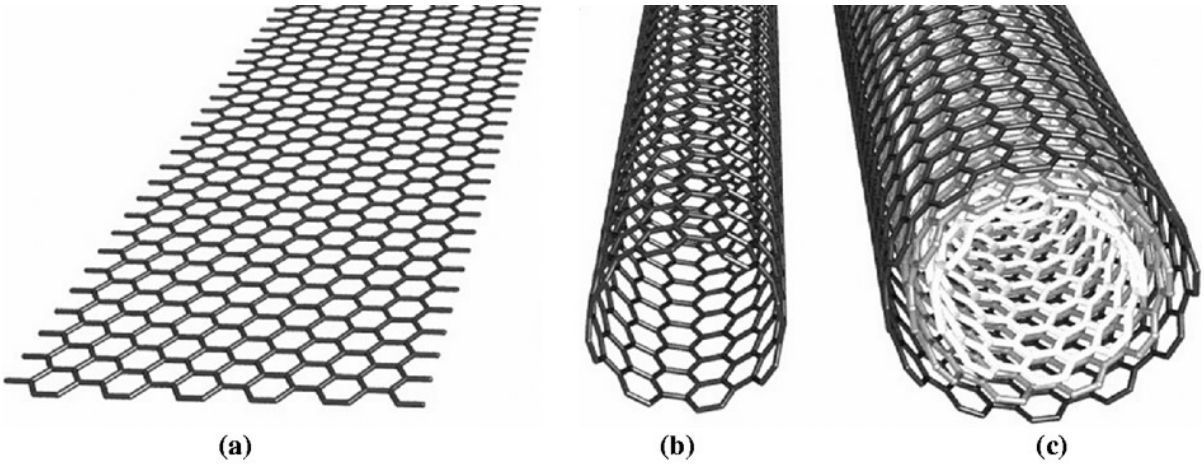

Figure 4.6 Graphical Depictions of a) graphene sheet b) SWNT and c) MWNT. Figure reproduced from reference 3.

Strong attraction forces between the nanotubes complicates purification and manipulation processes. The tightly bundled conformation and poor dispersal observed at

CNTs in both polar and non-polar solvents is credited to these forces, often requiring physical dispersion processes, such as sonication, to produce uniform mixture.

SWNTs and MWNTs obtained commercially are replete with defects, metal impurities and physical dissimilarities. Thus, these discrepancies between samples convolute research, having a substantial impact on the commercial application of CNTs. As such, the application of CNTs draws upon its bulk properties, like high surface area, rather than single nanotube characteristics such as high conductivity.

The bonding arrangement of fullerenes and nanotubes offer unique conductive, optical and thermal properties, tendering auspicious characteristics for applications within the electronic industry. Tuneable band gaps, high stability, remarkable current transport capability, low ionization potential, and efficient field emission are among the most desirable electronic characteristics of SWNTs. A vast amount of these properties occur via the electron flow confinement in one-dimensional nanotubes. The electronic behaviour observed at nanotubes is strongly coupled to chirality, diameter, length, and the number of concentric tubules. Metallic SWNTs act akin to quantum wires, with electron confinement in the radial direction as mentioned previously, quantizing the conduction bands into discrete energy levels. Electrons are transported via resonant tunnelling through these discrete electron states in the nanotube, delocalized over an extended length of the nanotube. This spatial extension of charge not only bolsters conductivity and current capability, but also diminishes the impact of defects occurring along the nanotube sidewalls.

4.2.2 CARBON BLACK

Carbon black is formed through the carbonization (conversion of an organic substance into carbon) of coke: a grey coloured, solid (porous) carbon material derived from the destructive distillation of bituminous coal. Although a less favourable electrode

material, owed to its increased electrical resistivity, it is extensively used as a key component of the inks developed in the production of screen-printed electrodes (see Chapter 5). Carbon black gives conductivity to the polymeric network provided via the binder, forming of a homogeneous mixture. The inks also contain graphite; at which the electro-catalytic processes primarily take place.

4.2.3 BORON-DOPED DIAMOND

The boron-doped diamond electrode (BDDE) is a commonly employed tool within electrochemistry. The BDDE does not interact or bind with organic compounds, the bi-products are not absorbed onto its surface during the redox reaction that occur at its surface, leaving it unpolluted and available for further redox reactions of further electroactive species present in solution. Boron-doped diamond is a tough, stable (does not form oxides) material, resistant to most chemicals. The reason for these distinctive characteristics lies in the BDDE structure.

Carbon atoms have a $1s^2$, $2s^2$, $2p^2$ electron configuration at the ground state. Once these atoms bond together in a diamond structure (similar to methane), the following electron configuration is present: $1s^2$ and four $2sp^3$ (hybrid orbitals). This raises the energy state of the electrons in the carbon atom, stabilised via the bonds found in the structure. The resulting hybridisation is the formation of four strong covalent bonds with an additional four carbon atoms (each sharing two electrons). The arrangement of the carbon atoms is a regular tetrahedron (see Figure 4.7).

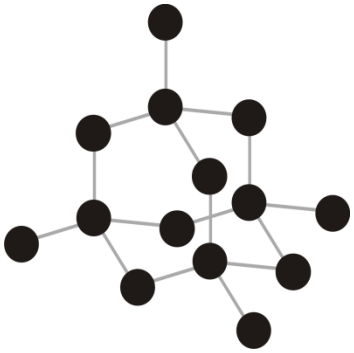

Figure 4.7 Schematic of sp^3 hybridised (tetrahedral) 'diamond' structure.

The four sp^3 valence electrons of the hybrid carbon atoms, in conjunction with a small atom size results in a strong covalent bond. This is enhanced as four of the six electrons found at the carbon atom formulate bonds.

Diamond is one of the best known electrical insulators, making it a poor candidate as an electrode material. Conversely its high strength, stability and chemical resistance make it ideal. This only occurs when the diamond is a pure crystal. The presence of impurities or defects diminishes these optimum properties. Thus doping diamond with metal impurities alters its electrical properties (increasing conductivity). Boron has a similar atom size to carbon and is a known electron acceptor, due to electron deficiencies found in its outer shell. To provide adequate conductivity, doping of the diamond electrode ranges from 10^{19} to 10^{21} atoms/cm^3. The resulting electrode, as mention previously has a wide operating potential window (ca. -1.35 to +2.3V versus a normal hydrogen electrode), low background currents and stability in aggressive media.

4.2.4 GLASSY (VITREOUS) CARBON

Glassy carbon offers unique properties compared to other types of carbon materials. Essentially non-porous, it offers low permeability, while free from surface defects and containing little or no impurities. These characteristics are attributed to the organic precursor

(polymer) from which it is produced. The crystallite arrangement is random (no long-range order) making the material isotropic and produces a 'ribbon' like structure (Figure 4.8). The aromatic rings are twisted and cross linked with covalent bonds, producing variable bond energies and thus the existence of sp^2 and sp^3 structures. The partial diamond structure (sp^3) is believed to give the glassy carbon its high strength and hardness. It is for this reason that this material is not easily graphitised (converted to graphite under high temperatures) and is highly resistant to chemical attack.

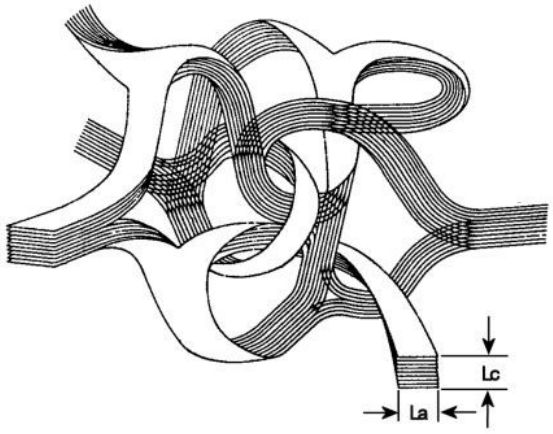

Figure 4.8 Glass carbon 'ribbon' network where L_a is the Intraplanar Microcrystaline Size and L_c is the Interplanar Microcrystaline Size. Figure reproduced from reference 5.

4.2.5 CARBON-PASTE ELECTRODES

Typically graphite powder combined with various water-immiscible organic binders (or pasting liquid), carbon paste electrodes offer an easily renewable and modified surface, low costs and low background currents. The paste composition strongly affects the electrodes reactivity. Elevated binder content decreases the rate of electron transfer. In absences of the binder, the dry graphite powder yields rapid transfer kinetics, approaching those displayed at metal surfaces. The precise behaviour observed at carbon paste electrodes is still not entirely understood with some electrochemical observations possibly involving the permeation of the binder layer by electroactive species (solvent extraction). Carbon-paste offers a suitable matrix for the incorporation of appropriate modifying agents. The modifier is simply mixed together with the graphite/binder paste without the requisite of devising unique and individual

attachment schemes for various modifiers. A disadvantage to the paste electrode is the tendency of the organic binder to dissolve in solutions containing an appreciable fraction of organic solvent.

4.2.6 METAL ELECTRODES

A wide variety of noble metal electrodes are available, the most commonly used being gold and platinum. Such electrodes offer favourable electron rate kinetics and a large potential range. However, the build-up of surface oxides results in the appearance of high background currents, such films strongly affect the rate kinetics of the electrode reaction, resulting in irreproducible data. This is less problematic in non-aqueous media. Gold electrodes, compared to that of a platinum electrode, are more inert and therefore less prone to surface contamination and/or the formation of surface oxides films.

4.2.7 REFERENCES

1. H. O. Pierson, *Handbook of carbon, graphite, diamond and fullerenes properties, Processing and Applications*, Noyes Publications, New Jersey.
2. M. S. Mauter and M. Elimelech, "*Environmental applications of carbon-based nanomaterials*," *Envir. Sci. and Tech.*, **2008**, 42, 16, 5843.
3. F. Kreupl: "*Carbon Nanotubes in Microelectronic Applications*". *Carbon Nanotube Devices*: *Properties, Modeling, Integration and Applications*. **2008**, Wiley-VCH.
4. J. Wang, "*Analytical Electrochemistry*", 2nd ed.; Wiley-VCH. **2001**.
5. G. M. Jenkins, K. Kawamura, *Nature*, **1971**, 231, 175.
6. D. A. C. Brownson, D. K. Kampouris, C. E. Banks, *Chem. Soc. Rev*., **2012**, 41, 6944.

4.3 CHARACTERISATION OF ELECTRON TRANSFER PROCESSES IN CARBON NANOMATERIALS

Section 4.3 contains published work [1,2] undertaken during this thesis in support of characterising and understanding electron transfer processes of carbon nanomaterials used in the development of energy-storage and production devices. A simple methodology based on cyclic voltammetry is presented allowing the density of defects, *viz* edge-plane-like sites/defects of carbon nanomaterial's to be readily quantified. The approach is based on the construction of carbon nanomaterial paste electrodes which is measured using cyclic voltammetry and a standard electrochemical redox probe. This protocol allows a quantitative relationship between the heterogeneous electron-transfer rate and the density of defects to be readily determined and also provides researchers with a methodology to quantify the density of defects for comparative purposes without resorting to impedance investigation which requires extensive time periods to conduct the analysis and expensive equipment.

It is also demonstrated that graphene-modified electrodes do not suffer from thin-layer effects which is commonly observed in carbon nanotube modified electrodes which preclude mechanistic information to be deduced and false claims of electro-catalysis to be inferred. Interestingly, in a comparison of graphene orientated on a surface with that of multi-walled carbon nanotubes, the latter have an identical % of electron transfer sites (edge-plane content) with that of the former.

1. P. M. Hallam, C. E. Banks, *Quantifying the electron transfer sites of graphene*, *Electrochem. Commun*., **2011**, 13 (1), 8.

2. P. M. Hallam, C. E. Banks, *A facile approach for quantifying the density of defects (edge-plane sites) of carbon nanomaterials and related structures*, *PCCP*, **2011**, 13 (3), 1210.

4.3.1 A SIMPLISTIC APPROACH FOR QUANTIFYING THE DENSITY OF DEFECTS (EDGE-PLANE SITES) OF CARBON NANOMATERIAL'S AND RELATED STRUCTURES

4.3.1.1 INTRODUCTION

Carbon nanostructures such as multiwalled carbon nanotubes and their single walled counterparts find use in a plethora of technological applications.[1–10] Carbon-based electrodes have become commonly used because of their low cost, good electron transfer kinetics and biocompatibility.[11] Lately, many researchers are discovering the benefits of having carbon nanotubes (CNTs) integrated into electrochemical technologies.[12–16] Structurally carbon nanotubes are rolled up layers of graphene and consist largely of basal-plane graphitic regions with edge-plane regions at the open ends of the nanotube, and in certain variants along the tube axis.[6] While they offer many similar properties to other types of carbon, CNTs tender unique advantages including enhanced electronic properties, a large edge/basal-plane ratio, and rapid electrode kinetics. Thus, CNT-based devices frequently display higher sensitivities, lower limits of detection, and faster electron transfer kinetics than traditional carbon electrodes.[11] It has been demonstrated that these edge-plane-like sites/ defects are the origin of electron transfer,[17–19] and the amount of edge-planes will dictate the overall electrochemical properties. Recent work has demonstrated that electron transfer may be amplified through the electrochemical activation of carbon nanotubes and determining the physical change of the carbon nanotube structure is of fundamental importance.[20–22] Carbon nanotubes find use in the design and development of nano-architectures, for example in the use of nano-scale circuitry through chemical and electrochemical modification utilising the high energy reactive sites of the edge-plane-like sites/defects on the nanotube structure.[23,24] Additionally carbon nanotubes act as excellent nano-templates and can be modified for example, producing metallic nanostructures for use in a plethora of technology applications ranging from fuel cells through to sensors.[25] Inevitably, the edge-plane-like sites/defects are the origin of the templates and consequently relating the density of sites, is of fundamental

importance and essential for researchers to reproduce work, this is especially true in the case where CNT are employed as sensors.[6] Currently the only way to determine the density of edge-planes is through capacitance,[26] Raman and visual identification (SEM/TEM, etc.) which can be extremely difficult and time consuming.[26,27] In this work a simple methodology for quantifying the density of edge-plane-like sites/defects of carbon nanomaterials is presented. Relating the amount of edge-plane-like sites/defects on carbon nanomaterials and other related carbon structures is fundamentally important in not only electrochemical sensing but also where there materials are used in technological important areas such as in fuel cells, supercapacitors and so on. Presently the literature lacks a simple methodology that allows the density of defects (*viz* edge-plane sites) of carbon nanomaterials to be readily quantified, giving researchers a reference point for comparative purposes.

4.3.1.2 EXPERIMENTAL

All chemicals used were of analytical grade and were used as received without any further purification and were obtained from Sigma-Aldrich. All solutions were prepared with deionised water of resistivity not less than 18.2 MΩ cm. Voltammetric measurements were carried out using a m-Autolab III (ECO-Chemie, The Netherlands) potentiostat. All measurements unless otherwise stated, were conducted using a three electrode configuration comprising of a working electrode (4.5 mm diameter) with a platinum wire and Saturated Calomel Electrode (SCE) acting as counter and reference electrode respectively. Carbon nanotube paste electrodes were fabricated in-house. The carbon-nanotube paste is a formulation of carbon nanotubes (~0.09 g, Nano-Lab™, length: 5–20 microns, diameter 30 ± 10 nm, purity 95%) and the inert binder Nujol (~0.36 g, neat), which is extensively mixed. It should be noted that different carbon nanotube powders may require (in our case as little as ~0.12 g Nujol) to produce similar paste consistencies. The nanotube paste was then placed into a modified 1 ml syringe (BD Plastipak™), which is connected via a copper wire to the

potentiostat. The piston of the syringe is ideal for renewing the surface. This methodology allows us to negate any surface changes that take place during the experiments. For comparative purposes a glassy carbon (GC, 3 mm diameter) electrode was first polished using diamond spray (Kemet international Ltd.) of decreasing particle size from 1 to 0.25 mm. Between each polishing step the electrode was washed to remove any adhered diamond microparticles. Carbon nanotubes were immobilised onto the electrode by dropping a 15 ml aliquot of the CNT solution (5 mg/1.5 ml ethanol) onto the electrode surface which was allowed to evaporate at room temperature.

4.3.1.3 RESULTS AND DISCUSSIONS

First, the voltammetric performance of a carbon nanotube modified glassy carbon electrode explored in 1 mM $[Ru(NH_3)_6]Cl_3$ / 1M KCl. Figure (4.9A) depicts the observed voltammetric profiles over the scan rate of 0.005 to 0.2 V s^{-1}. The method of Nicholson [28] is routinely used to deduce the standard electron transfer rate using the following equation:

$$k^{o} = \psi\,[D_0\,\pi\,v\left(\frac{nF}{RT}\right)]^{1/2}\ \left(\frac{D_r}{D_o}\right)^{\alpha/2} \qquad (4.1)$$

where k^{o} is the standard electron rate constant, ψ is the kinetic parameter, D_0 is the diffusion coefficient of ruthenium(III) hexamine (9.1×10^{-6} cm^2 s^{-1}, 0.1M KCl),[29] v is the scan rate, F is the Faraday constant, α is the transfer coefficient (0.5) and n is the number of electrons transferred in the electrochemical process.

Analysis of the peak-to-peak separation (Figure 4.9) at 0.1 V s^{-1} is 35 mV but the peak-to-peak separation is too small to be used, which is the case for all peak-to-peak separations observed over the scan rates employed.[30,31] Associated with equation (4.1) is the Randles–Ševćik equation (equation 2.1).[32] For both equations to be useful the voltammetric peak current should be proportional to the square root of the scan rate (equation (2.1)).

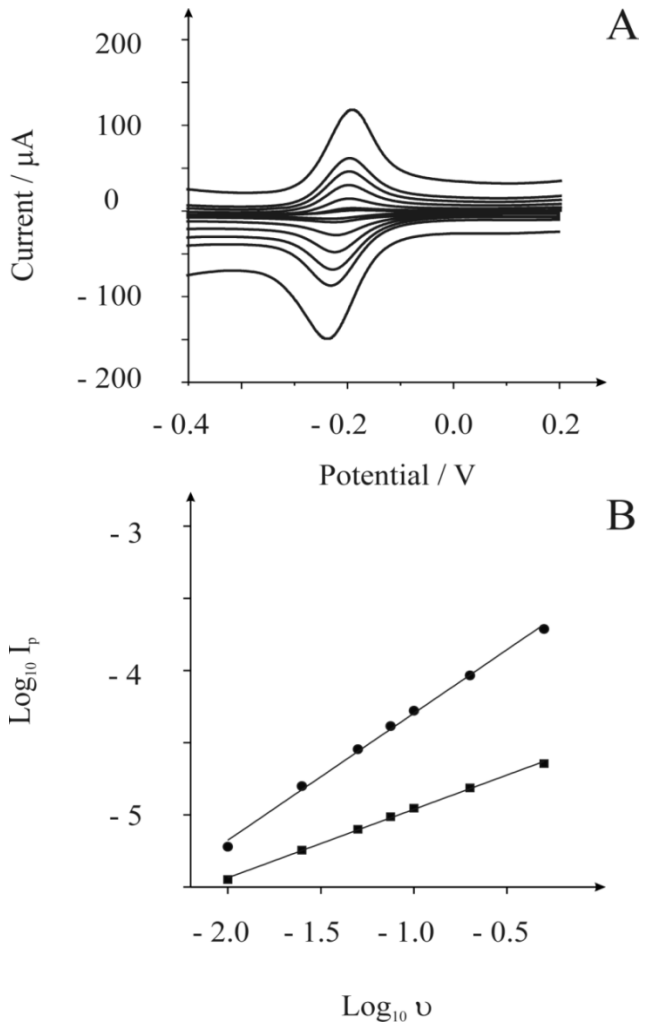

Figure 4.9 Cyclic voltammetry (A) of a carbon nanotube modified GC electrode in 1mM $Ru(NH_3)_6Cl_3$ / 1M KCl. Scan rates 0.005 - 0.2 Vs^{-1} (Vs. SCE). Part B shows the analysis of the peak current (I_p) versus applied scan rate (υ) recorded at a carbon nanotube modified (circles) and non-modified (squares) GC electrode in 1mM $Ru(NH_3)_6Cl_3$/ 1M KCl (Vs. SCE).

Figure 4.9B depicts the analysis of the cyclic voltammetric peak in terms of the $\log_{10}$ of peak current ($\log_{10} I_P$) versus $\log_{10}$ of the applied voltammetric scan rate which reveals a gradient of 0.879 which is clearly substantially more than the expected gradient of 0.5 as governed by equation (2.1). The response of a bare GC electrode is shown in Figure 4.9B which exhibits a gradient of 0.48 indicating that in this case, equations (4.1) and (2.1) are valid. Returning to the response of the carbon-nanotube modified GC electrode, the plot of the cyclic voltammetric peak in terms of the $\log_{10}$ of peak current ($\log_{10} I_P$) versus $\log_{10}$ of the applied

voltammetric scan rate as depicted in Figure 4.9B is very close to ‘‘1’’ which is as expected for a thin-layer cell, of thickness *l* for reversible electron transfer as given by: [33]

$$I_p = \frac{n^2F^2vlC}{4RT} \quad (4.2)$$

where I_p is the voltammetric peak current, *F* is the Faraday constant, *v* is the scan rate, c is the concentration of the electroactive species and *n* is the number of electrons transferred in the electrochemical process.[34] Work by Compton *et al*.[30] has demonstrated that carbon nanotube modified electrodes have two main diffusion contributions. The first from semi-infinite diffusion of the electro-active species towards the planar electrode surface and the second from the electro-active species trapped within the carbon nanotube network; Figure 4.10 shows a schematic representation of this, which is clearly observed in our work above (Figure 4.9B). Due to these two contributions, mechanistic information is not easily de-convoluted and requires knowledge of the exact film thickness, or best approximation. Thus it is clearly evident that the immobilisation of the carbon nanotube has resulted in a thin film upon the supporting GC electrode and information on the density of defects may not be readily determined.

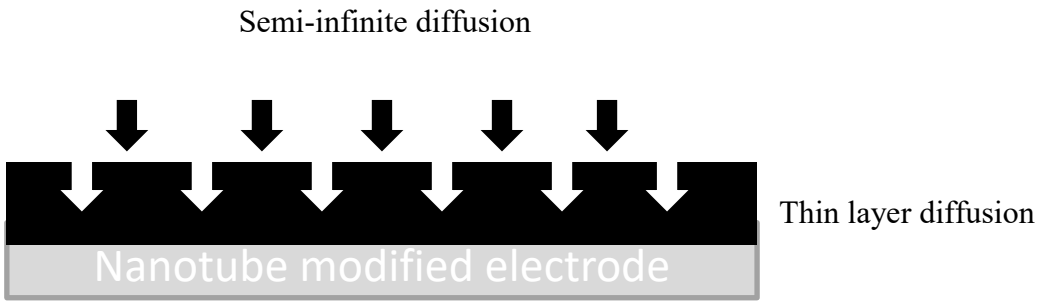

Figure 4.10 Schematic representation of a carbon, nanotube ‘film’ modified electrode which has two diffusional conditions. The black layer represents the CNTs on the electrode surface.

Next attention was turned to carbon-nanotube paste electrodes which were fabricated as described in the experimental section with their electrochemical explored in a 1 mM [Ru(NH3)6]Cl_3 /1 M KCl solution. Figure (4.11) depicts the observed voltammetric profiles where a peak-to-peak separation of 87 mV at 0.1 V s^{-1} (vs. SCE) is observed. The effect of scan rate on the peak height was explored over the range 0.005 to 0.2 V s^{-1}. Analysis of this data in the form of a plot of log I_P vs. log v generates a gradient of 0.46, indicating that the response is governed by equation (4.1) and the contribution is from semi-infinite diffusion. Analysis with equation (4.1) allows the standard electron transfer rate, k^0 to be calculated as 4.8×10^{-3} cm s^{-1}.

The observed electron transfer rate, k^0_{obs}, on graphite electrodes such as highly ordered pyrolytic graphite (HOPG) has been shown to be a contribution from two possible structural components edge-plane and basal-plane sites.[35] In the case of the carbon nanotubes, edge-plane-like sites/defects occur along the length of the nanotube and at the open ends (k^0_{edge}) and that of basal-plane-like sites (k^0_{basal}) allowing us to write:

$$k^0_{obs} = k^0_{edge}\left(\theta_{edge}\right) + k^0_{basal}\left(1 - \theta_{edge}\right) \tag{4.3}$$

It has been shown that electrochemical reactions at edge-plane graphite are ominously fast over that of basal-plane and are the major contribution in most general cases [35] , this has been shown to be applicable to carbon nanotubes [8] allowing us to write

$$k^0_{edge} \gg k^0_{basal}$$

and equation (4.3) now becomes:

$$k^0_{obs} = k^0_{edge}\left(\theta_{edge}\right) \tag{4.4}$$

allowing the microscopic coverage of edge-plane defects on the electrochemical platform (*viz* carbon nanomaterials) to be approximated. [35] Given that the dominant domain on the electrode surface is edge-plane, the microscopic coverage is approximate to the global coverage (Θ_{edge}), [35]

$$\theta_{edge} \approx \Theta_{edge} \tag{4.5}$$

allowing the global coverage of edge-plane-like sites/defects of carbon nanotubes that are electrochemically active to be readily determined. The electron transfer rate for edge-plane of for our redox probe (k^0_{edge}) has been determined with a commercial simulation package providing a value of 0.4 cm s^{-1}. [35] Using equation (4.4) the coverage of edge-plane defects, θ_{edge}, can be readily deduced as k^0_{obs} can be determined from the voltammetric profiles obtained using the carbon nanomaterials, such as those presented in Figure (4.11) and with the aid of equation (4.1).

Using equation (4.4) the percentage of edge-plane sites/defects was found to be ~3.01% (± 0.02). This is in excellent agreement with Pumera and co-workers [26] who have used capacitance measurements which clearly validates our approach. Our methodology of using a carbon-nanotube paste electrode minimises diffusion within the CNT network allowing the density of defects, *viz* edge-plane-like sites/defects to be readily determined via cyclic voltammetry; the presence of two diffusional contributions will preclude meaningful data from voltammetric experiments to be deduced as equation (4.1) is invalid (see above).

Last this methodology is used to deduce the density of edge-plane defects on carbon nanotube 'clusters' and carbon nanotube 'whiskers', recently reported carbon nanomaterials. [36,37] Using the above approach, the % density of the defects is found to be ~1.46% and ~13.29% respectively. Given the structure and electrochemical responses, these values are as expected. Interestingly, for comparative purposes the response of graphite is explored and

found to be similar to that of CNTs (Table 4.1) which is in agreement with previous studies that CNTs are no-more reactive than graphite.[18]

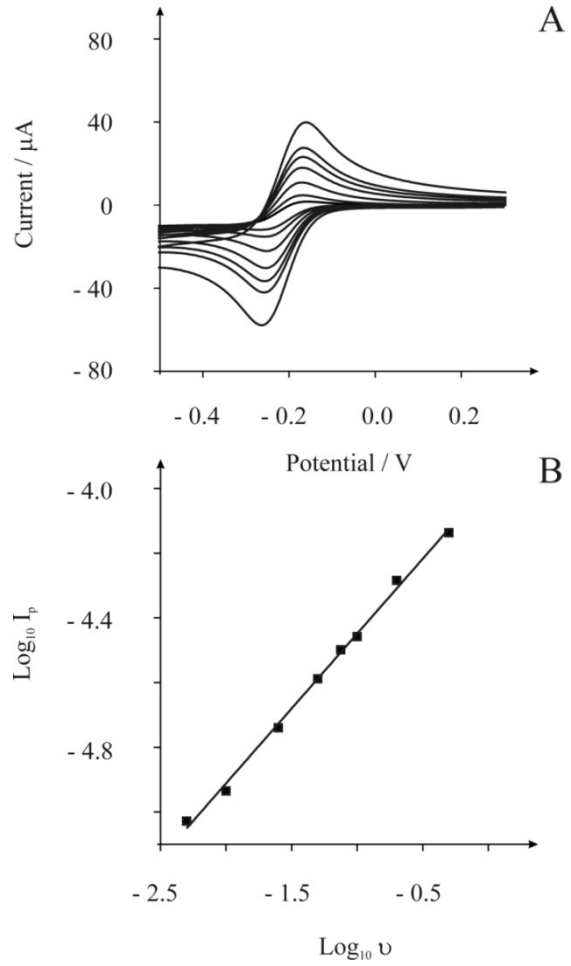

Figure 4.11 Cyclic voltammetric profiles (A) obtained using the Nano-Lab™ carbon nanotube paste electrode in 1mM $Ru(NH_3)_6Cl_3$/ 1M KCl over the scan rates of 0.005 and 0.2 Vs^{-1} (vs. SCE). Part B shows the analysis of (A) with a plot of log I_p vs. log υ producing a gradient of 0.46 indicating a semi-infinite diffusion mechanism.

Table 4.1 Calculated density of edge-plane-like sites/defects for studied carbon nanomaterials

Nano-Material	k^0 / cm s^{-1}	% edge (Θ_{edge})
Carbon Nanotube (Nano-Lab^{TM})	1.20×10^{-2}	3.01
Carbon Nanotube 'Clusters'	5.58×10^{-3}	1.46
Carbon Nanotube 'Whiskers'	5.32×10^{-2}	13.29
Graphite Powder	1.58×10^{-2}	3.96

4.3.1.4 CONCLUSIONS

A simple methodology is reported, currently lacking in literature, allowing a quantitative relationship between the heterogeneous electron–transfer rate and the density of defects to be readily determined providing researchers with a methodology to quantify the density of defects for comparative purposes. The methodology is valid as long as the electro-active species has been rigorously quantified on highly-ordered pyrolytic graphite (HOPG). We note however, that if the conditions of the plot of log I_p vs. log v has a gradient of 0.5, when using CNT 'film' modified electrode, then equation (4.4) is equally valid and can be used as a convenient tool via cyclic voltammetry for measuring the density of defects of the nanomaterial under investigation. However, the contribution of edge-plane coverage from the underlying electrode will need to be considered.

4.3.1.5 REFERENCES

1. M. J. Esplandiu, M. Pacios, E. Bellido, M. del Valle, *Z. Phys. Chem*., **2007**, 221, 1161.
2. J. Wang, *Electroanalysis,* **2005**, 17, 7.
3. J. J. Gooding, *Electrochim. Acta,* **2005**, 50, 3049.
4. M. Pumera, S. Sánchez, I. Ichinose, J. Tang, *Sens. Actuators B,* **2007**, 123, 1195.
5. A. Merkoçi, M. Pumera, X. Llopis, B. Perez, M. del Valle, S. Alegret, *TrAC Trends Anal. Chem.,* **2005**, 25, 826.
6. C. E. Banks, R. G. Compton, *Analyst*, **2006**, 131, 15.

7. J. M. Nugent, K. S. V. Sanhanam, A. Rubio, P. M. Ajayan. *Nano Lett.,* **2001**, 1, 87.
8. C. E. Banks, T. J. Davis, G. G. Wildgoose, R. G. Compton, *Chem. Commun.,* **2005**, 842.
9. A. Chou, T. Böcking, N. K. Singh, J. J. Gooding, *Chem. Commun.,* **2005**, 842.
10. M. Pumera, *Langmuir,* **2007**, 23, 6453.
11. C. B. Jacobs, M. J. Peairs, B. J. Venton, *Anal. Chim. Acta.,* **2010**, 662*,* 105.
12. J.H. Zagal, S. Griveau, K. I. Ozoemena, T. Nyokong, F. Bedioui, *J. Nanosci. Nanotechnol.,* **2009,** 9, 2201.
13. A.T. Chidembo, K. I. Ozoemena, B.O. Agboola, V. Gupta, G.G. Wildgoose, R. G. Compton, *EES*., **2010**, 3, 228.
14. S. A. Mamuru, K. I. Ozoemena, T. Fukuda, N. Kobayashi, T. Nyokong, *Electrochim. Acta*., **2010**, 55, 6367.
15. B. O. Agboola, K. I. Ozoemena, *J. Power Sources,* **2010**, 195, 3841.
16. B. O. Agboola, K. I. Ozoemena, T. Nyokong, T. Fukuda, N. Kobayashi, *Carbon*, **2010**, 48, 763.
17. C. E. Banks, R. R. Moore, T. J. Davies, R. G. Compton, *Chem. Commun*., **2004**, 16, 1804.
18. R. R. Moore, C. E. Banks, R. G. Compton, *Anal. Chem.,* **2004**, 76, 2677.
19. X. Ji, R. O Kadara, J. Krussma, Q. Chen, C. E. Banks, *Electroanalysis,* **2010**, 22, 1148.
20. J. Wang, M. Li, Z. Shi, N. Li, Z. Gu, *Anal. Chem.,* **2002**, 74, 1993.
21. C. M. Liu, H.–B. Cao, Y. P. Li, H. B. Xu, T. Zhang, *Carbon*, **2006**, 44, 2919.
22. M. Musameh, N. S. Lawrence, J. Wang, *Electrochem. Commun.,* **2005**, 7, 14.
23. G. G. Wildgoose, C. E Banks, H. C. Leventis, R. G. Compton, *Microchim. Acta*., **2006**, 152, 187.
24. K. Jurkshat, S. J. Wilkins, C. J. Salter, H. C. Leventis, G. G. Wildgoose, L. Jiang, T. G. J. Jones, A. Crossley, R. G. Compton, *Small*, **2006**, 2, No.1, 95.
25. G. G Wildgoose, C. E. Banks, R. G. Compton, *Small*, **2006**, 2, 182.
26. M. Pumera, T. Sasaki, H. Iwai, *Chem. Asia J.* **2008**, 3, 2046.
27. R. J. Rice, R. L. McCreery, *Anal Chem.* **1989**, 61, 1637.
28. R. S. Nicholson, I. Shain, *Anal. Chem*., **1965**, 37, 179.
29. C. E. Banks, R. G. Compton, A. C. Fisher, I. E Henley, *PCCP.* **2004**, 6, 3147.
30. I. Streeter, G. C. Wildgoose, L. Shao, R. G. Compton, *Sens. Actuators B*. **2008**, 133, 462.

31. G. P. Keeley, M. E. G. Lyons, *Int. J. Eletcrochem. Sci.* **2009,** 4, 794.
32. R. G. Compton, C. E. Banks, *Understanding Voltammetry*, World Scientific Ltd., 1st edn. **2007**.
33. A. T. Hubbard, *J. Electroanal. Chem.*, **1969**, 22, 165.
34. A. J. Bard, L. R. Faulkner, *Electrochemical Methods*. 2nd Ed.
35. T. J. Davies, M. E. Hyde, R. G. Compton, Angew. *Chem., Int. Ed.* **2005**, 44, 5121.
36. C. P. Jones, K. Jurkschat, A. Crossley, R. G. Compton, B. L. Riehl, C. E. Banks, *Langmuir*, **2007**, 23, 9501.
37. More information on these can be found from the website www.scnte.com, Accessed August 2010.

4.3.2 QUANTIFYING THE ELECTRON TRANSFER SITES OF GRAPHENE

4.3.2.1 INTRODUCTION

Carbon materials have been employed extensively in both analytical and industrial electrochemistry, outperforming traditional noble metals on numerous occasions. This success is owed largely to its structural polymorphisms, chemical stability, rich surface chemistry and low cost, allowing it to be utilised in a plethora of applications. [1] Recently, traditional carbon materials based on graphite, diamond, glassy carbon, and carbon black have been outperformed by the unique characteristics of micro-fabricated carbon structures, such as carbon nanotubes (CNTs), enabling the development of novel applications in sensing, electro-catalysis, and electronics. [1,2] In these cases the origin of the electron transfer has been shown to reside at the edge-plane-like sites/defects [3,4] and Figure 4.12 shows a schematical representation of a surface of highly ordered pyrolytic graphite (HOPG) showing discrete basal-plane and edge-plane islands (Figure 4.12A) and a side on view highlighting the edge-plane and basal-plane-like sites/defects which exhibit contrasting electrochemical behaviour where electrochemical reactions on the former has been shown to be anomalously fast over the latter.[3] However, with the introduction of graphene, which tenders many reported superior properties without exhibiting any of the disadvantages observed in CNTs, they are competing for the fore-front of innovation. [2,5] Graphene comprises a two-dimensional, single atomic, planar sheet of densely packaged sp^2 bonded carbon atoms arranged in a honeycomb lattice configuration, essentially fabricating a vast polyaromatic hydrocarbon.[1,5–8] Pending its experimental discovery in 2004 [6] graphene and other free-standing, two-dimensional materials were presumed not to exist. Graphene's unique electrochemical and physical properties have already enhanced specific technologies despite its relatively young age, with great promise for many future advancements, awarding it tremendous attention from various scientific communities. [9, 10]

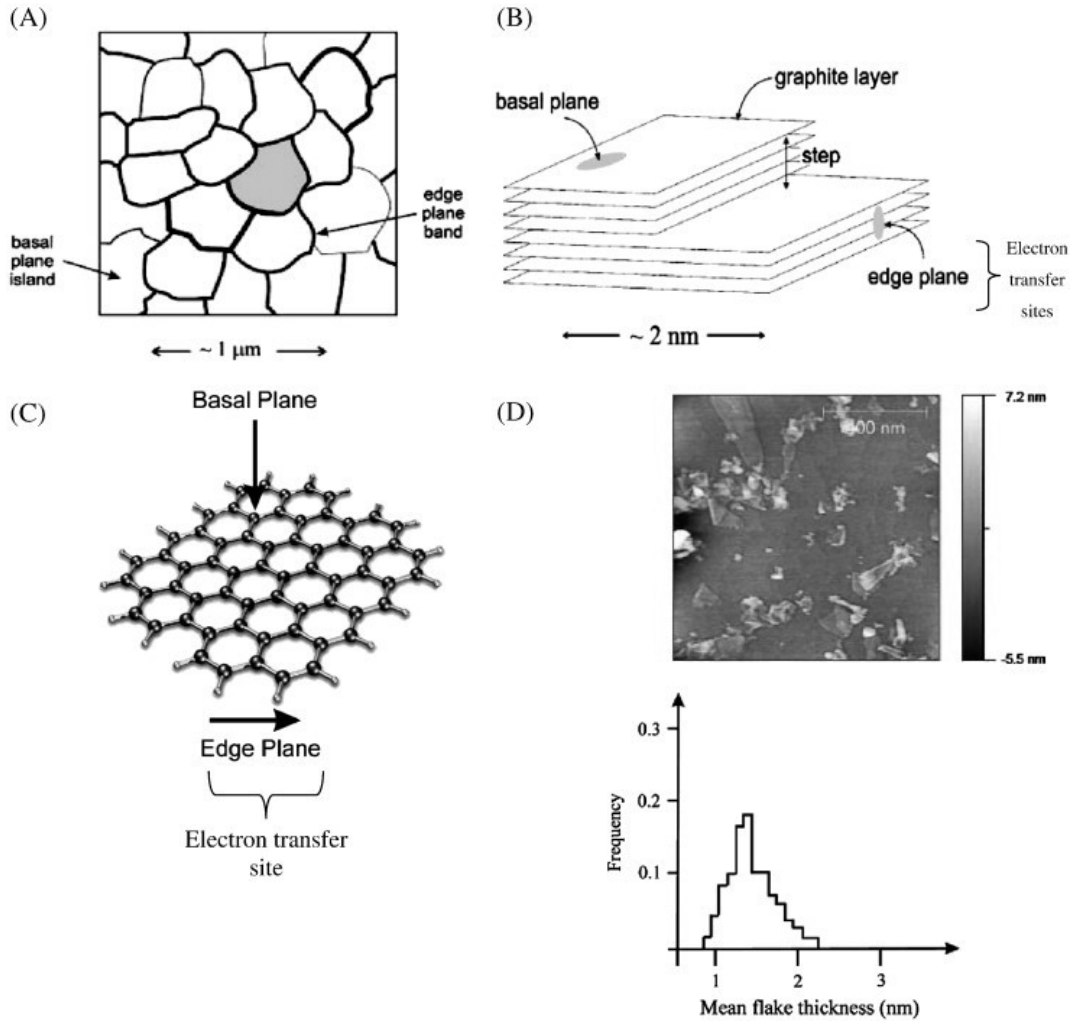

Figure 4.12 Schematic representation of a surface (A) of highly ordered pyrolytic graphite (HOPG) and a side view (B) of the edge-plane-like sites/defects and that of graphene (C) and graphene (D) immobilised onto SiO_2 substrate as imaged via AFM. A and B are reprinted from [4]. Flake thickness histogram for the graphene sample from the commercial supplier [12] via AFM analysis is also shown in D where the thickness of a single layer of graphene on a SiO_2 substrate, including absorbed surfactant and water, is estimated to be approximately 1.1 nm.

Recently it has been demonstrated that graphene structurally resembles the edge-plane of HOPG which is the origin of the reported 'electro-catalytic' effects of many graphene modified electrodes; [11] Figure 4.12C shows a schematical representation. Additionally the impact of surfactants, used to reduce the likelihood of graphene coalescing, on its

electrochemical response was also highlighted. [11] In this chapter, it is demonstrated that commercially available, well characterised graphene does not exhibit a detrimental thin-layer effect which is routinely observed for the case of carbon nanotube modified electrodes allowing mechanistic information for graphene to be deduced without the false inference of electro-catalysis to be made. A simple methodology is presented allowing the global % coverage of electron transfer sites of graphene (edge-plane sites) to be readily determined for the first time.

4.3.2.2 EXPERIMENTAL

All chemicals used were of analytical grade and were used as received without any further purification and were obtained from Sigma-Aldrich. All solutions were prepared with deionised water of resistivity not less than 18.2 MΩ cm. Voltammetric measurements were carried out using a μ-Autolab III potentiostat. All measurements unless otherwise stated, were conducted using a three electrode configuration comprising a glassy carbon (GC) working electrode (3 mm diameter) with a platinum wire and saturated calomel electrode (SCE) acting as counter and reference electrodes respectively. All solutions were vigorously degassed before electrochemical measurement.

Graphene was commercially obtained from NanoIntegris, (Illinois, USA) and is known as 'PureSheets™' (research grade) and comprise entirely of pristine graphene platelets that have not been oxidised, reduced or chemically modified in any way. Graphene is produced via density gradient ultracentrifugation and the methodology has been reported and characterised previously. [12, 13] The process involves the bile salt sodium cholate which promotes graphite exfoliation resulting in graphene-surfactant complexes having buoyant densities that vary with graphene thickness. This results in a 'sorting' of graphene and hence different fractions are observed meaning that graphite and multi-layer graphene are not inadvertently incorporated into the graphene samples. Graphene is in an aqueous solution

with an ionic surfactant (2% w/v) and consists of a mean flake area of 10,000 nm^2. Graphene consists of: 27% single layer, 48% double layer, 20% triple layer and 5% 4+ layer and due to the fabrication approach does not have any graphite impurities. Aliquots of graphene are carefully pipetted onto the electrode surface and allowed to dry at room temperature under nitrogen flow in order to eliminate oxidation of graphene by the presence of atmospheric oxygen, following which the electrode can either be further modified or is ready to use. XPS chemical analyses were performed with a VG-Microtech Multilab electron spectrometer. This reveals the presence of 74.66% atomic carbon, 16.43% atomic oxygen, 4.12% atomic nitrogen, 2.63% atomic sodium and 2.13% atomic sulphur. Interpretation of the XPS spectra for the case of the oxygenated species reveals the presence of hydroxyl, carbonyl, epoxy and ether functional groups. Identification of nitrogen via XPS likely indicated a pyridone type functionalization which is likely due to an acid treatment performed prior to the density gradient ultracentrifugation process. We however acknowledge that this information is not easily de-convoluted from the contribution of the sodium cholate surfactant which is present. Additionally the presence of sulphur, sodium and nitrogen suggests the presence of additional anionic and cationic surfactants added by the company following production of graphene (see earlier discussion); note however that the company is not willing to disclose this information.

4.3.2.3 RESULTS AND DISCUSSIONS

Firstly, modification of a glassy carbon (GC) electrode with 0.5 µg of graphene as described in the experimental section is considered. Figure 4.13 depicts the cyclic voltammetric responses observed using 1mM $[Ru(NH_3)_6]Cl_3$/ 1M KCl over the scan range of 0.005 to 0.2 Vs^{-1}. In comparison to carbon nanotube modified electrodes,[14] no thin-layer behaviour is observed since a plot of $\log_{10}$ of peak current ($\log_{10} I_p$) versus $\log_{10}$ of the applied voltammetric scan rate is linear (Figure 4.13B) with a gradient of ~0.50, as is expected for the

case of the semi-infinite diffusion model as governed by the Randles-Ševćik equation (equation 2.1). [15]

In comparison to the bare (unmodified) GC electrode (Figure 4.13A) it was found that a substantial increase in the voltammetric peak height is observed after the introduction of graphene to its surface. The effects of adding further amounts of graphene were explored and Figure (4.13C) shows the response of 2.5μg of graphene where again no thin-layer behaviour is observed. This amount of graphene, in our case, represents the maximum amount of graphene that can be immobilised onto the electrode surface which is completely covered with further additions of graphene not significantly increasing the magnitude of the voltammetric peak height. Recently, it has been elegantly shown that CNT modified electrodes produce a porous structure on modified electrodes with two diffusional contributions, [14] the first from semi-infinite diffusion of the electro-active species towards the planar electrode surface and the second from the electroactive species trapped within the carbon nanotube network. Due to these two contributions, deviation from equation (2.1) is readily observed and mechanistic information is not easily de-convoluted and requires knowledge of the exact film thickness, or best approximation. [14] However in our case, graphene, as demonstrated above does not show any such thin-layer effects and while the surface may be relatively rough, it is clearly not porous.

It has been shown that the observed electron transfer rate, k^0_{obs} on highly ordered pyrolytic graphite (HOPG) electrodes arises from two structural contributions, [3, 4] edge-plane and basal-plane (see Figure 4.12) which is a heterogeneous electrode surface with the overall electron transfer rate (k^0_{obs}) a function of these two contributions, , k^0_{edge} and k^0_{basal}:

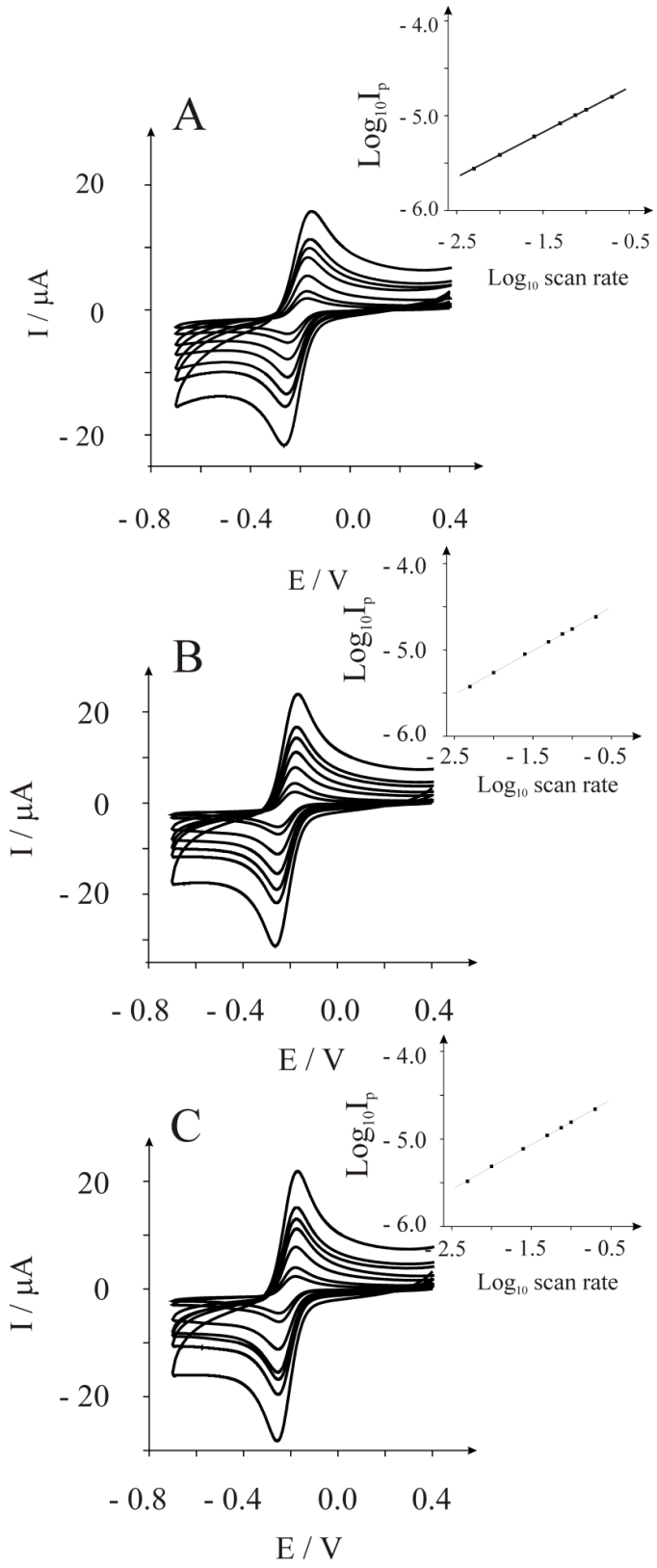

Figure 4.13 Cyclic voltammetry (A) of a GC electrode in 1mM $Ru(NH_3)_6Cl_3$ / 1M KCl and that of Graphene modified GC electrode, (B) 10µL (0.5µg), (C) 50 µL (2.5µg). Scan rates: 0.005 - 0.2 Vs^{-1} (vs. SCE).

$$k^0_{obs}\,(HOPG) = \; k^0_{edge}\left(\theta_{edge}\right) + \; k^0_{basal}\left(1 - \theta_{edge}\right) \tag{4.6}$$

It has been previously reported that the electron transfer rate of the edge-plane is much faster over that of the basal-plane. [3] It is acknowledged that recently Macpherson *et al.* [16] have claimed that the basal-plane is also highly electro-active but for the case of carbon nanotubes; this response has not been observed by anyone else and it is likely to be due to edge-plane defects occurring along the carbon nanotube wall as found by Banks *et al.* [17] Assuming that the edge-plane is much faster over that of basal-plane allows us to write:

$$k^0_{edge} \gg \; k^0_{basal} \tag{4.7}$$

which leads equation (4.6) to:

$$k^0_{obs}\,(HOPG) = \; k^0_{edge}\left(\theta_{edge}\right) \tag{4.8}$$

where the global coverage (Θ_{edge}) of edge-plane defects is approximate to the coverage of the edge-plane (θ_{edge}): [3]

$$\theta_{edge}(HOPG) \approx \Theta_{edge}\,(HOPG)$$

Figure (4.12D) shows a surface modified with graphene which generally shows that the immobilised graphene structurally resembles that of HOPG (see Fig. 4.12A) and agrees with literature reports [18] of graphene on a surface indicating that our approach is fundamentally valid. Thus, this methodology allows the global edge-plane coverage, Θ_{edge} (representing electron transfer sites) to be readily estimated. [3] In the case of graphene, as shown in Figure 4.12B and reported previously, [11] the edge-plane of graphene is the origin of the observed electrochemical response allowing us to write for the case of graphene:

$$k^0_{obs}\,(\text{graphene}) = \; k^0_{edge}\left(\theta_{edge}\right) + \; k^0_{basal}\left(1 - \theta_{edge}\right) \tag{4.9}$$

using the argument earlier and previous reports [11] allows us to write:

$$k^0_{obs}\,(\text{graphene}) \;=\; k^0_{edge}\left(\theta_{edge}\right) \tag{4.10}$$

Where the global coverage is:

$$\theta_{edge}\,(\text{graphene}) \;=\; \Theta_{edge}\,(\text{graphene}) \tag{4.11}$$

Thus, the electrochemical response, which is due to electron transfer residing at the edge of graphene, is caused by the edge-plane sites of graphene immobilised onto an electrode surface, the global coverage of electron transfer sites can be readily determined from equation (4.10) as long as k^0_{edge} has been rigorously determined. Assuming graphene is structurally similar to that of HOPG islands, when immobilised upon an electrode surface, and where the electron transfer is due to the edge-plane-like sites/defects [11], for the case of $[Ru(NH_3)_6]Cl_3$, k^0_{edge} = 0.4 cm s^{-1}. [3]

Using the approach above with equation (4.10) the global coverage of edge-plane defects of the graphene was determined with k^0_{obs} determined from the Nicholson method. [19] This method is routinely used to deduce the standard electron-transfer rate from equation (4.1). If graphene were to exhibit thin-layer behaviour, as for the case of carbon nanotubes, then this approach is not fundamentally valid and requires recourse to numerical simulations. [14]

The deduced global coverage of edge-plane sites/defects (% edge (Θ_{edge})) for graphene was found to be 2.55. To 'benchmark' this approach the global coverage of edge-plane sites/defects (% edge (Θ_{edge}) for multi-walled carbon nanotubes (MWCNTS, Nanolab, USA) was quantified. In this case, it is important to ensure that the electrode surface is completely covered to neglect the contribution from the underlying electrode yet avoiding

thin-layer behaviour. Using the approach set out above for graphene, it was found that global coverage of edge-plane sites/defects (% edge (Θ_{edge})) for the MWCNTs equates to ~3.01% which compares well with 2.54% as independently deduced via capacitance measurements.[21] It is interesting to compare the global coverage of edge-plane sites/defects (% edge (Θ_{edge})) of graphene with that of the MWCNTs and find that this is a similar order of magnitude in comparison to MWCNTs which is as expected given that MWCNTs may be simply considered as rolled up graphene. Additionally, graphite powder was found to have a % edge (Θ_{edge}) of 3.96 using the approach above. This value, when compared to graphene and MWCNTs indicates that the MWCNTs are no more reactive than graphite as reported in the literature; [22] thus it is clear than when graphene is claimed to enhance electrochemical processes, control experiments with graphite need to be performed. Finally, this method can be used when varying amounts of graphene are utilised so long as the conditions of thin-layer behaviour is avoided and that the electrode surface is completely covered. In this latter case, the % edge-plane content of the underlying GC electrode would need to be considered which will be an accumulative to that of the % edge-plane content. It is also possible that the coverage of edge-plane sites of graphene could be determined via capacitance measurements since edge and basal plane electrodes would exhibit very different capacitances. [23]

4.3.2.4 CONCLUSIONS

This work has shown for the first time a simple methodology utilising cyclic voltammetry which allows the density of defects, *viz* edge-plane sites (active sites) of graphene to be readily determined and also provides researchers with a methodology to quantify the density of defects for comparative purposes. Interestingly we find that graphene-modified electrodes do not suffer from thin-layer effects which are commonly observed in carbon nanotube modified electrodes which prevent mechanistic information from being easily de-convoluted and inferring claims of electro-catalysis falsely from the latter. In a comparison of graphene

orientated on a surface with that of multi-walled carbon nanotubes, it was found that the former has similar % edge-plane content with that of the latter, which has implications when choosing between different carbon structures for developing sensors, especially in the case of carbon nanotubes vs. graphene. This work elegantly contributes to the knowledge that the edge of graphene (edge-plane) is the origin of electron transfer, rather than the face (basal-plane). [11] The recent work by Pumera [24] has shown that the electrochemical response is independent of the number of layers, indicating that our approach is useful for single layer graphene through to multi-layer graphene. Recent work, undertaken during this thesis (see Chapter 5), has produced compelling evidence to suggest that the mechanistic process can in-fact move from a thin-layer regime on longer timescales, to semi-infinite diffusion on shorter timescales, thus presenting a 'Catch 22' when it comes to interpretation of peak potentials for electron transfer rates since, for a quasi-reversible system such as ours, one would ideally work at slow scan rates, however faster scan rates are required to avoid falling into the thin-layer regime.

4.3.2.5 REFERENCES

1. R. L. McCreery, *Chem. Rev.,* **2008**, 108, 2646.
2. D. A. C. Brownson, C. E. Banks, *Analyst*, 2010, 135, 2768.
3. T. J. Davies, M. E. Hyde, R. G. Compton, *Angewandte Chemie, Int. Ed.* **2005**, 44, 5121.
4. T. J. Davies, R. R. Moore, C. E. Banks, R. G. Compton, *J. Electroanal. Chem.,* **2004**, 574, 123.
5. M. Pumera, *Chem. Rec*, **2009**, 9, 211.
6. D. Chen, L. Tang and J. Li, *Chem. Soc. Rev.*, **2010**, 39, 3157.
7. W. Yang, K. R. Ratinac, S. P. Ringer, P. Thordarson, J. J. Gooding and F. Braet, *Angewandte Chemie*, **2010**, 49, 2114.
8. A.K. Geim, *Nat. Mater.*, **2007**, 6, 183.
9. Y-R Kim, S. Bong, Y-J Kang, Y. Yang, R. K. Mahajan, J. S. Kim and H. Kim, *Biosens. Bioelectron.*, **2010**, 25, 2366.

10. C. Liu, S. Alwarappan, Z. Chen, X. Kong and C-Z. Li, *Biosens. Bioelectron* **2010**, 25, 1829.
11. D. K. Kampouris, C. E. Banks, *Chem. Commun.,* **2010**, 46, 8986.
12. http://www.nanointergris.com.
13. A. A. Green, M. C. Hersam, *Nano Lett*. **2009**, 9, 4031.
14. I. Streeter, G. G. Wildgoose, L. Shao, R. G. Compton, *Sens. Actuators B*. **2008**, 133, 462.
15. R. G. Compton, C. E. Banks, *Understanding Voltammetry*, World Scientific Ltd., 1st edn. **2007**.
16. I. Dumitrescu, P. V. Dudin, J. P. Edgeworth, J. V. Macpherson, P. R. Unwin, *J. Phys. Chem. C,* **2010**, 114, 2633.
17. C. E. Banks, X. Ji, A. Crossley, R. G. Compton, *Electroanalysis.* **2006**, 21, 2317.
18. J-F. Wu, M-Q. Xu, G-C Zhao, *Electrochem. Commun.,* **2010**, 12, 175.
19. R. S. Nicholson, *Anal. Chem*., **1965**, 37 (11), 1351.
20. C. E. Banks, R. G. Compton, A. C. Fisher, I. E Henley, *PCCP.,* **2004**, 6, 3147.
21. M. Pumera, T. Sasaki, H. Iwai, *Chem. Asia J.,* **2008**, 3, 2046.
22. R. R. Moore, C.E. Banks, R.G. Compton, *Anal. Chem*., **2004**, 76, 2677.
23. M. S. Goh, M. Pumera, *Electrochem. Commun.*, **2010**, 12, 1375.
24. M. S. Goh, M. Pumera, *Chem. Asian. J.* **2010**, 5, 2355.

5.1 SCREEN PRINTING

Screen printing is becoming extensively used to fabricate disposable and economical electrochemical electrodes, and has helped to establish a 'lab-to-market' route for a plethora of applications. This section contains an overview of recent developments in screen-printed electrochemical electrodes, initially discussing the fundamental understandings, through to underlining new developments in bulk metal and modified electrodes, as well as advantageous, novel electrode designs, highlighting the extensive and diverse range of applications that electrodes based on this assembly have achieved. Below (Figure 5.1) is an illustration of a typical screen-printed electrode (including SEM of the electrode's surface). The screen-printed electrode displays a circular (typically 3mm in diameter) carbon working electrode in the centre, encompassed by a carbon counter electrode and a small Ag/AgCl reference electrode. Each track has a carbon current collector and connector exposed at the top of the platform (Figure 5.1). The working areas are defined by a dielectric cover printed finally over the top. Fabrication is performed in layers using stencils to produce the final product.

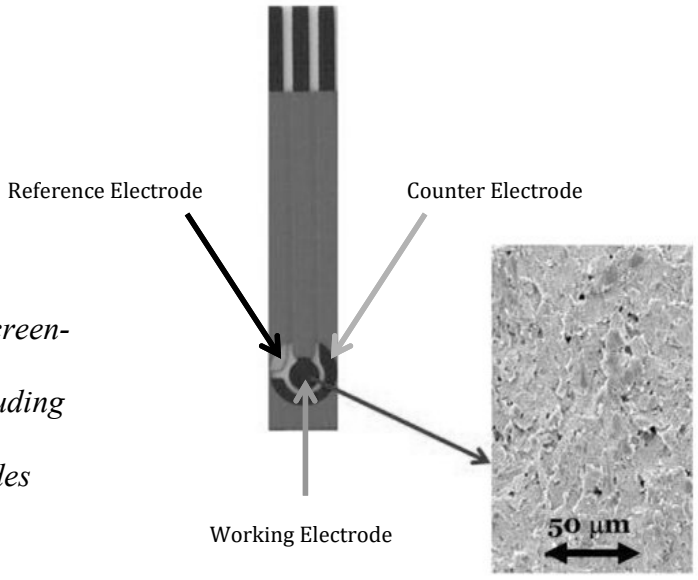

Figure 5.1 A typical screen-printed electrode including SEM of the electrodes

5.1.1 INTRODUCTION

Screen-printed electrodes are not only cost effective but also realise the much sought after ability to yield a highly reproducible and sensitive method of detection towards target analytes, whilst upholding the low cost through increased scales of production. The adaptability and customisation of screen-printed electrodes augments further benefits (especially in areas of research); the facility to alter the electrodes with ease, through differing inks available commercially for the working, counter, and reference electrodes, enables highly specific and uniquely calibrated electrodes to be produced for specific target analytes.[1] Screen printing entails printing a thixotropic (thick (viscous) under normal conditions, but flow (becoming thin or less viscous) over time when shaken, agitated, or otherwise stressed, taking a fixed time to return to a more viscous state) fluid through a mesh screen, defining the shape and size of the desired electrode. The thixotropic fluid contains a variety of substances including graphite, carbon black, solvents and polymeric binder. Figure 5.2 depicts a schematic representation of the process of screen printing, allowing multiple layers and complex designs can be readily applied. The inks used tender a high viscosity (3–10 Pa s at a sheer rate of 230 s^{-1}), however when forced through the screen mesh by the squeegee blade, the ink undergoes sheer thinning allowing it to penetrate through the screen mesh which defines the shape/design of the electrode. Upon contact with the substrate, classically a ceramic or plastic material, the ink returns to its viscous state forming the definitive edge of the (final) intended electrode shape/design. Such electrode designs typically have a thicknesses in the range of 20 to 100 mm and, as such, are thicker than those obtained by other printing methodologies and consequently termed ‘‘thick film technology’’. The thickness of the layer can be readily controlled via the thickness of the stencil design and mesh. As mentioned previously such designs can be printed onto ceramic substrates [7] or plastic substrates depending on the intended application. However, in the latter case the cost

is typically lower and the carbon print is better adhered to the substrate than in the former case.

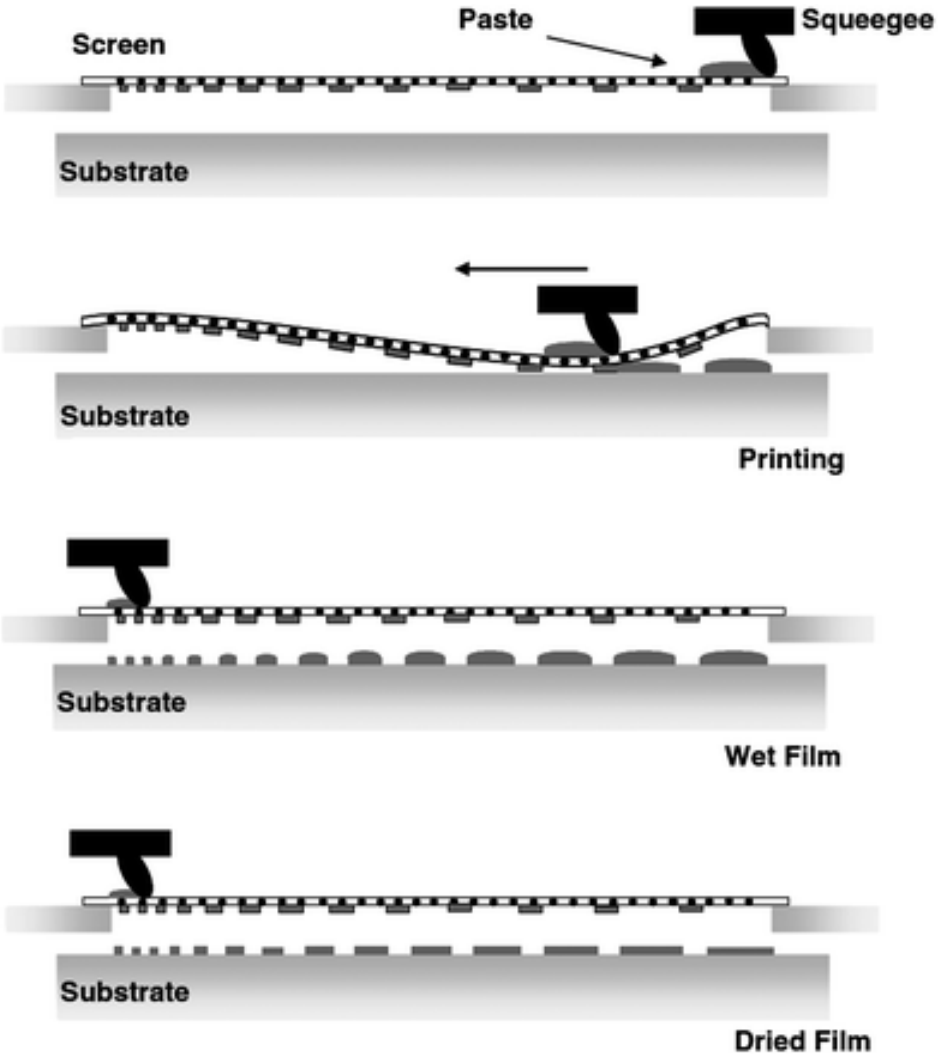

Figure 5.2 Schematic representation of the process of screen-printed manufacturing of electrodes (cross sectional side view) outlining the basic processes involved.
Figure reproduced from reference 3.

Normally these electrodes are operated in aqueous solutions but as there are many applications in non-aqueous systems, it is beneficial for screen-printed electrodes to operate in other types of media. Work by Krőger and Turner [1] has reported on solvent-resistant screen-printed electrodes for use in biosensor applications involving water-miscible organic solvents (methanol, isopropanol, and ethanol) using a rhodium catalyst towards the amperometric detection of hydrogen peroxide.

There are substantial research efforts into developing screen-printed biosensors and consequently there is a substantial wealth of literature. It is worth highlighting that there are many other exciting expanses of science, especially in electroanalysis, where screen printing is becoming increasingly established.

5.1.2 FUNDAMENTAL UNDERSTANDING

As discussed previously, the inks comprise of graphite particles, polymeric binder and other additives which are used for printing, dispersion and adhesion tasks. The exact ink formulation is regarded by the manufacturer as proprietary information and it has been shown that alterations in ink composition e.g., size, type or loading of graphite particles and in the printing and curing conditions can strongly affect the electron-transfer reactivity and the overall analytical performance of the resulting carbon electrode. Screen-printed electrochemical electrodes offer superb platforms for modification with a variety of nanoparticles and structurally related materials requiring no pre-treatments (such as electrode polishing or electrochemical pre-treatment via electro-deposition) common associated with other electrode materials.

Although these electrodes have found increasing implementation in scientific experimentation, the fundamental understanding of the electrochemical reactivity at these electrodes has been rarely explored. Sljukić *et al.* [2] have shown that the mass transport at a

macro-screen-printed electrode can be beneficially improved through the application of power ultrasound. The use of ultrasound not only increases the mass transport of the target analyte through convection, but furthermore, can remove the surface active species which would otherwise impede the electroanalytical measurement through passivation of the electrode's surface. Via a redox probe, the effect of surface changes upon the application of ultrasound was studied, displaying evidence of an improvement in the heterogeneous rate constant. The observed increase in the magnitude of the voltammetric peaks likely reflects a 'roughening' of the screen-printed electrode surface from either cavitation, high mass transport, or an amalgamation of these processes, likely removing inks covering carbon particles and thus increases the overall effective surface area of the electrode, suggesting that the levels of graphite within the ink is a key parameter and has a direct effect on the electrode's performance.

Choudhry *et al.* [3] have studied the role of the polymeric binder used in screen printing electrode fabrication. This work revealed a detrimental result on the electrode's morphology as the amount of the polymeric binder is dramatically increased, as illustrated in Figure 5.3; polymeric domains are readily formed, easily identifiable in Figure 5.3D and 5.3E. The resultant effect on the voltammetric response (owed to the increasing the mass of binder) was evaluated using an inner-sphere electron transfer redox probe. Figure 5.4 depicts the analysis of the voltammetric peak-to-peak separations, indicating that the heterogeneous electron transfer rate (k^0_{edge}) continuously decreases as the content of polymer binder is increased, represented as $\%M_B/M_I$, where M_B and M_I are the mass of the binder and the ink, respectively. The global coverage of edge-plane sites of the electrode surface was found to decrease from 5.5% to 0.3% for the range of 0–80% (M_B/M_I), respectively, indicating that the electron transfer characteristics can be tailored between that of an edge-plane-like electrode to that of a basal-plane-like electrode in nature.

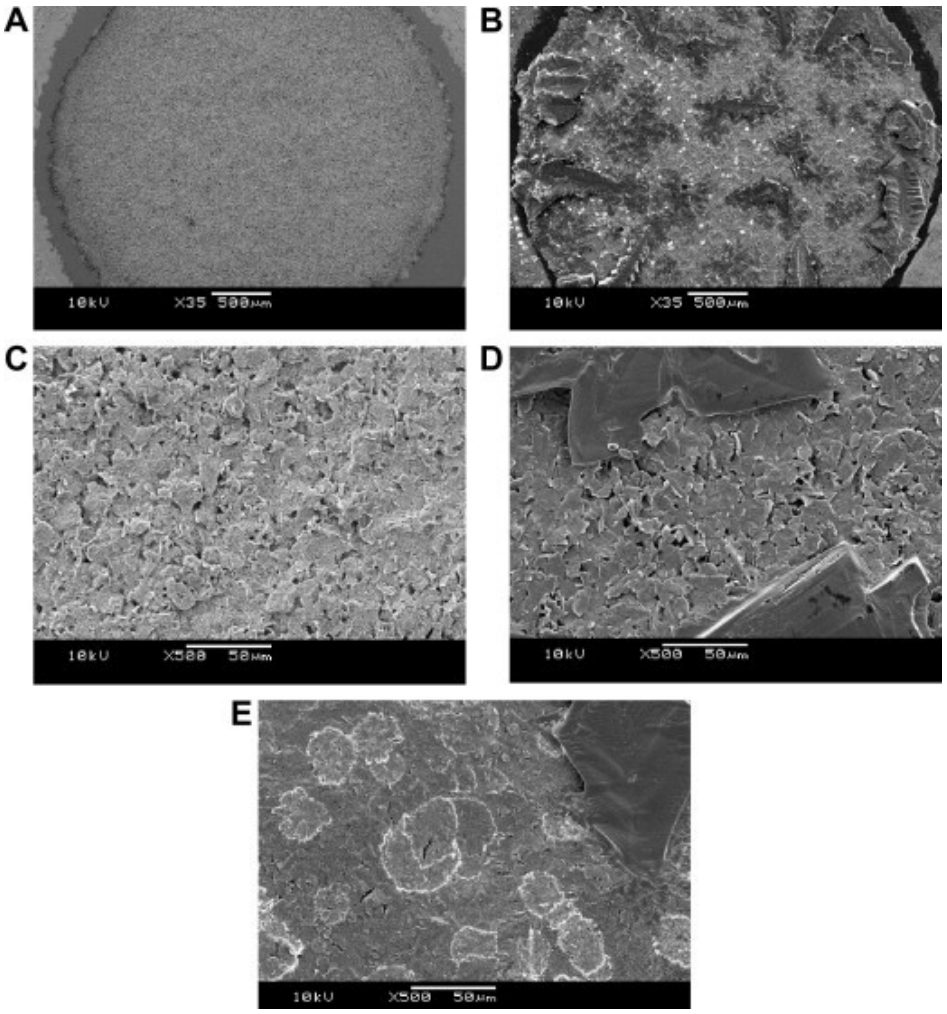

Figure 5.3 SEM images of the screen-printed electrochemical platforms. Figures A and C display the bare unmodified electrode surface alongside that of a 40% (M_B/M_I) modified (B and D) and 80% (M_B/M_I) (E) electrochemical platforms. Figure reproduced from reference 1.

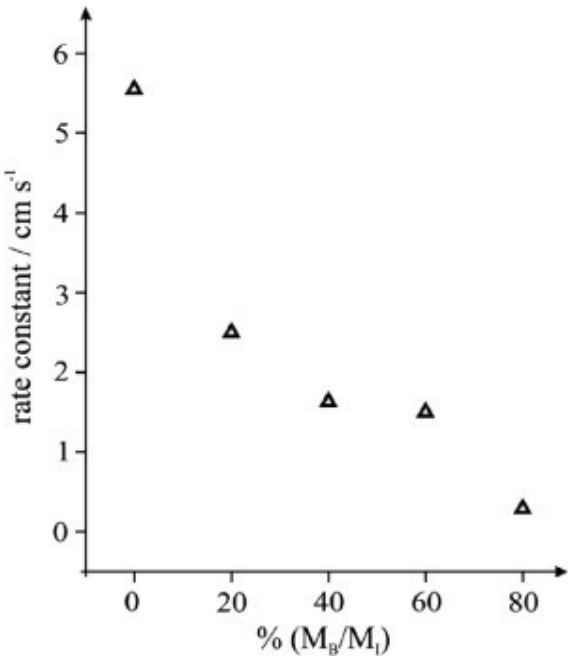

Figure 5.4 Plot of the heterogeneous electron transfer rate constant (k^0_{edge}) as a function of %M_B/M_I under a potassium ferrocyanide redox system. Figure reproduced from reference 7.

This has a profound influence on the fundamental electrochemistry, for example, when studying the electron-transfer dynamics of metal nanoparticles, there is a vital need to have as little or preferably no contributions from the underlying electrode in order to study the electrochemical response of the metal nanoparticles. This is typically achieved with a basal-plane electrode fabricated from the highly ordered pyrolytic graphite (which consequently displays slow electron transfer kinetics) but is highly expensive and requires renewal (cleaning) of the surface between investigations; the use of a basal-plane-like screen-printed electrode which are disposable and cost effective clearly offer substantial benefits over the former. The cyclic voltammetric response (I – E), observed at screen-printed electrochemical platforms, arises from several contributors which can be described by the following:

$$I - E_{SPE} = \beta[I - E_{basal}] + \gamma[I - E_{binder}] + \varepsilon[I - E_{edge}] \quad (5.1)$$

where β, γ and ε are complicated functions that take into account the relative areas and sizes of the materials comprising the electrode as well as the contribution from non-linear diffusion. It has been shown that in the case of non-linear diffusion over an electrode's surface, the resulting individual contributions of edge- and basal-plane graphites do not scale with relative areas, and that for electroactive species with diffusion coefficients of ~1×10^{-6} cm^2 s^{-1} or greater (as determined with potassium ferrocyanide / 1 M KCl), the basal-plane has little or no contribution. It has also been found that the polymeric formulation used within the ink is electrochemically inert (see Figure 5.3 and 5.4) and thus contributes nothing towards the voltammetric response, permitting for a suitable approach for adjusting the electrochemical reactivity of screen-printed electrochemical platforms. In addition, the electrochemical reactivity of the screen-printed electrode may be altered by tweaking the content ratio of carbon to graphite. Consequently equation (5.1) reduces to equation (5.2) describing the cyclic voltammetry ($I - E_{SPE}$) at screen-printed electrodes:

$$I - E_{SPE} = \varepsilon[I - E_{edge}] \tag{5.2}$$

This equation indicates that screen-printed electrodes are dependent primarily on the global coverage of edge-plane-like sites/defects which are the likely origin of electron transfer.

The facility to adapt and tailor the electron-transfer properties of the electrode surfaces has clear analytical implications. Figure (5.5) compares the voltammetric performance of a standard unmodified screen-printed electrode with that of a polymeric modified screen-printed electrode where a distinct variance is observed; the latter produces a significantly slower electron-transfer rate to that of the former; copper plating via the two screen-printed electrodes results in a significant difference in the morphology of the copper metal. Choudhry *et al*. demonstrated that this can be beneficial for the electrolytic modification of various electro-catalytic metals where the bespoke electrode surface acts as a

micron-sized template. The modification requires a reduced amount of metal during the fabrication of these metal ensembles and thus has a strong implication on costs, especially where precious materials are concerned. The term ensemble is used to indicate that the spacing between each metal deposit, *viz* the metal domain, is not uniform, as in the case of arrays. A dramatic change in the mass transport prevails when an ensemble is used over that of an electrolytically-modified macroelectrode, facilitating low detection limits and enhancements in the analytical performance even though only a small proportion of the overall electrode surface is covered.

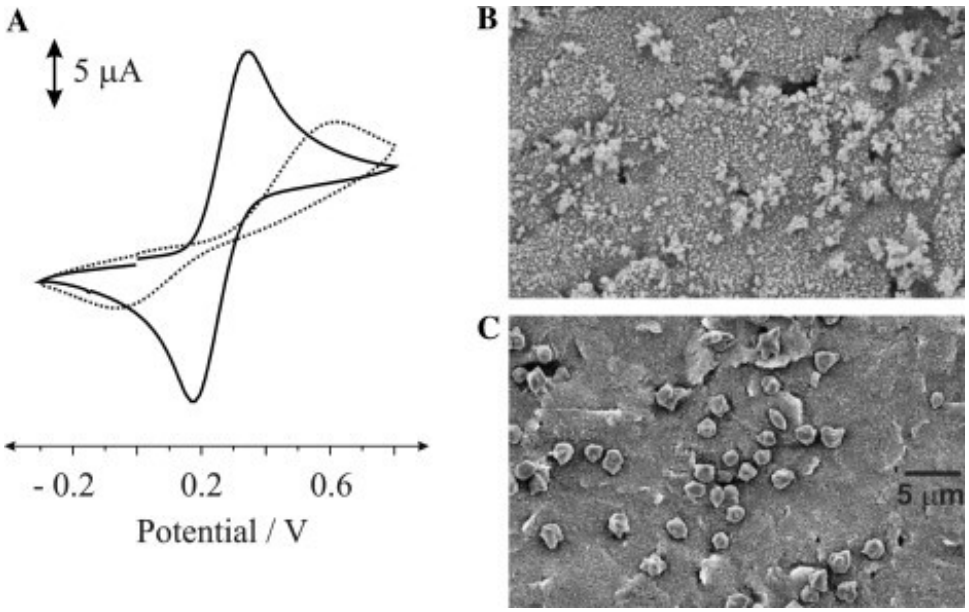

Figure 5.5 Cyclic voltammetric profiles (A) obtained in 1 mM potassium ferrocyanide in 1 M KCl using the standard electrochemical platform (solid line) with that of a bespoke electrochemical platform (dashed line). Scans recorded at 100 mV s^{-1} vs. SCE. SEM images of the copper plated standard (B) and bespoke (C) screen-printed electrochemical platforms. Figure reproduced from reference 1.

It has been shown that the bespoke screen-printed electrodes could be electrolytically modified with palladium (electro-catalytic towards the electrochemical oxidation of hydrazine) where the underlying (unmodified) electrode exhibits slow (basal-plane-like)

electron transfer. The screen-printed electrode substrates act as a template for the deposition of the target metal, where an average palladium particle size of 2.7 μm was found. This equates to a global coverage of only 0.27 (where 1.0 indicates a fully covered electrode surface). The electrochemical performance of the electrode towards hydrazine was investigated where a limit of detection of ~9 μM was established, this compares well with electrodes modified with nanoparticle, albeit only with 27% surface coverage. Evidently the mass transfer tendered via employing a microdomain electrode, over that of a macroelectrode, is highly beneficial and acts akin to a nanoparticle-modified electrode.

Metal deposition through nucleation requires understanding of the mechanism undertaken during the process (deposition and stripping) when quantifying metals at screen-printed electrodes. Honeychurch *et al*. [4] have illustrated that the redox behaviour of lead is not as straightforward as typically thought in this case. In the stripping phase, two or three peaks were observed and attributed to the heterogeneity of the screen-printed electrode surface, where deposition ensues in a competitive nature; the target metal deposits first onto desirable active sites as a monolayer, after these sites are depleted, the deposition process becomes competitive and proceeds between metal deposition on the un-favoured, unoccupied bare electrode sites or on the already deposited metal.

Recently Banks *et al*. [5] have revealed that when an electrochemical modification designed for generating nickel nanoparticles on boron-doped diamond was recreated employing a standard screen-printed electrode, the observed resulting nickel morphology was in fact microrod-like. The assembly of such structures typically requires complicated fabrication strategies (non-electrochemical), this was the first instance of producing such structures electrochemically; the change in the deposition morphology is attributed to the differing nucleation dynamics, permitting the derivatisation of new and exciting structures.

Further fundamental work has been undertaken, based on understanding and exploring oxygen functionalities residing on the electrode surface of screen-printed electrodes. Zen *et al*. [6] have reported a 'pre-anodized' screen-printed electrode for the detection of a range of target analytes. The most beneficial results were exhibited towards the simultaneous sensing of ascorbic acid, dopamine and uric acid where using a standard screen-printed electrode, resulted in the observation of broad, overlapping voltammetric peaks whereas in the case of the pre-anodized screen-printed electrodes, three distinguishable signals are clearly perceived which, using Raman and XPS, was credited to an increment of the carbon–oxygen species residing on the graphite surface and/or surface reorientation through the generation of edge-plane sites (likely caused through the removal of ink from edge-plane-like sites/defects on the graphite).

5.1.3 METAL-MODIFIED SCREEN-PRINTED ELECTRODES

Surface modification of the electrode with electro-catalytic metals is often desirable, typically realised through the use of metallic screen-printed inks producing 'film' modified screen-printed electrodes, or alternatively, incorporation of metallic electro-catalysts into a carbon paste electrode is an aspect which has been investigated extensively. Ordinarily, in bulk modified screen-printed electrodes, micron sized particles of the electro-catalytic metal are incorporated into the electrode. It is found that these tailored screen-printed electrodes display analytically similar characteristics to that of a nanoparticle modified carbon electrode.

The reason can be understood by considering the diffusion zones observed at each micro or nanoparticle (each particle can be considered to be as an individual working electrode) accessible at the surface. Figure 5.6 depicts a schematic representation of the diffusional zones at the microelectrode and nanoparticle ensembles.

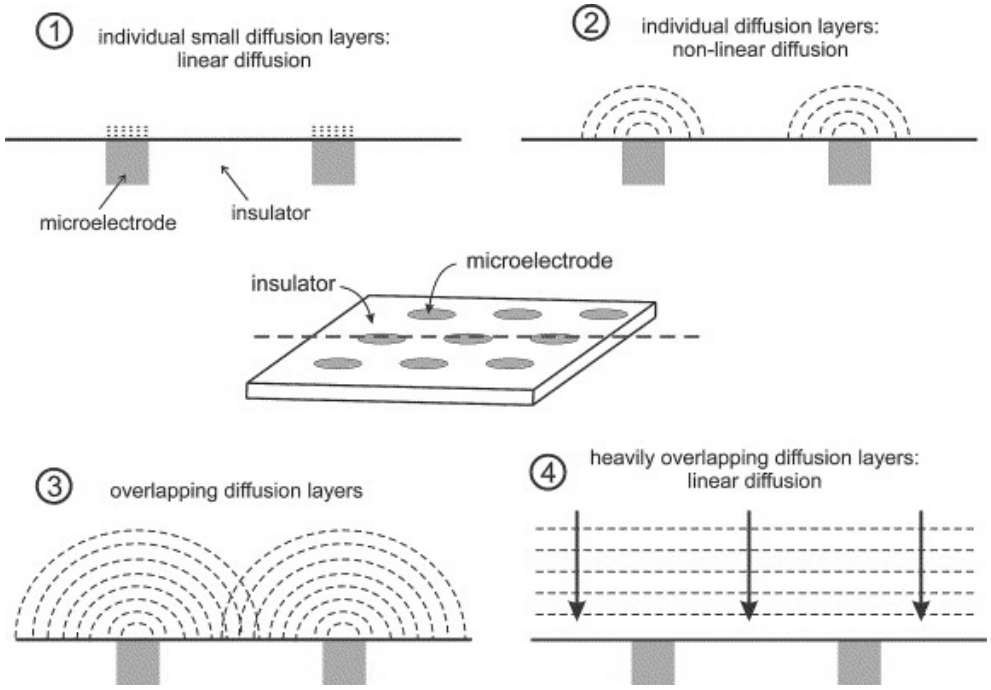

Figure 5.6 Schematic representations of possible diffusion zones at micro and nano particle ensembles. Figure reproduced from reference 8.

It is clear that the similar parameters, such as the distance between the particles, apply here as in the case of microelectrode arrays. Diffusion zones build up at the individual electrodes (micro or nanoparticles), akin to irregular spacing, diffusional overlap ensues to a sufficient degree (modest scan rates), resulting in fundamentally similar voltammetric profiles observed at the microelectrode arrays. The extent of the overlap is important; if the overlap is not substantial the ensemble displays a faster mass transport than that of an electrode tendering a heavily overlapping diffusional regime, thus improving the electro-analytical performance. The voltammetric responses observed are indistinguishable from each other as their diffusional profiles are alike, indicating that a nanoparticle modified electrode does not always confer enhancements in electrochemical analysis. Accordingly, it is clear that traversing from a micro- to nano-particle size ensemble is not always favourable since adjacent nanoparticles will produce heavily overlapping diffusion zones; acting akin to a

micro-particle of the same geometric area. The advantageous approach of this methodology (consequently utilised in this thesis), as described above, is that any metallic element or oxide can be readily integrated, permitting a true platform technology.

5.1.4 REFERENCES

1. S. Kroger, A. P. F. Turner, *Anal. Chim. Acta*, **1997**, 347, 9.
2. B. Sljukic, N. A. Malakhova, K. Z. Brainina, C. E. Banks, R. G. Compton, *Electroanalysis*, **2006**, 18, 928.
3. N. A. Choudhry, D. K. Kampouris, R. O. Kadara, C. E. Banks, *Electrochem. Commun*., **2009**, 12, 6.
4. K. C. Honeychurch, J. P. Hart, D. C. Cowell, *Electroanalysis*, **2000**, 12, 171.
5. N. A. Choudhry, C. E. Banks, *Anal. Methods*, **2011**, 3, 74–77.
6. M. H. Chiu, H. H. Yang, C. H. Liu and J. M. Zen, *J. Chromatogr.,B: Anal. Technol. Biomed. Life Sci*., **2009**, 8, 991.
7. J. P. Metters, R. O. Kadara, C. E. Banks, *Analyst*, **2011**, 136, 1067.
8. T.J. Davies,S. Ward-Jones, C. E. Banks, J. D. Compc, R. Mas, F. X. Munoz, R. G. Compton, *J. Electroanal. Chem.*, **2005**, 585, 51.
9. L. Gonzalez-Macia, A. Morrin, M. R. Smyth, A. J. Killard, *Analyst*, **2010**,135, 845.

5.2 DETERMINATION OF OXYGENATED SPECIES AT SCREEN-PRINTED ELECTRODES

This section describes [1] work undertaken during this thesis to confirm the presence of oxygenated species at the surface of screen-printed electrodes and to try to ascertain the specific oxygenated species present at the surface of carbon/graphite electrodes. A brief abstract is given here:

It is demonstrated that graphite screen-printed macroelectrodes allow the low ppb sensing of chromium(VI) in aqueous solutions over the range 100 to 1000 mg L^{-1} with a limit of detection of 19 mg L^{-1}. The underlying electrochemical mechanism is explored indicating an indirect process involving surface oxygenated species. The drawbacks of using hydrochloric acid as a model solution to evaluate the electrochemical detection of chromium(VI) are also pointed out. The analytical protocol is shown to be applicable for the sensing of chromium(VI) in canal water samples at levels set by the World Health Organisation, simplified over existing analytical methodologies, and given its analytical performance and economical nature, holds promise for the de-centralised screening of chromium(VI).

*Dr Kampouris and Dr Kadara from the Banks research group were consultants during this project.

1. P. M. Hallam, D. K. Kampouris, R. O. Kadara, C. E. Banks, *Graphite screen-printed electrodes for the electrochemical sensing of chromium (VI)*, *Analyst*, **2010**, 135 (8), 1947.

5.2.1 GRAPHITE SCREEN-PRINTED ELECTRODES FOR THE ELECTROCHEMICAL SENSING OF CHROMIUM(VI)

5.2.1.1 INTRODUCTION

The ability to detect trace amounts of toxic chromium species has always been of vast interest while remaining a challenge in its own right due to the numerous oxidation states in which the element can reside.[1] With regard to the environment and health, there are two valence states that have considerable impact, Cr(III) and Cr(VI).[1] Reported to be the second major inorganic contaminant in hazardous waste sites[2] and owing to its high chemical oxidation potential, a provisional World Health Organisation guideline value of 50 mg L^{-1} (50 ppb) has been introduced for hexavalent Cr in groundwater.[3] The chromate anions pass readily through cell membranes and are easily reduced inside the cell to Cr(III) which binds more effectively to DNA, causing detrimental impairment to cellular components.[4] A number of sensitive techniques have been employed for the determination of Cr, such as atomic adsorption spectrophotometry,[5, 6] plasma mass spectrometry,[7] spectrofluorimetry,[8] spectrophotometry,[9] and chemiluminescence,[10, 11] but each of these processes is time consuming and necessitates expensive equipment. Various advantages are demonstrated when electrochemical methodologies are utilised for the determination of Cr including speed of analysis, good selectivity and sensitivity, which have resulted in a variety of highly responsive systems, utilising platinum[12] and gold[12–14] to be fashioned. Primarily mercury electrodes were used for the electrochemical detection of Cr(VI),[15–19] and although they are extremely sensitive, their application in analytical practice is limited due to its potential toxicity. The electrochemical characteristics of Cr(VI) are well documented for various electrode substrates such as gold, glassy carbon, platinum and boron-doped diamond.[12,20,23,29] Compton *et al*. have extensively explored the electrochemical reduction of Cr(VI) in aqueous solutions at a range of macroelectrodes.[20] It was demonstrated that gold macroelectrodes exhibited the greatest electrochemical reversibility over glassy carbon and

boron-doped diamond macroelectrodes.[20] Recently Hood *et al*. have explored the electro-analytical sensing of Cr(VI) at gold ultra-microelectrodes arrays where it was demonstrated that the spacing between neighbouring ultramicroelectrodes is critical in allowing analytical useful measurements.[21] Current state-of-the-art for Cr(VI) sensing has been reported by Jena and Raj who claim sub-ppb level detection employing amperometry at gold nanoparticle sol gels.[22] The development of screen-printed electrodes has led to the assembly of intelligent sensors which can be integrated into portable systems, a significant requirement of analytical methods intended for direct analysis of a sample in its ‘‘natural environmental conditions’’ without alteration.[23] Screen-printed electrodes are mass produced and have scales of economy and may be used as a one shot sensor which precludes problems that may be encountered with memory effects and alleviates the need for electrode pre-treatment.[24, 25] Herein the electrochemical reduction of Cr(VI) is revisited, but moreover, it has been detected for the first time, using a non-modified, non-metallic, graphite screen-printed electrode for the electroanalytical sensing of low ppb levels of Cr(VI) in aqueous solutions at levels set by the World Health Organisation (WHO). The methodology is demonstrated to be possible for the electro-analytical sensing of Cr(VI) in water samples and holds promise for high throughput screening.

5.2.1.2 EXPERIMENTAL

All chemicals used were of analytical grade and were used as received without any further purification and were obtained from Sigma-Aldrich. All solutions were prepared with deionised water of resistivity not less than 18.2 MΩ cm. Voltammetric measurements were carried out using a m-Autolab III (ECO-Chemie, The Netherlands) potentiostat. All measurements were conducted using a screen-printed three electrode configuration with a geometric working electrode area of 3 mm diameter. Connectors for the efficient connection of the screen-printed electrochemical sensors were purchased from Kanichi Research

Services Ltd (UK).[26] Screen-printed carbon electrodes were fabricated in-house with appropriate stencil designs as described in section 5.1. using a microDEK 1760RS screen-printing machine (DEK, Weymouth, UK). A carbon–graphite ink formulation was first screen-printed onto a polyester flexible film (Autostat, 250 mm thickness) defining the carbon contacts, counter and working electrodes. This layer was cured in a fan oven at 60 degrees for 30 minutes. Next a silver/silver chloride reference electrode was included by screen printing Ag/AgCl paste (Gwent Electronic Materials Ltd, UK) onto the plastic substrate, which after curing at 60 degrees for 30 minutes is ready to use. In the work presented here, a Saturated Calomel Electrode (SCE) was selected as the reference electrode to allow a direct comparison with literature reports. Last a dielectric paste ink (Gwent Electronic Materials Ltd, UK) was printed to cover the connections and define the 3 mm diameter graphite working electrode. After curing at 60 degrees for 30 minutes, the screen-printed electrode is ready to use. These electrodes have been characterised electrochemically in a prior paper and have heterogeneous rate constants of 1.7×10^{-3} cm s^{-1} as determined with potassium ferrocyanide / 1 M KCl. [27] Figure (5.7) displays SEM images of the graphite screen-printed electrochemical sensor where a well-defined electrode surface [27, 28] is observed from randomly orientated graphite particles bound together with an inert polymeric binder which is free from cracks and holes. Canal water was sampled in Bury, Lancashire which was simply acidified to pH 1 with H_2SO_4 before electro-analytical measurements. Carbon powder was used as received and was purchased from Gwent electronic materials Ltd. Amperometry was performed using a stirrer bar rotating at ~250 rpm. Scanning electron microscope (SEM) images and surface element analysis were obtained with a JEOL JSM-5600LV model.

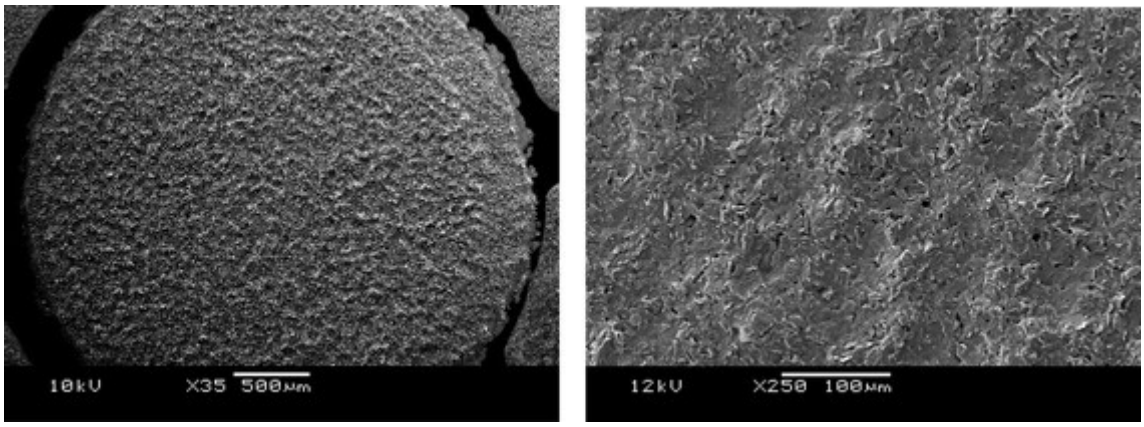

Figure 5.7 SEM images of a graphite screen-printed electrochemical electrode.

5.2.1.3 RESULTS AND DISCUSSION

Chromium(VI) can exist, depending on its speciation in aqueous solutions in a variety of forms. Based on the possible reactions that may occur, the dissociation and complexation constants may be defined as:

$$K_{\mathrm{a}} = \frac{[\mathrm{HCrO_4^-}][\mathrm{H^+}]}{[\mathrm{H_2CrO_4}]} \tag{5.3}$$

$$K_1 = \frac{[\mathrm{HCrO_4^-}][\mathrm{Cl^-}][\mathrm{H^+}]}{[\mathrm{CrO_3Cl^-}]} \tag{5.4}$$

$$K_2 = \frac{[\mathrm{HSO_4^-}][\mathrm{HCrO_4^-}]}{[\mathrm{CrSO_7^{2-}}]} \tag{5.5}$$

Literature values are: K_a = 0.18 M;[29] K_1 = 0.09 M^2;[30] K_2 = 0.24 M.[31] Equations (5.3)–(5.5) allow the calculation of different concentrations of monochromate anions in aqueous solutions in either HCl or H_2SO_4. Typically obtained results are summarised in table (5.1) where it can be readily observed that in 0.1 M H_2SO_4 the $HCrO_4^-$ species is the most dominant.

Table 5.1 Estimated concentration of species calculated for H_2SO_4 and HCl within a 0.1M Solution.

	H_2SO_4 / 0.1 M	**HCl / 0.1 M**
$\boldsymbol{K_a = 0.18\ M}$	$HCrO_4^-$	$HCrO_4^-$
	50.4%	60.0%
$\boldsymbol{K_1 = 0.24\ M^2}$	H_2CrO_4	H_2CrO_4
	30.7%	33.3%
$\boldsymbol{K_2 = 0.24\ M}$	$CrSO_7^{2-}$	CrO_3Cl^-
	18.9%	6.7%

A literature survey reveals that Welch and Compton found equivalent sensitivity in acid electrolytes (0.1 M HCl, 0.1 M H_2SO_4 and 0.lM HNO_3) towards the sensing of Cr(VI) with gold electrodes.[32] Additionally, it was noted glassy-carbon (GC) should not be recommended as a working electrode for analytical purposes for the sensing of Cr(VI) in HCl.[32] A voltammetric response is observed at GC electrodes attributed towards the irreversible reduction of hexavalent chromium in acidic conditions, however the poor reproducibility of results along with pre-wave shoulders, explained by the influence of the corrosive environment hinder its applicability in this experiment. Conversely, Danilov and Protsenko reported that the sensitivity in various electrolytes diminished in the following order: H_2SO_4 > HCl > HNO_3.[13] Results reported by Pezzin *et al.*[33] suggest that the reduction of Cr in oxidising acids, not involving a conventional reducing species such as chloride, advocates that the proton may be the defining reagent in the reduction pathway. In discussing the reduction of Cr(VI) in formic acid, Archundia *et al.*[34] concluded that the process is promoted by H^+ and is conceivably independent to the nature of the acid anion, thought the latter may contribute to the formation of CrL_n-type species, whose stability may

manipulate the overall kinetics of the acid-reduction process and the consequential product distributions. Given the information derived above, exploring the electrochemical detection of Cr(VI) at a range of commercially available electrodes in 0.1 M H_2SO_4 [21] using linear sweep voltammetry. Figure (5.8) depicts the voltammetric profiles where at the gold electrode a large reduction wave is observed at approx. +0.85 V (vs. SCE) due to the electrochemical reduction of gold oxide and a reduction wave at approx. +0.45 V (vs. SCE). Based on previous reports, [21, 32] the reaction mechanism on the gold electrode likely involves the electrochemical reduction of Cr(VI) to Cr(V) with the transfer of one electron and one proton with follow up chemical steps.[32] Also shown in Figure (5.8) is the response of screen-printed and glassy carbon electrodes which exhibit reduction waves at approx. +0.075 V and approx. +0.32 V (vs. SCE) respectively. No voltammetric waves are observed on the boron-doped diamond electrode. Inspection of Figure (5.8) reveals that the gold electrode appears to exhibit a more reversible electrochemical process over that of the glassy-carbon and screen-printed electrodes.

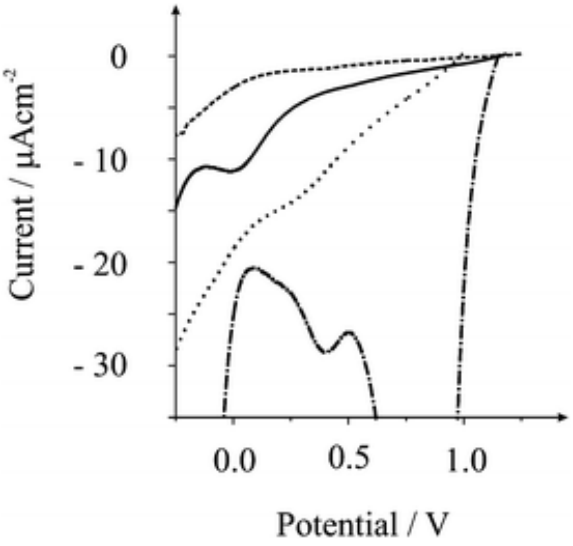

Figure 5.8 Linear sweep voltammograms using gold (dot-dashed line), glassy carbon (dotted line) and boron doped-diamond (dashed line) electrodes with that of the non-modified graphite screen-printed sensor (solid line) in an aqueous solution of 0.1M H_2SO_4 containing 1000 mg L^{-1} Cr(VI). All scans recorded at a scan rate of 50 m V s^{-1} (vs. SCE).

If the change in reversibility is considered, as is possible through the careful choice of electrode substrates, the ratio of the voltammetric peak current resulting from a reversible

electrochemical reduction, $I_{\mathrm{p}}^{\mathrm{rev}}$, and that of a irreversible reduction, $I_{\mathrm{p}}^{\mathrm{irr}}$, can be defined by the appropriate Randles–Ševćik expression:[35]

$$\frac{I_p^{rev}}{I_p^{irr}} = \frac{2.69 \times 10^5 ACD^{1/2}v^{1/2}}{2.99 \times 10^5\, \beta^{1/2} ACD^{1/2}v^{1/2}} \approx 1.27 \qquad (5.6)$$

Clearly an improvement in the reversibility of the electrochemical reaction by applying gold as an electrode material is observed but theoretically only increases the magnitude of the voltammetric peak current by only a factor of ~1.3. This implies that a change in reversibility is not always beneficial in electroanalysis but what is most appropriate is where in relation to interferents these voltammetric signatures occur. Given that the voltammetric signal observed at the screen-printed electrode is around ~0.0 V (vs. SCE), which is well resolved from likely interferents and the low cost of production and disposable nature compared to the glassy carbon and gold electrodes, screen-printed electrodes are highly desirable for the portable screening of Cr(VI). Next the electro-analytical performance of the screen-printed electrodes towards the sensing of Cr(VI) is explored. Using linear sweep voltammetry, additions of Cr(VI) were made into a 0.1 M H_2SO_4 aqueous solution and as depicted in Figure 5.9 the magnitude of the electrochemical signal increases as a function of added Cr(VI) concentrations. Analysis of the peak current (I_p) reveals a linear response is observed over the range 100 to 1000 µg L^{-1} (I_p/A = 7.9 × 10^{-10} A/µg L^{-1} – 3.6 × 10^{-9} A; R^2 = 0.999; N = 11) with a limit of detection (3σ) [36] found to correspond to 19 (±0.5) µg L^{-1} respectively. The inter-reproducibility of the sensor evaluated from five separate measurements using new screen-printed electrodes was found to produce a % Relative Standard Deviation of 4.8%.

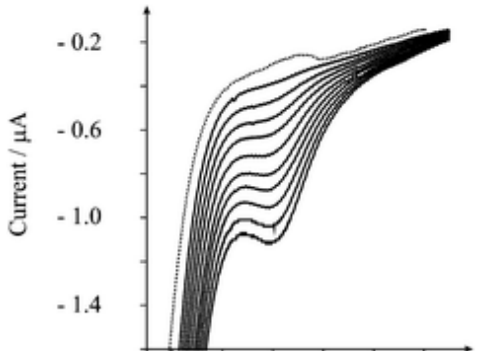

Figure 5.9 Linear sweep voltammograms using a screen-printed sensor resulting from additions of Cr(VI) into a 0.1 M H_2SO_4 aqueous solution. Scan rate: 50 m V s^{-1}.

Next the electrochemical sensing of Cr(VI) in canal water was explored, allowing a comparison of performance in lab with that in natural environmental conditions and to determine if any materials present could hinder the screen-printed sensors ability to detect trace amounts of Cr(VI). As described in the experimental section, the canal water sample was acidified to pH 1 with additions of Cr(VI) made into the sample. As shown in Figure (5.10), the addition of Cr(VI) is observed to be linear over the range 100 to 1000 µg L^{-1} (I_P/A = 7.3 ×10^{-10} A μg^{-1} L^{-1} + 1.2 × 10^{-8} A; R^2 = 0.999; N = 11) with a limit of detection (3σ)[36] found to correspond to 21 (±0.7) µg L^{-1} which is close to the guideline limit set by the WHO (50 µg L^{-1}) in groundwater.[3] In comparison with the results depicted in Figure (5.9), it is interesting to point out that there is no decrease in the sensitivity for the sensing of Cr(IV) in the water sample using the screen-printed sensors which the reduction in sensitivity or lack thereof likely arises due to the position of the electrochemical signal in the potential window.

It is noted that copper, usually present in water samples, appears not to interfere with our methodology and caution should be used when using this methodology that the voltammetric potential is not set to scan too negative a position which would induce the electrochemical reduction of copper ions to copper metal such that the corresponding stripping peak, which usually occurs at ~0.0 V, does not interfere with the voltammetric signal for the sensing of Cr(VI).

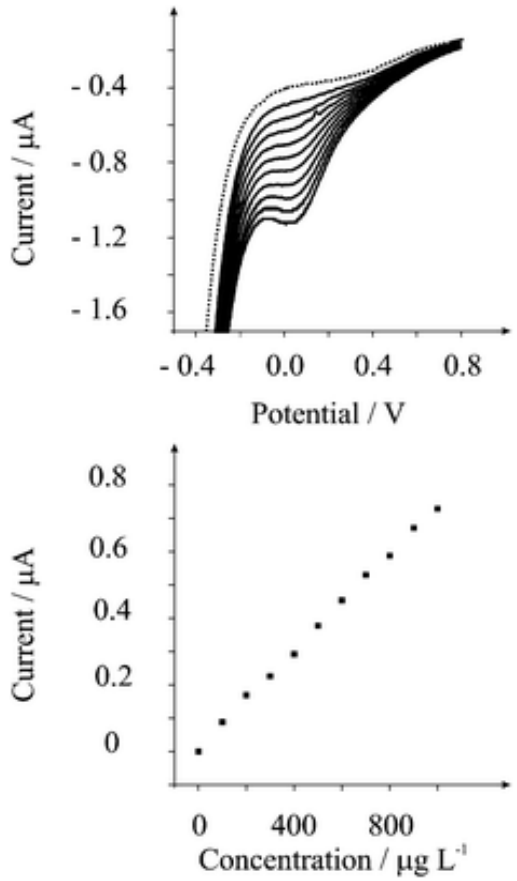

Figure 5.10 Linear sweep voltammograms using a screen-printed sensor resulting from additions of Cr(VI) into a canal water sample (pH 1). Scan rate: 50 m V s^{-1}.

Lastly the analytical performance using un-optimised amperometry is explored. Figure (5.11) shows the response of 25 µM additions of Cr(VI) made in the canal water sample with analysis of the current as a function of added Cr(VI) concentration depicted in Figure (5.12) where a linear range is observed over the range 25 to 1000 µg L^{-1} (I_P/A = 7.6 ×

10^{-10} A/µg L^{-1} – 8.4×10^{-10} A; R^2 = 0.99; N = 13). The inset of Figure (5.11) shows the response of the lower additions clearly indicating that the sensing of Cr(VI) at levels below the WHO limit is possible.

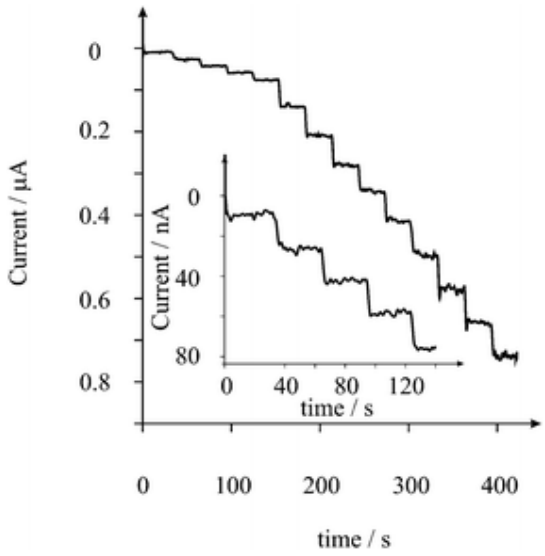

Figure 5.11 Amperometric response using a screen-printed sensor resulting from additions of Cr(VI) into a canal water sample (pH 1). Potential held at + 0.025 V.

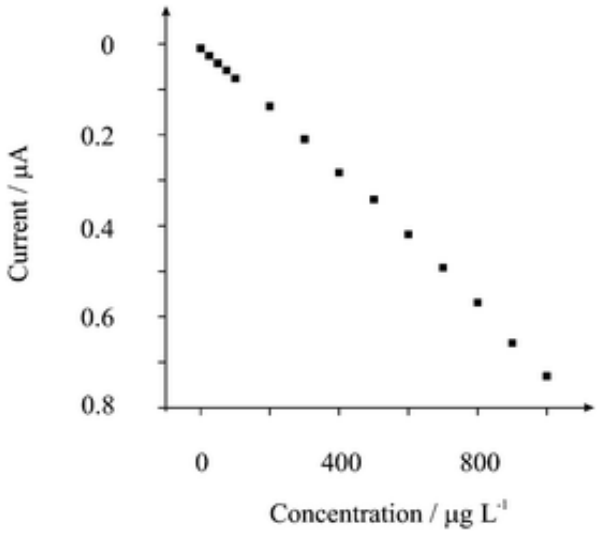

Figure 5.12 Analysis of the amperometric data presented in Figure 5.11.

In considering the concept of interferents it is clear that in the intended application of sensing Cr(VI) in water samples, it appears that this protocol is extremely promising and has clear advantages over existing analytical and electro-analytical techniques. One potential interferent is the use of water softeners to remove the hardness from water which is used in a

plethora of applications through the introduction of chloride salts. The chloride present can, in the presence of Cr(VI), be oxidised to chlorine:

$$2Cr^{6+} + 6Cl^{-} \rightleftharpoons 2Cr^{3+} + 3Cl_2 \quad (5.7)$$

Figure (5.13) displays the electrochemical reduction of Cr(VI) in a 0.1 M H_2SO_4 aqueous solution using a glassy carbon electrode and after the addition of sodium hypochlorite which releases chlorine gas in acidic media:

$$NaOCl + H^{+} + Cl^{-} \rightarrow NaOH + Cl_2 \quad (5.8)$$

It is clearly evident that the magnitude of the initial voltammetric peak is considerably increased following the addition of sodium hypochlorite which produces chlorine gas in aqueous solution with the electrochemical processes now due to the electrochemical reduction of chlorine gas:

$$Cl_2 + 2e^{-} \rightleftharpoons 2Cl^{-} \quad (5.9)$$

The potential of the electrochemical reduction wave in the voltammetric window (Figure 5.13), which is attributed to the electrochemical reduction of chlorine, is in excellent agreement with that reported by Lowe *et al*.[37] who have studied the electrochemical sensing of chlorine in aqueous solutions at a range of commercially available electrode substrates. Thus it is suggest that: (i) in aqueous solutions other than H_2SO_4, the electrochemical reduction of Cr(VI) may not actually be that as suggested previously [32] but is actually an indirect methodology, which is especially true when using electrolyte solutions such as HCl; (ii) in solutions and real samples, where high levels of chloride may be present, care needs to

be taken to ensure the true origin of the electrochemical signal which would become particularly evident in real samples, for example in trying to determine Cr(VI) in sea water, but this indirect methodology (equation (5.7)–(5.9)) might prove analytically useful.

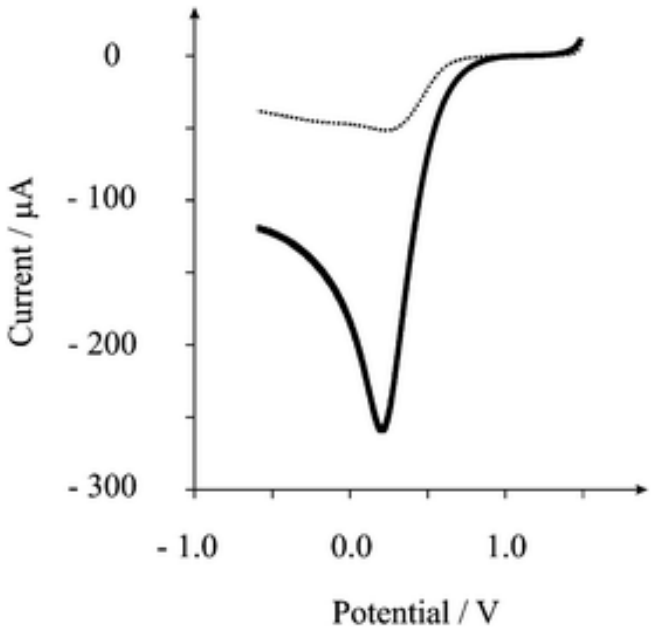

Figure 5.13 Linear sweep voltammograms of a GC electrode in an aqueous solution of 0.1 M H_2SO_4 containing 1000 mg L^{-1} Cr(VI) only (dotted line), alongside the observed response for a solution containing both 1000 mg L^{-1} Cr(VI) and 100 mL sodium hypochlorite, 10-13% (thick solid line) at a scan rate of 50 m V s^{-1} (vs. SCE).

Returning to the analytical performance of the screen-printed sensors towards Cr(IV) sensing, to gain an insight into the electrochemical mechanism, the effect of scan rate over the range 0.1 to 1 V s^{-1} using an aqueous solution of 0.1 M H_2SO_4 containing 1000 mg L^{-1} Cr(VI) using a screen-printed electrode was explored. Analysis of the current as a function of scan rate and square-root of scan rate revealed a linear response only in the former case (I/A = 3.3×10^{-6} A/V s^{-1} + 2.0×10^{-8} A; R^2 = 0.995). It should also be noted that when applying fast scan rates (>400 mV s^{-1}) a distinctive pre-wave was observed indicating that the electrochemical reaction may be adsorption controlled, which might likely proceed via a CE

route. Thus, in the case of the screen-printed electrode, the mechanism is different to that above (not involving Cl^-/Cl_2) since it involves a surface bound species.

Reactive surface groups and a vast surface area make carbon an effective reductant for Cr(VI).[37] The interaction of Cr(VI) with carbon has a two-phase mechanism: the sorption of Cr(VI) and the resulting reduction of Cr(VI) to Cr(III) via the oxidation of functional groups.[38] IR spectra were obtained for carbon black used in fabrication of the electrodes, to distinguish the surface functional groups responsible for Cr(VI) reduction. Bands at 1604, 1737, 2725, 2850 and 3400 cm^{-1} were observed within the IR spectrum. Assignment of the band at 1604 cm^{-1} was accredited to the stretching of conjugated C–C bonds. The C=O stretching of aldehyde and ketone functional groups was present at 1737 cm^{-1} while the vibrations from the C–H bonds within alkyl groups contribute to the band shown at 2725 and 2850 cm^{-1}. Finally the intense band at 3400 cm^{-1} was assigned to the presence of O–H from either alcohol or phenol active groups. It is feasible to theorize that the absorbed Cr(VI) is reduced to Cr(III) with the oxidation of the functional groups C–H, C–OH and C=O. Results published by Yue *et al*. provide additional data that support this hypothesis.[39]

To quantify these results, a commercially available carbon powder abrasively modified glassy-carbon electrode was explored towards the sensing of Cr(VI) which had previously shown a limited response to the presence of Cr(VI). Figure (5.14) depicts the pertinent voltammetric profiles where a substantial improvement in the electrochemical signal towards Cr(VI) sensing is revealed through the introduction of surface-oxygen-rich carbon powder.

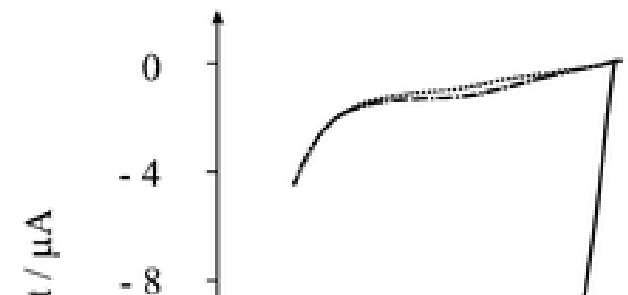

Figure 5.14 Linear sweep voltammograms of a glassy carbon electrode in an aqueous solution of 0.1 M H_2SO_4 in the absence (dotted line) and in the presence (dot-dashed line) of 1000 mg L^{-1} Cr(VI) and a surface-oxygen-rich carbon-black abrasively modified glassy-carbon electrode (solid line) in the presence of 1000 mg L^{-1} Cr(VI). Scan rate: 50 m V s^{-1} (vs. SCE).

This observation coupled with the current being proportional to the scan rate employed leads us to believe that the mechanism involves active functional groups found on carbon which are oxidised by Cr(VI):

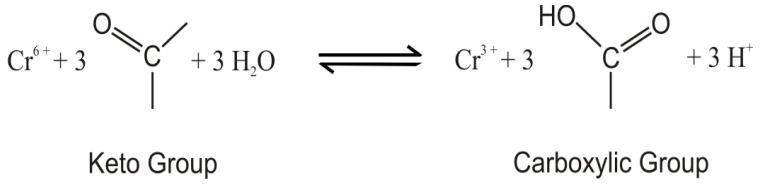

which are electrochemically reduced, generating the observed electrochemical signal due to the following processes:

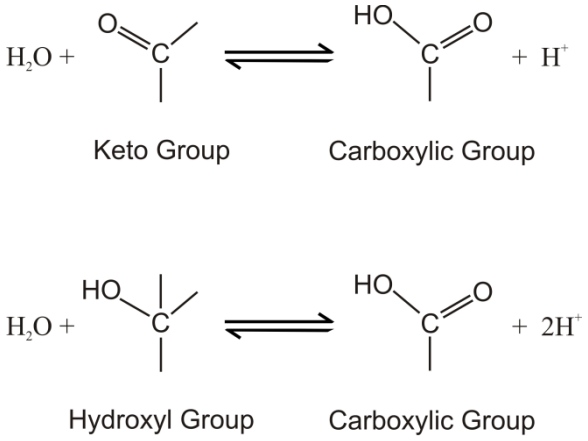

which allows for the indirect measurement of Cr(VI) using the screen-printed sensor. The electrochemical reduction of surface functional groups is consistent with the observation above from the scan rate data. Returning to Figure (5.8) it is evident that the glassy carbon and boron-doped diamond electrodes have fewer surface active groups resulting in a poor electrochemical signal. Such observations have never been reported before in the literature and the screen-printed sensor, while providing the required sensitivity yet is cost effective, lends itself towards the de-centralised testing of Cr(VI) in water samples.

5.2.1.4 CONCLUSIONS

The electrochemical reduction of Cr(VI) has been explored and reported for the first time, using non-modified, non-metallic, graphite screen-printed electrode for the electro-analytical sensing of low ppb levels of Cr(VI) in aqueous solution which are at WHO levels. The methodology is demonstrated to be possible for the electro-analytical sensing of Cr(VI) in water samples. Given the analytical performance and low cost of the screen-printed sensors, this protocol holds promise for the portable sensing of the toxic pollutant Cr(VI) in water samples. Investigation of the electrochemical mechanism indicates that the electro-analytical protocol is an indirect sensing approach involving surface oxygenated species. It is

well known that the porous structure of carbon electrodes affects its performance as a supercapacitor. Aside from physical considerations, the chemical characteristics, for instance, the distribution of heteroatoms (atoms that are not carbon or hydrogen, typically nitrogen or oxygen) along the electrode's surface also influence the capacitor's performance. Carbon–oxygen complexes at the electrode's surface have been reported to affect the wettability, chemical reactivity, and electrical attributes of the material. How these complexes influence the performance of the resulting EDLCs has rarely been reported in the literature. The degree of physically adsorbed molecular oxygen, or surface complexes, is believed to strongly influence the mechanistic process and rate of capacitative self-discharge (or leakage). This has been found particularly true for carbons with a high concentration of acidic surface functionalities; prone to high rates of self-discharge. The rise in leakage current suggests that the oxygen functional groups may act as active sites, catalysing the electrochemical oxidation or reduction of the carbon electrode, or assist in the decomposition of the electrolyte components. The presence of oxygenated functional groups has also been linked with capacitor instabilities, resulting in increased ESR (equivalent series resistance) and deteriorating capacitance values. Oxygen surface functional groups have also been discovered to have a profound impact on the resting potential of carbon electrodes. The relative resting potential of the electrode was found to correlate to the logarithm of the oxygen content /concentration of acidic surface sites. Electrodes displaying high rest potential typically experience undesirably higher voltages when charged, resulting in the possible evolution of gas. Conversely, while charge storage on carbon electrodes is predominantly capacitive, contributions from rapidly charging and discharging surface functional groups give rise to pseudo-capacitance. It was established that the Faradaic current, a direct measure of pseudo-capacitance, increased substantially following oxygen treatment, while the change in the double-layer capacitance was insignificant. The large increase in specific capacitance

(from ~120 to 150 F g^{-1}) [40] was, however, accompanied by the undesirable side effects of increased resistance along with instabilities and higher resting potentials.

5.2.1.5 REFERENCES

1. R. M. Cespón-Romero, M. C. Yebra-Biurrun, M. P. Bermejo-Barrera, *Anal. Chim. Acta*, **1996**, 327, 37.
2. D. Blowes, *Science*, **2002**, 295, 2024.
3. *Guidance for Drinking Water Quality—Second Edition—Volume 1 Recommendations*, WHO, Geneva, **1993**, pp. 45–46.
4. S. D. Flora, *Carcinogenesis*, **2000**, 21, 533.
5. S. D. P. Eiras, U. M. Custodio, L. A. Pavanim, *Talanta*, **2003**, 59, 621.
6. H. Bag, A. R. Turker, M. Lale, A. Tunceli, *Talanta*, **2000**, 51, 895.
7. S. Hirata, K. Honda, O. Shikino, N. Maekawa, M. Aihara, *Spectrochim. Acta*, Part B, **2000**, 55, 1089.
8. B. Tang, T. Yue, J. Wu, Y. Dong, Y. Ding, H. Wang, *Talanta*, **2004**, 64, 955.
9. M. Kaneko, M. Kurihara, S. Nakano, T. Kawashima, *Anal. Chim. Acta*, **2002**, 474, 167.
10. B. Gammelgaard, Y. P. Liao, O. Jons, *Anal. Chim. Acta*, **1997**, 354, 107.
11. K. Muto, K. Ohno, J. M. Lin, M. Yamada, Jpn. *J. Iron Steel*, **2003**, 89, 68.
12. L. D. Burke, P. F. Nugent, *Electrochim. Acta*, **1997**, 42, 399.
13. F. L. Danilov, V. S. Protsenko, Russ. *J. Electrochem*., **1998**, 34, 276.
14. S. B. Faldini, S. M. L. Agostinho, H. C. Chagas, *J. Electroanal. Chem*., **1990**, 284, 173.
15. S. T. Crosmun, T. R. Mueller, *Anal. Chim. Acta*, **1975**, 75, 199.
16. C. Harzdof , G. Janser, *Anal. Chim. Acta*, **1984**, 165, 201.
17. J. A. Cox, J. L. West, P. J. Kuleza, *Analyst*, **1984**, 109, 927.
18. M. Boussemart, C. M. G. van den Berg, M. Ghaddaf, *Anal. Chim. Acta*, **1992**, 262, 103.
19. M. A. Ghandour, S. A. EI-Shatoury, A. M. M. Aly, S. M. Ahmed, *Anal. Lett*., **1996**, 29, 1431.
20. C. M. Welsh, O. Nekrassova , R. G. Compton, *Talanta*, **2005**, 65,74.
21. S. Hood, D. K. Kampouris, R. O. Kadara, N. Jenkinson, F. J. del campo, F. X. Francesc, C. E. Banks, *Analyst*, **2009**, 134, 2301.

22. B. K. Jena, C. R. Raj, *Talanta*, **2008**, 76, 161.
23. M. Tudorache, C. Bala, *Anal. Bioanal. Chem*., **2007**, 388, 565.
24. R. O. Kadara, N. Jenkinson, C. E. Banks, *Electrochem. Commun*., **2009**, 11, 1377.
25. K. Z. Brainina, N. Y. Stozhko, Z. V. Shalygina, *J. Anal. Chem*., **2002**, 57(10), 945.
26. http://kanichi-research.com.
27. R. O. Kadara, N. Jenkinson, C. E. Banks, *Sens. Actuators, B*, **2009**, 138, 556.
28. N. A. Choudry, D. K. Kampouris, R. O. Kadara, C. E. Banks, *Electrochem. Commun*., **2010**, 12, 6.
29. E. Deltombe, N. De Zoubov, M. Pourbaix, in *Atlas of Electrochemical Equilibria in Aqeuous Solutions*, *ed.* M. Pourbaix, Pergamon Press, New York, **1966**, pp. 256–271.
30. J. Y. Tong, R. L. Johnson, *Inorg. Chem*., **1966**, 5, 1902.
31. G. P. Haight, D. C. Richardson, N. H. Colburn, *Inorg. Chem*., **1964**, 3, 1777.
32. C. M. Welsh, O. Nekrassova, R. G. Compton, *Talanta,* **2005,** 65, 74.
33. S. H. Pezzin, J. F. L. Rivera, C. H. Collins and K. E. Collins, *J. Braz. Chem. Soc*., **2004**, 15(1), 58.
34. C. Archundia, C. H. Collins, K. E. Collins, *J. Radioanal. Nucl. Chem*., **1990**, 146, 49.
35. B. R. Kozub, N. V. Rees, R. G. Compton, *Sens. Actuators, B,* **2010**, 143(2), 539.
36. C. M. A. Brett, A. M. O. Brett, *Electroanalysis* (Oxford ChemistryPrimers, 64), Oxford Science Publications.
37. E. R. Lowe, C. E. Banks, R. G. Compton, *Anal. Bioanal. Chem*., **2005**, 382, 1169.
38. N.-H. Hsu, S.-L. Wang, Y.-C. Lin, G. Daniel Sheng, J.-F. Lee, *Environ. Sci. Technol.*, **2009**, 43, 8801.
39. Z. Yue, S. E. Bender, J. Wang, J. Economy, *J. Hazard. Mater.*, **2009**, 166, 74.
40. C.-T. Hsieh*,* H. Teng*, Carbon*, **2002**, 40, 667.

This section contains work [1,2] undertaken during this thesis describing two dissimilar methods of electrode modification: 1) the incorporation of metals within the electrode's surface and 2) deposition of carbon nanomaterials to the surface of the electrode, plus investigations into their electrochemical characteristics. Further details of this work are found below.

Nickel-oxide bulk-modified screen-printed electrodes are developed for the first time and explored towards the electro-analytical sensing of hydroxide ions and shown to be analytically useful. The nickel-oxide screen-printed sensor allows the detection of hydroxide ions over the low micro-molar to milli-molar range with a detection limit of 23 μM. The sensor is simplified over existing analytical methodologies and given its disposable and economical nature holds promise for the sensing of hydroxide ions and consequently the measurement of pH in aqueous solutions.

Solid-carbon nanorod (SCNR) whiskers (a derivative of carbon nanotubes) are introduced, which are fabricated via a solid-state methodology and are completely free from metallic impurities. The electrochemical properties of these unique carbon nanostructures are explored towards the electrochemical oxidation of NADH, dopamine and uric acid, and compared and contrasted with other carbon nanomaterials/composites where appropriate. It is shown that thin-layer behaviour dominates when the coverage of the nanomaterials is increased giving the false impression of electro-catalysis. The SCNR whiskers are analytically similar to other reported carbon nanotube structures and yet do not suffer from problems associated with metallic impurities, suggesting their beneficial use in many areas of electrochemistry.

*Dr Kampouris and Dr Kadara from the Banks research group were consultants during this project. Mr Jenkinson performed SEM analysis of the products.

1. P. M. Hallam, D. K. Kampouris, R. O. Kadara, N. Jenkinson, C. E. Banks, *Nickel-oxide screen-printed electrodes for the sensing of hydroxide ions in aqueous solutions, Analytical Methods,* **2010**, 2 (8), 1152.

2. P. M. Hallam, C. E. Banks, *Solid Carbon Nanorod Whiskers: Application to the Electrochemical Sensing of Biologically Relevant Molecules, RSC Advances,* **2011**, 1 (1), 93**.**

5.3.1 NICKEL-OXIDE SCREEN-PRINTED ELECTRODES FOR THE SENSING OF HYDROXIDE IONS IN AQUEOUS SOLUTIONS

5.3.1.1 INTRODUCTION

Reliable sensors for the monitoring of hydroxide ion concentrations which can operate in harsh environments are urgently sought.[1–3] Hydroxide is used worldwide in many industrial processes, and rapid and reliable methodologies for the sensing of hydroxide ions for quality control purposes and monitoring during industrial processing are required.[4] Problems arise quite simply due to the corrosive nature of the concentrated alkali conditions, where glass pH electrodes become insensitive and unstable at high concentration levels. [1,2,5] Sensors based on fluorescence and absorbance have been reported but have been criticised due to tedious fabrication processes.[6]

Daniele *et al*. have extensively explored the electrochemical oxidation of hydroxide ions in aqueous solution using gold microelectrodes.[7–11] The electroanalytical signal resulting from the electrochemical oxidation of hydroxide ions is well documented to be proportional to the hydroxide ion over a wide concentration range[8] providing a novel methodology for the measurement of pH as an alternative to potentiometry, particularly at high alkaline concentrations beyond the limit of applicability of the glass electrode.[11] Current state-of-the-art for hydroxide ion sensing has been reported by Compton and coworkers who reported the low micro-molar level detection of hydroxide ions using gold ultra-microelectrode arrays.[12]

The electrochemical oxidation of hydroxide ions always occurs at high oxidation potentials typically in the region of 1.3 to 1.6 V (vs. SCE).[5] Recently Mentus *et al.* have

explored the role of cathodic pre-treatment on the electrochemical oxidation of hydroxide ions using gold electrodes where it was demonstrated that the electrochemical oxidation potential can be reduced to lower oxidation potentials through forming different types of gold oxide.[5] Generally the electrochemical oxidation of hydroxide ions has been undertaken on gold and platinum electrodes. The modification of gold electrodes with metal ion phthalocyanines and porphyrins has reported modest decreases in the electrochemical oxidation potentials of hydroxide ions.[4] It was observed by Daniele *et al.*[9] that the electrochemical oxidation of hydroxide ions occurred at lower oxidation potentials than that at gold and platinum electrodes through the use of a nickel electrode. However, it was noted that the background oxide formation potentially makes measurements difficult.[9]

Herein the electrochemical oxidation of hydroxide ions is revisited using nickel-oxide screen-printed electrodes which have micron-sized nickel-oxide incorporated into the bulk of screen-printed working electrodes. These nickel-oxide screen-printed sensors have been developed for the first time and are explored towards the electro-analytical sensing of hydroxide ions.

5.3.1.2 EXPERIMENTAL

All chemicals used were of analytical grade and were used as received without any further purification and were obtained from Sigma-Aldrich. Micron-sized nickel-oxide (NiO 97.3%, 10 microns) was used as received. All solutions were prepared with deionised water of resistivity not less than 18.2 MΩ cm. Voltammetric measurements were carried out using a m-Autolab III (ECO-Chemie, The Netherlands) potentiostat. All measurements were conducted using a screen-printed three electrode configuration with a geometric working electrode area of 3 mm diameter. Connectors for the efficient connection of the screen-printed electrochemical sensors were purchased from Kanichi Research Services Ltd.[13]

Screen-printed carbon electrodes were fabricated in-house with appropriate stencil designs (see section 5.1, further details can be found below) using a microDEK 1760RS screen-printing machine (DEK, Weymouth, UK). A carbon–graphite ink (Gwent Electronic Materials Ltd, UK) formulation previously explored by Kadara *et al.* [14] was first screen-printed onto a polyester flexible film (Autostat, 250 mm thickness). This layer was cured in a fan oven at 60 degrees for 30 minutes. Next a silver/silver chloride reference electrode was included by screen printing Ag/AgCl paste (Gwent Electronic Materials Ltd, UK) onto the plastic substrate. Last a dielectric paste ink (Gwent Electronic Materials Ltd, UK) was printed to cover the connection and define the 3 mm diameter graphite working electrode. After curing at 60 degrees for 30 minutes the screen-printed electrode is ready to use.

Nickel-oxide screen-printed electrodes were fabricated as described above with commercially purchased nickel-oxide efficiently mixed into the ink formulation prior to screen printing. In doing so, the rheology of the ink changes such that the careful addition of organic solvents, for example cyclohexanone, may be needed along with modification of the standard printing parameters (print height/layer thickness). Increasing amounts of nickel-oxide were incorporated into the screen-printed electrodes over the range of 0–10% (M_P/M_I), where M_P is the mass of particulate and M_I is the mass of ink formulation used in the printing process. Scanning electron microscope (SEM) images and surface element analysis were obtained with a JEOL JSM-5600LV model having an energy-dispersive X-ray microanalysis package. SEM imaging was conducted by N. Jenkinson.

5.3.1.3 RESULTS AND DISCUSSION

Nickel-oxide (NiO) screen-printed electrochemical sensing platforms were fabricated as described in the Experimental section (5.3.1.2) where increasing amounts of nickel-oxide were incorporated into the screen-printed electrodes over the range of 0–10% (M_P/M_I), where

M_P is the mass of particulate and M_I is the mass of ink formulation used in the printing process. SEM images of the nickel-oxide sensor are shown in Figure (5.15) where a relatively rough surface is observed but is not distinctly different to that expected for a non-modified screen-printed electrode. [14]

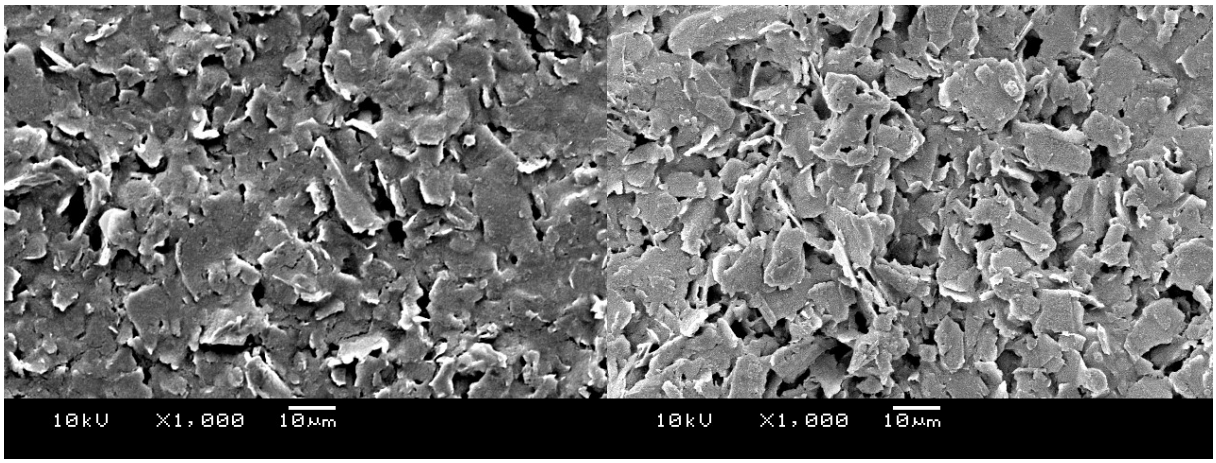

Figure 5.15 SEM images of a standard, non-modified screen-printed sensor (left image) compared with a 2 % (M_P/M_I) nickel-oxide modified screen-printed sensor (right image).

EDAX was performed with typical values revealing that the examined surface is 92.59% atomic carbon, 4.49% atomic oxygen, 2.72% atomic chloride and 0.2% atomic nickel. The micron-sized nickel-oxide likely resides in the carbon layer as random dispersed micron-sized particles, or larger, which are clearly exposed to the electrolyte solution. The response of a 2% (M_P/M_I) nickel-oxide screen-printed sensor towards the electro-analytical sensing of hydroxide was initially explored. Figure (5.16) shows typical cyclic voltammetric responses resulting from 250 µM additions of hydroxide into a 0.01 M Na_2SO_4 solution. Inspection of the cyclic voltammetric response in the absence of hydroxide (dotted line, Figure 5.16) reveals a small reduction wave at ~0.11 V (vs. SCE) which is likely due, based on inspection of the nickel Pourbaix diagram, to the electrochemical reduction of the nickel-oxide,[15] likely to Ni^{2+}. The nickel then likely reacts with the added hydroxide analyte forming $Ni(OH)_2$ in accordance with the Pourbaix diagram where the electrochemical oxidation wave at +0.65 V

is likely due to two processes: $Ni(OH)_2 \rightarrow NiOOH + H^+ + e^-$ and $Ni(OH)_3^- \rightarrow NiOOH + H_2O + e^-$. On the reverse scan a pre-wave and large reduction wave are observed. Analysis of the peak potential (E_p) as a function of pH for both waves, where the pH of the solution is changed through the addition of hydroxide ions, reveals a small non-Nerstian response for the pre-wave and a linear response for the large reduction wave at +0.05 V (vs. SCE) with a gradient of 51 mV per pH indicating a one proton and one electron process. Thus the pre-wave and the large reduction is likely due and tentatively assigned to the electrochemical reduction of $NiOOH + H_2O + e^- \rightarrow Ni(OH)_3^-$ and $NiOOH \rightarrow Ni(OH)_2 + H^+ + e^-$ respectively. Following the additions of hydroxide, a large voltammetric wave is observed at +0.65 V (vs. SCE) which is likely due to the following process: [5, 12]

$$4OH^- - 4e^- \rightleftharpoons O_2 + 2H_2O$$

which is likely catalysed by the Ni^{2+}/Ni^{3+} couple as discussed above. Consequently the reduction wave at ~0.54 V (vs. SCE) is likely due to the electrochemical reduction of oxygen.

Returning to the analytical performance of the nickel-oxide screen-printed sensor, the electrochemical oxidation of hydroxide, which is observed at +0.65 V (vs. SCE), occurs at a lower overpotential compared to previous literature reports using nickel microelectrodes which was observed to exhibit an electrochemical oxidation wave at ~1.0 V (vs. SCE), [9] and additionally that observed at gold and platinum microelectrodes[9] indicating some possible 'electro-catalytic' activity of the nickel-oxide domains.

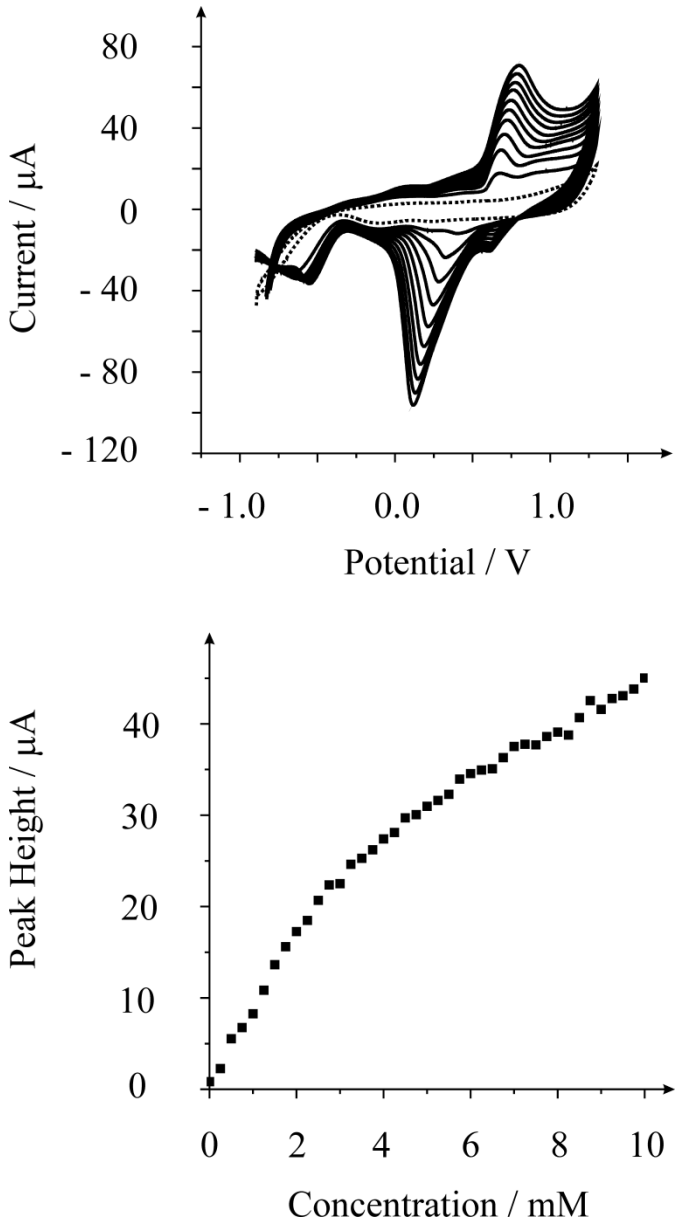

Figure 5.16 Cyclic voltammetric profiles resulting from the addition 250 µM of NaOH into a 0.01M Na_2SO_4 aqueous solution using a 2% (M_p/M_i) nickel-oxide screen-printed sensor. Scan rate: 50 mV s^{-1}(vs. SCE). Also shown is the analysis of the peak height as a function of hydroxide concentration.

Analysis of the oxidation wave observed at +0.65 V (vs. SCE) as a function of hydroxide additions is shown in Figure 5.16 where a linear response is observed from 250 µM to 2.75 mM (I_H/A = 8.0 × 10^{-3} A/M + 9.3 × 10^{-7} A; R^2 = 0.996; N = 11) with a second linear range observed from 3 mM to 10 mM (I_H/A = 2.9 × 10^{-3} A/M + 1.6 × 10^{-5} A; R^2 =

0.992; N = 29). Based on the first linear range the limit of detection (based on three sigma) was found to correspond to 137 μM. The response of differing % (M_P/M_I) nickel-oxide screen-printed sensor towards the electroanalytical sensing of hydroxide was initially explored where it was found that as the % (M_P/M_I) nickel-oxide content in the screen-printed sensor was increased, the background current also enlarged until at the 10% (M_P/M_I) nickel-oxide screen-printed sensor, the large background engulfs the electro-analytical oxidation signal which arises from the electrochemical oxidation of hydroxide. This phenomenon has been observed before which is due to the reduced number of conductive pathways throughout the electrode. [16,17]

Next, the above experiment was replicated under identical conditions with the 2% (M_P/M_I) nickel-oxide screen-printed sensor towards smaller additions of NaOH. Figure (5.17) displays the analysis of cyclic voltammetric responses resulting from successive additions of NaOH (25 μM) into a solution containing 0.01 M Na_2SO_4. Analysis of the anodic wave (Figure 5.17A) reveals two linear ranges: the first from 25 μM to 275 μM ($I_H/A = 31 \times 10^{-3}$ A/M + 8.2×10^{-7} A; $R^2 = 0.985$; N = 11) and the second from 300 μM to 500 μM ($I_H/A = 16 \times 10^{-3}$ A/M + 4.1×10^{-6} A; $R^2 = 0.923$; N = 9). Based on the first linear region, a limit of detection (based on three sigma) was found to correspond to 21(±3) mM. The analytical performance of the nickel-oxide screen-printed sensor is competitively comparable to gold ultra-microelectrodes. [12] Given the disposable nature and low cost, the nickel-oxide screen-printed sensor is highly desirable for the analytical sensing of hydroxide. As shown in Figure (5.17B), the cathodic wave can also be used as an indirect analytical measurement of hydroxide where a linear response takes place at concentrations greater than 125 μM to 500 μM ($I_H/A = 38 \times 10^{-3}$ A/M – 4.3×10^{-6} A; $R^2 = 0.992$; N = 16). The reproducibility of the screen-printed batch was explored using a fixed hydroxide concentration of 7 mM with electrode randomly selected from the batch. The percentage relative standard deviation

(%RSD) found to correspond to 3.84% (n = 7) indicating sufficient reproducibility throughout the batch indicating that an electrode selected randomly should act quantitatively similar to the rest.

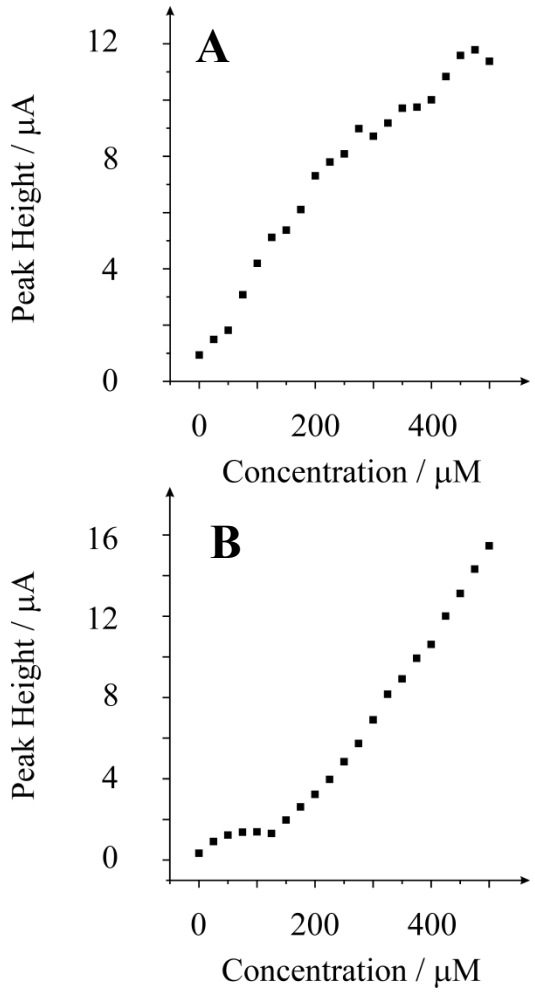

Figure 5.17 Analysis of cyclic voltammetric profiles resulting from 25 μM additions of NaOH into a 0.01 M Na_2SO_4 aqueous solution using a 2% (M_P/M_I) nickel-oxide screen-printed sensor. Scan rate: 50 mV s^{-1} (vs. SCE). Plot A is the analysis of the anodic wave while plot B is the cathodic wave.

Next, the application of chronoamperometry as an electrochemical measurement was explored as it can be simpler to analyse. Figure (5.18A) illustrates the chronoamperometric responses of a 2% (M_P/M_I) nickel-oxide screen-printed sensor from additions of hydroxide

into a 0.01 M Na_2SO_4 solution. Analysis of the limiting current (I_L) as a function of hydroxide concentration (current taken at a time of 20 second) is also shown (Figure 5.18B) which reveals two linear regions: the first over the range 50 to 250 µM (I_L/A = 1 × 10^{-3} A/M – 2.4 × 10^{-8} A; R^2 = 0.98; N = 9) and the second over the range 275 to 500 µM (I_L/A= 0.8 × 10^{-3} A/M – 6.5 × 10^{-9}A; R^2 = 0.987; N = 10). Based on the first linear region, a limit of detection (based on three sigma) was found to correspond to 27 µM even though the sensitivity is considerably less than observed above but still suggests that this approach is analytically viable. It has been shown that the measurement of hydroxide concentrations can allow the pH of the solution under investigation to be determined. [10]

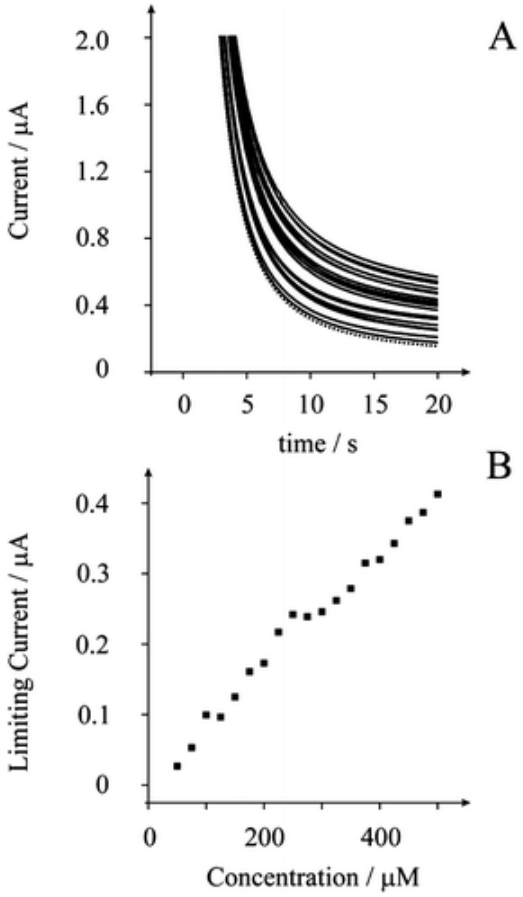

Figure 5.18 Part A displays the chronoamperometric responses obtained using a 2% (M_P/M_I) nickel-oxide screen-printed sensor towards the sensing of hydroxide in 0.01 M Na_2SO_4. Parameters: +0.74 V (vs. SCE). Analysis of the limiting current (I_L), taken after 20seconds, as a function of hydroxide concentration is shown in part B.

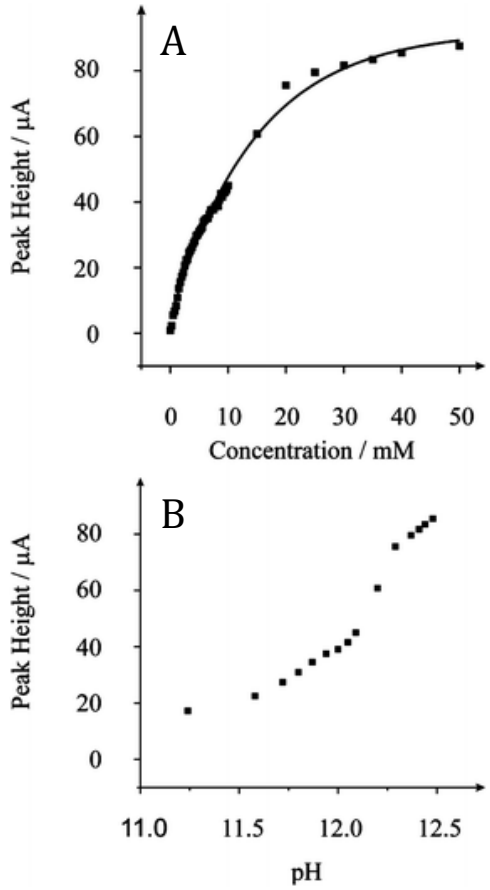

Figure 5.19 Analysis of cyclic voltammetric responses resulting from additions of hydroxide into a 0.01 M Na_2SO_4 aqueous solution using a 2% (M_P/M_I) nickel-oxide screen-printed sensor (A). Also shown is the response of the peak height as a function of solution pH (B).

Figure (5.19) depicts an overview of the entire analytical response using the voltammetric peak height as a function of hydroxide concentration. Analysis of this plot in terms of voltammetric peak height and a function of the solution pH, which changes as increasing amounts of hydroxide are added to the 0.01M Na_2SO_4 solution, (shown in Figure 5.19) which correspond to hydroxide additions of 2 to 50 mM. Clearly a direct correlation between the peak height of the voltammetric profiles obtained using the nickel-oxide screen-printed electrodes and the concentration/ pH is observed, this in turn means that there is the possibility of using this electrode as a single use, disposable pH sensor for systems that are either beyond the limit of applicability of the glass electrode [5] or can be utilised in extreme

environments where the glass electrode is non-operational and can be easily incorporated into existing devices. Interestingly a titration type curve is observed at pH 12.2 corresponding to a hydroxide concentration of 15 mM. At this point the peak height versus hydroxide concentration plot deviates from linearity and inspection of the nickel Pourbaix diagram reveals that as the pH has been changed the dominate nickel species becomes $Ni(OH)_3^-$. Further additions of hydroxide using the nickel-oxide screen-printed sensor were explored but were found to produce no response indicating the upper pH limit which is in accordance with previous studies using gold microelectrodes. [11]

5.3.1.4 CONCLUSION

This is the first reported literature of a screen-printed electrode bulk modified with nickel-oxide. The nickel-oxide screen-printed sensor has been explored towards the analytical quantification of hydroxide ions which was found to be analytically useful over the low micro-molar to milli-molar range. The disposable sensor is competitively comparable to current state-of-the-art arrays which employ ultra-microelectrode but is greatly simplified and cost effective, thus holds promise for hydroxide sensing and potential for the sensing of pH in aqueous solutions which is inaccessible for the standard glass pH electrode and may be incorporated into existing sensing devices as appropriate.

5.3.1.5 REFERENCES

1. R. J. Berman, G. D. Christian and L. W. Burgess, *Anal. Chem*., **1990**, 62, 2066.
2. L. R. Allain and Z. Xue, *Anal. Chem*., **2000**, 72, 1078.
3. T. A. Canada and Z. Xue, *Anal. Chem*., **2002**, 74, 6073.
4. K. De Wael and A. Adriaens, *Talanta*, **2008**, 74, 1562.
5. A. Abu-Rabi, D. Jasin and S. Mentus, *J. Electroanal. Chem*., **2007**, 600, 364.
6. H. Xu and O. A. Sadik, *Analyst*, **2000**, 125, 1783.
7. I. Ciani and S. Daniele, *J. Electroanal. Chem*., **2004**, 564, 133.

8. S. Daniele, C. Bragato, M. E. Abdelsalam and G. Denualt, *Anal. Chem*., **2002**, 74, 3290.
9. M. E. Abdelsalam, G. Denualt, M. A. Baldo, C. Bragato, S. Daniele, *Electroanalysis* (N. Y.), **2001**, 13, 289.
10. S. Daniele, M. A. Baldo, C. Bragato, G. Denualt, M. E. Abdelsalam, *Anal. Chem*., **1999**, 71, 811.
11. M. E. Abdelsalam, G. Denualt, M. A. Baldo, S. Daniele, *J. Electroanal. Chem*., **1998**, 449, 5.
12. O. Ordeig, C. E. Banks, T. J. Davies, F. Javier del Campo, F. X. Munoz, R. G. Compton, *Anal. Sci*., **2006**, 22, 679.
13. http://kanichi-research.com/.
14. R. O. Kadara, N. Jenkinson, C. E. Banks, *Electrochem. Commun*., **2009**, 11, 1377.
15. D. Giovanelli, N. S. Lawrence, L. Jiang, T. G. J. Jones, R. G. Compton, *Analyst*, **2003**, 128, 173, and articles cited therein.
16. N. A. Choudhry, D. K. Kampouris, R. O. Kadara, N. Jenkinson, C. E. Banks, *Anal. Methods*, **2009**, 1, 183.
17. R. O. Kadara, N. Jenkinson, C. E. Banks, *Electroanalysis* (N. Y.), **2009**, 21, 2410.

5.3.2 SOLID CARBON NANOROD WHISKERS: APPLICATION TO THE ELECTROCHEMICAL SENSING OF BIOLOGICALLY RELEVANT MOLECULES

5.3.2.1 INTRODUCTION

Carbon nanotubes (CNTs) are considered by many to be a novel class of nanomaterial, consequently having a profound impact on several diverse areas of science and technology, none more so than in electroanalysis and electrochemistry where their use has risen considerably.[1–10] The properties and applications that make carbon nanotubes of vast interest have been well summarised in the literature with many reviews having an electrochemical emphasis.[11] Structurally CNTs can be portrayed as ‘‘rolled up’’ sheets of graphene:[12] a single rolled sheet in the case of a single walled (SWCNTs) or concentric tubes fitted one inside the other in the case of multi-walled carbon nanotubes (MWCNTs).[13] It should also be noted that the way in which the graphene sheets are rolled influences the electronic properties of the CNTs. CNTs tender unique advantages including enhanced electronic properties, a large edge/basal-plane ratio, and rapid electrode kinetics.[4,14] Thus, CNT-based devices frequently display higher sensitivities, lower limits of detection, and faster electron transfer kinetics than traditional carbon electrodes.[14] Electrochemists have efficiently exploited CNTs, taking advantage of these distinctive properties to accelerate the electron transfer reaction involving a wide range of biomolecules and environmentally significant compounds such as proteins, nucleic acids, NADH, neurotransmitters, cytochrome c, cysteine and hydrazine compounds.[2] Several unique morphological variations of the MWCNTs are possible;[14] such as ‘‘hollow tube’’, ‘‘herringbone’’ or ‘‘bamboo-like’’ MWCNTs.[13] The divergence between these different MWCNT configurations is that herringbone and bamboo variants contain a proportionally higher number of edge-plane-like sites/defects when compared to that of the hollow-tube MWCNTs; this is owed, in these two cases, to the plane of the graphite sheet, which is at an angle to the axis of the tube, necessitating a high percentage of the graphite sheets to terminate at the surface of the tube. It

has been established that CNTs have two distinctive electrochemical reactive sites: basal-plane sites which occur along the side wall of the CNTs and edge-plane-like sites/defects at the open ends of the nanotube, certain variants may also include these edge-plane-like sites defects along the tubes axis.[13,15] The term basal- and edge-plane-like sites/ defects arise from a structural comparison with that of highly ordered pyrolytic graphite.[3] It has been established that it is these edge-plane-like sites/defects that are responsible for a large proportion of the chemical and electrochemical activity of the CNTs.[3–4,14] Carbon nanotubes can be produced from a range of methods such as via arc discharge,[16] laser ablation,[17] and most commonly, chemical vapour deposition (CVD).[18] Such fabrication processes unavoidably take advantage of a metal catalyst, resulting in the assembly of carbon nanotubes which contain metal impurities.[19] The notion that a homogenous material is attained is often a false one, even a small amount of heterogeneity in the sample can yield potentially erroneous results.[20] This has implications in producing sensors based on carbon nanotubes since the amount of metallic impurities can vary between samples, producing large divergences in the electrochemical response from sensor to sensor.[21] Thus mechanistic information is not easily de-convoluted as these trapped metallic impurities can result in the misinterpretation of the electrochemical origins of the heterogeneous charge transfer.[22] Conversely, technological advancements are dependent on the high purity of the carbon nanotube material. This difficulty can be overcome by using a novel solid-state production method, which can fabricate high-purity (99.99+%), metal-impurity-free MWCNTs, providing an obvious advantage over other commercially available carbon nanotubes.[22] Recently fabricated derivatives of carbon nanotubes are solid carbon nanorod ‘‘whiskers’’ formed through a Carbo-Thermal Carbide Conversion process.[23] A previous literature report has demonstrated a facile approach to quantifying the global coverage of the origin of electron transfer, *viz* edge-plane-like sites/ defects which were shown to be ~13% for SCNR

whiskers,[24] which is significantly more than standard, commercially available nanotubes.[24] Consequently in this paper, solid carbon nanorod (SCNR) whiskers are explored for the first time and electrochemically ‘‘benchmarked’’ with the model electrochemical systems of NADH, dopamine and uric acid.

5.3.2.2 EXPERIMENTAL

All chemicals used were of analytical grade and were used as received without any further purification and were obtained from Sigma-Aldrich. All solutions were prepared with deionised water of resistivity not less than 18.2 MΩ cm. Voltammetric measurements were carried out using a m-Autolab III (ECOChemie, The Netherlands) potentiostat. All measurements were conducted using a three electrode configuration comprising a screen-printed carbon working electrode (3.1 mm diameter), a carbon counter and a Ag/AgCl reference electrode. The manufacture of the screen-printed electrodes (SPEs) has been reported previously and the SPEs were shown to exhibit a heterogeneous rate constant of $\sim 1.7 \times 10^{-3}$ cm s^{-1} using the ferro/ferricyanide redox probe in 1 M KCl.[25] Basal-plane-like screen-printed electrodes were obtained commercially (Product: KS 520).[26] These sensors are on a flexible substrate consisting of a graphite working electrode (3.1 mm diameter), a carbon counter, and on-board silver/silver chloride reference electrode. These electrodes are basal-plane-like in nature with electron transfer rates of the order $\sim 10^{-4}$ cm s^{-1} as determined with potassium ferrocyanide/ 1M KCl.[26] Connectors for the efficient connection of the screen-printed electrochemical sensors were purchased from Kanichi Research Services Ltd.[26] Metallic impurity free SCNR ‘‘whiskers’’, formed through a Carbo-Thermal Carbide Conversion (CTCC) are commercially available. [23] Solid carbon nanorod whiskers were immobilised onto the electrode by dropping aliquots of a solid carbon nanorod whisker solution (25 mg/2 ml ethanol/water 50:50) onto the electrode surface which was allowed to

evaporate at room temperature. Fabrication and Characterisation of the SCNR whisker was conducted externally, data supplied by manufacturing company.

5.3.2.3 RESULTS AND DISCUSSIONS

A typical SEM image of the solid carbon nanorod (SCNR) whiskers is depicted in Figure (5.20) which shows cylindrical type structures with lengths in the order of 1–5 microns with a diameter of 20 nm to 1 mm. Closer inspection, as depicted in Figure (5.20), reveals that these are made up of highly 'kinked' bundles of nanorods.

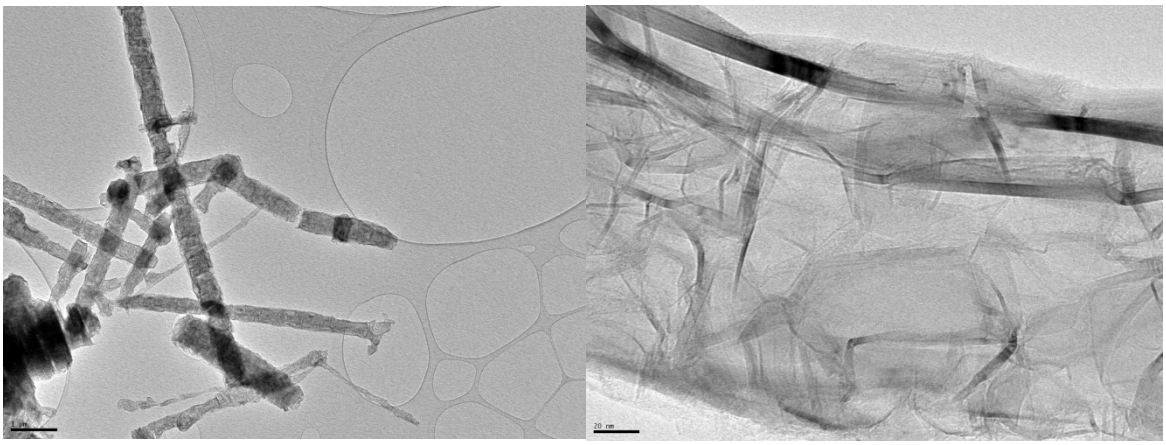

Figure 5.20 Typical SEM images of the SCNR Whiskers. Scales bars represent 1 µm (left) and 20 nm (right) on their respective images.

Raman Spectroscopy is arguably the most powerful analytical tool available for the study of nanophase crystalline allotropes of carbon such as carbon nanotubes.[27] There are 3 main features in the spectra of a CNT sample: the Radial Breathing Mode (RBM), the tangential mode (G band), and disorder induced mode (D band, G* band). Raman analysis of the SCNR whiskers, shown in Figure (5.21), (using a 785 nm laser excitation wavelength) exhibits sharp/well defined G peaks with a very large G* intensity and a smaller D : G ratio as compared with the commercial CNT material. The 785 nm excitation frequency allows

observation of two key features in SCNR morphology as compared with MWCNTs, alluding to the consistency and utility of the material. The first feature of note is the RBM vibrations, present at 115 and 170 cm^{-1}. Secondly, the D and G peaks are significantly narrower in width than commercial MWCNT materials, [22] indicating a homogeneous material, in particular the G band, highlighting the consistency of the SCNR whiskers. This is supported by the Thermogravimetric Analysis (TGA) data (see below). Peak locations vary with material dimensions and defect content and type, resulting in a smearing of multiple peaks into a single, broader peak present in commercial material. Thus greater consistency is evident in the material produced via the fabrication process by the G peak separation (into G+ and G2). This separation is a result of the variation in the elastic vibrations of the crystal structure in the direction of the rod axis, and that of the vibration tangential to the tube circumference. G-Band splitting is typically used in order to determine the chirality of individual CNTs. A typical spectrum is shown in Figure (5.21B) (magnification of Figure 5.21A) which demonstrates that the SCNR whiskers are highly consistent since isolation of individual structures is not necessary to obtain spectra in which G-Band splitting can be observed. The Raman data also show that SCNRs produced *via* CTCC are metallically conductive. Analysis of the purity (measured via ICP-MS) reveals a carbon mass % of 99.98 with an oxygen mass % of <0.05 and a silicon mass % of 0.01 indicating the complete absence of metallic impurities as is the case in other commercially available nanomaterials.[28] TGA has been used successfully in the past to study homogeneity and degree of functionalization of SWCNTs and MWCNTs.[29] In this paper, TGA is used to demonstrate the high degree of homogeneity. This is shown in Figure (5.22A) by the near zero loss of mass until approximately 550 °C and the peak in the derivative plot (Figure 5.22B) at 718 °C. Amorphous carbon content has the effect of shielding CNT electron transfer, effectively reducing the active electrode sites. This leads to reduced electrode efficiency.

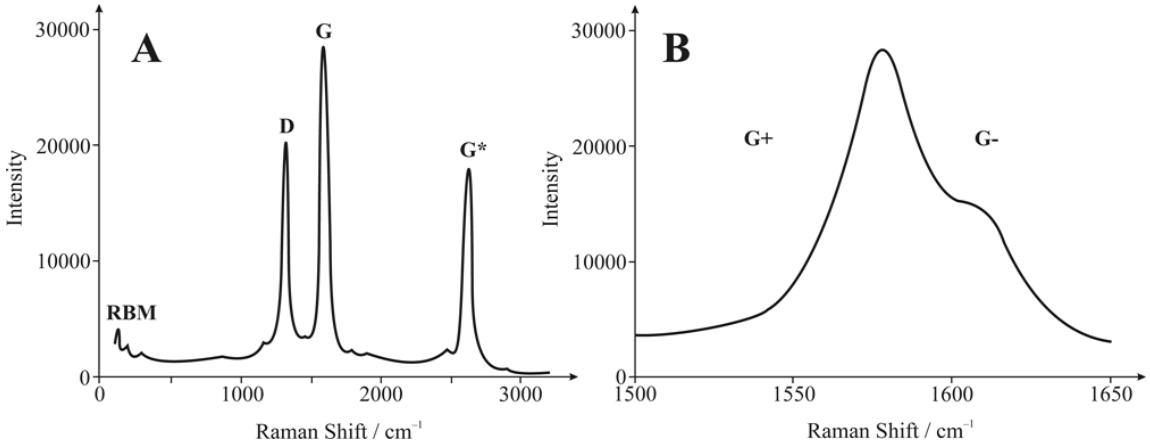

Figure 5.21 Typical Raman Spectra of SCNR Whiskers

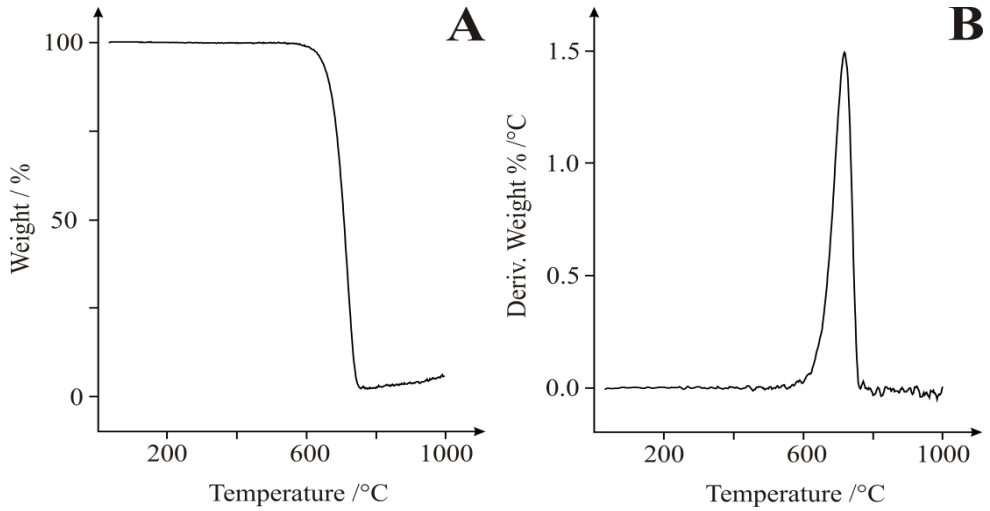

Figure 5.22 Thermal Gravimetric Analysis of SCNR whiskers between 0 and 1000°C at a rate of 10°C/min in air. A: Weight % vs Temp, B: Derivative weight % vs Temp.

The SCNR whiskers are a unique subset of single-walled carbon nanotubes (SWCNTs) and clearly as a result of the unique process have no residual transition metal catalyst is present in the final product making them ‘‘ultra-pure’’. In section 4.3, a facile methodology to allow the density of defects of carbon nanomaterials to be readily determined was presented [24] which demonstrated that this material had a high % of defects (*viz* edge-

plane-like sites defects) over that of commercially available MWCNTs. Consequently the suitability of this unique material toward the sensing of biologically relevant molecules is explored. IR spectra were obtained for the SCNR whiskers with the aim of distinguishing the functional surface groups present. Bands at 1625, 1759, 2850, 2920 and 3416 cm^{-1} were observed within the IR spectrum. Assignment of the band at 1625 cm^{-1} was accredited to the stretching of conjugated C–C bonds. The C=O stretching of aldehyde and ketone functional groups was present at 1759 cm^{-1} while the vibrations from the C–H bonds within alkyl groups contribute to the band shown at 2850 and 2920 cm^{-1}. Finally the intense band at 3416 cm^{-1} was assigned to the presence of O–H from either alcohol or phenol active groups.

Next the voltammetric performance of screen-printed electrodes (SPE) modified with 75 mg SCNR whiskers is considered and explored towards the electrochemical sensing of 1 mM NADH in a pH 7 phosphate buffer solution. Figure (5.23) depicts a large voltammetric oxidation wave exhibiting a peak at ~+0.148 V (at 0.1 Vs^{-1}) which is observed to shift to higher potentials upon increasing the scan rate. The response of the bare basal-plane-like-SPE is found to exhibit a voltammetric peak at ~+0.685 V (Figure 5.23A) which is as expected for an electrode with a low global coverage of edge-plane-like sites/ defects which is in agreement with previous studies of NADH on basal-plane pyrolytic graphite.[30] It is clear that the voltammetric peak in Figure (5.23B) lacks a diffusional tail suggesting thin-layer behaviour.[22]

Analysis of the data presented in Figure 5.23C in the form of Log *I*p vs. Log *v* should yield a gradient of 0.5 (δLog I_p/δLog v = 0.5) for a diffusional controlled process while δLog *I*p/δLog v = 1 for thin-layer behaviour. As shown in Figure (5.23C), a low scan rate results in a gradient (δLog I_p/δLog v) of 1 which is clearly substantially more than the expected gradient of 0.5 as governed by the *Randles–Ševćik* equation (as seen previously for multi-walled carbon nanotubes),[31] while high scan rates produce a gradient (δLog Ip/δLog v) of

0.5. This is compelling evidence to suggest that the mechanistic process is in fact moving from a thin-layer regime on longer timescales, to semi-infinite diffusion on shorter timescales, thus presenting a 'Catch 22' when it comes to interpretation of peak potentials for electron transfer rates since for a quasi-reversible system such as ours, one would ideally work at slow scan rates, however faster scan rates are required to avoid falling into the thin-layer regime. Therefore the response is clearly a contribution from both semi-infinite and thin-layer diffusion.

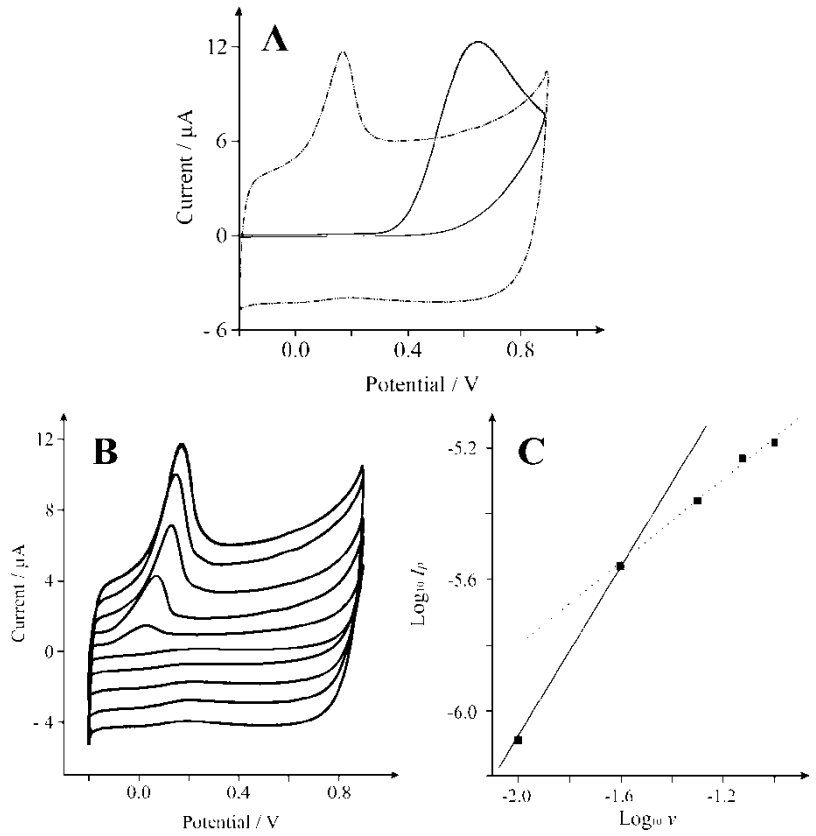

Figure 5.23 Typical cyclic voltammetric responses resulting from the electrochemical oxidation of 200µM NADH in pH 7 at A: SCNR whiskers (75µg) modified SPE (dot-dash) and a basal-plane-like electrode (solid line) recorded at a scan rate of 0.1 Vs^{-1}, B: SCNR whiskers (75µg) modified SPE recorded over the scan rate range of 0.01 to 0.1 Vs^{-1}. Part C depicts analysis of A in the form of Log_{10} Ip vs. Log_{10} v.

In the literature, it is common to explore the effect on the peak height as a function of added nano-material. To further explore this and to determine the optimum coverage of nanomaterial which exhibits the most beneficial electrochemical response, as commonly

undertaken in electroanalysis, the effect of increasing amounts of SCNR whiskers over the range 25 - 100µg was explored. A notable shift in the peak potential is clearly displayed, from +0.685 V as observed at the bare underlying electrode, to + 0.148 V (vs. Ag/AgCl) when 75µg of the SCNR whiskers is added (Figure 5.23A). At each mass addition of SCNR whiskers, the voltammetric peaks compared to the electrochemical oxidation was performed over a range of scan rates and analysed as a function of Log I_p vs. Log v. A plot depicting the response of this gradient as a function of the mass addition of SCNR whiskers is shown in Figure (5.24); clearly showing a thin-layer effect once a mass of 50µg or greater is utilized. No significant change in the electrochemical response (E_p/I_p towards NADH) was found between 75 and 100µg SCNR whiskers; this is attributed to the complete coverage of the electrode surface.

Table (5.1) depicts the peak potential (*E*p) for the observed voltammetric profiles of various carbon based electrode materials towards NADH. It is clear that the response of the SCNR whiskers exhibits a facile electrochemical response but on further investigations it is clear that this is actually due to a thin-layer response as identified above where the diffusional contribution has changed and thus cannot be directly compared to the response of EPPG, GC, and BPPG, as is commonly (misleadingly) undertaken in the literature. [31] The peak potential shifts with a function of coverage as the thin-layer behaviour dominates which is often mistaken for 'electro-catalysis'; clearly in comparing CNT modified electrodes, the coverage is critical. Additionally, a comparison across the literature is also misleading as it has been shown, there is a clear demonstration that *E*p varies with both scan rate (quasi-reversible electrode kinetics) and coverage, and thus a comparison without an explicit knowledge of which scan rate/coverage was employed is meaningless; this approach is rife within the scientific literature.

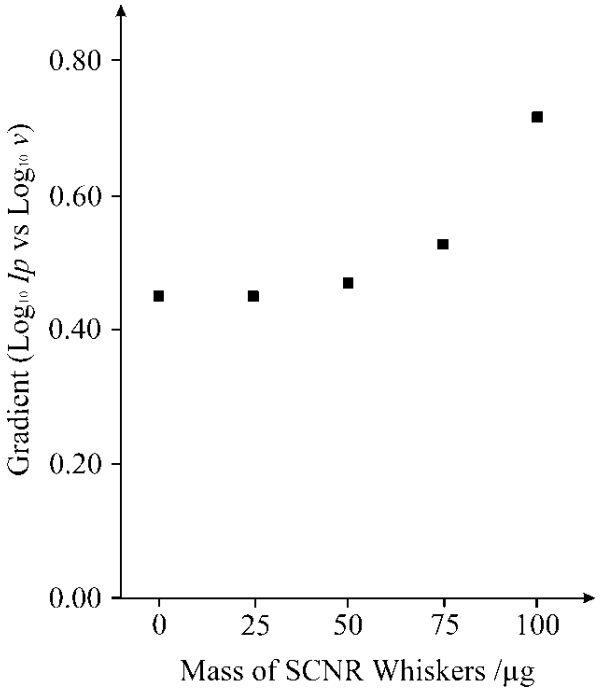

Figure 5.24 A plot depicting the response of the gradient (Log I_p vs. Log v) as a function of the mass addition of SCNR whiskers onto a basal-plane-like screen-printed electrode over the range 0-100µg.

Material	Ep/V (NADH)	Ref
SCNR Whiskers*	+0.148	Present work
BPPG	+0.81	[30]
EPPG	+0.50	[30]
CNT (MWCNT)*	+0.38	[30]
GC	+0.55	[30]
Basal-plane-like Screen-printed Electrode	+0.685	Present work

* Thin-layer behaviour

Table 5.1 Observed Peak potentials, Ep for the electrochemical oxidation of NADH using SCNR Whiskers and compared to other carbon based electrode materials in pH7 Buffer solution.

Returning to the electrochemical response in Figure (5.23), the electrochemical mechanism for NADH on carbon surfaces has been reported to be: [30]

$$NADH - e^{-} \rightarrow NADH^{\bullet+} \qquad (5.10)$$

$$NADH^{\bullet+} \rightarrow NAD^{\bullet} + H^{+} \quad (5.11)$$

$$NAD^{\bullet} - e^{-} \rightarrow NAD^{+} \quad (5.12)$$

where NADH is irreversibly oxidised through loss of an electron to produce radical $NADH^{+}$ equation (5.10), which then de-protonates to produce a neutral radical NAD equation (5.11). $NAD^{\bullet}$ is immediately oxidised to NAD^{+} at the electrode surface at the positive potential involved (typically 0.5V) as described by equation (5.12). $NAD^{\bullet}$ can also exchange an electron with the cation radical in the bulk solution.[30] It is highly likely that the same mechanism is apparent on the SCNR whiskers. Work by Pumera has shown that NADH binds onto carboxylic groups residing on carbon nanotubes[32] which limits their analytical utility. Recent work by Gorski [33] has shown that carbon nanotubes exhibit an oxidation peak at +0.38V which can be manipulated to ~0.04 V after being microwaved in nitric acid for 20 minutes. The reduction in overpotential was reported to be due to the mediation of NADH by redox active quinine groups. [33] In our case the peak potential of NADH occurs at a facile overpotential (+ 0.148 V, see Table 5.1) which is due to thin-layer diffusional processes, however it cannot rule out the additional contribution from surface oxygenated species (see earlier for characterisation) but likely the former is the greater contributor over that of the latter.

The electro-analytical performance of the SCNR whiskers towards the electrochemical sensing of NADH was examined next. Additions of NADH were made into a pH 7 buffer solution and as depicted in Figure (5.25), two linear regions are observed over the range of 20 to 65μM ($I_P/A = 6x10^{-8}$ A/μM – $9x10^{-7}$ A; $R^2 = 0.998$; $N = 4$) and 0.2 to 2.5mM ($I_P/A = 1x10^{-5}$ A/μM + $5x10^{-6}$ A; $R^2 = 0.995$; $N = 5$). Both ranges are analytically relevant and based on the former, a limit of detection (based on 3-sigma) is found to

correspond to 10µM (n = 3) which is in excellent agreement with previous studies on edge-plane pyrolytic graphite. [28]

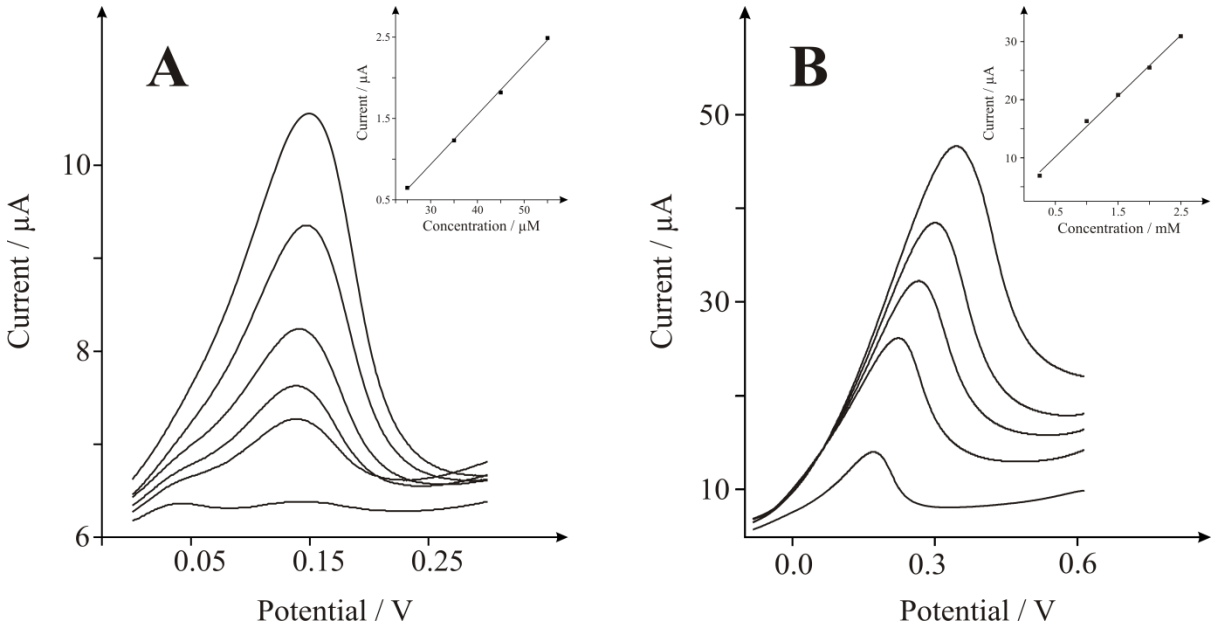

Figure 5.25 Cyclic voltammetric responses from the electrochemical oxidation of NADH A) 25-65µM B) 0.2-2.5mM at a solid carbon nanorods (SCNR) Whiskers (75µg) modified SPE in 0.1M PBS at pH 7 vs. Ag/AgCl at 0.1 V s^{-1}.

Next, attention was turned to exploring the response of the SCNR whiskers towards the electrochemical oxidation of dopamine (DP), an essential neurotransmitter that plays a crucial role within the central nervous, renal, hormonal, and cardiovascular systems. [34, 35] Neurotransmitters are chemical messengers, able to transmit signals from one neuron to the next. The determination of DP has therefore become of significant importance and the focus of much research. Fundamental investigation of its physiological function and improved diagnosis has resulted in an improved understanding of central nervous diseases, ensuing from atypical DP metabolism such as epilepsy, senile dementia, Parkinson and HIV infection

[36, 37]. Many studies of dopamine optimize its electrochemical detection in the presence of other commonly occurring neurochemical interferents such as uric acid (UA), which is the primary end product of purine metabolism [38] and often present in biological samples. Unusual levels of UA is a symptom displayed by several diseases such as hyperuricaemia, gout, and lesch-Nyhan disease [39], thus making its determination an important topic in clinic medicine. [38] As depicted in Figure (5.26), a voltammetric response is observed at -0.018 V (vs. Ag/AgCl) which increases with additions of dopamine. The observed peak potential compares well with + 0.42 V at commercially available SPE, [40] + 0.3 V at ionic liquid modified SPEs [40] and + 0.175 V reported for magnetic particle (MP)/SWCNT modified SPE. [41]

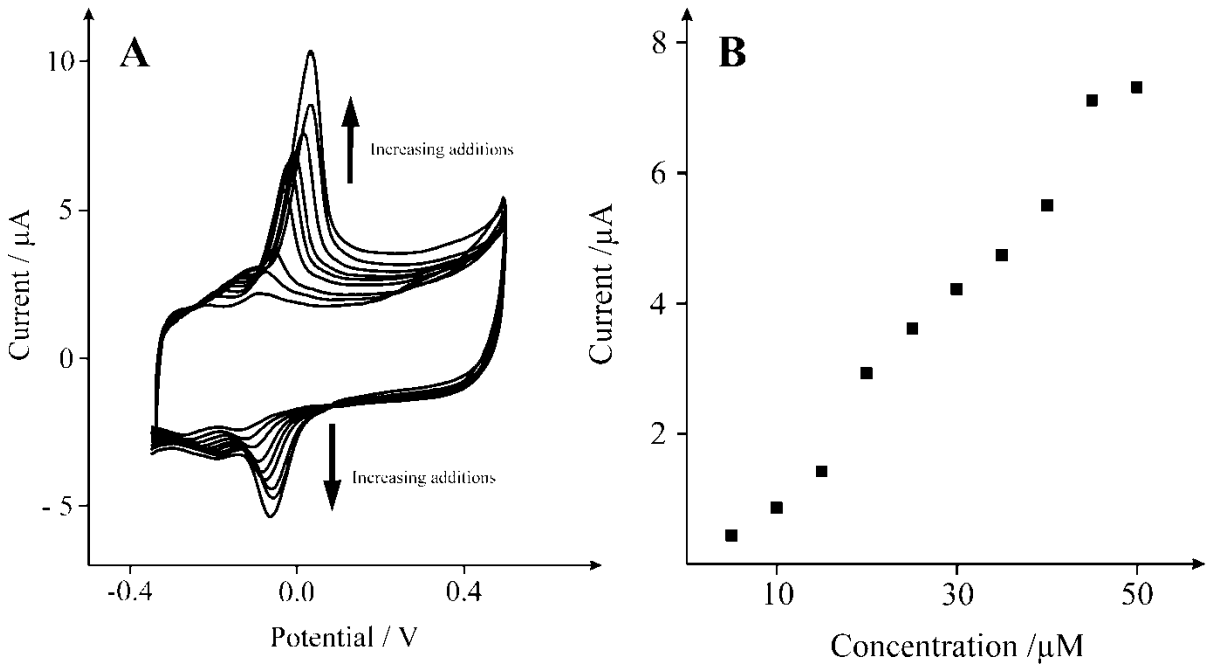

Figure 5.26 A: Typical cyclic voltammetric responses from the electrochemical oxidation of dopamine 10-50 µM at a solid carbon nanorods (SCNR) Whiskers (75 µg) modified SPE in 0.1M PBS at pH 7 vs. Ag/AgCl at 0.005 V s^{-1}. Part B depicts analysis of A in the form of concentration vs. peak height.

Inspection of the voltammetric profile reveals prominent oxidation and reduction waves at ~0.00 and ~–0.074 V (at 0.005 V s^{-1}) respectively. Figure (5.26B) shows the analytical response of dopamine at the SCNR whisker modified SPE in a pH 7 buffer solution over the range of 10 to 50 µM ($I_P/A = 6.5x10^{-9}$ A $\mu M^{-1} – 6.0x10^{-7}$ A; $R^2 = 0.985$; $N = 10$). A limit of detection (based on 3-sigma) is found to correspond to 3.8 µM (n = 3), which compares favourably with the reported detection of 1µM at SWCNTs via cyclic voltammetry. [42]

Figure (5.27) shows square wave analysis towards additions of dopamine over the range of 10 to 50 µM ($I_P/A = 7.3x10^{-8}$ A/µM $– 6.2x10^{-7}$ A; $R^2 = 0.953$; $N = 4$) at the SCNR whisker modified electrode, corresponding to a limit of detection (based on 3-sigma) of 7 µM (n = 3). Next the simultaneous sensing of dopamine and uric acid was explored which is required from an analytical sensing view point. As shown in Figure 5.27, a new voltammetric peak close to the voltammetric peak arising from the electrochemical oxidation of dopamine is observed at +0.120V with the inclusion of uric acid over the range of 20 to 120 µM ($I_P/A = 1.99x10^{-8}$ A/µM $– 3.54x10^{-7}$ A; $R^2 = 0.982$; $N = 4$), where a 16 µM limit of detection (based on 3-sigma) was calculated, showing that the SCNR whisker electrode exhibits superior sensing performance over traditional noble metal (Au/Pt) nanoparticle modified carbon electrodes, with a detection limit of 24 µM and 21 µM reported for dopamine and uric acid (UA) respectively. [43]

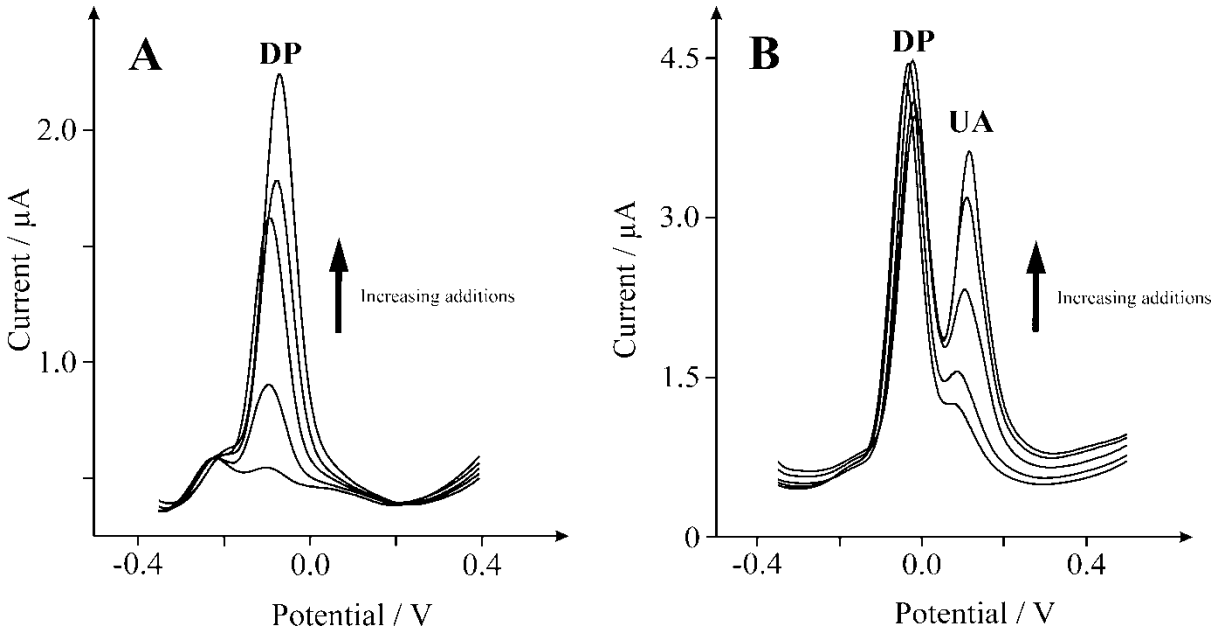

Figure 5.27 A: Typical square wave responses from the electrochemical oxidation of 10-50 µM dopamine (DP) in a 0.1M PBS at pH 7 (frequency: 25 Hz). Part B depicts the addition of Uric Acid (UA) 20-120 µM.

5.3.2.4 CONCLUSIONS

This work reports for, the first time, the electrochemical performance of SCNR whiskers (a derivative of carbon nanotubes) which exhibit metallic conductivity and are completely free from metallic impurities unlike other available CNTs which imposes limitations due to inter and intra data viability. The electrochemical properties of these unique carbon nanostructures have been explored towards the electrochemical and analytical quantification of NADH, uric acid and dopamine, which has found to be useful over the low micro-molar to milli-molar range. These nanomaterials show great promise for sensing biologically relevant molecules and are clearly advantageous due to their high purity and high proportion of edge-plane-like sites/defects and should be considered when designing electrochemical devices such as electro-analytical sensors.

1. J. J. Gooding, *Electrochim. Acta.*, **2005**, 50, 3049.
2. J. Wang, *Electroanalysis*, **2005**, 17, 7.
3. C. E. Banks, R. R. Moore, T. J. Davies, R. G. Compton, *Chem. Commun.*, **2004**, 16, 1804.
4. C. E. Banks, R. G. Compton, *Analyst*, **2006**, 131, 15.
5. R. R. Moore, C. E. Banks, R. G. Compton, *Anal. Chem.*, **2004**, 76, 2677.
6. M. Pumera, S. Sánchez, I. Ichinose, J. Tang, *J. Sens. Actuators. B.*, **2007**, 123, 1195.
7. A. Merkoçi, M. Pumera, X. Llopis, B. Perez, M. Del valle, S. Alegret, *S. Trends Anal. Chem.*, **2005**, 24, 826.
8. A. Fennimore, T. Yuzvinsky, T. D. Han, W.-Q. Han, M. S. Fuhrer, J. Cumings, A. Zettl, *Nature*, **2003**, 424, 408.
9. J. A. Misewich, R. Martel, Ph. Avouris, J. C. Tsang, S. Heinze, J. Tersoff, *Science*, **2003**, 300, 783.
10. G. G. Wildgoose, C. E. Banks, H. C. Leventis, R. G. Compton, *Microchin. Acta.*, **2006**, 152, 187.
11. X. Ji, R. O. Kadara, J. Krussma, Q. Chen, C. E. Banks, *Electroanalysis*, **2010**, 22, 7.
12. D. A. C. Brownson, C. E. Banks, *Analyst*, **2010**, 135, 2768.
13. B. Šljukić, C. E. Banks, R. G. Compton, *Nano Lett.*, **2006**, 6, 1556.
14. C. E. Banks, T. J. Davies, G. G. Wildgoose, R. G. Compton, *Chem. Commun.*, **2005**, 7, 892.
15. C. E. Banks, A. Crossley, C. Salter, S. J. Wilkins, R. G. Compton, *Angew. Chem. Int. Ed.*, **2006**, 45, 2533.
16. R. B. Mathur, S. Seth, C. Lal, R. Rao, B. P. Singh, T. L. Dhami, A. M. Rao, *Carbon*, **2007**, 45, 132.
17. A. P. Moravsky, E. M. Wexler, R. O. Loutfy, *Carbon Nanotubes*, **2005**, 65.
18. V. Ivanov, J. B. Nagy, Ph. Lambin, A. Lucas, X. B. Zhang, X. F. Zhang, D. Bernaerts, G. Van Tendeloo, S. Amelinekx, J. Van Landuyt, *Chem. Phys. Lett.*, **1994**, 223, 329.
19. T.-J. Park, S. Banerjee, T. Hermraj-Bennya, S. S. Wong, *J. Mater. Chem.*, **2006**, 16, 141.
20. M. E. Itkis, D. E. Perea, R. Jung, S. Niyogi, R. C. Haddon, *J. Am. Chem. Soc.*, **2005**, 127, 3439.

21. C. P. Jones, K. Jurkschat, A. Crossley, C. E. Banks, *J. Iranian Chem. Soc.*, **2008**, 5, 279.
22. C. P. Jones, K. Jurkschat, A. Crossley, R. G. Compton, B. L. Riehl, C. E. Banks, *Langmuir*, **2007**, 23, 9501.
23. www.scnte.com; accessed Jan 2011.
24. P. M. Hallam, C. E. Banks, *PCCP*, **2011**, 13, 1210.
25. R. O. Kadara, N. Jenkinson, C. E. Banks, *Sens. Actuators. B.*, **2009**, 138, 556.
26. http://kanichi-research.com; accessed Jan 2011.
27. A. Jorio, M. A. Pimenta, A. G. Souza Filho, R. Saito, G. Dresselhaus, M. S. Dresselhaus, *New J. Phys.*, **2003**, 5, 139.131.
28. M. Pumera, Y. Miyahara, *Nanoscale*, **2009**, 1, 260.
29. D. Bom, R. Andrews, D. Jacques, J. Anthony, B. Chen, M. S. Meier, J. P. Selegue, *Nano. Lett.*, **2002**, 2, 615.
30. C. E. Banks, R. G. Compton, *Analyst*, **2005**, 130, 1232.
31. I. Streeter, R. G. Compton, *Sen. Actuators. B.*, **2008**, 130, 620.
32. R. Scipioni, M. Pumera, M. Boero, Y. Miyahara, T. Ohno, *J. Phys. Chem. Lett.* , **2010**, 1, 122.
33. M. Wooten, W. Gorski, *Anal. Chem.*, **2010**, 82, 1299.
34. J. R. Cooper, F. E. Bloom, R. H. Roth, The biochemical basis of neuropharmacology. Oxford University Press, Oxford, **1982**.
35. P. Damier, E. C. Hirsch, Y. Agid, A. M. Graybiel, The substantia nigra of the human brain: II. Patterns of loss of dopamine containing neurons in Parkinson's disease. *Brain*, **1999**, 122, 1437.
36. J. W. Mo, B. Ogorevc, *Anal. Chem.*, **2001**, 73, 1196.
37. R. M.Wightman, L.J.May, A.C. Michael, *Anal. Chem.*, **1998**, 60, 769.
38. S-H Huang, H-H Liao, D-H Chen, *Biosens. Bioelectron.*, **2010**, 25, 2351.
39. V. V. S. E. Dutt, H. A. Mottola, *Anal. Chem.*, **1974**, 46, 1777.
40. J. Ping, J. Wu, Y. Ying, *Electrochem. Commun.*, **2010**, 12, 1738.
41. R. G. E. Baldrich, G. Gabriel, F. X. Muñoz, *Biosens. Bioelectron.*, **2011**, 26, 1876.
42. C. B. Jacobs, M. J. Peairs, B. J. Venton, *Analytica Chim. Acta.*, **2010**, 662, 105.
43. S. Thiagarajan, S. M. Chen, *Talanta*, **2007**, 74, 212.

6.1 NANOPARTICLES

Metal nanoparticles, shown to enhance the electro-catalytic response of the electrode surface at which they are incorporated, are extensively used in the modification of carbon-based electrodes. The use of nanoparticles, principally with the use of precious metals, substantially reduces the overall cost of the electrode compared to that of a solid electrode comprised of the same material (e.g. Au/Pt electrodes). Their high surface area, along with the small volume of material required for effective coverage of the electrode surface (see chapter 5) offers beneficial characteristics in a variety of electrochemical applications. Note; nanoparticles are intended solely for the modification of a working electrode's surface and not as a replacement for the electrode material itself. The observed electrochemical and electro-catalytic behaviour observed at the modified electrode is a combination of both the bulk electrode material and nanoparticles present at its surface, though the prevailing characteristics may reflect those typical to the latter.

6.2 DEVELOPMENT OF SCREEN-PRINTED HYBRID SUPERCAPACITORS USING TRANSITION METAL MODIFIED ELECTRODES

This section describes work [1,2] undertaken during this thesis. Firstly a simplistic approach for the synthetic fabrication of iron oxide (Fe_3O_4) particles is presented and their potential application towards energy-storage (as an electrode material within a supercapacitor) is explored. The Fe_3O_4 asymmetric supercapacitor is found to deliver a maximum specific capacitance of ~120 F g^{-1} at a current density of 0.1 A g^{-1} in an aqueous electrolyte solution (3M KOH) retaining 93.70 % of its initial capacity over 1000 cycles. Additionally an iron-based hydrogen-superoxide (FeO(OH)) supercapacitor is readily

fabricated which is found to exhibit a maximum specific capacitance of ~400 F g^{-1} at a discharge current of 0.1 A g^{-1} in a 3M KOH solution.

Secondly, cobalt hydroxide (β-$Co(OH)_2$) thin-film supercapacitors are developed for the first time via screen printing and their potential application towards energy-storage (as an electrode material within a supercapacitor) explored. The highly uniform, porous nanostructures were synthesized via a novel, hydrothermal, template-free approach. The nanostructures consist of amassing, arbitrarily layered, interconnecting nanosheets, resulting in a flower-like structure with many fissures. These nanostructures were fabricated into flexible thin-film supercapacitors via screen printing for the first time. The β-$Co(OH)_2$ asymmetric supercapacitor is found to deliver a maximum specific capacitance of ~170 F g^{-1} at a current density of 0.5 μA in an aqueous electrolyte solution (3M KOH) retaining 99.69% of its maximum capacity over 600 cycles. Given the ability to mass produce such supercapacitors via screen printing, where readily, synthetically fabricated nanostructures can be incorporated, the application of this approach will likely be widely implemented.

*Dr Kampouris and Dr Kadara from the Banks research group were consultants during these projects. Material characterisation was performed by Maria Gómez-Mingot at the University of Alicante. Prof Ji provided the cobalt nanomaterial and characteristic analysis data. Mr Houssein worked in collaboration, under my supervision during the latter project.

---

1. P. M. Hallam, M. Gómez-Mingot, D. K. Kampouris, C. E. Banks, *Facile synthetic fabrication of iron oxide particles and novel hydrogen superoxide supercapacitors, RSC Advances,* **2012**, 2 (16), 6672.

2. X. Ji, P. M. Hallam, S. M. Houssein, R. O. Kadara, L. Lang, C. E. Banks, *Printable thin film supercapacitors utilizing single crystal cobalt hydroxide nanosheets*, *RSC Advances*, **2012**, 2 (4), 1508.

6.2.1 A SIMPLE SYNTHETIC FABRICATION OF IRON OXIDE PARTICLES AND NOVEL HYDROGEN SUPEROXIDE SUPERCAPACITORS

6.2.1.1 INTRODUCTION

In response to the increasing energy needs of modern society and the emerging ecological concerns, it has become essential to find new, alternative and innovative energy-storage systems, where it has become apparent that conventional technologies (batteries and electrolytic capacitors) are not capable of providing efficient solutions for new market applications.[1,2] Supercapacitors (also called electrochemical capacitors or ultracapacitors), [3,4] are considered the most promising candidate and one of the newest innovations in electrical energy-storage. These devices have gained significant interest of late,[2,5] exhibiting desirable characteristics such as low equivalent series resistance (ESR), long charge/discharge life, and several orders of magnitude higher power density (able to store and deliver energy at relatively high rate, beyond those accessible by a typical battery). [6,7] Furthermore, the deficiencies of other power sources, for example fuel cells, could be complemented by the inclusion of supercapacitors.[8]

Depending on the fundamental mechanisms that presides over the capacitance, supercapacitors can be placed into one of two types: 1) Electrical double layer capacitor (EDLC), where the capacitance arises from the accumulation of ionic charges at the electrode-electrolyte interface, where a high surface area (carbon-based material) is favourable,[9-11] 2) Redox capacitors, where a reversible Faradaic reaction of the electro-active species (like an actual battery) occurs leading to the pseudo-capacitance, typically conducting polymers and metal oxides belong to this kind of capacitance material, [12-14] (see Chapter 3). Carbon, in its various forms, [3,15-22] has been extensively used as an electrode material within supercapacitors, with the intent of attaining high specific capacitance, together with high power densities. Bauer *et al.* investigated the electrochemical and

capacitative properties of basal and edge-planes, utilizing ordinary pyrolytic graphite, demonstrating capacitance values of 12 and 60 μF/cm^2 for cleaving (basal) and polishing (edge), respectively.[23] The capacitance contributed by the basal-planes can be characterised as a space charge at its interface, behaving like the ionic diffuse-layer capacitance shown in metal-electrolyte systems. [7] Exposed edge-plane-like defects display characteristic behaviour similar to those found at a metal/solution interface where the capacitance is determined by a combination of ionic/electronic Helmholtz compact-layer capacitance and ionic diffuse-layer capacitance, thus exhibiting a significantly larger capacitance.[7] Therefore, the contribution from the ionic/electronic Helmholtz compact-layer towards the total capacitance is positively larger than that from the ionic diffuse-layer capacitance. This is attributed to the edge-planes providing a larger number of adsorption sites and a larger surface charge, which is responsible for the increased capacitances. In contrast, basal-plane offers fewer adsorption sites and a decreased surface charge, generating smaller capacitance values.

While porous carbon materials exhibit a high specific surface area, its low conductivity limits its application in high power density supercapacitors.[24] Carbon nanotubes (CNTs), with excellent electrical conductivity have been incorporated into supercapacitors for over a decade. [15,20,24,25]

However, CNT-based supercapacitors have been unable to realise their expected performance; likely due to the observed contact resistance between the electrode and current collector,[22,26] resulting in many studies turning their attention to the morphology of the carbon materials in order to boost the performance of the capacitor.[19,20,22,26-28] Recently, a significant amount of research has focused on hybrid supercapacitors because of their high working voltage and energy density.[2] Thus far, various transition metal oxides, such as RuO_2, CoO and IrO_2, [29-31] have been reported to be used as pseudo-capacitance electrode materials. However, application of these oxides has been hindered by their high cost. It is

therefore essential to find a low-cost pseudo-capacitance material as the main focus in supercapacitor research. Inexpensive and innocuous, iron oxides demonstrate significant potential to undertake this challenge. Earlier studies using Fe_3O_4 as supercapacitors electrodes have displayed relatively low capacitance values, ranging between 60 and 80 F g^{-1}, [32,33] owed mainly to its low electrical conductivity to enable effective ion diffusion.[34] Blending Fe_3O_4 to form composites with conductive phases, *e.g.* carbon nanotubes, has shown to effectively increase the overall capacitance two fold.[35]

In this work, two new facile methodologies towards the formation of carbon/iron oxide composite supercapacitors are reported. Additionally a method where iron oxide particles are synthesised *in-situ* in the presence of carbon, producing capacitance values exceeding those of carbon oxygenated/oxidised modified electrodes or Fe_3O_4 carbon modified electrodes is presented.

The assembly process of supercapacitors should be inexpensive and high-throughput, just like batteries. Supercapacitors can be made flexible with sheet-like structures, which are light-weight. Costly and expensive methods exist but are not appropriate to be used to make millions of supercapacitors. State-of-the-art flexible thin-film supercapacitors based on sprayed networks of single-walled carbon nanotubes (SWCNTs) have been constructed, producing a device that displays very high energy (6 Wh kg^{-1}). [36] These results demonstrate the underlying potential of printable thin film supercapacitors. Despite this scientific advance towards semi-printable/production supercapacitors, there have been limited reports using printing processes for fabricating flexible supercapacitors; to the best of our knowledge there have been little or no reports of using true screen printing despite its inherent advantages.[37,38]

Innovative and unique electrochemical designs can be readily produced via screen printing by designing and producing screens which derive the geometry and thickness of the screen-printed material, typically graphite but it can be applied to other novel materials [37]. This paper presents the utilization of screen printing as a new methodology to fabricating flexible and reproducible supercapacitors with high surface areas and minimal wasted space with respect to geometric arrangement and in terms of multiple printing. The benefit of this methodology is that it can be readily scaled up and economical, producing reproducible surface shapes and thicknesses, something which is currently lacking in this area. Ultimately this results in a reduction of both the weight and resistance of the printed electrodes via the elimination of the interface between the charge collectors and working electrodes, leading to higher power density.

6.2.1.2 EXPERIMENTAL

All chemicals used were of analytical grade and were used as received without any further purification and were obtained from Sigma-Aldrich. All solutions were prepared with deionised water of resistivity not less than 18.2 MΩ cm.

Voltammetric measurements were carried out using a μ-AutolabIII (ECO-Chemie, The Netherlands) potentiostat. All measurements were conducted using a three electrode configuration comprising a screen-printed carbon working electrode (9 mm diameter), a carbon counter and a Ag/AgCl reference electrode. The manufacture of the screen-printed electrodes (SPEs), using a layered stencil system as described in previously, has been reported previously and shown to exhibit a heterogeneous rate constant of ~6.2 $\times 10^{-5}$ cm s^{-1} using the ferro/ferricyanide redox probe in 1M KCl.[39] Basal-plane-like screen-printed substrates were obtained commercially (Product: KS 540) [40]. This flexible substrate consists of a graphite working electrode (3.1 mm diameter), a carbon counter, and onboard

silver/silver chloride reference electrode. These electrodes are basal-plane-like in nature with electron transfer rates of the order ~10^{-4} cm s^{-1} as determined with potassium ferrocyanide / 1 M KCl. [39] Connectors for the efficient connection of the screen-printed substrate were purchased from Kanichi Research Services Ltd. [40] Iron oxide particles were immobilised onto the screen-printed electrode by dropping a 25 µl aliquot of the iron solution (1mL 1000 ppm $FeCl_3$ /3 mL hydrogen peroxide) onto the electrode surface which was allowed to evaporate at room temperature.

Scanning electron microscope (SEM) images and surface element analysis were obtained with a JEOL JSM-5600LV model. X-ray photoelectron spectroscopy (XPS, K-Alpha, Thermo Scientific) was used to analyze the filter surface. All spectra were collected using Al-K radiation (1486.6 eV), monochromatized by a twin crystal monochromator, yielding a focused X-ray spot with a diameter of 400µm, at 3 mA × 12 kV. The alpha hemispherical analyser was operated in the constant energy mode with survey scan pass energies of 200 eV to measure the whole energy band and 50 eV in a narrow scan to selectively measure the particular elements. Thus, XPS was used to provide the chemical bonding state as well as the elemental composition of the filter surface. Charge compensation was achieved with the system flood gun that provides low energy electrons and low energy argon ions from a single source. These analyses were performed on my behalf at the University of Alicante. Diamond ATR-FTIR analysis of the electrode surface was conducted using a Thermo Scientific Nicolet 380 FT-IR Spectrometer.

6.2.3 RESULTS AND DISCUSSION

Alkaline synthesis

It is widely accepted that Fe_3O_4, effectively 'rust' has an orthorhombic structure comprising of iron in two different oxidation states, Fe^{2+} and Fe^{3+}, in a ratio of 1:2

respectively which has been reported to produce relatively high specific capacitances ranging from 27 to 80 F g^{-1}. [32,33,41]

The initial approach is the alkaline synthesis of iron oxide (Fe_3O_4) where both Fe^{2+} and Fe^{3+} are incorporated into the microcrystal structure. Ferric chloride, $FeCl_3$ is dissolved into distilled water (1000 ppm, 1 mL), to this, a mixture of hydrogen peroxide (30 %, 5 mL) and sodium percarbonate (0.005 g) was added. Ferric ions (Fe^{2+} and Fe^{3+}) are produced via the catalytic decomposition of hydrogen peroxide as described by the following scheme: [42]

$$2Fe^{3+} + H_2O_2 \rightleftharpoons 2Fe^{2+} + 2\,H^+ + O_2 \quad (6.1)$$

$$2Fe^{2+} + H_2O_2 + 2H^+ \rightleftharpoons 2H_2O + 2Fe^{3+} \quad (6.2)$$

The overall reaction of (6.1) and (6.2) can be summarised as:

$$2\,H_2O_2 \overset{Fe^{3+}}{\rightleftharpoons} 2\,H_2O + O_2$$

Due to the strong alkaline conditions created via the inclusion of sodium percarbonate, simultaneous precipitation of ferric and ferrous hydroxide, $Fe(OH)_2$ and $Fe(OH)_3$ respectively, takes place as described via equations (6.3) and (6.4). The K_{SP} of $Fe(OH)_2$ and $Fe(OH)_3$ is 1.8×10^{-15} and 6×10^{-38}, respectively. [43] The K_{SP} values gives an indication to the order of reaction, to begin with Fe^{3+} precipitates as $Fe(OH)_3$, consequently changing the acidity of the solution. When the K_{SP} value for $Fe(OH)_2$ is satisfied, the remaining Fe^{3+} reduced to Fe^{2+} by the hydrogen peroxide, instantly forms the metal oxide.

$$Fe^{2+} + 2OH^- \rightleftharpoons Fe(OH)_2 \quad (6.3)$$

$$Fe^{3+} + 3OH^- \rightleftharpoons Fe(OH)_3 \quad (6.4)$$

The aqueous solution is then allowed to evaporate, permitting the formation of Fe_3O_4 in the presence of excess hydrogen peroxide (3 mL) as shown in equation (6.5).

$$2\ Fe(OH)_3 + Fe(OH)_2 \overset{H_2O_2}{\rightleftharpoons} Fe_3O_4 + 4H_2O \qquad (6.5)$$

The synthesised iron structures are suspended in ethanol and immobilised upon the working surface of the SPE. SEM imaging (Figure 6.1) clearly depicts the structure of the Fe_3O_4 particles which, following immobilisation, exhibits unique rectangular features, typically 20 µm in size.

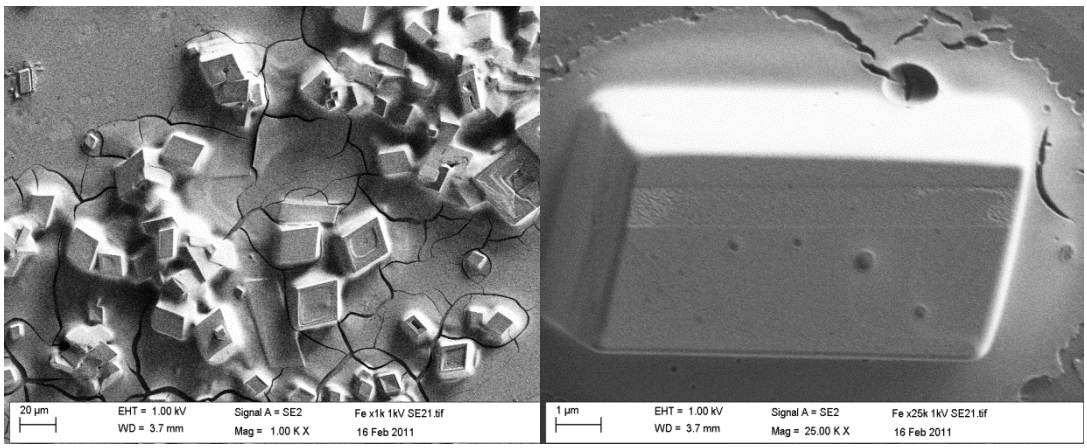

Figure 6.1 Typical SEM images of the iron oxide (Fe_3O_4) particles immobilised upon the surface of a carbon screen-printed electrode.

Acidic synthesis

The acidic synthesis of iron oxide is similar to the alkaline synthesis. Ferric chloride, $FeCl_3$ dissolved in distilled water (1000 ppm, 1 mL) and the addition of hydrogen peroxide (30 %, 5 mL) resulting in the catalytic decomposition of ferric ions as described by equation (6.1). The hydrolysis of water, described below, leads to the eventual formation of ferric hydroxide (equation 6.6): [42]

$$H_2O \rightleftharpoons H^+ + OH^-$$

$$Fe^{3+} + 3\ OH^- \rightleftharpoons Fe(OH)_3 \text{ (colloidal, yellow)} \quad (6.6)$$

As mentioned previously, $Fe(OH)_3$ has a very low K_{SP} value, typically 6 x10^{-38}.[43] In strong acidic conditions, typically at a pH value of 1, the concentration of the hydroxide ions are 10^{-13} M and with a high concentration of ferric ions present, precipitation of ferric hydroxide occurs since $[Fe^{3+}][OH^-]^3 > K_{SP}$. Noting that ferric chloride has a reported solubility of approximately 92 g/100 mL in water [44] resulting in the exclusive precipitation of $Fe(OH)_3$ despite the high concentrations of chloride ions. Only a infinitesimally small amount of iron is required. Through evaporation, the H^+ ions will form hydrochloric (HCl) gas, consequentially reducing the acidity and thus increasing the concentration of hydroxyl ions $[OH^-]$, satisfying the K_{SP} prerequisite, ensuing the precipitation of $Fe(OH)_3$. Due to the limitation of available iron, a colloidal solution is readily formed. This solution containing colloidal ferric hydroxide is simply dried upon a hot plate and reacts further following the addition of excess hydrogen peroxide (30 %, 3 mL), undergoing the following mechanism:

$$Fe(OH)_3 \overset{H_2O_2}{\rightleftharpoons} FeO(OH) + H_2O \quad (6.7)$$

Aliquots of this solution are then dispersed on the surface of a screen-printed electrode and allowed to dry at room temperature. Thermal decomposition as described in equation 6.8, is avoided since this requires elevated temperatures (~300 ºC), far higher than those employed here, confirming no undesirable degradation of $Fe(OH)_3$ in our synthetic methodology, since Fe_2O_3 has a poor specific capacitance (as determined above).

$$2\ Fe(OH)_3 \rightleftharpoons Fe_2O_3 + 3\ H_2O \quad (6.8)$$

As shown above (equation 6.7) the addition of excess hydrogen peroxide to the precipitated ferric hydroxide leads to the formation of ferric hydroperoxide (FeO(OH)), and, as shown on page 193, is found to have a significantly higher capacitance compared to that of Fe_2O_3.

Characterisation of material

Characterisation and interpretation of the results was performed by Maria Gómez-Mingot at the University of Alicante. The surface electronic states and the chemical composition of the iron products were examined by X-ray photoelectron energy spectroscopy (XPS). The XPS analysis curve (Figure 6.2) reveals the presence of Fe, C and O with the binding energies of the Fe^{2+} $2p_{3/2}$ and Fe^{3+} $2p_{3/2}$ states located at 711.7 and 713.9 eV respectively. This is in excellent agreement with the values illustrated in the literature,[45] establishing substantial evidence towards a structural configuration of Fe_3O_4 and FeO(OH). The first structure of Fe_3O_4 is emphasized by the Fe $2p_{3/2}$ main peak including two satellite peaks on the higher binding-energy side, (718.8 and 733.1 eV) indicating the Fe ion is in a divalent state. [46] The contribution at 725.6 and 727.6 eV are transition peaks due to Fe $2p_{1/2}$ and are associated with the main peaks of Fe $2p_{3/2}$ at 711.7 and 713.9 eV, respectively. The binding energy of the O 1s states at 530.6 eV is presumably coupled to Fe_3O_4, [47] while the peaks at 532.1 eV and 534.4 eV are consistent with the binding energies previously allied to the presence of R–O and O–H bonds associated with FeO(OH) [48] and $Fe(OH)_3$. [46] Additionally, the binding energies of the C 1s states at 286.6 eV and 289.2 eV confirm the presence of C-O, and C=O.

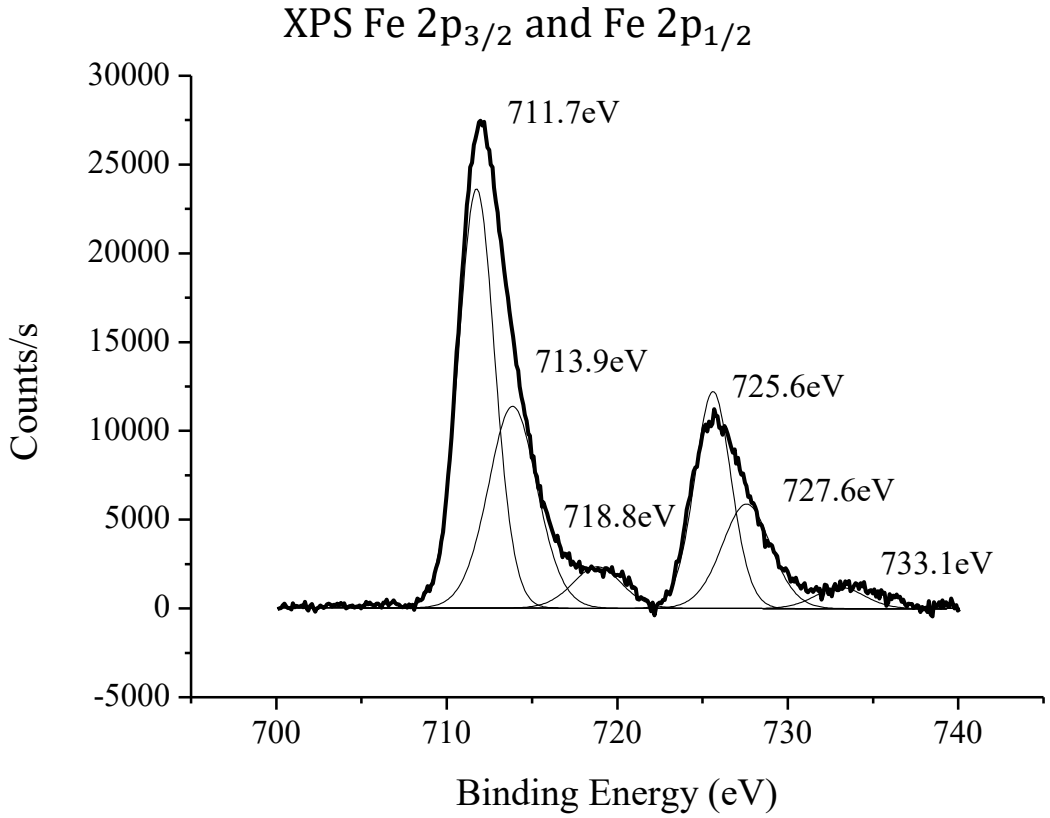

Figure 6.2 XPS spectrum of the iron oxide (FeO(OH)) product.

To substantiate this, the difference IR spectra were obtained by subtracting the spectra for a standard carbon/graphite screen-printed electrode from that of the hydrogen-superoxide screen-printed electrodes after treatment, to distinguish the new surface functional groups responsible for the observed capacitance values. New bands at 1006, 1267, 1394, 1562, and 2984 were observed within the IR spectrum (Figure 6.3). Assignment of the band at 1006 cm^{-1} and 1267 cm^{-1} was accredited to the stretching of C–O bonds typically associated with alcohols and carboxylic groups respectively. The C=O stretching of carboxylic functional groups was present at 1562 cm^{-1} while the vibrations from the bending of O–H bonds within carboxylic groups contributes to the band shown at 1394 cm^{-1}. These two bands agree well with the binding energies found within the XPS spectra. Finally the broad, shallow band at 2984 cm^{-1} was assigned to the presence of O–H offered by carboxylic groups. The large trailing shoulder in partnership with this band is compelling evidence that supports the

presence of alcohols. XRD was attempted but due to the lack of crystallinity, no substantive information could be obtained.

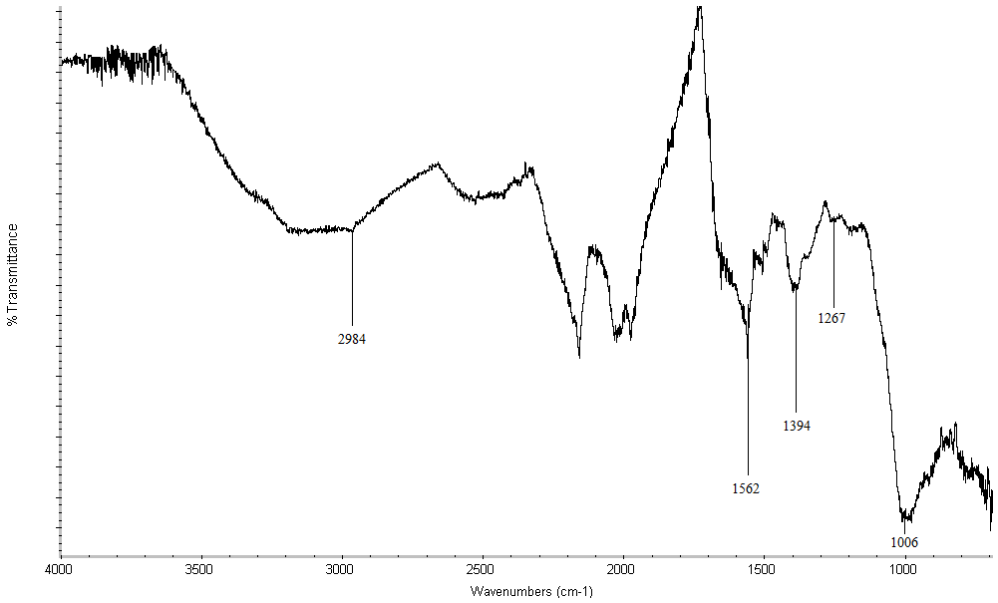

Figure 6.3 IR spectrum of the iron oxide (FeO(OH)) modified screen-printed electrode.

Capacitance Measurements

Supercapacitors are not dissimilar to a battery in their fabrication in that there are two electrodes immersed in an electrolyte, with an ion permeable separator situated amidst the electrodes. Double-layer capacitors exploit a combination of high surface-area with exceptionally small charge separation to generate their extremely high capacitance.[49] In such a device, the interphase between an electrode and the adjacent electrolyte (which facilitates a build-up of charge separated over a minute distance) constitutes a capacitor; therefore a complete cell can be represented as two capacitors in series. Specific capacitance reported in literature is often derived from both cyclic voltammetry and galvanostatic charge-discharge methods using a three-electrode system that includes a reference and counter electrode. [50]

First, the voltammetric performance of the Fe_3O_4 modified SPE hybrid supercapacitor (Figure 6.4A) in a 3 electrode-cell, with a Fe_3O_4 modified carbon working and carbon counter

electrode in a 3M KOH solution, between -1.0 and +1.0 V at a scan rate of 0.02 V s^{-1} (vs Ag/AgCl) is examined. This was considered a suitable test to determine the mechanistic process of the reaction (Faradaic and non-Faradaic). Figure 6.4A displays a predominantly rectangular shaped CV curve, strongly resembling the characteristics of electrochemical double-layer, frequently observed for carbon-based materials but also Faradaic pseudo-capacitance, evident from the oxidation waves at ~0.4 V, often associated with metal oxides and likely attributed to the reaction mechanisms shown in 6.9 and 6.10: [51]

$$Fe_3O_4 + 4\ H^+ \rightleftharpoons 2\ Fe^{3+} + \ Fe^{2+} + 4\ OH^- \quad (6.9)$$

$$Fe^{2+} \rightleftharpoons \ Fe^{3+} + e^- \quad (6.10)$$

A typical charge-discharge plot for the Fe_3O_4 supercapacitor is depicted in Figure 6.4. The hybrid supercapacitor exhibits good electrochemical capacitance performance, demonstrated by a linear variation of the voltage during the charging-discharging process as observed in Figure (6.5).

The specific capacitance of the supercapacitor can be determined from the charge/discharge test, using with the following equation: [2]

$$C_m = \frac{I\,\Delta t}{\Delta V\ m} \quad (6.11)$$

where C_m is the specific capacitance of the capacitor (F g^{-1}), I is the current of the charge-discharge, Δt is the discharging time period in seconds for the potential ΔV, in volts and m is the mass load of the active materials (including the positive and negative electrode).

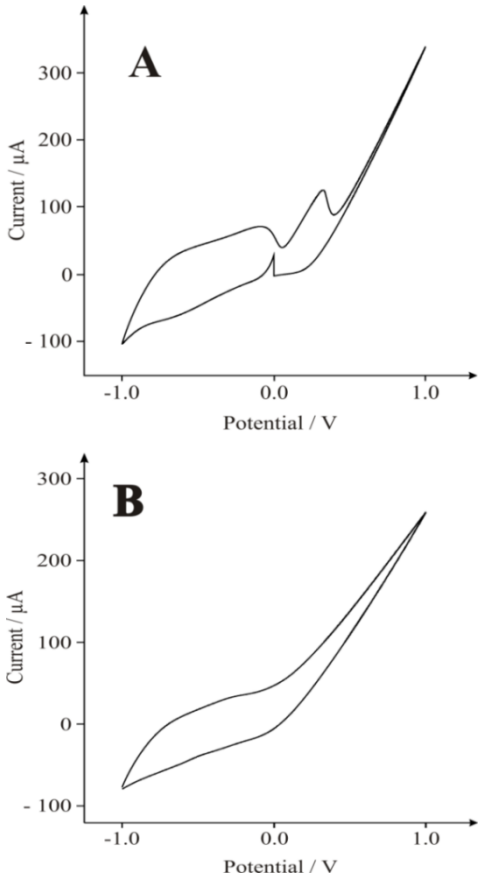

Figure 6.4 Typical voltammetric signatures of (A) Fe_3O_4 (start point 0.0 V) and (B) FeO(OH) modified screen-printed electrodes, recorded in a 3M KOH solution at a scan rate of 0.02 V s^{-1} (vs. Ag/AgCl).

Electrodes modified with Fe_2O_3 (α configuration - obtained commercially) offered low specific capacitance, which (in our case) was found to have a specific capacitance of ~6 F g^{-1} in 3M KOH at a discharge current of 0.1 Ag^{-1}, however the specific capacitance of the Fe_3O_4 supercapacitor was calculated to be ~120 F g^{-1} at a discharge current of 0.1 A g^{-1}. This is a significant improvement over previously recorded values for Fe_3O_4 based supercapacitors, [41] and easily comparable to the capacitance achieved by Fe_3O_4 composite (MWCNT) supercapacitors [52] which typically exhibits values of 27 and 165 F g^{-1} respectively. Reliability of the capacitance measurements was investigated through the deposition of increasing quantities of active material on the surface of the screen-printed electrode; where a direct correlation between the mass and capacitance is evidently observed (Figure 6.6). The cyclic performance of the hybrid supercapacitor is impressive, retaining 93.7 % of its initial capacity over 1000 cycles as shown in Figure (6.7), indicating the

stability and suitability of the Fe_3O_4 particles for high-performance supercapacitor applications.

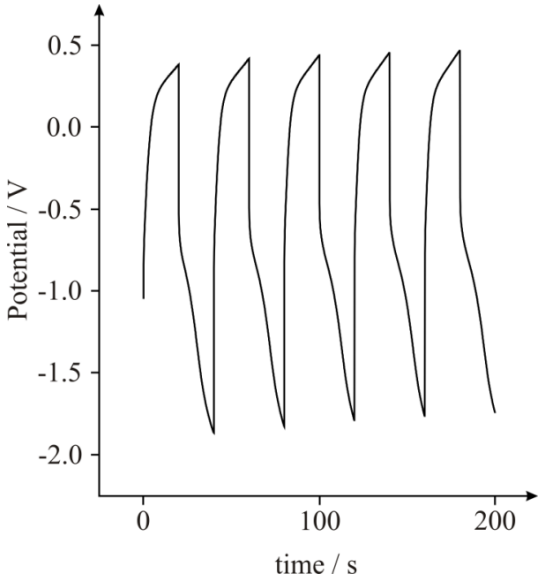

Figure 6.5 Typical galvanostatic charge-discharge of a Fe_3O_4 modified screen-printed electrode; 5 cycles over 200 seconds in a 3 M KOH solution at 0.1 A g^{-1}.

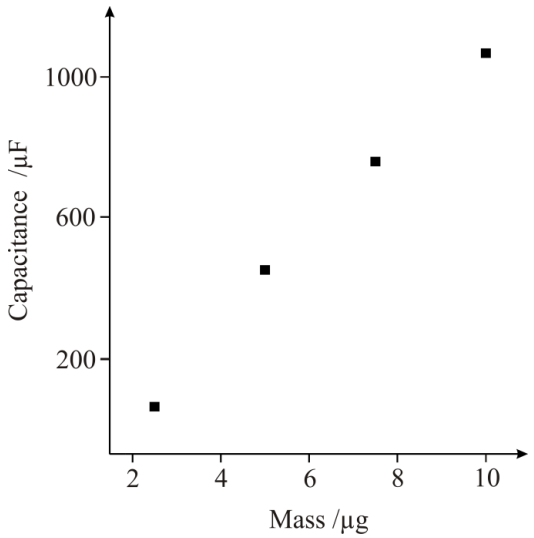

Figure 6.6 Plot of Capacitance (µF) vs. mass (µg) of Fe_3O_4 deposited.

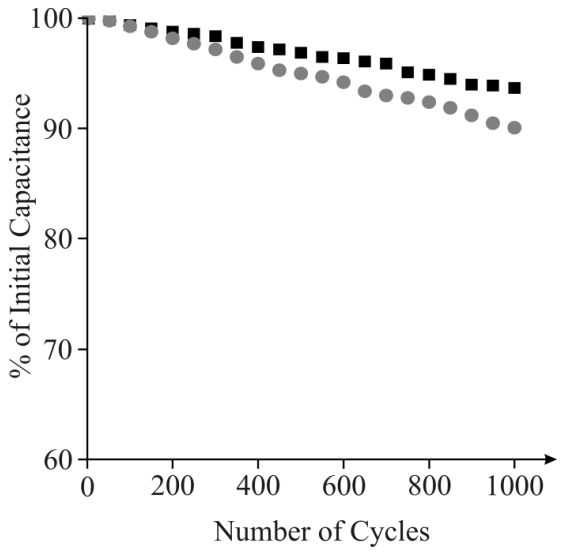

Figure 6.7 A plot showing number of charge-discharge cycles vs. % of initial capacitance for a Fe_3O_4 modified SPE (square) and the hydrogen-superoxide SPE (circle) over 1000 cycles in 3M KOH.

It has been reported that oxygenated surface groups, commonly found on carbon materials, increase the electrical capacitance of the material, [53] such as from a value of 80 to ~130 F g^{-1} following introduction of C-O species. [54] Frequently used techniques exploit oxidising agents such as nitric acid [55] and oxygen plasma [55] to increase the number of oxygenated groups present at the surface of carbon-based materials. Presented in this work is a new facile methodology for the introduction of oxygenated surface groups at carbon-based materials.

Hydrogen Superoxides

As previously explained, ferric chloride, $FeCl_3$ is dissolved in distilled water (1000 ppm, 1 mL) with the addition of hydrogen peroxide (30 %, 5mL). The ferric ions catalyse the hydrogen peroxide reaction, forming a range of peroxide radical's *in-situ*, via Fenton's reagent: [56]

$$Fe^{3+} + H_2O_2 \rightarrow Fe^{2+} + OOH\cdot + H^+ \qquad (6.12)$$

$$Fe^{2+} + H_2O_2 \rightarrow Fe^{3+} + OH\cdot + OH^- \quad (6.13)$$

when this solution is dispersed on the surface of the working electrode, the radicals formed attack the accessible carbon material along the surface of the SPE (Figure 6.8) increasing the percentage of oxygenated species present. Such radicals are very powerful and are even capable of initiating the hydroxylation of arenes (*e.g.* benzene to phenol). [57] It is evident from SEM imaging (Figures 6.8 and 6.9) that the iron particles in this case are much smaller than those examined previously. EDAX analysis of the working surface shows a significant increase in oxygen content subsequent to treatment. Many different parameters (such as temperature or carbon content) can affect the number of oxygenated surface groups present and in turn the capacitance, as such, further investigation into such factors is recommended. Last, the iron is likely in the form of Fe_3O_4 as described by the equations and characterisation presented earlier.

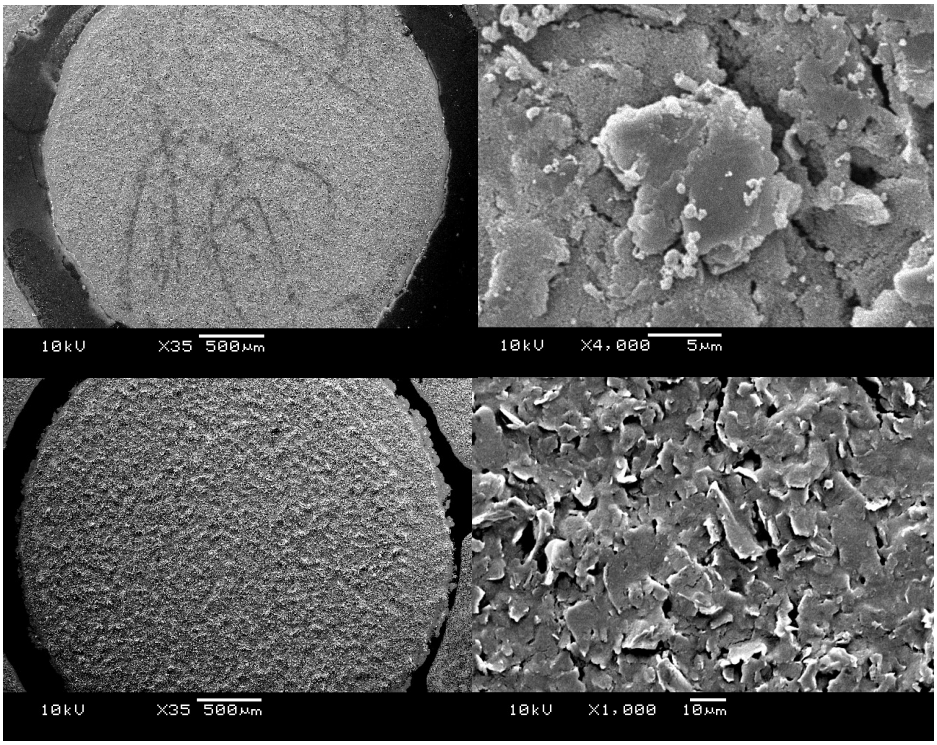

Figure 6.8 SEM images of the hydrogen superoxide (FeO(OH)) SPE (above) and standard SPE (below).

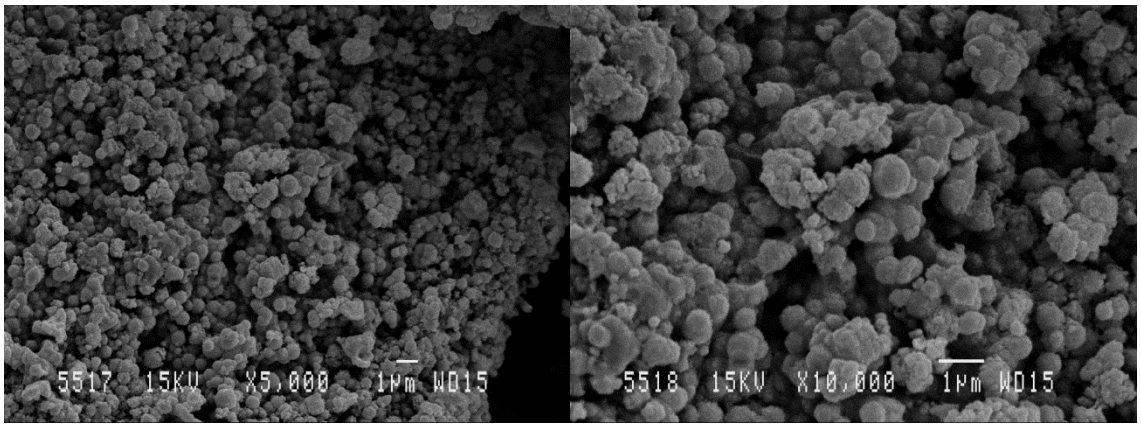

Figure 6.9 SEM images of the Iron Oxide nanoparticles formed during the treatment of the hydrogen superoxide (FeO(OH)) electrodes.

Finally, exploration and comparison towards the performance of the fabricated FeO(OH) (hydrogen superoxide) supercapacitor in a 3M KOH solution as mentioned previously. Interestingly, no significant redox coupling is observed in the voltammetric profile (Figure. 6.4B). From equation (6.11), galvanostatic charge-discharge was used to directly evaluate the applicability of the hydrogen superoxide based supercapacitor (Figure. 6.10); revealing a specific capacitance of ~400 F g^{-1} at a discharge current of 0.1 Ag^{-1}. This may be attributed to the number of surface defects and the number of sites accessible to attack by the radical oxides. Stability is comparable with that of the Fe_3O_4 supercapacitor, showing a ~10 % decrease in capacitance over 1000 cycles (see above).

It was found that the hydrogen superoxide (FeO(OH)) electrode displayed superior specific capacitance than that of both pure graphene (69.2 F g^{-1}) [58] and CNTs (58 F g^{-1}). [52] Our observed 400 F g^{-1} compares well with the 480 F g^{-1} seen at Fe_3O_4 nanoparticles attached to graphene oxide sheets,[34] while vastly out performing capacitance values measured at Fe_3O_4 (27 F g^{-1}),[41] AC/Fe_3O_4 (37.9 F g^{-1})[2] and Fe_3O_4/MWCNT (165 F g^{-1})[52] electrodes.

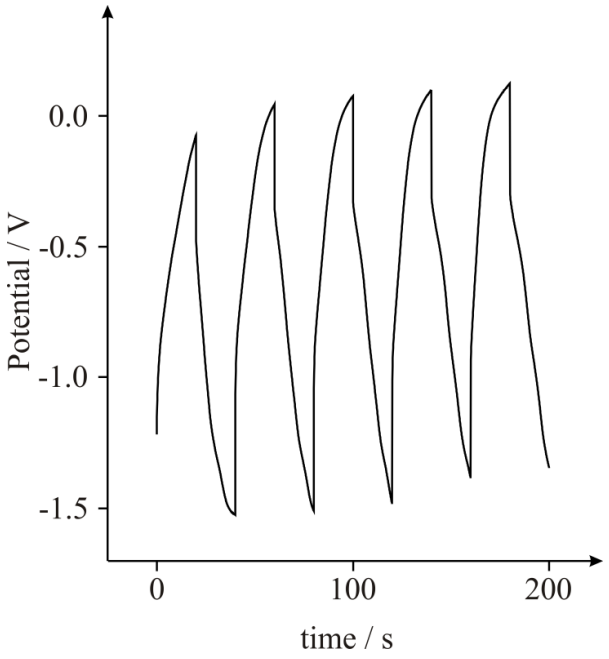

Figure 6.10 Galvanostatic charge-discharge of the hydrogen superoxide (FeO(OH)) based screen-printed electrode; 5 cycles over 200 seconds in a 3M KOH solution at 0.1 Ag^{-1}.

The specific energy density (E) and power density (P) are evaluated according to the following equations: [59]

$$E = (I\int V\mathrm{d}t)/m \tag{6.14}$$

$$P = \mathrm{d}E/\mathrm{d}t \tag{6.15}$$

where I is the current, the integral $\int V\mathrm{d}t$ is obtained from the area under the galvanostatic discharge curve, m is the mass of the active material and t is the discharge time. The energy density of the Fe_3O_4 and FeO(OH) electrodes reached 0.08 and 0.62 Wh kg^{-1} at a power density of 16.06 and 125.60 W kg^{-1} respectively.

6.2.4 CONCLUSIONS

A simplistic approach towards the fabrication of iron oxide particles and their electrochemical performance towards energy-storage has been presented. The Fe_3O_4

asymmetric supercapacitor delivered a maximum specific capacitance of ~120 F g^{-1}, retaining 93.7 % of its initial capacity over 1000 scans. In comparison the hydrogen superoxide (FeO(OH)) based supercapacitor showed a maximum specific capacitance of ~400 F g^{-1}. These micromaterials show great promise and should be considered when designing electrochemical devices such as energy-storage/generation devices. Future work involves the scale up and incorporation of these methodologies into the fabrication of screen-printed electrodes and explores the application of different metal catalysts towards the formation of -OOH groups at the surface of carbon-based electrodes.

6.2.5 REFERENCES

1. A. S. Arico, P. Bruce, B. Scrosati, J. M. Tarascon, S. W. Van, *Nat. Mater.* **2005**, 4, 366.
2. X. Du, C. Wang, M. Chen, Y. Jiao, J. Wang, *J. Phys. Chem. C*. **2009**, 113, 2643.
3. A. G. Pandolfo, A. F. Hollenkamp, *J. Power Sources.* **2006**, 157, 11.
4. M. Winter, R. Brodd, *J. Chem. Rev*. **2004**, 104, 4245.
5. Y. Wang, Z. Shi, Y. Huang, Y. Ma, C. Wang, M. Chen, Y. Chen, *J. Phys. Chem. C*. **2009**, 113, 13103.
6. A. Burke, *J. Power Sources.* **2000**, 91, 37.
7. B. E. Conway, *Electrochemical supercapacitor and technological applications:* Kluwer-Plenum Press: New York, 1999.
8. P. Simon, Y. Gogotsi, *Nat. Mater.* **2008**, 7, 845.
9. H. Nagawa, A. Shudo, K. Miura, *J. Electrochem. Soc.* **2000**, 147, 38.
10. S. T. Mayer, R. W. Pekala, J. L. Kaschmitter, *J. Electrochem. Soc.* **1993**, 140, 446.
11. A. Yoshida, S. Nonaka, I. Aoki, A. Nishino, *J. Power Sources.* **1996**, 60, 207.
12. W. Li, J. Chen, J. Zhao, J. Zhang, J. Zhu, *J. Mater. Lett.* **2005**, 59, 800.
13. Y. Takasu, Y. Murakami, *Electrochim. Acta.* **2000**, 45, 4135.
14. C. C. Hu, Y. H. Huang, *Electrochim. Acta.* **2001**, 46, 3431.
15. L. Diederich, E. Barborini, P. Piseri, A. Podesta, P. Milnai, *Appl. Phys. Lett.* **1999**, 75, 2662.
16. S. Lipka, *IEEE Aerosp. Electron Syst. Mag.* **1997**, 12, 27.
17. D. N. Futaba, K. Hata, T. Yamanda, T. Hiraoka, Y. Hayamizu, Y. Kakudate, O.

Tanaike, H. Hatori, M. Yumura, S. Iiyima, *Nat. Matter.* **2006**, 5, 987.

18. S. Talapatra, S. Kar, S. K. Pal, R. Vajtai, L. Ci, P. Victor, M. M. Shaijumon, S. Kaur, O. Nalamasu, P. M. Ajayan, *Nat. Nanotechnol.* **2006**, 1, 112.
19. G. Lota, T. A. Centeno, E. Frackowiak, F. Stoecki, *Electrochim. Acta.* **2008**, 53, 2210.
20. K. H. An, W. S. Kim, Y. S. Park, J.–M Moon, D. J. Bae, S. C. Lim, Y. S. Lee, Y. H. Lee, *Adv. Funct. Mater.* **2001**, 11, 387.
21. D. Y. Qu, *J. Power Sources.* **2002**, 109, 403.
22. M. M. Shaijumon, F. S. Ou, L. J. Ci, P. M. Ajayan, *Chem. Commun.* **2008**, 2373.
23. H. H. Bauer, M. S. Spritzer, P. J. Elving, *J. Electroanal. Chem.* **1968**, 17, 299.
24. C. G. Liu, M. Liu, F. Li, H. M. Cheng, *Appl. Phys. Lett.* **2008**, 92, 143108.
25. C. M. Niu, E. Sichel, R. Hoch, D. Moy, H. Tennent, *Appl. Phys. Lett.* **1997**, 70, 1480.
26. D. Hulicova, J. Yamashita, Y. Sonede, H. Hatori, M. Kodama, *Chem. Mater.* **2005**, 17, 1241.
27. C. M. Yang, Y. J. Kim, M. Endo, H. Kanoh, M. Yudasaka, S. Iijima, K. Kaneko, *J. Am. Chem. Soc.* **2007**, 129, 20.
28. E. Raymundo-Pinero, F. Leroux, F. Beguin, *Adv. Mater.* **2006**, 18, 1877.
29. J. P. Zeng, T. R. Jow, *J. Electrochem Soc.* **1995**, 142, 6.
30. A. A. F. Groupioni, T. A. F. Lassali, *J. Electrochem. Soc.* **2001**, 148, 1015.
31. J. M. Skowronski, K. Jurewiez, *J. Power Sources.* **1993**, 45, 263.
32. T. Cottineau, M. Toupin, T. Delahaye, T. Brousse, D. Belanger, *Appl. Phys. A: Mater. Sci. Process.,* **2006**, 82, 599.
33. X. Du, C. Y. Wang, M. M. Chen, Y. Jiao, J. Wang, *J. Phys. Chem. C*. **2009**, 113, 2643.
34. W. Shi, J. Zhu, D. H. Sim, Y. Y. Tay, Z. Lu, X. Zhang, Y. Sharma, M. Srinivasan, H. Zhang, H. H. Hng, Q. Yan, *J. Mater. Chem.* **2011**, 21, 3422.
35. Y.-H. Kim, S.-J. Park, *Curr. Appl. Phys*. **2011**, 11, 462.
36. M. Kaempgen, C. K. Chan, J. Ma, Y. Cui, G. Gruner, *Nano Lett.* **2009**, 9(5), 1872.
37. J. P. Metters, R. O. Kadara, C. E. Banks, *Analyst*, **2011**, 136 (6), 1067.
38. Y. Zhang, X. Sun, L. Pan, H. Li, Z. Sun, C. Sun, B. K. Tay, *J. Alloy. Compd.*, **2009**, 480 (2), L17-19.
39. R. O. Kadara, N. Jenkinson, C. E. Banks, *Sens. Actuators B.* **2009**, 138, 556.
40. http://kanichi-research.com; accessed Jan 2011.
41. N. L. Wu, S. Y. Wang, C. Y. Han, D. S. Wu, L. R. Shiue, *J. Power Sources*. **2003**, 113, 173.

42. H. B. Dunford, *Coord. Chem. Rev.,* **2002**, 233, 311.
43. J. Bassett, R. C. Denny, G. H. Jeffery, J. Mendam, *Vogel's Textbook of quantitative inorganic analysis* (4th edn.), **1980**.
44. P. Patnaik. *Handbook of Inorganic Chemicals*. McGraw-Hill, 2002, ISBN 0070494398X.
45. A. P. Grosvenor, B. A. Kobe, M. C. Biesinger, N. S. Mclntyre, *Surf. Interface Anal.*, **2004**, 36, 1564.
46. S. Tang, S. Vongehr, Y. Wang, L. Chen, X. Meng, *J. Solid State Chem.*, **2010**, 183, 2166.
47. D. Brion, *Appl. Surf. Sci.*, **1980**, 5, 133.
48. T. L. Barr, *J. Phys. Chem. A*, **1978**, 82, 1801.
49. A. K. Shukla, S. Sampath, K. Vijamohanan, *Curr. Sci*. **2000**, 79, 1656.
50. D. Qu, H. Shi, *J. Power Sources*. **1998**, 74, 99.
51. P. Kanatharana, M. S. Spritzer, *Anal. Chem.*, **1974**, 46 (7), 958.
52. Y.-H. Kim, S.-J. Park, *Curr. Appl. Phys*. **2011**, 11, 462.
53. Y.-R. Nian, H. Teng, *Fuel Chem. Division*. **2002**, 47, 429.
54. E. Frackowiak, S. Delpeux, K. Jurewicz, K. Szostak, D. Cazorla-Amoros, F. Beguin, *Chem. Phys. Lett*. **2002**, 361, 35.
55. A. M. Yacynych, T. Kuwana, *Anal. Chem.* **1978**, 50, 640.
56. F. Haber, J. Weiss, *Naturwissenschaften.* **1932**, 20, 948.
57. G. I. Panov, A. K. Uriarte, M. A. Rodkin, V. I. Sobolev, *Catalysis Today*. **1998**, 41, 365.
58. J. Yan, *Carbon*. **2010**, 48, 1731.
59. Y. Cao, T. E. Mallouk, *Chem. Mater.* **2008**, 20, 5260.

6.2.2 PRINTABLE THIN FILM SUPERCAPACITORS UTILIZING CRYSTALLINE COBALT HYDROXIDE NANOSHEETS

6.2.2.1 INTRODUCTION

The rapidly growing market in portable electronic devices, electric vehicles and the ever worsening global warming issues call for not only urgent development of clean alternative energies and emission control of global warming gases, but also more environmentally friendly, high-performance energy-storage systems. [1,2] Supercapacitors, also known as electrochemical capacitors or ultracapacitors,[3,4] are electronic components that can be rapidly charged and discharged and relied upon to store energy reliably for long periods, offering transient but extremely high powers, and are probably the most important next generation energy-storage device. [5] Emerging as an ideal model, they have been touted as a solution to the mismatch between the fast growth in power required by devices and the inability of batteries in various applications which require transient but high/peak power pulses for the time-dependent usage. [6]

The materials mostly used as electrochemical double layer capacitors (EDLC) are based on carboneous materials such as activated carbon, carbide-derived carbon, graphene and carbon nanotubes [7-15] which have a large surface area for the charge to reside. Capacitors in the alternative class, called pseudo-capacitors, utilise transition metal oxides or electrically-conducting polymers as electrode materials.[16] The storage mechanism in this case is the undergoing of fast surface Faradaic reactions while the amount of charge held is proportional to the voltage.[16] While supercapacitors benefit from the highest known power capability (10 kW kg^{-1}), high current capability, ease of maintenance, and long-term cycling stability (>10^6cycles).[6,16] Their moderate energy density for the widespread deployment in everyday technology as clean and renewable energy media are still far away to meet the performances and cost requirements, in

particular providing power boosts to start the engine or to assist acceleration.

To make capacitors commercially viable and become extensively used, the energy that they can store needs to increase significantly and hence to attain supercapacitors with sufficient energy for higher requirements in the future still remains very challenging. Extensive efforts have been devoted to improve the specific capacitance of supercapacitors by introducing pseudocapacitive metal oxides. Compared with the EDLC-based capacitors, pseudocapacitors based on transition metal oxide electrodes such as RuO_2,[5] MnO_2,[17,18] CoO_x,[19] and NiO[20] are available for charge storage through Faradaic or redox-type reactions because they can produce much higher capacitances than double-layer carbonaceous materials. Impressively, cobalt oxide is very attractive in view of its outstanding pseudocapacitive behaviour (theoretical capacitance, 3460 F g^{-1}) [21], practical availability, environmental compatibility and lower cost when compared to the state-of-the-art supercapacitor material RuO_2. Despite its importance, efforts are still needed to further improve the practical use of cobalt materials in supercapacitors.

A key methodology to boost the specific capacitance of such electroactive cobalt-based materials is their morphological and/or chemical composition design at the nanometer-scale, because high surface-to-volume ratio with suitable pore sizes is desirable for the penetration of electrolytes and reactants into the whole electrode matrix, and can promote the electric double-layer capacitances and accommodate a large amount of superficial electroactive species to participate in Faradaic redox reactions. Thus, considerable effort has been done to improve the electrochemical performances of β-$Co(OH)_2$ by developing effective strategies to synthesize β-$Co(OH)_2$ nanostructures particularly with more controllable and uniform sizes.

Also it should be noted that supercapacitors can be made flexible with sheet-like structures, which are light-weight. The fabrication method of the supercapacitors should be inexpensive

and high-throughput, just like batteries. Various methods exist but are costly and expensive and not appropriate to be used to make millions of supercapacitors. State-of-the-art flexible thin-film supercapacitors based on sprayed networks of single-walled carbon nanotubes (SWCNTs) [22] were fabricated, showing the performances of the devices with very high energy (6 Wh kg^{-1}). The results underline the potential of printable thin film supercapacitors. Despite this scientific advance towards semi-printable/production supercapacitors, there have been limited reports using printing processes for fabricating flexible supercapacitors; to the best of our knowledge there have been NO reports of using true screen printing despite its inherent advantages.[22, 23]

Novel electrochemical designs can be readily fabricated via screen printing by designing and producing screens which derive the geometry and thickness of the screen-printed material, usually graphite but can be applied to other novel materials [22, 23], and in this section, screen printing is utilized as a new methodology to fabricating flexible and reproducible supercapacitors with high surface areas and minimal wasted space with respect to geometric arrangement and in terms of multiple printing. The advantage of this fabrication approach is that it can be readily scaled up and is economical which produces reproducible surface shapes and thicknesses, something which is lacking in this area. Thus both the resistance and weight of printing electrodes were reduced via eliminating the interface between the charge collectors and working electrodes, leading to higher power density.

This work reports a novel, hydrothermal, template-free approach towards the fabrication of flower-like β-$Co(OH)_2$ produced from the aggregation of single crystal nanosheets structure, integrated into the working surface of a screen-printed electrode. The electrochemistry of the nanostructure is explored, comprised of layered transition β-$Co(OH)_2$, towards understanding how to increase Faradaic capacitance. In doing so,

enhanced pseudo-capacitance is revealed, achieved using this unique structure of layered *single* crystalline β-$Co(OH)_2$, attributed to the ability of the material to accommodate elevated numbers of electroactive ions and is consequently accessible to fast Faradaic reactions.

6.2.2.2 EXPERIMENTAL

Materials

Cobalt(II) chloride hexahydrate ($CoCl_2 \cdot 6H_2O$), hexamethylenetetramine (HMT), cetyltrimethylammonium bromide (CTAB) and monoethanolamine were purchased from Shanghai Chemical Co. LTD, China. All chemicals used were of analytical grade and were used as received without any further purification.

Synthesis of $Co(OH)_2$

Cobalt(II) chloride ($CoCl_2$, 2 mmol) and HMT (2 mmol) was dissolved into distilled water (20 mL) including CTAB (1mmol) under vigorous stirring. After the mixture becomes transparent, monoethanolamine (1 mL) is added and the resulting solution immediately transferred into a Teflon stainless steel autoclave. The autoclave was sealed and maintained at 100 °C for 24 hours, and was then allowed to cool to room temperature. The resulting solid is then washed repeatedly with distilled water and finally dried at 80 °C in air. Synthesis is an adaptation from previous literature.[24]

Characterization

The morphologies are characterized using a scanning electron microscopy (SEM) (EDAX-4800) and transmission electron microscopy (TEM) (Japan JEOL JEM-200CX, transition electron microscope). The high-resolution TEM (HRTEM) images were obtained using a JEOL-2010 TEM at an acceleration voltage of 200 kV. The phase purity of the products was characterized by X-ray powder diffraction (XRD), (Shimadzu XD-3A X-ray

diffractometer with Cu α radiation, λ = 0.15417 nm). The BET (Brunauer-Emmett-Teller) surface area was measured and interpreted (by collaborators at) using a ASAP2020 (Micromeritics, United States). The X-ray photoelectron energy spectroscopy (XPS) was recorded on a VG ESCALAB MKII, using an accelerating voltage and working current of 12.5 kV and 20.0 mA respectively. This analyses, and interpretation of their results, along with the fabrication of the Co nanomaterials was performed by Prof Xiaobo Ji at the College of Chemistry and Chemical Engineering and State Key Laboratory for Powder Metallurgy, Central South University, Changsha.

Screen-printed Electrodes

Voltammetric measurements were carried out using a μ-Autolab III (Eco Chemie, The Netherlands) potentiostat/galvanostat and controlled by Autolab GPES software. Screen-printed electrodes (SPEs) were fabricated in-house with appropriate stencil designs using a microDEK 1760RS screen-printing machine (DEK, Weymouth, UK). A carbon-graphite ink formulation (C2000802D2, Gwent Electronic Materials Ltd, UK) was first screen-printed onto a polyester flexible film (Autostat, 250 μm thickness) defining the carbon contacts, counter and working electrodes. This layer (5-10 microns in depth) was cured in a fan oven at 60 degrees for 30 minutes. Next a silver/silver chloride reference electrode was included by screen printing Ag/AgCl paste (Gwent Electronic Materials Ltd, UK) on to the plastic substrate. Last a dielectric paste ink (Gwent Electronic Materials Ltd, UK) was printed to cover the connections and define the 9 mm diameter graphite working electrode. After curing at 60 degrees for 30 minutes the screen-printed electrode is ready to use. An example of a flexible screen-printed electrode is shown in Figure 6.11. The printed carbon material displays a heterogeneous rate constant of 1.7×10^{-3} cm s^{-1} as determined with potassium ferrocyanide / 1 M KCl.[25]

Cobalt-hydroxide screen-printed electrodes were fabricated as described above with β-$Co(OH)_2$ efficiently mixed into the ink formulation prior to screen printing. In doing so, the rheology of the ink changes such that the careful addition of solvents is needed along with modification of the standard printing parameters. Increasing amounts of cobalt hydroxide were incorporated into the screen-printed electrodes over the range of 10, 20 and 30% (M_P/M_I), where M_P is the mass of particulate and M_I is the mass of ink formulation used in the printing process. The printing process facilitated the homogenous coverage of the electrode surface by the cobalt hydroxide

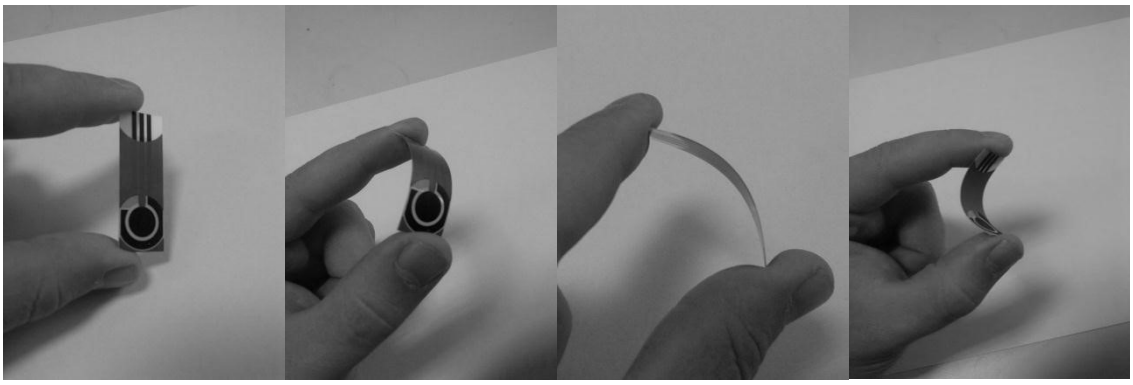

Figure 6.11 Images depicting a flexible graphite screen-printed electrode.

6.2.2.3 Results and discussion

Characterisation of capacitance material

X-ray diffraction (XRD) analysis (Figure 6.12) was used to determine the chemical composition and the crystalline structure of the synthesised material over the range $15° \leq 2\theta \leq 70°$ (2θ). The diffraction peaks show excellent conformity with the standard XRD pattern expected for β-$Co(OH)_2$ (JCPDS: 74-1057), confirming the synthesized product is high purity hexagonal brucite-like β-$Co(OH)_2$. The peak intensities of diffraction planes (001), (100) and (011) are significantly larger than that of the other diffraction peaks, not dissimilar to the standard XRD pattern produced by bulk β-$Co(OH)_2$. The morphology and microstructure of

the sample was observed by scanning electron microscopy (SEM) and Transmission electron microscopy (TEM). SEM imaging of the β-$Co(OH)_2$ microflower at low magnification (Figure 6.13A) demonstrates excellent uniformity throughout, with an average diameter of ~10 μm. Upon magnification (Figure 6.13B), SEM imaging reveals the β-$Co(OH)_2$ microflower is fundamentally an accumulation of individual nanosheets, each displaying a thickness of ~20 nm. The structure of the porous β-$Co(OH)_2$ microflower was further investigated by TEM and high-resolution TEM (HRTEM). TEM analysis (Figure 6.13C) of the β-$Co(OH)_2$ nanosheet petal, indicates that several nanosheets are overlaped together. It further demonstrates that the β-$Co(OH)_2$ microflower is an assembly of the nanosheets. The selected area electron diffraction (SAED) analysis on the nanosheet petal, renders its single crystalline nature and the surface of the nanosheet is the (001) plane of β-$Co(OH)_2$ (inset Figure 6.13C). HRTEM imaging of the β-$Co(OH)_2$ nanosheet (Figure 6.13D) illustrates the porous character of the nanosheet, typically 2-4 nm in size whilst the inter-planar spacing of 0.276 nm coincide with that expected for a (100) lattice plane.

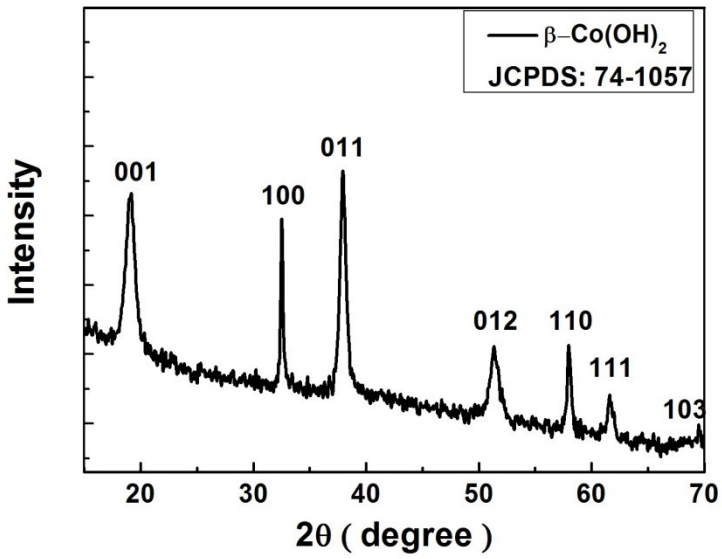

Figure 6.12 X-ray diffraction spectrum of the β-$Co(OH)_2$ nanosheets.

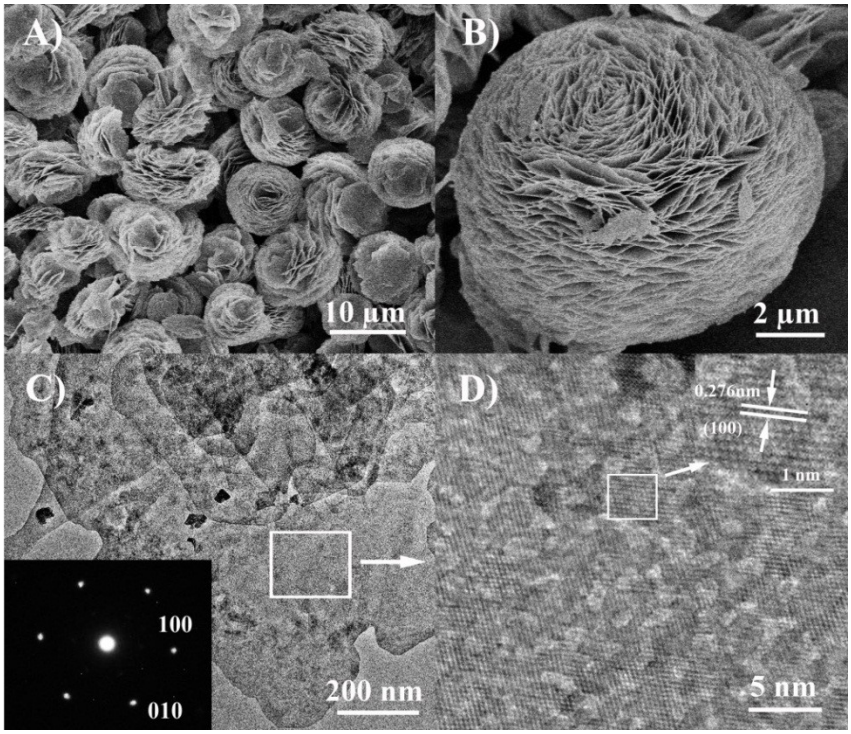

Figure 6.13 SEM images of as-prepared porous β-Co(OH)$_2$ microflower assembled by nanosheets; C) TEM image and corresponding SAED pattern (inset) of β-Co(OH)$_2$ nanosheets and D) HRTEM image of the nanosheet (magnification of Figure 6.13C).

The surface electronic states and the chemical composition of the β-Co(OH)$_2$ was examined by x-ray photoelectron energy spectroscopy (XPS), see Figure 6.14. The survey XPS curves reveal the presence of Co and O, as confirmed by XRD analysis. The binding energies of the Co 2p$_{3/2}$ and 2p$_{1/2}$ states are located at 781.3 and 797.4 eV respectively (Figure 6.14A), which agree with the value illustrated in the literature. [26] The Co 2p main peaks include a satellite peak on the higher binding-energy side, indicating the Co ion is in a divalent state. [25] The binding energy of the O 1s state at 531.0 eV (Figure 6.14B) is consistent with values previously reported and confirms the presence of O–H bonds [27]. The N_2 adsorption/desorption isotherm showed a type IV curve with a hysteresis loop with the pore distribution curve exhibiting a peak at approximately 40 nm, demonstrating the porous characteristics of the material. The BET (Brunauer-Emmett-Teller) surface area (see Chapter

2) and single point total pore volume were found to correspond to 26 m^2 g^{-1} and 0.03 cm^3 g^{-1} respectively. The pore size calculated by the BJH (Barrett-Joyner-Halenda) method (a method for calculating pore size distributions based on a model where the adsorbent is perceived to be a collection of cylindrical pores) was found to be ~40 nm, corresponding to the result illustrated in the inset of Figure (6.13).

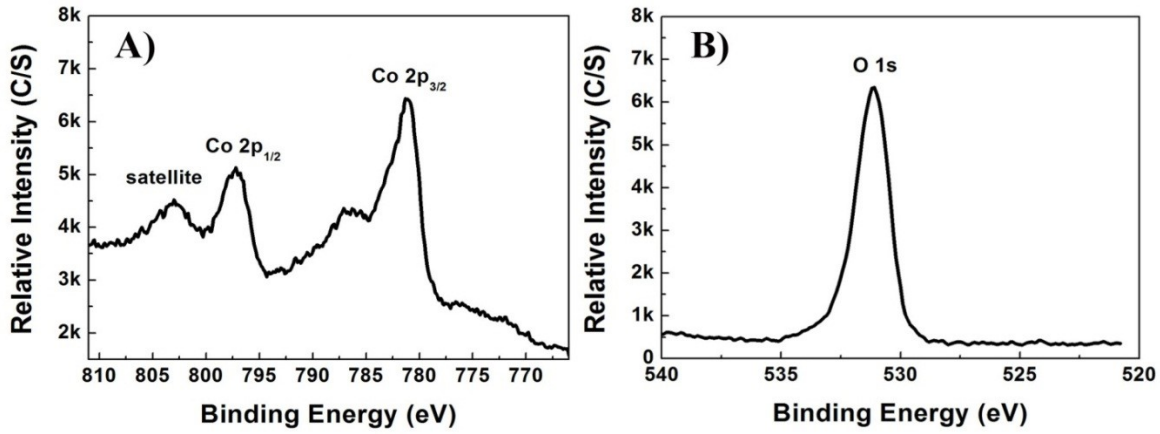

Figure 6.14 Typical XPS spectra of the β-$Co(OH)_2$ microflower; A) Co 2p and B) O 1s.

In order to gain an insight into the formation mechanism of the β-$Co(OH)_2$ microflower, time-dependent experiments were carried out at 100 °C and the products inspected by SEM. It was found that the reaction time played a crucial role in the formation of flower-like products. The evolution process can be clearly seen from Scheme (6.1) and Figure (6.15).

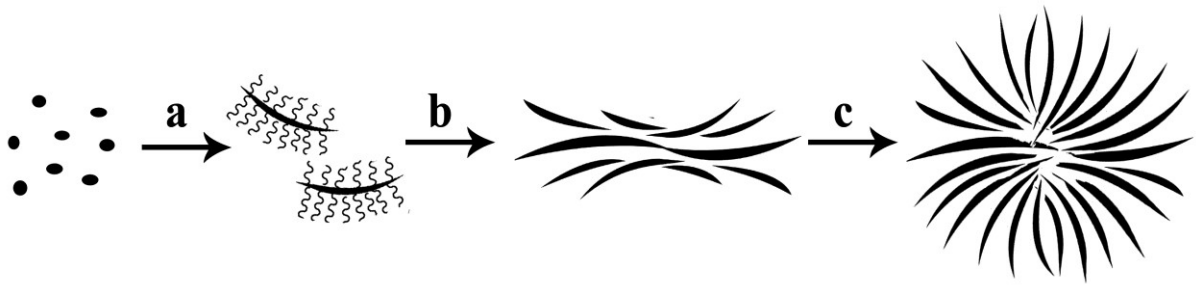

Scheme 6.1 The formation process of the β-$Co(OH)_2$ microflower fashioned from individual nanosheets; The conversion of cobalt-monoethanolamine tertiary complex nanoparticles to $Co(OH)_2$ nanosheets affixed with CTAB (〰) (a), The aggregation of $Co(OH)_2$ nanosheets with the help of CTAB (b) and the assembly of the β-$Co(OH)_2$ microflower (c).

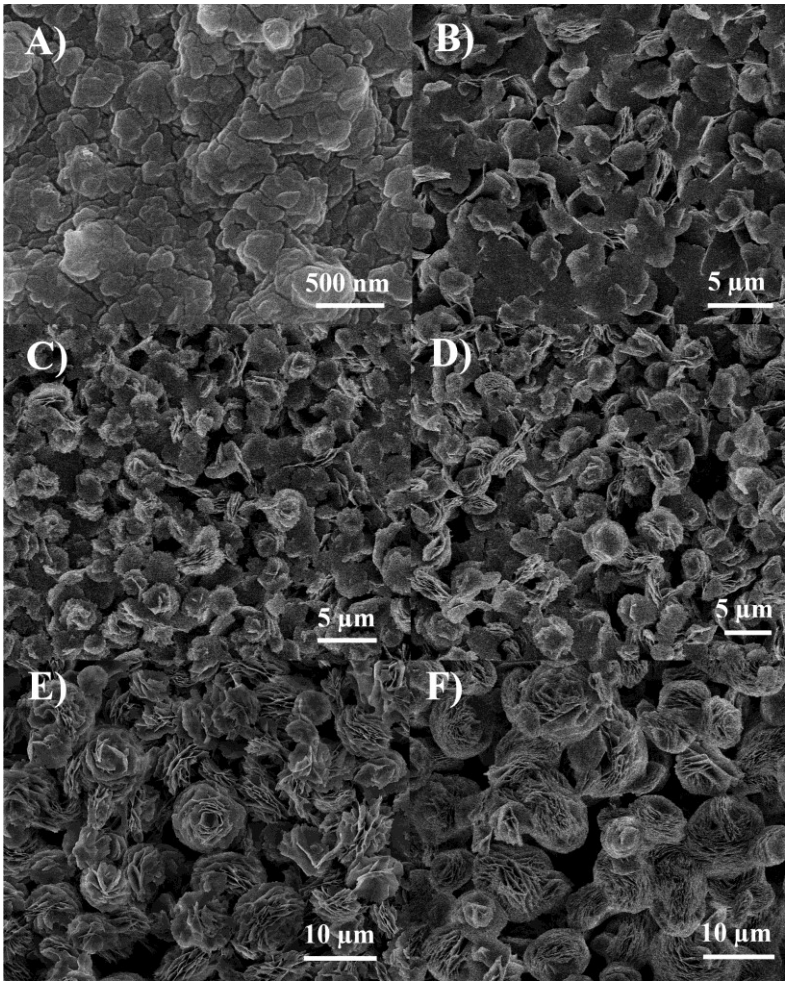

Figure 6.15 SEM images of β-$Co(OH)_2$ produced over a time period of: A) 0, B) 2, C) 4, D) 6, E) 12 and F) 24 hours.

At the beginning of the reaction, nanoparticles of the cobalt-monoethanolamine tertiary complex are primary formed (Figure 6.15A), which are sap green in colour. At elevated temperature (up to 90 °C in this experiment), the cobalt-monoethanolamine complex decomposes slowly, resulting in the increase of Co^{2+} concentration. Meanwhile, OH^- concentration increases gradually because of the hydrolysis of both hexamethylenetetramine (HMT, shown below) and monoethanolamine.

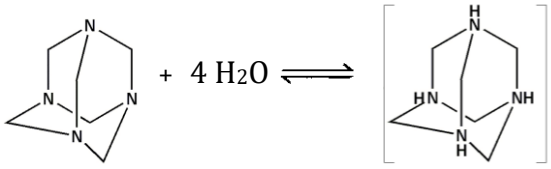

(6.16)

When the reaction continues for 2 hours, most of nanoparticles have been converted to nanosheets accompanied by the colour change of the products from 'sap green' to that of 'wine', which demonstrates the appearance of β-$Co(OH)_2$ (Figure 6.15B). With the increase of reaction time, more and more β-$Co(OH)_2$ nanosheets are obtained (Figure 6.15C). Some of these overlap together through layer-by-layer assembly to form flower-like $Co(OH)_2$ with the diameter of 3-5 μm when the reaction time is up to 6 hours (Figure 6.15D). As the reaction proceeding, large β-$Co(OH)_2$ microflowers with a diameter of 10 μm can been observed in Figure 6.15E, which are larger than those of the 6 hours reaction, but the structure of the flower-like β-$Co(OH)_2$ is not perfect. The SEM image of the product reacted for 24 hours (Figure 6.15F) indicates that well-assembled β-$Co(OH)_2$ microflowers can be readily achieved; the morphology of the product will not change if the reaction time is prolonged.

To examine the function of CTAB and monoethanolamine, comparable β-$Co(OH)_2$ nanomaterials with different morphologies were prepared. When HMT is used as the sole supplier of OH^- and no monoethanolamine is added, irregular β-$Co(OH)_2$ nanosheets were obtained, rather than flowerlike β-$Co(OH)_2$ (Figure 6.15A). This indicates that monoethanolamine has significant effects on the morphology of β-$Co(OH)_2$. In this reaction system, cobalt-monoethanolamine tertiary complexes are formed at the beginning of the reaction and release Co^{2+} slowly with the reaction proceeding, which is favoured for the formation of flowerlike β-$Co(OH)_2$. When no CTAB is used, many individual β-$Co(OH)_2$ nanosheets were obtained instead of flowerlike β-$Co(OH)_2$ (Figure 6.15B). CTAB serves as not only the surfactant for the assembly of the β-$Co(OH)_2$ nanosheets (Scheme 6.1b

and 6.1c), but also the structure-directing agent for the formation of the mesoporous β-$Co(OH)_2$. Therefore, Both CTAB and monoethanolamine cannot be indivisible for the synthesis of β-$Co(OH)_2$ microflowers.

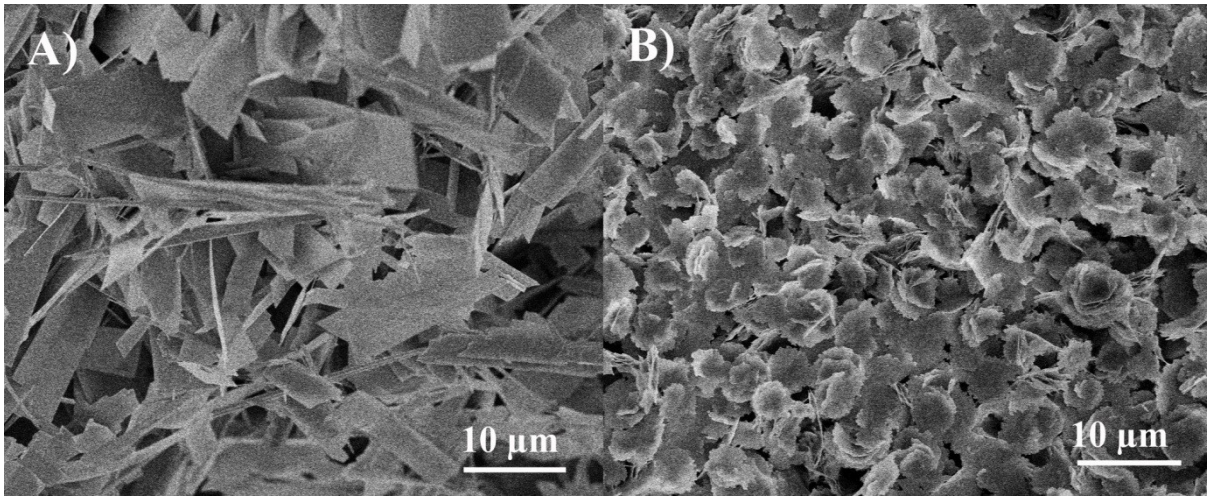

Figure 6.16 SEM images of β-$Co(OH)_2$ produced under varied reaction condition: A) without monoethanolamine and B) without CTAB.

Electrochemical evaluation of the $Co(OH)_2$ microflowers

First the voltammetric performance, conducted by Said M. Houssein and myself, of the β-$Co(OH)_2$ modified screen-printed supercapacitor (20 %, (M_p/M_I)) is considered in a 3 electrode-cell, with 3 M KOH using a potential range between -0.3 and +0.5 V at an applied scan rate of 0.02 Vs^{-1} (vs Ag/AgCl). This was considered a suitable test to determine the mechanistic process of the reaction (Faradaic and non-Faradaic). Figure 6.17A displays a predominantly rectangular shaped CV curve, strongly resembling the characteristics of electrochemical double-layer, commonly observed for carbon-based materials but also Faradaic pseudo-capacitance, evident from the oxidation and reduction waves at -0.10, -0.11, 0.12 and 0.3V (P_1, P_2, P_3 and P_4 respectively, Figure 6.17A), typical to metal oxides (β-

$Co(OH)_2$ in our case). The two redox couples observed in the voltammetric profile are likely attributed to two reaction mechanisms: [28]

$$Co(OH)_2 \rightleftharpoons CoO(OH) + H^+ + e^- \ (P_1 / P_2) \ \textit{and} \ CoO(OH) \rightleftharpoons CoO_2 + H^+ + e^- \ (P_3 / P_4).$$

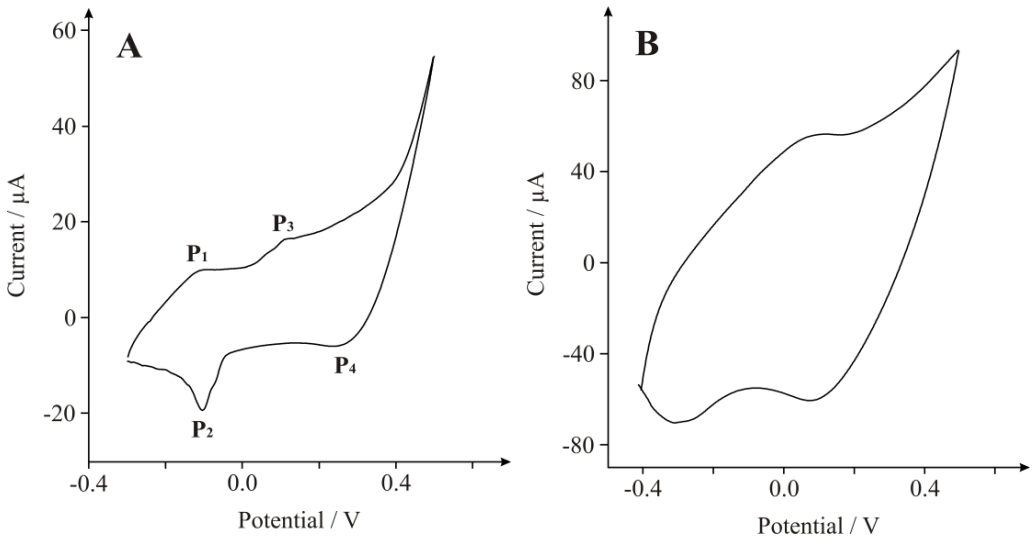

Figure 6.17 Cyclic Voltammograms of a β-$Co(OH)_2$ (20%, (M_p/M_I)) modified SPE at scan rate of A) 20 and B) 130 mVs^{-1} in 3 M KOH.

To determine the optimum coverage of nanomaterial which exhibits the most beneficial electrochemical response, consequently the effect of increasing amounts of cobalt hydroxide (β-$Co(OH)_2$) is explored over the range 10-30% (M_p/M_I). The response of the 10% and 20% (M_p/M_I) cobalt hydroxide electrodes were initially explored. It was found that the specific capacitance, calculated using galvanostatic charge-discharge method (see below) increased exponentially in relation to the β-$Co(OH)_2$ content. However once a critical mass is reached, in our case 30% (M_p/M_I), the electrochemical performance of the electrode drops-off. This suggests that excessive quantities of β-$Co(OH)_2$ amplifying the volume of

nanosheets superimposed on the surface of the electrode, decreases porosity, consequently diminishing the ability to store large amounts of charge within the active material. As a result, there is a significant reduction in the specific capacitance of the working electrode. This phenomenon has been observed before when metal oxide modified SPE's have been used in electroanalysis, credited to the reduced number of conductive pathways throughout the electrode. [29,30]

Galvanostatic charge-discharge was used to directly evaluate the applicability of the cobalt hydroxide screen-printed electrodes. A typical charge-discharge plot for the β-$Co(OH)_2$ electrode is depicted in Figure 6.18. The hybrid cobalt electrode exhibits good electrochemical capacitance performance, demonstrated by a linear variation of the voltage observed during the charging-discharging process (Figure 6.18). The specific capacitance of the electrode can be determined from the charge/discharge test, using equation (6.11): [1]

The specific capacitance of the β-$Co(OH)_2$ electrode was calculated to be ~170 F g^{-1} at a discharge current of 5 μA. This is in the middle of previous literature values recorded for β-$Co(OH)_2$.[31,32,33] α-$Co(OH)_2$ nanosheets, fabricated through electrochemical methods have demonstrated a specific capacitance of up to 860 F g^{-1}.[34] However, electrochemical deposition techniques suffer with limitation such as a small area of deposition, severe cleaning subsequent to each deposition and high working cost, thus restricting its application on a large scale. While the α form has higher activity, its hydrotalcite-like phase is metastable and easily undertakes a phase transformation into the more stable brucite-like compounds in strong alkaline media.

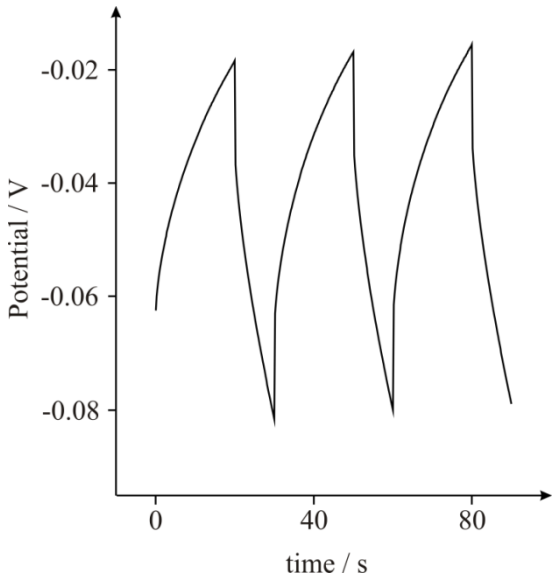

Figure 6.18 Typical galvanostatic charge-discharge of β-Co(OH)$_2$ modified screen-printed electrode in 3 M KOH at a discharge current of 5μA.

A long cycle life constitutes one of the core characteristic sought-after in any energy-storage device. The cyclic performance of the hybrid electrode is impressive, retaining 99.69% of its maximum capacity over 600 cycles as shown in Figure 6.19, indicating the stability and suitability of the β-Co(OH)$_2$ particles for high-performance energy-storage applications. It is apparent from the cycling process, that an activation process is required to attain the optimum energy-storage from the cobalt modified electrode (Figure 6.20). The thickness of the working electrode area is an important parameter to consider in future studies as increased values (in our case) have exhibited detrimental effects, possibly attributed to a decrease in conductive pathways.

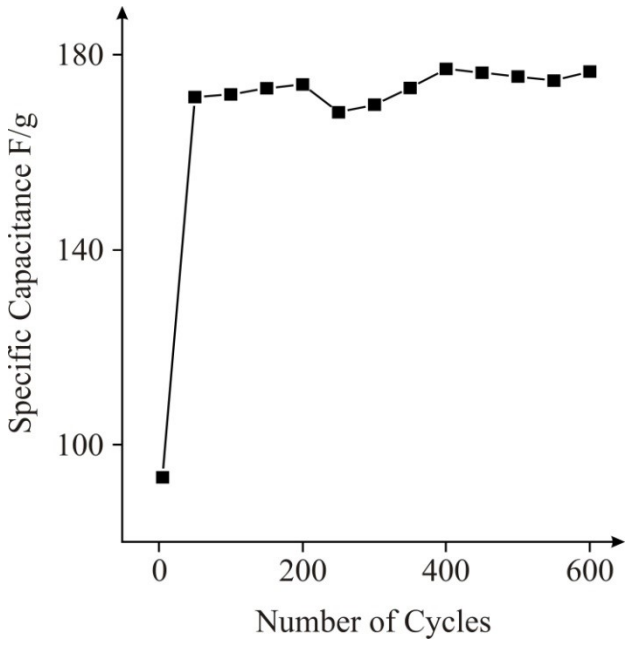

Figure 6.19 A plot showing number of charge-discharge cycles vs. specific capacitance for a β-$Co(OH)_2$ modified SPE over 600 cycles in 3 M KOH.

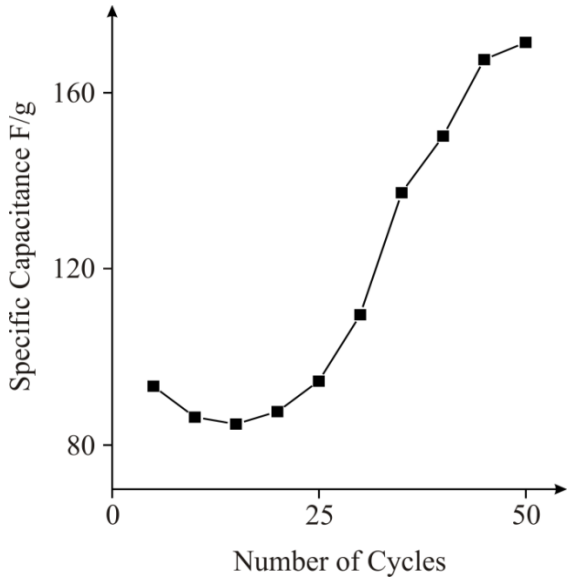

Figure 6.20 Activation process of the β-$Co(OH)_2$ electrode; galvanostatic charge-discharge cycles 1-50 in 3 M KOH.

6.2.2.4 CONCLUSIONS

It has been reported for the first time of a supercapacitor fabricated solely by screen printing. This simple methodology, allows for the mass fabrication of inexpensive, reproducible supercapacitors, where potentially any material can be incorporated. This chapter reports the novel chemical synthesis of cobalt hydroxide β-$Co(OH)_2$, incorporated via screen-printing into a supercapacitor, and explored the electrochemical performance towards energy-storage. The β-$Co(OH)_2$ asymmetric supercapacitor delivered a maximum specific capacitance of 170 F g^{-1} (0.1% RSD), retaining 99.9% of its maximum capacity over 600 scans. The capacitance can likely be improved upon in subsequent studies, through possible manipulation of design, morphology and chemical composition which makes these materials an exciting prospect and should be considered when designing electrochemical devices such as energy-storage devices.

6.2.2.5 REFERENCES

1. X. Du, C. Wang, M. Chen, Y. Jiao, J. Wang, *J. Phys. Chem. C.* **2009**, 113, 2643.
2. A. S. Arico, P. Bruce, B. Scrosati, J. M. Tarascon, S. W. Van, *Nat. Mater.* **2005**, 4, 366.
3. A. G. Pandolfo, A. F. Hollenkamp, *J. Power Sources.* **2006**, 157, 11.
4. M. Winter, R. Brodd, *J Chem. Rev*. **2004**, 104, 4245.
5. C-C. Hu, K-H. Chang, M-C. Lin, Y-T. Wu, *Nano Lett.* **2006**, 6 (12), 2690.
6. A. Burke, *J. Power Sources.* **2000**, 91, 37.
7. M. Winter, R. Brodd, *J Chem. Rev*. **2004**, 104, 4245.
8. S. Lipka, *IEEE Aerosp. Electron Syst. Mag.* **1997**, 12, 27.
9. D. N. Futaba, K. Hata, T. Yamanda, T. Hiraoka, Y. Hayamizu, Y. Kakudate, O. Tanaike, H. Hatori, M. Yumura, S. Iiyima, *Nat Matter.* **2006**, 5, 987.
10. S. Talapatra, S. Kar, S. K. Pal, R. Vajtai, L. Ci, P. Victor, M. M. Shaijumon, S. Kaur, O. Nalamasu, P. M. Ajayan, *Nat. Nanotechnol.* **2006**, 1, 112.
11. G. Lota, T. A. Centeno, E. Frackowiak, F. Stoecki, *Electrochim. Acta.* **2008**, 53, 2210.
12. K. H. An, W. S. Kim, Y. S. Park, J.–M Moon, D. J. Bae, S. C. Lim, Y. S. Lee, Y. H. Lee, *Adv Funct. Mater.* **2001**, 11, 387.

13. D. Y. Qu, *J. Power Sources.* **2002**, 109, 403.
14. M. M. Shaijumon, F. S. Ou, L. J. Ci, P. M. Ajayan, *Chem. Commun.* **2008**, 2373.
15. C. G. Liu, M. Liu, F. Li, H. M. Cheng, *Appl. Phys. Lett.* **2008**, 92, 143108.
16. B. E. Conway, *Electrochemical super capacitor and technological applications:* Kluwer-Plenum Press: New York, **1999**.
17. J. H. Jiang, A. Kucernak, *Electrochim Acta.* **2002**, 41, 2381.
18. B. Djurfors, J. N. Broughton, M. J. Brett, D. G. Ivey, *J. Power Sources.* **2006**, 156, 741.
19. C. Lin, J. A. Ritter, B. N. Popov, *J. Electrochem Soc.* **1998**, 145, 4097.
20. J. W. Lang, L. B. Kong, W. J. Wu, Y. C. Luo, L. Kang, *Chem Commun*. **2008**, 35, 4213.
21. L. Cao, F. Xu, Y. Y. Liang, H. L. Li, *Adv. Mater.* **2004**, 16, 1853.
22. M. Kaempgen, C. K. Chan, J. Ma, Y. Cui, G. Gruner, *Nano Lett.* **2009**, 9(5), 1872.
23. J. P. Metters, R. O. Kadara, C. E. Banks, *Analyst*, **2011**, 136 (6), 1067.
24. C. Yuan, X. Zhang, L. Hou, L. Shen, D. Li, F. Zhang, C. Fan, J. Li, *J. Mater. Chem.* **2010**, 20, 10809.
25. R. O. Kadara, N. Jenkinson, C. E. Banks, *Sens. Actuators B.* **2009**, 138, 556.
26. J.H. Yang, H. Hyodo, K. Kimura, T. Sasaki, *Nanotechnology.* **2010**, 21, 045605.
27. S. Tang, S. Vongehr, Y. Wang, L. Chen, X. Meng, *J. Solid State Chemistry*, **2010**, 183, 2166.
28. Z. Hu, L. Mo, X. Feng, J. Shi, Y. Wang, Y. Xie, *Materials Chemistry and Physics*. **2009**, 114, 53.
29. N. A. Choudhry, D. K. Kampouris, R. O. Kadara, N. Jenkinson, C. E. Banks, *Anal. Methods*, **2009**, 1, 183.
30. R. O. Kadara, N. Jenkinson, C. E. Banks, *Electroanalysis*, **2009**, 21 (22), 2410.
31. E. Hosono, S. Fujihara, I. Homma, M. Ichihara, H. Zhou, *J. Power Sources.* **2006**, 158, 779.
32. Z. A. Hu, L. P. Mo, X. J. Feng, J. Shi, Y. X. Wang, Y. L. Xie, *Mater. Chem. Phys.* **2009**, 114, 53.
33. J. Zhang, L-B. Kong, J-J. Cai, Y-C. Luo, L. Kang, *J. Solid State Elecrochem.* **2010**, 14, 2065.
34. V. Gupta, T. Kusahara, H. Toyama, S. Gupta, N. Miura, *Electrochem Commun.* **2007**, 9, 2315.

7.1 DRAWBACKS AND FLAWS IN CURRENT CAPACITANCE MEASUREMENTS

This section describes work undertaken during this thesis. A simple galvanostatic circuit methodology is reported that allows the capacitance of an electrochemical – electrolytic capacitor to be accurately measured without recourse to expensive instrumentation and avoiding problems found in current electrochemical impedance spectroscopy (EIS) analysis which gives rise to profiles which may results in false or inaccurate capacitance to be derived. This work arises from problems encountered during the calculation of capacitance values from non-linear galvanostatic charge-discharge profiles, where the gradient of $\frac{dt}{dV}$ vary along the resulting line or curve.

7.1.1 INTRODUCTION

As a result of the ever-increasing energy needs of a modern society and escalating environmental concerns, it has become imperative to discover new, alternative and innovative energy-storage systems, where it is evidently clear that conventional technologies, for instance batteries, offer inept solutions for new market applications.[1,2] Electrochemical supercapacitors are passive and static electrical energy-storage devices, utilised in applications such as memory back-up systems, portable electronics and high power devices such as hybrid/electric vehicles, where rapid charging and discharging is of fundamental importance.[3]Additionally they are relied upon to store-energy for long periods, while offering transient but extremely high powers, beyond those accessible by a typical battery and are probably the most important next generation energy-storage device.[4]

Capacitance is a measurement of the stored charge ratio between two conducting bodies separated by a dielectric material when a potential is applied, resulting in the formation of an electrostatic field. Capacitors are constructed by compressing an insulating material

(dielectric) between two conductors (plates).[5] Capacitors incur various losses, attributed to several characteristics such as; resistance in the conductors (plates) or leads, current leakage and dielectric absorption, likely having a significant impact on the power factor of the capacitor. [5] Theoretically, an ideal capacitor would demonstrate a power factor of zero; however, the losses listed above cause the power factors of realistic capacitors to range from approximately 0 to potentially 100%. The average power factor of high-quality capacitors (excluding electrolytic) typically lies between 2% and 3%. Current leakage, an inverse function of frequency, is important at low frequencies, becoming almost negligible at increased values. Dielectric absorption (sometimes referred to as dielectric viscosity) results in losses through the production of heat, this type of loss has similar effects to resistance in series with the capacitor.

Electrochemical techniques offer insightful evaluations of batteries and other energy-storage devices during the charge and discharge process. In particular, electrochemical impedance spectroscopy (EIS), a relatively new technique in electrochemistry, has become a powerful tool for electrochemists with the ability to characterise the electrical properties (including capacitance) of materials and their interfaces.[6] Although, a non-intrusive and highly sensitive technique, EIS necessitates basic but vital precautions, often overlooked, to attain error free data.

EIS measurements involve the imposing of a time harmonic electric potential with a particular frequency at the electrode. This harmonic potential encloses two elements, a time-independent “direct current potential” alongside a periodically oscillating potential with a small amplitude (typically less than 10 mV).[7-9] The resulting electric current is measured. The level of electrochemical impedance can be defined as the ratio between the amplitudes of oscillating potential [between the reference electrode (RE) and the working electrode (WE)] and current, measured as a potential drop over a precision resistor in series with the cell.

Clearly, the cell properties, electronic device characteristics, experimental parameters, or design restrictions, may influence the potential and current measurements, affecting the accuracy of the EIS experiment.[10]

Lufrano *et al.*[11] measured the capacitance of electric-double-layer capacitors (EDLCs) at carbon composite electrodes in a H_2SO_4 aqueous solution. The authors observed that the EDLC capacitances measured using EIS were reduced (potentially in the order of 20%) in comparison to those measured using galvanostatic charge/discharge.[11] The origins of this difference has been the subject of some controversy for some time.[12] Various hypotheses have been offered attempting to explain these observations[13–19] including the presence of "deeply trapped" counter-ions remaining immobile in EIS experiments,[13,17] changes in the electrode materials conformation,[15,18] and large hindrances to AC current penetration into porous electrodes.[20,21] There is still no clear or definitive explanation accounting for the observed discrepancies. Thus, EIS has been considered "the least reliable and accurate technique for determining the supercapacitive properties of materials" [12].

Herein, we highlight the nature of these limitations and report a novel yet simplistic (galvanostatic) circuit methodology that offers benefits over the for-mentioned system. The overall cost of construction (< £5) is insignificant in comparison to the advantages tendered.

7.1.2 EXPERIMENTAL SECTION

All chemicals used were of analytical grade and were used as received without any further purification and were obtained from Sigma-Aldrich. All solutions were prepared with deionised water of resistivity not less than 18.2 MΩ cm.

Voltammetric measurements were carried out using a μ-AutolabIII (ECO-Chemie, The Netherlands) potentiostat. All measurements were conducted using a three electrode configuration comprising a screen-printed carbon electrode on a flexible substrate consisting

of a carbon working electrode (9 mm diameter), a carbon counter, and on board silver/silver chloride reference electrode. Connectors for the efficient connection of the screen-printed electrochemical electrodes were purchased from Kanichi Research Services Ltd. [22]

The electrical circuit consists of a 500µF electrolytic capacitor situated between the two electrodes. Precision resistors (in the order of kΩ) are placed between; 1) the counter and reference contacts 2) the working connection and its corresponding electrode.

7.1.3 BACKGROUND

In an EIS investigation, the electric potential $\psi_s(t)$ imposed at the electrode is a harmonic function of time *t*. This produces a harmonic current density J_s (in A/m^2), providing the amplitude of the harmonic potential is small (e.g., less than 10 mV). By means of complex notations, the imposed electric potential and the corresponding current density can be written as: [7, 23-25]

$$\psi_s(t) = \psi_{dc} + \psi_0 e^{i2\pi ft} \text{ and } J_s(t) = J_{dc} + J_0 e^{i(2\pi ft-\phi)} \quad (7.1)$$

where ψ_{dc} and J_{dc} are the time-independent direct current potential and the direct current density, respectively. ψ_0 and J_0 define the amplitudes of the potential and current density, around their direct current components, respectively. i is the imaginary unit, f is the frequency (in Hz), while $\phi(f)$ is the frequency-dependent phase angle between the harmonic potential $\psi_s(t)$ and the current density $J_s(t)$. The complex electrochemical impedance Z is expressed below:[7, 23-25]

$$Z = \frac{\psi_0}{J_0} e^{i\phi} = Z' + iZ'' \quad (7.2)$$

where Z' and Z'' (expressed in Ωm^2) are the real and imaginary parts of the impedance, respectively. Built on the equivalent RC circuit shown in Figure 7.1C, the resistance and

capacitance per unit of surface area (also called specific resistance and capacitance) is given by: [7, 23-26]

$$R_S^{EIS} = \text{Z'} \text{ and } C_S^{EIS} = \frac{-1}{2\pi f Z''} \quad (7.3)$$

The resistance and capacitance for a given frequency are retrieved from the in/out-phase components of the measured electrochemical impedance.[7, 23-25] The phase angle (φ) often used in these calculations is defined as the shift by which the current is ahead of the potential.[7, 23-26] Equation (7.3) is the most frequently used formula in defining the capacitance obtained from EDLCs in EIS experimentation.[12, 26-30} Experimental modelisation of pure (non-Faradic) electric double layers, which form at the electrode/electrolyte interface (Figure 7.1A), involves a simple RC circuit consisting of a resistor and a capacitor in series (Figure 7.1C).[7, 23-31] Figure 7.1B provides an alternative circuit representation of the electric double layer coupled with the diffuse layer capacitance (formed through ion migration under the influence of electrostatic and diffusion forces).[23, 32-34]

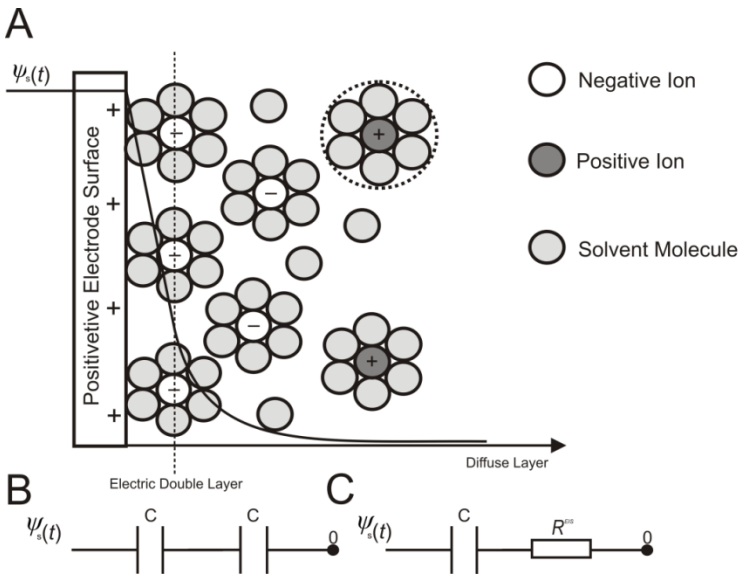

Figure 7.1 Schematic of (A) the electric double layer structure, displaying the arrangement of ions present at the electrode/electrolyte interface. Shown below is the computational electric circuit models of the electric double layer and diffuse layer capacitances in series (B), and the equivalent RC circuit used in EIS, (C).

In RC circuits, such as those commonly used in EIS, the capacitance is presumed to be either constant or dependent only on frequency,[23] however, this is not the case. Computationally studies have established that the specific capacitance also varied harmonically. [35] Consequently, the assumptions used for the equivalent RC circuits in EIS experimentation are invalid when representing the charging dynamics of electric double layers at high frequencies. This institutes an integral limitation to the RC circuits and EIS analysis. This constraint can be attributed to the RC circuit models used to describe the electric double layer shown in Figure 7.1. Thus, more complex RC circuits[32,42,43] or transmission line models[32,44–48] have also been developed through the introduction of additional electric circuit elements to represent electric double layers. Experimental EIS data is then fitted to these models in order to retrieve the resistance and capacitance values. These models are not without flaw; it is possible for two diverse models to produce the same impedance response, furthermore, the resulting impedance expression gives little or no direct information about the physical meaning of the elements that constitute the models. Capacitance values, fitted to complex RC circuits, using low frequency EIS, has been reported to systematically underestimate the observed capacitance values achieved by cyclic voltammetry at low scan rates [13-15,20,42,43,] and low current galvanostatic charge/discharge.[11,20,21,43] This was first witnessed during the measurements of pseudo capacitances found at various conducting polymers.[12-15, 44] This behaviour was also reported for various electrochemical capacitors.[11,12,20,21,42,43]

Previous studies have illustrated that the RC circuits or transmission line models can accurately represent the linearized model when both the potential and electrolyte concentration are low.[45–51] These models are not valid under large electric potential. Consequently, EIS measurements appears to be inadequate in determining the double layer

capacitances for ‘real’ applications where both concentrations and direct current potentials are typically high, such as those found at electrochemical capacitors developed for energy-storage applications. [12,20,21,43] In a dilute electrolyte environment, the EIS simulations overestimated the electric double layer capacitance, while the converse is found for concentrated electrolyte solutions. This substantiates existing experimental observations, reporting a discrepancies between EIS measurements[11–15,20,21,42-44] and other techniques such as cyclic voltammetry and galvanostatic charge/discharge. It has been documented that for large direct current potentials (conditions typical to the energy-storage mechanisms of EDLCs); the series RC circuit used in EIS to model the electric double layer (Figure 7.1C) is not valid. Consequently, more dependable and consistent techniques such as the galvanostatic charge/discharge or cyclic voltammetry should be favoured in defining the double layer capacitance.[12,20,21,43] Herein, we discuss further the physical considerations and model extraction parameters, often overlooked, which may have a significant impact on EIS experimentation.

7.1.4 RESULTS AND DISCUSSION

EIS - PHYSICAL ELECTROCHEMICAL CONSIDERATIONS: LINEARITY OF ELECTROCHEMICAL SYSTEMS

Electric circuit theory differentiates between linear and non-linear systems (circuits). Impedance analysis of linear circuits is far easier than that of a non-linear system. Within a typical potentiostatic electrochemical measurement, the input is the potential and the output the current; however doubling the voltage doesn’t necessarily double the current, thus making the system non-linear. Conversely, if a small enough segment of the current vs. voltage curve is taken under consideration, it can appear to be linear as shown in Figure 7.2. As mentioned previously, EIS applies a small alternating current (AC) signal to the cell, producing a system that appears pseudo-linear, but still large enough to measure a response. The impedance of a

capacitor decreases as the frequency is raised. This can result in the cells larger non-linear response to the direct current potential to be obscured as the measurement only takes place at the excitation frequency.[10] Linear dependence of capacitance on voltage is an approximation which improves the modelisation precision by 10% compared to constant capacitance approximation.[52] Today almost all electrical engineers involved in the development of supercapacitors fail to take into account the voltage dependence of capacitance in assigning devices to applications.

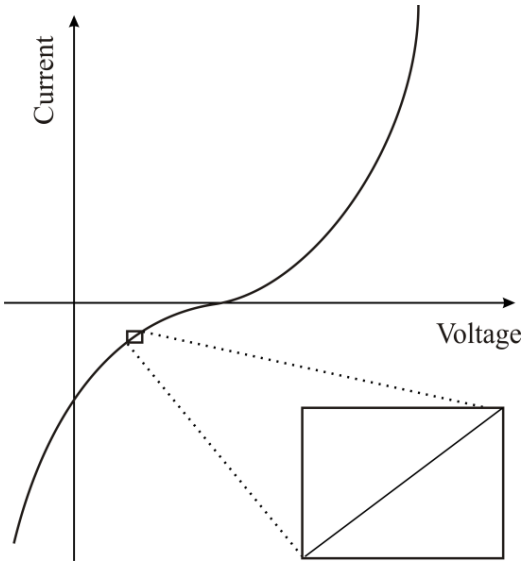

Figure 7.2 Example of a Current vs. Voltage curve for a pseudo-linear system.

STEADY STATE SYSTEMS

EIS analysis takes time (often many hours). The system must be at a steady state throughout the time required to measure the EIS spectrum, a common cause of problems in EIS analysis is drift in the system being measured.[6,10] Reaching a steady state can often be difficult to achieve, alteration caused through adsorption of solution impurities, production of oxide layers, reaction of products in solution, coating degradation or even temperature fluctuations affect the cell.

ELECTRIC CIRCUIT ELEMENTS

EIS data is commonly analysed by fitting the spectrum to an equivalent electrical circuit model. The elements that comprise these circuits are typical electrical elements such as resistors, inductors and capacitors. To be practically relevant, the elements in the model should have a basis in the physical electrochemical cell, thus most models contain a resistor that models the electrolytes resistance. Therefore, some knowledge of the impedance of the standard circuit components is quite useful. Very few electrochemical cells can be modelled using a single equivalent circuit element to obtain a reasonable fit. Instead, EIS models typically consist of a number of elements in a network.[6,10,53-57] However, when capacitors are connected in series; impedance increases, resulting in a decrease in the capacitance. This is caused by the inverse relationship between capacitance and impedance.

ELECTROLYTE RESISTANCE

Resistance offered by the electrolyte solution is often a significant contributor to the impedance of the cell.[10] A modern 3 electrode potentiostat compensates for the solution resistance between the counter and reference electrodes. However, the resistance between the reference and working electrodes must be considered when you model a cell. The resistance of an ionic solution is dependent of the concentration, type of ions, temperature and geometry of the area in which the current is transferred. Unfortunately, most electrochemical cells do not contain a uniform current distribution through a definite electrolyte area. Thus, a major problem in calculating the solution resistance concerns the determination of the current flow path and the geometry of the electrolyte that transmits the current.

CHARGE TRANSFER AND POLARIZATION RESISTANCE

Whenever the potential of an electrode is forced away from its open-circuit, the electrode is deemed to be polarised, causing current to flow through electrochemical

reactions that occur at the electrode's surface. The flow or rate of current transferred is controlled by the kinetics of the reactions, the diffusion of reactants both towards and away from the electrode, temperature and the potential.[6, 10]

DIFFUSION

The Warburg impedance,[10] based on diffusion, is dependent on the frequency of the perturbing potential. At high frequencies, diffusing reactants have only to travel a small distance, resulting in a small Warburg impedance. Conversely, low frequencies yield elevated impedance levels.

CONSTANT PHASE ELEMENTS

Capacitors (including double layer) in EIS experiments often do no display ideal behaviour. Instead, they act like a constant phase element (CPE). The impedance of a capacitor/CPE can be described as: [10]

$$Z_{CPE} = \frac{1}{(j\omega)^{\alpha} Y_0} \tag{7.4}$$

where Y_0 is the capacitance (C), ω is the circular frequency and α is generally a value between 0.9 and 1 (α = 1 for an ideal capacitor). For a constant phase element, α is less than 1. The 'double layer capacitor' in actuality, typically behaves like a CPE, not a capacitor. Several theories (surface roughness, "leaky" capacitor and non-uniform current distribution) have been proposed to account for the observed non-ideal behaviour of the double layer. [10] In contrast to a dielectric capacitor, the electric double layer capacitance of porous electrodes is known to depend on frequency. The origin of this so-called "capacitance leakage" observed at the electrode material[24,40,41,58–61] has been attributed to various phenomena such as surface defect,[61] surface roughness,[24, 58–61] pore size distribution (in porous electrodes),[40,41] and

specific ion adsorption,[24,60] among others. Interestingly, it has been shown that electric double layers display capacitance 'leakage' at high frequencies, even for perfectly planar electrodes where electrostatic phenomena are solely accountable.[35] This is attributed to the fact that at high frequencies, ion transport cannot follow the rapid variations in the electric potential.

7.1.4.2 EIS - EXTRACTION OF MODEL PARAMETERS

MODELLING OVERVIEW

EIS data is typically analysed in terms of an equivalent circuit model. The analyst must find an impedance model that correlates to the measured data. The electrical components within the model and there interconnections determine the shape of the model's impedance spectrum. The models parameters, such as the resistance value of the resistor, also have a direct impact on the size of each feature in the spectrum. These factors influence the degree to which the impedance spectrum matches the measured EIS spectrum.[6]

In a physical model, each component that makes up the model is postulated to come from a physical process in the electrochemical cell. Knowledge of the cells physical characteristics will influence the choice of which model is applied to a given system. It is important to note however that it is possible for one spectrum to have multiple equivalent circuit models. Experienced EIS analysts are able to use the shape of a cell's EIS spectrum to select a model for that cell. Models can also be partially or completely empirical.[10] In this case the circuit components are not assigned to a physical process in the cell; instead the model is a 'best' possible match between the model's impedance and the actual measured impedance. The model is constructed by successively subtracting impedance components from a spectrum. If the subtraction of an impedance element simplifies the spectrum, the component is added to the model, and the next impedance component is subtracted from the

simplified spectrum. This process ends when the spectrum has been completely void. Thus physical models are preferred to empirical models.[10] EIS spectra for ideal EDLCs remain independent of the applied direct current voltage; however, real devices do not show this behaviour.

SIMPLIFIED RANDLES CELL

Since the ideal capacitor very rarely/does not actually exist in reality, owed to various imperfections in the system, many systems models are used to describe the investigated system. Nonetheless, the simplified Randles cell is one of the most common cell models. It contains a solution resistance, a double layer capacitor and a charge transfer (or polarization) resistance. This has also been termed as the 'leakage' resistance. A small leakage resistance results in a high leakage current; responsible for self-discharge of a charged capacitor although no external load is connected. The double layer capacitance and charge transfer resistance are parallel to each other. Although useful in its own right, the simplified Randles model is the basis for more complex models. Figure 7.3B displays a circuit representation of the electrolytic capacitor where $R_{leakage}$ defines the leakage resistance; R_{ESR} is the equivalent series resistance (ESR) and L_{ESL} the equivalent series inductance. The Bode spectrum (a plot of phase versus frequency) of a typical Randles model displays three regions:[10] above 10 Hz, the equivalent series (or solution) resistance is dominant, only between 100μHz and 100mHz does capacitance control the impedance of the cell, while below 10μHz, the impedance begins the transition back towards resistive behaviour as the leakage current becomes dominant; this transition is incomplete even at 1μHz.

EIS spectra of real devices seldom gives relevant information about leakage resistance as its effects are seen at impractical low frequencies and measurements at these frequencies take extensive periods of time. While at higher frequencies the simple models 0° phase prediction is never actually met. Poor fits of actual capacitors to the Randles model can be a

result of electrode porosity, resulting in a no-uniform access of electrolyte towards the electrode's surface along with the occurrence of Faradaic reactions, thus simple resistor and capacitor models are not appropriate.[6, 10]

NON-LINEAR LEAST SQUARE FITTING

Currently, EIS analysis exploits computers to find model parameters that have the best agreement between the model impedance spectrum and the actual measured spectrum. This is done through a non-linear square fitting (NLLS) algorithm.[10]

NLLS begins with initial estimates for all model parameters. The algorithm performs adjustments to one of the parameter values and evaluates the resulting fit. If the alteration improves the fit, the new parameter is accepted. If the change worsens the fit, the old parameter value is retained. This test is then repeated on a different parameter and the subsequent results either retained or rejected. These iterations continue until the fit exceeds the acceptable criterion or until the number of iterations has reached a limit. These algorithms are far from perfect and in some cases cannot converge on a useful fit, with poor agreement when superimposed on the data spectrum, sometimes appearing as thought the fit has ignored a region in the data.[6,10,52-57]This is because the fit is an optimisation over the entire spectrum and deems a poor fit over a small section of the spectrum insignificant.

IMPROVED GALVANOSTATIC ANALYSIS

A potentiostat applies a voltage between the reference electrode (RE) and the working electrode (WE), forcing the WE to move to a more electropositive or electronegative region, in order to force the electrochemical reaction of any redox compound present in the solution. The applied voltage (or the potential waveform applied $-E_i$) is fed through an operational amplifier (OPA), which constantly monitors and ensures that the voltage source fed (E_i) is constant between the working and reference electrodes. In the case of changing conductivity (a impedance caused by transport phenomena occurring at the electrode's surface during

electrochemical reaction), the voltage values at the WE's surface fluctuates in comparison to the original E_i-fed value, thus the OPA compensates by feeding the circuit with a correction voltage. The correction voltage is applied through the counter electrode (CE), via the donation or acceptance of electrons, in order to eliminate the potential difference between E_{WE} and E_i, resulting in a current flow, measured through a precision resistor (Rm). A simple circuit schematic of a potentiostat is presented in Figure 7.3A.[5]

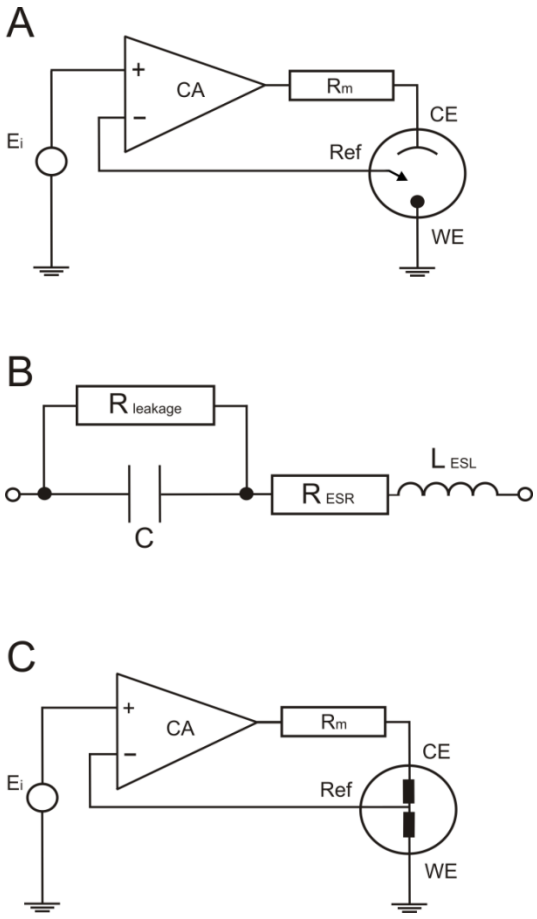

Figure 7.3 Basic internal schematic of: (A) a potentiostat, (B) electrolytic capacitor with impedance and leakage resistance elements, lastly the new circuit merged into the potentiostat system (C).

The measurement of capacitance for an electrolytic capacitor can be performed with either a direct current or alternating current (AC) system. The materials used to make the electrolytic capacitor introduce resistance and conductance characteristics affecting the observed values of capacitance.

The introduction of an electrode to a solution generates an interface; this interface (due to the dual phases) adds impedance to the circuit as mentioned previously. Additionally, the counter, reference and working electrodes each have their own impedance (a scheme of the impedance associated with the electrode is shown in Figure 7.3B).Therefore the capacitance measurement of the working electrode is not entirely accurate. The impedance incurred through the use of a counter and reference electrodes necessary during the analysis, can be eliminated via the introduction of an electrolyte into the solution. Unfortunately, electrolytes vary and thus different characteristics/values (capacitance) offered by the working electrode can be observed in different electrolytes, where KCl (considered an optimum electrolyte) is no longer used. The counter electrode (for instance Pt wire in a potassium hydroxide electrolyte, 6M) introduces another electrochemical reaction which many times is not considered when measuring the capacitance of the working electrode.

Presented herein is a new circuit which tenders an alternative, non-destructive solution to many of the problems discussed earlier in EIS investigation, along with enhancement to typical galvanostatic analysis of capacitance. The circuit eliminates the interferences and impedance introduced by both the counter and reference electrodes (Figure 7.3C). Precise resistors are introduced in series between; 1) the reference and counter contacts, 2) the WE connection and its corresponding electrode, limiting the rate at which the charge reaches the capacitor. A variable capacitor (or a group of parallel capacitors), producing a similar capacitance value to the supercapacitor under investigation, with a known (highly accurate) value is then introduced in series with these connections. This forces the system to become linear upon analysis (discussed below). Furthermore it offers improved control over the upper voltage limits, as extreme or elevated voltages may source irreversible electrochemical reactions at the electrode's surface. Parallel to the variable precision capacitor there are two connections where 'ideally' two similar working electrodes are

connected. The two working electrodes are then placed in the electrolyte solution; a schematic representation and its position within the potentiostatic system are shown in Figure 7. 4 and 7.3C, respectively.

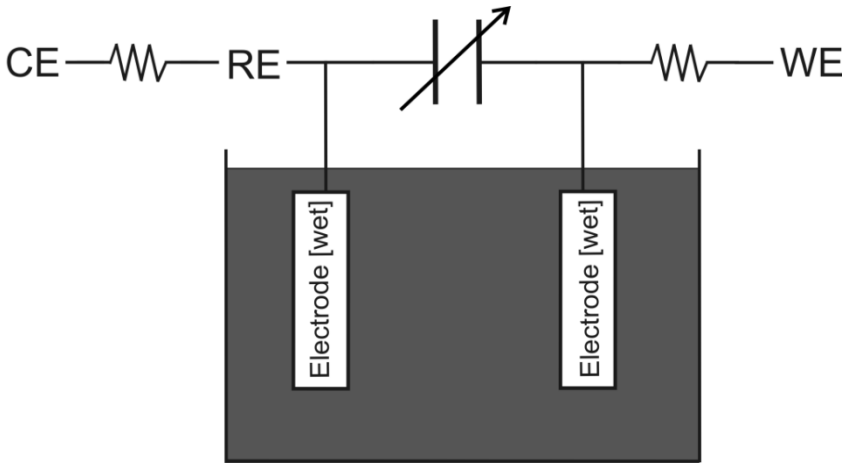

Figure 7.4 Scheme of the circuit for the measurement of the electrode capacitance where CE, RE, WE are the connections to the potentiostat for the counter, the reference and the working electrodes respectively, —WW— represent the Precise resistor and lastly ⊣/⊢ represents the Variable non polarized capacitor.

The total capacitance measured for the circuit (using a constant direct current) is given below:

$$C_{\text{Total}} = \frac{\text{dQ}}{\text{dV}} \tag{7.5}$$

$$C_{\text{Total}} = \frac{(\text{dQ/dt})}{(\text{dV/dt})} \tag{7.6}$$

$$C_{\text{Total}} = \frac{\text{I}}{(\text{dV/dt})} \tag{7.7}$$

or

$$C_{\text{Total}} = \text{I}\left(\frac{\text{dt}}{\text{dV}}\right) \tag{7.8}$$

or

$$C_{\text{Total}} = \frac{\text{I}}{\text{slope of } V \text{ vs } t} \tag{7.9}$$

After calculating the total capacitance, deduction of the capacitance contribution, tendered by the working electrode under investigation, can be calculated via the following equations:

$$C_{\text{Total}} = C_{\text{Known}} + 2\, C_{\text{WE}} \tag{7.10}$$

or

$$C_{\text{WE}} = \frac{(C_{\text{Total}} - C_{\text{Known}})}{2} \tag{7.11}$$

or

$$C_{\text{WE}} = \frac{\left(\frac{\text{I}}{(\text{dV/dt})} - C_{\text{Known}}\right)}{2} \tag{7.12}$$

where I is the charging current, C_{known} is the known value of the precise capacitor and dV/dt is the slope of voltage versus time. On many occasions, the slope (gradient) of V vs. t does not have a standard value (e.g. slope is non-linear) and thus difficult to measure its true value. Such a response is shown in Figure 7.5A. The addition of the known value capacitor(s) (in parallel with the working electrodes) is for this exact purpose, to produce a linear slope, thus allowing the value of dV/dt to be constant throughout and easily measurable. The variable capacitor(s) equate to that of the predicted capacitance value produced by the unknown working electrode (e.g. same units: μF, mF, etc. not exceeding two orders of magnitude difference in order to avoid the known capacitors dominating the response).

Galvanostatic analysis (charge-discharge) [57] of a carbon screen-printed electrode in 3M KOH at 0.1 Ag^{-1} without (Figure 7.5A) and with (Figure 7.5B) the new incorporated circuit, resulted in a capacitance measurement of 1 and 24 F g^{-1} respectively for identical

electrodes. A noticeable improvement in the linear slope of V vs. t is clearly shown, thus permitting a more accurate analysis of the capacitative characteristics to be established. The improvement in data analysis was seen for various electrode systems. The enhanced accuracy may decrease the capacitance values observed if the system was originally interpreted incorrectly.

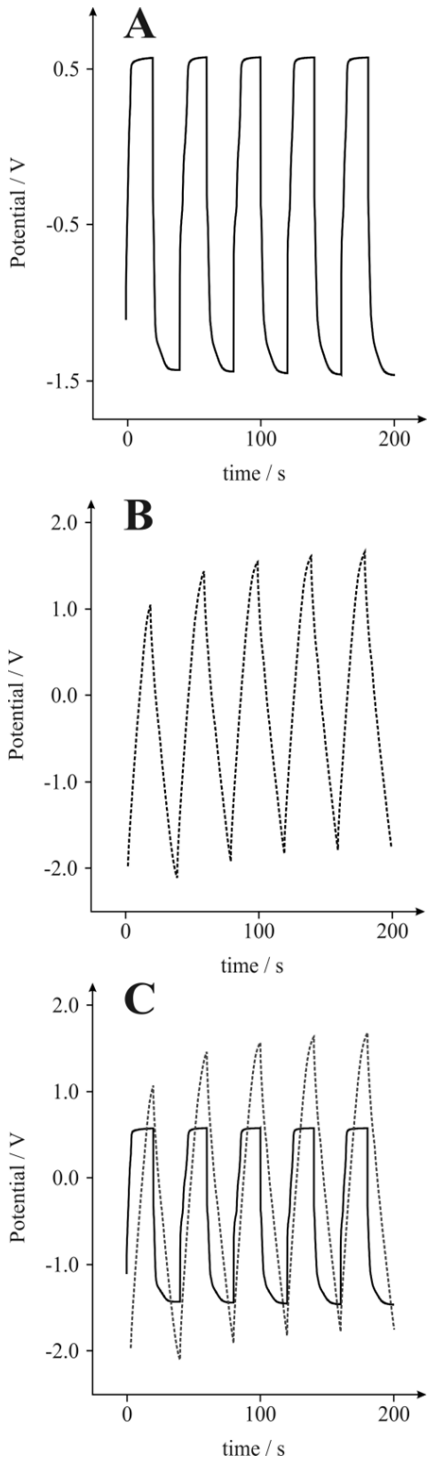

Figure 7.5 Typical galvanostatic charge-discharge of a graphite screen-printed electrode without (A), and with (B) the new incorporated circuit, generating slopes that produce capacitance values of 1 and 24 F g^{-1}, respectively. (C) displays an overlay of graphs (A) and (B); 5 cycles over 200 seconds in a 3M KOH solution at 0.1 Ag^{-1}.

7.1.5 CONCLUSIONS

Electrochemical impedance spectroscopy (EIS) is typically used in characterising the electrochemical behaviour of energy-storage devices. Several authors propose electric models, based on a 'best fit' approximation, that describe the electric behaviour of a supercapacitor , however, do not take into account their dynamic behaviour, consequently, the 'full' or 'true' behaviour of the capacitor is obscured. As shown in Figure 7.2, a linear AC response may not represent the overall response characteristics of the electrode. Considering the physical phenomena in the double-layer interface, the supercapacitor cannot be represented by a simple capacitor model formed only by a capacitance along with a series and a parallel resistance. The inconvenience of these models is the complex determination of the different elements and the simulation time required. EIS analysis can produce multiple equivalent circuit models that could correlate to a single observed spectrum. This paper presents a new (galvanostatic) circuit that enhances capacitance analysis through improved interpretation of results (linear slope of V vs. t). The direct measurement of capacitance means there is no model interpretation based on a 'best' fit. Rapid testing allows for steady state experimentation, negating the dynamic tendencies of some supercapacitors while eliminating the impedance sourced from interfaces found at the surface of the counter and reference electrodes.

7.1.6 REFERENCES

1. A. S. Arico, P. Bruce, B. Scrosati, J. M. Tarascon, S. W. Van, *Nat. Mater.,* **2005**, 4, 366.
2. X. Du, C. Wang, M. Chen, Y. Jiao,J. Wang, *J. Phys. Chem. C.*,**2009**, 113, 2643.
3. D. A. C. Brownson**,** D.K. Kampouris**,** C.E. Banks,*J. Power Sources,***2011**, 196, 4873.
4. C-C. Hu, K-H. Chang, M-C. Lin, Y-T. Wu, *Nano Lett.,* **2006**, 6 (12), 2690.
5. B. E. Conway, Electrochemical super capacitor and technological applications:

Kluwer-Plenum Press: New York, **1999**.

6. E. Barsoukov, J. R. Macdonald, *Impedance Spectroscopy; Theory, Experiment, and Applications*, *2nd ed*, Wiley Interscience Publications, **2005**.
7. X. Z. Yuan, C. Song, H. Wang, J. Zhang, *Electrochemical Impedance Spectroscopy in PEM Fuel Cells: Fundamentals and Applications*, Springer-Verlag, London, UK, **2010**.
8. D. Pech, M. Brunet, H. Durou, P. Huang, V. Mochalin, Y. Gogotsi, P. L. Taberna, P. Simon, *Nat. Nanotechnol*. **2010**, 5, 651.
9. H. Itoi, H. Nishihara, T. Kogure, T. Kyotani, *J. Am. Chem. Soc*. **2011**, 133, 1165.
10. M. E. Orazem, B. Tribollet, *Electrochemical Impedance Spectroscopy,* John Wiley & Sons, **2008**.
11. F. Lufrano, P. Staiti, M. Minutoli, *J. Power Sources*, **2003**, 124, 314.
12. A. T. Chidembo, K. I. Ozoemena, B. O. Agboola, V. Gupta, G. G. Wildgoose, R. G. Compton, *Energy Environ. Sci.* **2010**, 3, 228.
13. J. Tanguy, J. L. Baudoin, F. Chao, M. Costa*, Electrochim. Acta* **1992**, 37, 1417.
14. X. Ren, P. G. Pickup, *J. Electrochem. Soc*. **1992**, 139, 2097.
15. X. Ren, P. G. Pickup, *J. Electroanal. Chem*. **1994**, 372, 289.
16. I. Rubinstein, E. Sabatani, J. Rishpon, *J. Electrochem*. *Soc*. **1987**, 134, 3078.
17. J. Tanguy, N. Mermilliod, M. Hoclet, *J. Electrochem*. *Soc*. **1987**, 134 795.
18. M. Kalaji, L. M. Peter, *J. Chem. Soc*., *Faraday Trans*. **1991**, 87 853.
19. J. Bobacka, A. Lewenstam, A. Ivaska, *J. Electroanal. Chem*. **2000**, 489, 17.
20. A. B. Fuertes, G. Lota, T. A. Centeno, E. Frackowiak, *Electrochim. Acta*. **2005**, 50, 2799.
21. W. Xing, S.Z. Qiao, R. G. Ding, F. Lid, G. Q. Lu, Z. F. Yan, H. M. Cheng, *Carbon*. **2006**, 44, 216.
22. http://kanichi-research.com; accessed Aug 2012.
23. A. J. Bard, L. R. Faulkner, *Electrochemical Methods: Fundamentals and Applications*, John Wiley & Sons, New York, NY, **2001**.
24. A. Lasia, *Electrochemical impedance spectroscopy and its applications, in: B*. Conway, J. Bockris, R. White (Eds.), Modern Aspects of Electrochemistry, No. 32, Kluwer Academic Publishers, New York, NY, **2002**, p. 143.
25. M. E. Orazem, B. Tribollet, *Electrochemical Impedance Spectroscopy*, John Wiley & Sons, Hoboken, New Jersey, **2008**.
26. P. L. Taberna, P. Simon, J. F. Fauvarque, *J. Electrochem. Soc*. **2003**, 150, 292.

27. R. Kotz, M. Carlen, *Electrochim. Acta*. **2000**, 45, 2483.
28. J. Segalini, B. Daffos, P.L. Taberna, Y. Gogotsi, P. Simon, *Electrochim. Acta.* **2010**, 55, 7489.
29. J. R. Miller, R. A. Outlaw, B. C. Holloway, *Science.* **2010,** 329, 1637.
30. Y. Zhu, S. Murali, M.D. Stoller, K.J. Ganesh, W. Cai, P.J. Ferreira, A. Pirkle, R.M. Wallace, K. A. Cychosz, M. Thommes, D. Su, E. A. Stach, R. S. Ruoff, *Science.* **2011**, 332, 1537.
31. B.-Y. Chang, S.-M. Park, *Annu. Rev. Anal. Chem.* **2010**, 3, 207.
32. B.E. Conway, *Electrochemical Supercapacitors: Scientific Fundamentals and Technological Applications*, Kluwer Academic/Plenum Publishers, New York, NY, **1999**.
33. R. de Levie, in: P. Delahay, C. Tobias (Eds.), *Advances in Electrochemical Science and Engineering, vol. 6,* Interscience Publishers, New York, NY, **1967**, p. 329.
34. H. Keiser, K.D. Beccu, M.A. Gutjahr, *Electrochim. Acta,* **1976**, 21, 539.
35. H. Wang, L. Pilon, *Electrochim. Acta,* **2012**, 63,55.
36. J. R. Macdonald, *Electrochim. Acta*, **1990,** 35, 1483.
37. L.A. Geddes, *Ann. Biomed. Eng*. **1997**, 25, 1.
38. R. de Levie, *Electrochim. Acta,* **1963**, 8, 751.
39. I.D. Raistrick, *Electrochim. Acta,* **1990**, 35, 1579.
40. H.K. Song, Y.H. Jung, K.H. Lee, L.H. Dao, *Electrochim. Acta,* **1999**, 44, 3513.
41. H.K. Song, H.Y. Hwang, K.H. Lee, L.H. Dao, *Electrochim. Acta,* **2000**, 45, 2241.
42. J.P. Zheng, P.C. Goonetilleke, C.M. Pettit, D. Roy, *Talanta,* **2010**, 81, 1045.
43. K. Kierzek, E. Frackowiak, G. Lota, G. Gryglewicz, J. Machnikowski, *Electrochim. Acta,* **2004**, 49, 515.
44. C. Peng, J. Jin, G. Z. Chen, *Electrochim. Acta*., **2007**, 53, 525.
45. R. P. Buck, *J. Electroanal. Chem*., **1969**, 23 219.
46. T. R. Brumleve, R. P. Buck, *J. Electroanal. Chem*., **1981**, 126, 73.
47. M. Z. Bazant, K. Thornton, A. Ajdari, *Phys. Rev*., E 70 (021506) **2004**, 1.
48. R. P. Buck, *J. Electroanal. Chem*., **1986**, 210, 1.
49. G. C. Barker, *J. Electroanal. Chem*., **1973**, 41, 201.
50. K.T. Chu, M.Z. Bazant, *Phys. Rev.,* E 74 (011501) **2006** 1.
51. E. J. F. Dickinson, R. G. Compton, *J. Electroanal. Chem*., **2011**, 655, 23.
52. F. Rafik, H. Gualous, R. Gallay, A. Crausaz, A. Berthon, *J. Power Sources,* **2007**, 165, 928.

53. G.W. Walter, *Corrosion Science*, **1986,** 26, 681.
54. F. Mansfeld, *Electrochim.Acta.*, **1990**, 35, 1533.
55. E. Karden, S. Buller, R.W. De Doncker, *Electrochim. Acta*, **2002**, 47, 2347.
56. D. Qu, H. Shi, *J. Power Sources*, **1998**, 74, 99.
57. A. Burke, *J. Power Sources*, **2000**, 91, 37.
58. G. J. Brug, A. L. G. van den Eeden, M. Sluyters-Rehbach, J. H. Sluyters, *J. Electroanal. Chem.,* **1984**, 176, 275.
59. T. Pajkossy, *J. Electroanal. Chem*., **1991**, 300, 1.
60. T. Pajkossy, *J. Electroanal. Chem*., **1994**, 364, 111.
61. Z. Kerner, T. Pajkossy, *Electrochim. Acta*, **2000**, 46, 207.

8.1 CONCLUSIONS

The question set out prior to this thesis was “can screen-printed electrochemical platforms form the basis of next generation energy-storage devices?” The unpretentious answer is yes. The investigation contained within this report contribute towards the understanding of next-generation electrochemical energy-storage devices through the assessment and development of new supercapacitors based upon true screen-printed platforms, identifying and understanding their physical interactions with novel carbon and metal-based nanomaterials, offering inherent advantages over current systems. The incorporation of the various nanomaterials into the screen-printed electrochemical platform tenders enhanced affinities towards stored charge (capacitance), while retaining the unique and highly sort-after characteristics typical to the screen-printed electrode. A differing assortment of modified electrodes (Chapter 6) were developed, each contributing to the optimisation of the screen-printed supercapacitors, however I believe there are still important findings to be made, this is discussed further in the subsequent ‘Future Work’ section (8.2). Key progress in identifying the impact of oxygenated species, present both in the stabilisation of metal nanomaterials and at the SPEs surface have been uncovered, displaying improved electrode performance that may hold significant importance in future developments. The inks that form the underpinning basis of the electrode are fundamental. This thesis describes the importance of understanding and characterising the electron transfer processes of carbon based (nano) materials that may comprise the foundations of the platform. Chapter 4 shows how the basal and edge-plane content of carbon nanomaterials can be calculated without recourse to expensive equipment typically required to conduct such analysis. This simple

methodology can be applied to establish the impact of new carbon nanomaterials designed for the possible enhancement of energy-storage devices.

Finally, this work highlights and transcends many of the difficulties, frequently ignored during EIS analysis, which may results in false or inaccurate measurements of capacitance. This was accomplished through the development of a simplistic circuit working in conjunction with galvanostatic charge discharge analysis, offering a more precise interpretation of results.

8.2 SUGGESTIONS FOR FUTURE WORK

Following the investigations described in this thesis, there are several lines of research arising from this work which should be pursued. One such direction, following on from chapter 6, would be to investigate the results of integrating other transition-metal nanomaterials on the energy-storage characteristics of the electrochemical screen-printed platforms. Rare metals may hold the greatest potential, but often entail a much higher cost, this is important when considering industrial-style production. Possible assimilation of multiple nanomaterials, each tendering different energy-storage mechanisms or potential windows (in the case of pseudo-capacitance), may offer an alternative approach. This could be extended into looking at the integration or layering of electroactive polymers at the electrode's surface. As seen in chapters 5 and 6, the influence of oxygen cannot be overlooked. Commonly residing along the surface of carbon compounds and found in conjunction with most metals, a greater understanding of the behaviour, interactions and impact of oxygen on the charge storage characteristics of the electrochemical platform is required before it can be manipulated appropriately and it's true potential harnessed. Some research has seen adverse effect from the inclusion of oxygen groups, but with improved knowledge these observed deficiencies may be overcome.

A secondary line of research may focus on the exploitation of new ink formulations and blends that may offer unique and interesting bases on which to build new electrodes. Interestingly, companies such as Nanolab have recently developed purely based CNT inks. Investigations into the properties of this ink would be prudent in the advancement and understanding of carbon nanomaterial behaviour towards stored charge and Faradaic reaction. Previously, the benefits of integrating nanomaterials, especially in small quantities, could be masked by the bulk carbon ink domain, conversely large percentage blends will affect the rheology and thus the printability of the ink. This interesting material offers an ideal starting platform for future studies. Alternatively, research into the fabrication of novel, high surface area carbon screen-printed electrodes may yield improved performances to those observed in this work. These studies may be complemented by an investigation into the consequence of new electrode designs, altering the geometric parameters such as layer thickness and working surface area.

Finally, the influence of organic and ionic liquid electrolytes towards enhanced charge storage characteristics should be explored. The electrolyte will have an impact on the voltage window accessible to the electrochemical device as well as the environmental conditions of the cell, assisting specific reaction mechanisms or more energy dense metals to improve performance.

Note; changing multiple parameters at once may cause results to become convoluted and conclusion deduced incorrectly.

1. P. M. Hallam, D. K. Kampouris, R. O. Kadara, N. Jenkinson, C. E. Banks, *Nickel-oxide screen-printed electrodes for the sensing of hydroxide ions in aqueous solutions, Analytical Methods,* **2010**, 2 (8), 1152.

2. P. M. Hallam, D. K. Kampouris, R. O. Kadara, C. E. Banks, *Graphite screen-printed electrodes for the electrochemical sensing of chromium (VI), Analyst*, **2010**, 135 (8), 1947.

3. P. M. Hallam, C. E. Banks, *Quantifying the electron transfer sites of graphene*, *Electrochem. Commun*. **2011**, 13 (1), 8.

4. P. M. Hallam, C. E. Banks, *A facile approach for quantifying the density of defects (edge-plane sites) of carbon nanomaterials and related structures*, *PCCP*, **2011**, 13 (3), 1210.

5. P. M. Hallam, C. E. Banks, *Solid Carbon Nanorod Whiskers: Application to the Electrochemical Sensing of Biologically Relevant Molecules, RSC Advances,* **2011**, 1 (1), 93**.**

6. X. Ji, P. M. Hallam, S. M. Houssein, R. O. Kadara, L. Lang, C. E. Banks, *Printable thin film supercapacitors utilizing single crystal cobalt hydroxide nanosheets*, *RSC Advances*, **2012**, 2 (4), 1508.

7. P. M. Hallam, M. Gómez-Mingot, D. K. Kampouris, C. E. Banks*, Facile synthetic fabrication of iron oxide particles and novel hydrogen superoxide supercapacitors, RSC Advances,* **2012**, 2 (16), 6672.